The Search for the Standard Model Higgs Boson in $H \to \gamma\gamma$ Decays with the ATLAS Detector in 4.9 fb^{-1} of 2011 Data at $\sqrt{s} = 7$ TeV

Lillian Smestad

Department of Physics
University of Oslo
Norway

Dissertation presented for the degree of
Philosophiae Doctor (PhD) in Physics

February 2013

Series of dissertations submitted to the
Faculty of Mathematics and Natural Sciences, University of Oslo
No. 1348

ISSN 1501-7710

Cover: Inger Sandved Anfinsen.
Printed in Norway: AIT Oslo AS.

Produced in co-operation with Akademika Publishing.
The thesis is produced by Akademika publishing merely in connection with the thesis defence. Kindly direct all inquiries regarding the thesis to the copyright holder or the unit which grants the doctorate.

Abstract

The ATLAS detector at the LHC collider located at CERN is designed to unveil physics of the smallest building blocks of Nature in energy domains previously unseen. Integrated in the Standard Model of elementary particle physics is a mechanism for breaking the electroweak symmetry, which performs the non-trivial task of assigning mass to the elementary constituents, commonly called the Brout-Englert-Higgs (BEH) mechanism. In order to examine whether the field introduced in this mechanism exists or not, searches for the manifestation of the field, often called the Higgs boson, are performed. This thesis addresses the search for the Standard Model Higgs boson through its decay to two photons, one of the most promising ways of discovering the particle, should it exist.

Diphoton candidate events in 4.9 fb^{-1} of 2011 data at a center-of-mass energy of $\sqrt{s} = 7$ TeV are selected and sorted into nine different categories, based on mass resolution and signal-to-background ratio. One of the criteria for selecting these Higgs boson candidate events is lower thresholds on the transverse momenta of the two photons. These cuts had not been re-evaluated since the 1990's; in this thesis, cuts which vary linearly with the Higgs boson invariant mass are studied.

The high production rate of jets at the LHC, in combination with the high jet rejection factor needed to be able to resolve a signal in this decay channel, make it impossible to produce full Monte Carlo background simulation samples with sufficient statistics. Therefore, the normalization and shape of the background is taken solely from fits to the nine categories of data. Properties of several background parametrizations were investigated in detail, and the choice of which ones to use for the different categories was made "blindly" in Spring 2012, *i.e.* before looking at the 2012 data.

As an alternative to the statistical procedure of ATLAS for evaluating the support or lack of evidence for a Higgs boson signal in data, a method in which each event is given a weight based on the expected sensitivity of the category it belongs to is implemented. The resulting weighted invariant mass spectrum was used to evaluate the significance of the excess seen in 2011 data. At the mass where the maximum excess is seen, $m_{\text{H}} = 126.5$ GeV, the significance expected for the SM Higgs boson is 1.4σ, while the observed significance is 1.9σ. These results are roughly compatible with published ATLAS results for $\text{H} \to \gamma\gamma$, which were used for the combined result in the article claiming the discovery of a 'Higgs boson'-like particle in July 2012.

Acknowledgements

I give my warmest thanks to my supervisor Alexander Lincoln Read for his guidance, advice, help and caring. His support, which has taken place on many levels, has been tremendously important to me. I am very grateful that he was willing to "get his hands dirty" and submerge in the gritty details of coding the times I was stuck. Over the course of the six years we have been working together, he has gotten to know me as a person, seeing me both in my weakest and strongest states. I value that he was attentive to the degree that he learned to take one look at me, and immediately understand what state I was in, or how I felt about a topic up for discussion. Our (gallows) humour and level of communication is something I cherish.

My thankfulness also goes to the High Energy Physics group in Oslo in general – a group full of very nice people of very different characters. The variety of topics discussed over lunch is a good indicator of the diversity and playfulness of the group. I am particularly grateful for the opportunity to travel and take courses, allowing me to expand my horizons both on the professional and personal level. Thank you for giving me the chance to work with what undeniably is my profound passion, and letting me realizing my dreams. Additional thanks is also due for extending the financing of my PhD, supporting me in finishing up this life-project.

Are Raklev deserves thanks for making sure the theoretical chapter was sound, and for dealing with my insisting on posing fundamental questions until exhausting both me and the target of my inquiries. He let me realize that not knowing the answer to some of my questions was utterly legitimate. Indeed, one must work extensively and learn a lot, to feel this ignorant.

I want to extend my gratitude to the LaL group at Orsay, Paris, for their passion for the field, their willingness to help, their keen attention to details, and for giving me the opportunity to come repeatedly to work with them. The Higgs Hunting workshops are still the best conferences I ever went to. A special thanks to Jana Schaarschmidt for welcoming my inputs and for her sarcastic humour, to Narei Lorenzo for all her answers and for sharing her office with me, and to Marc Escalier for his inspiring and supporting words, his firm belief in that problems could be solved – and not least, for having seen me when I was invisible.

I feel deeply grateful for my family, who was there to pick me up the times I broke apart. I love you to the end of time. A thank you to my mother, Liv Mobæk Smestad, for staying cool and giving practical advice on how to deal with problems, and for listening the times I called and was in desperation. A thank you to my father, Tore Smestad, for his enthusiasm and curiosity about the details of my

work, and for his input to my thesis. Without his passion for the field of physics, I have my doubts that I would be where I am today. A thank you to my sister, Bente Smestad, for the close and honest relationship we share, for the humour, and for the encouraging words before every trial in the course of the PhD.

My heartfelt thanks go to all my dear friends, without whom my life would be so much poorer, and my mental health much worse. This include both Oslo and CERN people, too many to mention, but some few would be Kosovare Olluri, Kristin Mikkelsen, Tuva Hope, Ingvar Andersen, Nicolaas Groeneboom, Eirik Berntsen, Zofia Czyzuła, Alexandros Attikis, Monica Moen, Simon Kvernmo Mailand, Erlend Sand Bruer, Espen Pettersen and Henriette Carstensen. Thank you for all the get-togethers, messages, movies, games, experiences in nature (ranging from frost bitten cross-country tours to mountain biking in the Alps), creative inspiration (both in music and handcraft), conversations, face-slaps, jokes, calm nights and crazy mornings.

Daniel Fink receives my warmest gratitude for giving my life a new dimension. Emerging out of it were, in addition to so many other things, hope, inspiration and motivation for finishing the PhD. Thank you for repeatedly telling me I was doing better than I felt myself, for the wordless backing-up, and for understanding my being absorbed in such a project, which sometimes resulted in times where I was low, distant and stressed. The love and care you have given has been invaluable to me. My black hole and supernova – You are the best.

The difference

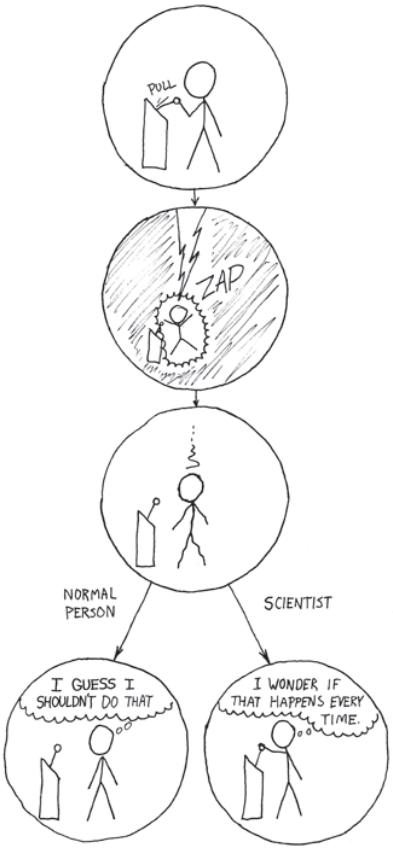

From http://xkcd.com/242/

Contents

Chapter 1

Introduction

The concept of mass is to us humans no mystery; we are used to dealing with objects being massive in our everyday life. Which, when thinking about the origin of the mass itself, is fine – almost. Almost, because most of the mass we deal with in our macro-world is free of problems. Take the proton and neutron, which we mainly consist of: 99% of their mass is due to energy stored in them ($E = mc^2$), arising from the motion of the elementary building blocks inside them. Although we are comfortable with the origin of mass for composite particles, like the proton and neutron, assigning mass to elementary particles, constituents without any inner structure, has proven to be a cumbersome task. In the case of the proton and neutron, this concerns the up- and down-type quarks that they are built up of. It also concerns the electron, one of the most well-known fundamental constituents. Without the mass of these smallest building blocks of Nature, the world as we know it would not exist; if elementary particles did not have mass, they would inevitably travel at the speed of light, in every possible direction – meaning nothing would lump together – and there would be no galaxies, planets, octopi nor humans, not even hydrogen.

One of the most established theories of today that attempts to explain the mass of point-like particles, is the Brout-Englert-Higgs (BEH) mechanism. This mechanism is an integral part of the Standard Model of particle physics (SM), describing the known elementary constituents and their behaviour. We will learn more about the theory of elementary particle physics and the BEH mechanism in Chapter 2. The BEH mechanism predicts the existence of a new particle; the Higgs boson. Unlike any other fundamental particle observed in Nature, this fundamental constituent has spin 0. Albeit rigorous hunting since its prediction in the mid-sixties, a candidate for such a particle was not observed – not until the

summer of 2012 (there were tantalizing hints at the end of 2011), in the course of this PhD thesis, which we will come back to shortly. It took nearly 50 years, but an era has now ended; the hunt for a 'Higgs boson'-like particle is successfully completed. Now begins the era of measuring the new particle that was observed, pinpointing its properties, to see whether they are in compliance with the ones of the Standard Model Higgs boson. The new particle may also have siblings, so searches for additional Higgs bosons should continue.

The Large Hadron Collider (LHC) at the CERN laboratory produces conditions similar to the ones present shortly after the Big Bang, by colliding protons travelling at speeds close to the speed of light against each other. Given these conditions, the Higgs boson would be created, if it did exist. The ATLAS detector was built to be able to observe the Higgs boson if produced by the LHC. The Higgs boson is a very unstable particle, and will almost immediately be transformed to other, lighter particles. The different ways the Higgs boson can be transformed are called *decay channels*, and always consist of pairs of elementary particles. Since the Higgs boson is so unstable, it cannot be detected directly, and one must search for the decay products. One of the most promising ways to search for the Higgs boson, given that it has a low mass (which was preferred by the combination of theory and precision measurements of electroweak processes, and now possibly confirmed by experimental results), is via the decay of the Higgs boson to two photons; $\mathrm{H} \to \gamma\gamma$. The electromagnetic calorimeter of ATLAS was designed such that it guaranteed the ability to resolve a resonance in this decay, a true challenge because of the large background noise. We will learn more about CERN and the ATLAS detector in Chapter 3.

To render possible a discovery with a limited amount of data, different decay channels should be combined. Most important for discovery are the sensitive, high mass resolution $\mathrm{H} \to \gamma\gamma$ channel, the sensitive, high mass resolution $H \to ZZ \to 4l$ channel, and the sensitive, but poor mass resolution $H \to WW \to l\nu l\nu$. The work of this thesis has been performed as part of the ATLAS Higgs working group called HSG1 (Higgs SubGroup 1), occupied with the Higgs decay into two photons. The object of this thesis was to aid to the search of the Higgs boson in the diphoton ($\gamma\gamma$) decay channel, and to perform cross-checks of the official results.

Results from global fits to electroweak precision measurements give an indirect limit on the Higgs boson mass of $m_{\mathrm{H}} < 158$ GeV at the 95% CL [1]. Direct searches at LEP constrained the mass from below, to $m_{\mathrm{H}} > 114$ GeV [2]. Previously, both ATLAS and CMS experiments at the LHC continuously increased the domain of excluded masses up to 600 GeV with the 2011 data, apart from a small window between 116 GeV and 127 GeV. With this same data, ATLAS and CMS reported on an excess in the mass region of 124 – 126 GeV compatible with the production

and decay of the Higgs boson, at a local significance of 3.5 and 3.1 standard deviations, respectively [3, 4]. With the additional data taken in 2012 before the summer conferences, this excess got more pronounced, up to the level of 5.9 standard deviations for ATLAS and 5.0 standard deviations for CMS [5, 6] – and the discovery of a new particle was announced by CERN the 4^{th} of July 2012.[1] The DØ and CDF experiments at Tevatron reported at the same time a combined, broad excess in the $b\bar{b}$ decay channel of associated production with a W or Z boson of globally 3.1 standard deviations from the background-only hypothesis, largest in the region 120 – 135 GeV [7].

Throughout the time of data harvesting at the LHC until the discovery was announced, I was part of the HSG1 group, working on the $H \to \gamma\gamma$ search. The thesis is based on the data gathered with the ATLAS detector in 2011, comprising 4.9 fb^{-1}, and the analysis results presented in this thesis are not all official results, but are meant to serve as an independent cross-check. Work has naturally also been put into aiding HSG1, performing small studies to improve or investigate, which is part of the big picture, hidden behind the final, official results. When finishing up the analysis of this thesis, a new particle in agreement with the SM Higgs boson was discovered. Performing analysis after this discovery, it was naturally difficult to stay unaffected. However, to the degree possible, the methods were aimed at being removed from human bias. For instance, modeling of the background was decided upon using a "blind" approach; the data of 2012 was not looked at before the choice of background models had been made. The input to this study is one of the main contributions of this thesis. This is a central aspect of the search. In order to be able to claim a discovery of the Higgs boson, one needs to know the background noise, to separate it from the signal, such that one can make an as accurate as possible statement about the probability of the data being in compliance or not with the production and decay of the SM Higgs boson.

The identification of photons in the ATLAS detector is, needless to say, a crucial point for the $H \to \gamma\gamma$ search; this is described in Chapter 4. In order to assess the performance of analysis, to give a feeling for what might be possible to obtain with data, Monte Carlo simulations were made and used. These should as closely as possible reproduce the data. In order to achieve this, various corrections were

[1] This was a truly amazing day for me as a person and scientist. As one of the available scientists working on the Higgs search in Norway, I got the opportunity to tell people about the discovery, and featured in multiple news of Norway from 9 o'clock in the morning, among others NRK (national broadcasting company) radio shows 'Ekko', 'Nyhetslunsj', 'Ukeslutt', 'Dagsnytt18' as well as television news at 12, 15 and 17 o'clock, and the main news broadcast 'Dagsrevyen' at 19 o'clock. I was also a guest at the show 'Sommeråpent', half past nine in the evening, watched by approximately 600.000 citizens. In addition, interviews and articles for news papers like 'Aftenposten', 'Dagbladet', 'Nettavisen' and the scientifically based blog 'Higgsjegerne' on forskning.no were given or written, some in cooperation with other scientists.

applied to the simulations. Corrections to data were also made, based on knowledge about the detector response. The corrections applied to the data and Monte Carlo samples used for this thesis are listed in Chapter 5. The $H \to \gamma\gamma$ signal is described in Chapter 6, whereas the background to this decay channel, consisting both of an irreducible part of true photons, and a reducible part of fake photons, is addressed in Chapter 7. Reducing as much as possible of the background is essential in order to be able to reveal a signal. How to reject the large Quantum ChromoDynamics (QCD) background, mostly consisting of $\pi^0 \to \gamma\gamma$, is presented here. Aiming at reducing the background while keeping the signal, a study of variable cuts on the transverse momenta of the two photons was performed (this is a potential improvement to the official analysis). Also in this chapter, is how to select the signal candidate events for the analysis, as well as the categorization of these. We will have a look at the invariant mass distributions of the categories, both for standard and variable p_T cuts, and give a rough estimation of the performance of the analysis under these two sets of cuts.

An introduction to the statistical procedure of ATLAS, as well as the signal and background models applied for the search, can be found in Chapter 8. The modeling of the background to the $H \to \gamma\gamma$ search is, as already mentioned, a main ingredient for being able to exclude or discover a signal, and is therefore addressed more thoroughly. The implementation and study of a "spurious signal", as a means to describe the residual uncertainty on the background, is detailed. As an alternate way to the HSG1 statistical procedure to evaluate the final result of the analysis, an approach in which the events are weighted according to the expected sensitivity of the categories is performed in Chapter 9. The findings of the various analyses will be summarized in the conclusions, presented in Chapter 10. Lastly, the historical development of the HSG1 analysis, and the result of combining the various decay channels will be addressed in the epilogue.

In the field of experimental particle physics, abbreviations and unfamiliar expressions flourish. Each such is introduced in the text, but should the term be forgotten in the course of reading, please be referred to Appendix A, containing an overview along with some comments on relevance. In order to become an author for the ATLAS experiment, a rather extensive, designated task must be undertaken. In my case, this task was performed as part of the e/gamma trigger community and is described in Appendix B. For the implementation of systematic uncertainties as part of the statistical procedure, the log-normal constraint term is sometimes applied. However, this term seems not to be properly documented within the community. Aiming at doing so, the log-normal term is described in Appendix C. The cut values on the shower shape variables used in the identification of photons are listed in Appendix D, and in Appendix E a list of the datasets used in the thesis is given.

Chapter 2

Theoretical Stage

The knowledge mankind presently possesses concerning the physics of elementary particles has naturally evolved over time, driven by the curiosity of individuals about the world surrounding them. In this chapter, a brief outline of the history of gaining knowledge about the smallest, known building blocks of Nature will be given, aimed at non-experts. In the coming sections, more detail about the Standard Model of particle physics (SM), which describes the elementary particles, their properties and behaviour, is presented. Particular attention will be given to the description of mass. In introducing the Standard Model, the content will be increasingly more advanced, and the section concerning the Lagrangian of the Standard Model is intended for experts. Addressing the problem of mass has the same structure; a low-level introduction, followed by an advanced section describing the BEH mechanism. At the end of the chapter, we will address some problems and shortcomings of the Standard Model, and briefly mention some models of physics beyond the Standard Model, before sketching how to proceed in gaining more knowledge about the physical world at the most fundamental level.

2.1 A Brief History: Gaining Knowledge About Elementary Particles

Looking to outline the history of gaining knowledge about fundamental particles, a natural starting point is the Greek philosopher Democritus, who first introduced the idea of a smallest constituent around the year 460 BC. Following the thought that if matter was cut into smaller and smaller pieces, eventually one had to arrive at a piece which was impossible to further divide. This smallest building block of Nature, he called the *atom*. The atom as we know it today, is not

an elementary constituent – it is built up of electrons surrounding a nucleus of protons and neutrons, and even the proton and neutron are built up of smaller constituents.

The electron was the first elementary particle to be discovered, by J.J. Thompson in 1897 [8]. The electromagnetic force, working on charged particles like the electron and the proton, was the first force, beside gravity, to be systematically studied. It was also taken advantage of, through electricity, revolutionizing the way humans lived (this was, however, before the electron was discovered). Later, in showers of cosmic radiation, the close relative (almost identical, only heavier and with a different quantum number) of the electron, the *muon*, was unexpectedly discovered. The degree of incongruousness of this particle was captured by Isidor Isaac Rabi's outburst upon hearing the news: "who ordered that!?". Later also a third particle of this kind was found, the *tau*. These, together with their respective neutrinos, are what we call *leptons*, from a Greek work meaning "small" or "thin".

Going back to the nucleus of the atom, the protons therein are positively charged, and thus repel each other electromagnetically – nevertheless, they are lumped together in the nucleus. There must be some force stronger than the repellence of the electromagnetic force holding them together. This force was accordingly called the *strong force*. Colliding particles in the fifties and sixties at ever growing energies revealed a zoo of hundreds of new strongly interacting particles, leading physicists to believe there had to be some simpler underlying structure to the mess. As a result, the quark model was proposed. This model introduced some smaller constituents, *quarks*, which other particles are built up of. Different combinations of these few quarks gave the rich spectra of particles observed, of which some are represented in Fig. 2.1. Particles made up of quarks are in general called *hadrons*, from a Greek word meaning "heavy" or "thick". Electric charge seems only to come in packages of certain sizes – only an integer amount of the electric charge carried by the electron, e, is observed in Nature.[1] Quarks, however, have charges of $\pm\frac{2}{3}e$ or $\pm\frac{1}{3}e$; and only some combinations of the quarks are allowed, which happen to be the ones with unit charge. Another important particle property is the quantum number *spin*. Particles can be grouped according to whether they have half-integer spin, called *fermions*, or integer spin, called *bosons*. Bosons and fermions act very differently; spin is a very important property. To take two of the most famous particles, the electron and photon: the electron is a fermion with half-integer spin, and the photon, is a boson, with spin 1. Coming back to the particles built up of quarks: of the hadrons, there are the *mesons*, consisting of one quark and one anti-quark, which give an integer total spin – thus mesons are bosons, like *e.g.* the pion ($\pi^{\pm,0}$) and kaon ($K^{\pm,0}$), and then there are the *baryons*, consisting

[1] The electrical charge in units of Coulomb is $e \simeq 1.602 \cdot 10^{19}$ C – one Coulomb being the amount of electrical charge that is transported by a current of one ampere during one second.

of three quarks giving a half-integer total spin – thus, baryons are fermions, like *e.g.* the proton and the neutron. The quark model proved to be a successful one; it predicted for instance the spin-$\frac{3}{2}$ Ω^- baryon, which later was found.

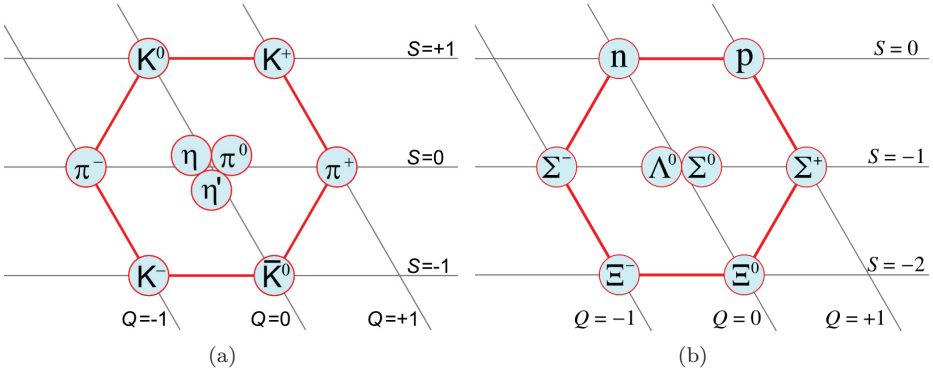

Figure 2.1: Some of the members of the hadron zoo [9]: (a) the pseudoscalar mesons, and (b) the lightest spin-1/2 baryons – both sorted according to different strangeness,[2] S, and electrical charge, Q.

Such experimental confirmation of the theoretical idea gave great support to the model. This is a good example of how solid theories should work: they should have the power to predict phenomena before they are seen. The interplay between theoretical physics and experimental physics is of vital importance. Theoretical physicists come up with a rich spectra of (to various degrees exotic) ideas about how Nature might work, and experimental physicists go out and test these ideas, to check whether Nature is playing that tune or not. Sometimes, experiments surprise,[3] giving theoreticians food for thought, and work on how to incorporate this into the theory. Experimental measurements give direction for development of theories, they indicate which options are less likely, and which are more likely. This serves to illustrate that science moves forward on two feet: both theory and experiment.

It became apparent when studying the zoo of hadrons that there was need for another property of quarks, in addition to the known ones, as spin and electric charge: constellations of three identical quarks were observed, *e.g.* the Δ^{++} baryon,

[2]Strangeness is based on how many strange quarks the hadron contains, quarks with a specific quantum number different from the up and down quarks. Strange hadrons were abundantly produced in early particle interactions, but lived for too long a time to match the ease with which they were produced – which inspired the name *strange*. The postulated reason was that these particles were produced through strong interactions, but decayed through weak interactions.

[3]Some examples of surprises are the results of Rutherford scattering, the discovery of the muon and the cosmic microwave background.

consisting of three up-quarks. However, quarks are fermions: two fermions cannot exist in the same state (with exactly the same quantum numbers) – here, this seemed to happen! Thus, a new quantum number, babtized *color*, was postulated. This could take on three different states, called *green*, *red* and *blue*.[4] All observed hadrons are color neutral, or *white*, meaning that the quarks they are build up of either have one of each three colors (baryons), or color and anti-color (mesons). Due to color being the key to understand the strong force, the theory of it is called *quantum chromodynamics* (QCD), *chroma* being the Greek word for color.

The protons and neutrons are baryons built up of three quarks; two up and one down quark for the proton, one up and two down quarks in the case of the neutron. In contrast to the proton, which has, despite quite some effort, never been observed to decay (the lower limit on the lifetime of the proton is set to around $1.6{\cdot}10^{33}$ years [10], while the age of the universe is around $1.4{\cdot}10^{10}$ years), the neutron is unstable: a free neutron has mean lifetime of 880.1 ± 1.1 seconds, a half-life of around 10 minutes [11], mostly via the process

$$n \to p + e^- + \nu_e \ . \tag{2.1}$$

In the beginning of the 19^{th} century, radioactivity was discovered. This involved a lump of matter seemingly sitting there and radiating energy out of nothing, disobeying the fact that energy could never be created or lost, only transformed to other forms. What was observed, to be understood much later, was the weak force – transforming one kind of matter into another. One of the puzzles that was met in the history of building up our current understanding of the world of the elementary particles was exactly the decay of the neutron as indicated in Eq. (2.1). The neutrino, ν, escaped detection, and carried a bit of energy along with it, resulting in a process that seemingly disobeyed the law of conservation of energy. Niels Bohr was inclined to give up this well-established law of Nature, whilst Wolfgang Pauli would rather introduce a new particle, which was elusive enough not to be measured. Some physicists felt uncomfortable with the idea of such a "ghost" particle, put in to make the equations add up, but which was next to impossible to measure. It turned out that Pauli was indeed right, and the neutrino was first observed in 1956 [12]. Today, the neutrino remains one of the most mysterious particles of the Standard Model of particle physics. This is of course next to the Higgs boson, an even more elusive particle that we will come back to in Section 2.3.1. The experience with the neutrino is a suggestive precedent, which indicates that, sometimes, expanding a well-established theory, instead of going back on first principles, might be a good choice.

[4] Mind that this has nothing to do with color as we know it, the labels are arbitrary and simply meant to uniquely define a state.

To the great astonishment of the people involved, the world of these elementary building blocks was utterly different to the one in the immediate grasp of man's sense experience. The movement of the particles inside atoms was found to take place in sudden jumps (so-called *quantum leaps*), meaning that a particle could be observed in 'orbit' (energy level) A, or 'orbit' B, but *never* anywhere in between. This quantization is essential to the dynamics of the particles, and stabilizes systems that otherwise would disintegrate. Furthermore, the individual occurrences taking place at the quantum level were not deterministic, but rather governed by probabilities. This is a profound characteristic – Nature seems to be random at these small scales: knowing the state of a system would not suffice to uniquely determine how it would look some time later. The frustration of this fact caused the famous quote of Albert Einstein: "God does not throw dice with the world". This probabilistic nature also leads to strange features, like the *tunneling effect*[5] and particle-wave duality. The latter involves something even more contra-intuitive than a particle only being observed in chosen, distinct states: a particle can seemingly be in two places at the same time! The particle-wave duality means that small objects behave both as (probability)waves and as particles, depending on how you choose to look at them. These attributes are very peculiar and hard to incorporate in the intuition of humans.

In this strange world of quantum physics, there seems to be some most important units.[6] One of them is Planck's constant h,

$$h \simeq 6.63 \cdot 10^{-34}\,\mathrm{Js} = 4.14 \cdot 10^{-15}\,\mathrm{eVs}\ . \tag{2.2}$$

More often used in particle physics is the reduced Planck's constant $\hbar \equiv h/2\pi$. Observables are quantized with respect to this constant, *e.g.* energy, momentum and spin. The 'orbits' that the electron take around the nucleus are defined by having an integer amount of energy with respect to Planck's constant, and the transition from one state of the electron in the atom to another is done via packets of energy, quanta, also related to this constant. It is clear that in the macroscopic world, we do not see the strange effects of the quantum world; Planck's constant indicates at which scale quantum effects become important. There is seemingly an upper speed limit in Nature, namely the speed of light (the speed of any massless particle), $c \simeq 3.0{\cdot}10^8\,\mathrm{m/s}$. This quantity is also of utmost important for the theory, and shows up in fundamental formulae like Einstein's famous equation $E = mc^2$,

[5] In quantum mechanics, a particle, despite not having sufficient energy to pass a barrier, *has* after all a small probability to do so – when this happens, it is called tunneling.

[6] Or rather, most important relations, which give these most important units: like the fundamental relationship between momentum and position. Their operators do not commute; $[x, p] = xp - px = i\hbar$, which is linked to Heisenberg's uncertainty principle. Every set of observables whose operators do not commute can only be observed to limited precision at the same time.

telling us that energy and mass are equivalent, and that there is a tremendous amount of energy stored in mass, c^2 times as much as the mass. As mentioned earlier, electric charge is also quantized. It is, however, not an independent natural constant, but a function of $\hbar$ and c. We will use so-called natural units in the rest of this thesis, meaning that $c = \hbar = 1$, and we will give electric charge in units of e and spin in units of $\hbar$.

2.2 Introducing the Standard Model (SM)

Slowly, but surely, knowledge was gathered about particles and the forces that work between them. In the emerging picture, the force, or interaction, is carried out through the exchange of particles called force carriers – much like force is transferred between two persons on roller-skates by throwing a basketball between them. The sum of the knowledge about the constituents and their interactions was gathered in a theory named *The Standard Model of Elementary Particle Physics*, or simply the Standard Model (SM) [13–15]. We will go into more detail on this theory in the coming sections. But before delving into details about the particle content of the Standard Model and the properties and dynamics of the constituents, let us briefly draw a historical line. The development of the Standard Model was a painstaking journey, and what might seem like a matter of course in hindsight was all but obvious at the time. In this introductory section aimed at drawing the big picture, some terms will be mentioned which will be explained only in the coming sections.

Electromagnetism was the first force to be successfully described in the framework of Quantum Field Theory, and was given the name *Quantum ElectroDynamics*, QED. It was a beautiful theory which could to great precision foresee and explain observations like emittance and absorption of quanta of light. In building it, several problems were encountered. The calculations predicted that, among other things, the strength of the interactions, attributed to the magnitude of the electrical charge, was infinite – however, observations tell that this is not the case. The theory needed to be *renormalized*, in such a manner that the predictions of observables were sensible. In renormalizing the theory, the picture of electrical charge changed, but this way of looking at it absorbed theoretical infinities and made experimental observables finite in the theory. The renormalization of QED by Feynman, Tomonaga and Schwinger served as a model of renormalization of the SM. With this in place, QED was sound again, and is without doubt one of the most precise and successful theories of physics.

However, QED could not be the entire story; as already mentioned, weak forces were known to exist, but their nature was not known. They behaved differently

than the electromagnetic force, by not respecting hadron flavor and maximally violating parity. Yukawa came up with the idea that perhaps the coupling to particles were the same as in QED, but that the force was being transmitted through heavy bosons instead of the massless photons. This would explain the weakness (the short range) of the force. Some of these heavy particles needed to be electrically charged to do the job, and it turned out to be impossible to describe such heavy, charged bosons together with the massless photon in Yukawa's theory. Weinberg and Salaam thought about marrying the BEH mechanism to QED, and through this, a joint framework describing three heavy, weak bosons, W^+, W^- and Z^0, and the massless photon emerged. This was too good not to be true, and indeed, in the early 1980's, the weak bosons were discovered at CERN [16]. At the core of this description, however, the BEH mechanism played a key role, and the quanta of the BEH field, the Higgs boson, proving the existence of the field, was yet to be confirmed for decades.

In order to extract information, the equations were expanded in a power series of coupling constants,[7] called perturbation theory,[8] but, as with QED, the calculations diverged. This meant that the electroweak theory did not have the power to predict. Therefore, this way of describing Nature was not truly believed in until G. 't Hooft and Veltman were able to demonstrate that the theory was renormalizable [17] – meaning, that at the price of introducing some finite number of constants that had to be measured in data, the expansion series did no longer diverge, and one could calculate quantities of the model, *e.g.* physical observables like cross sections, to arbitrary precision.

However, the gauge theory did not make sense with the three quarks observed at that time, and a fourth quark (the *charm* quark) was postulated. Renormalizing the SM, with the strong force, mediated by the massless *gluons*, incorporated did not pose particular problems. It it the sum of the knowledge on electroweak and strong forces that is called the Standard Model, which was established in the second half of the 1970's. The fourth known force, gravity, is not included in the Standard Model, because a consistent description of this force in the framework of quantum field theory is yet to be found.

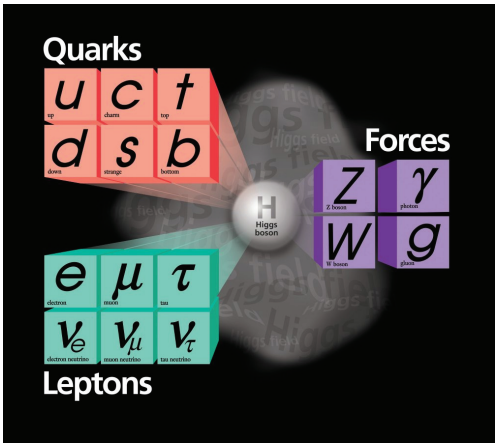

Figure 2.2: Schematic overview of the constituents of the Standard Model. On the left: the spin-$\frac{1}{2}$ fermions; the matter particles. On top in red are the quarks, on bottom in green the leptons. On the right: the spin-1 bosons; the force particles (in purple). To the left are the weak bosons $W^{\pm}$ and Z^0, on upper right the electromagnetic force carrier the photon, γ, and on lower right the strong force carrier the gluon, g. In the middle: the spin-0 Higgs boson and the BEH field, giving mass to the elementary particles.

2.2.1 The Particle Content

Now that we had a little taste of the history of studying the smallest constituents of Nature, let us have a look at which elementary particles we know to exist today. These constituents of the SM can be seen in Fig. 2.2. The particles can firstly be divided into two groups; matter particles and force carriers. The matter particles are fermions and have spin-$\frac{1}{2}$. The force carriers are called gauge bosons and have spin-1. The matter constituents are divided into two groups of fermions: quarks (to the left, on top in red) and leptons (to the left, on bottom in green). There are twelve matter particles: six quarks – *up* and *down*, *charm* and *strange*, *top* (or *truth*) and *bottom* (or *beauty*) – and six leptons – the *electron*, the *muon* and the *tau*, and their respective *neutrinos*. Which type, as chosen among this list, a fermion is, is called its *flavour*. The fermions are placed in three[9] generations of families of four, according to the time of their discovery and their characteristics. For instance the up and down quark, the electron and the electron-neutrino make up generation one. This is the only stable generation of fermions. All the fermions also have a sibling in the Standard Model: the anti-fermions. These anti-particles, called so despite being perfectly good particles, differ from the particles by having opposite charge and opposite magnetic moment

[7]The name *coupling constant* is rather misleading. The 'constants' are the values for the coupling of the forces to the particles, and these vary with the energy which is transferred. One says that they *run* with energy.

[8]Perturbation theory is only valid for coupling constants smaller than unity, such that the higher order terms are smaller than the previous ones. This works well with the electromagnetic coupling constant $\alpha_{em} \approx 1/137$, but not for the strong interactions at low energies, where $\alpha_s \simeq 1$.

[9]There is no *a priori* reason why there should be three generations in Nature, but studies of how the Z^0 boson decays, give strong evidence that there are only three neutrinos with mass less than $m_Z/2$ (and thus three generations).

in the direction of the spin. They were postulated by Dirac, in his formulation of spin-$\frac{1}{2}$ particles (like electrons) uniting quantum mechanics and special relativity. In this formulation, nothing prohibited negative energies, which naturally was problematic. Dirac's interpretation was that most of the (infinite) negative energy states were inhabited, restraining particles to cascade down to lower energies. The unfilled 'holes' in this negative energy sea could be viewed as positively charged electrons. Although the interpretation of holes has changed, such a particle turned out to exist. It is the *positron*, the anti-particle of the electron, discovered by Anderson in 1933 [18]. The anti-particles are indicated by writing a bar over the fermion symbol, for instance $\bar{u}$ and $\bar{\nu}_\tau$. For the charged leptons, it is normal to write the antiparticles in the following manner, indicating their electric charge: e^+, μ^+ and τ^+. Moving on to the forces, there are three of them present in the SM: the electromagnetic force, as mediated by the massless *photon*, γ, the weak force, represented by the massive $W^\pm$ and Z^0 bosons and the strong force, as carried by eight massless *gluons*, g. All these force carriers are shown in purple to the right in Fig. 2.2. In addition, there is the massive Higgs boson, connected to the BEH field, which has spin-0 (it is a scalar) in contrast to the other gauge bosons. The BEH field is responsible for breaking the electroweak symmetry and generating the mass of elementary particles – we will come back to this in Section 2.3.1.

2.2.2 The Properties and Interactions of the Particles

An overview of the properties of the elementary particles can be seen in Tables 2.1 and 2.2. These properties are very important: they decide how the particles behave, which particles interact and which do not;[10] what forces the particles can and cannot feel. The interactions of the particles are schematically illustrated in Fig. 2.3. In this section, we will go through which particles feel which forces, based on their properties, and learn a bit more about some of the forces.

The particles having electric charge feel the electromagnetic force, meaning that they interact with the photon. The electric charges of the up-type quarks are $+\frac{2}{3}$ and the electric charges of the down-type quarks $-\frac{1}{3}$. The electric charges of the up-type leptons are -1 and the electric charges of the down-type leptons (the neutrinos) are zero. The $\mathrm{W}^\pm$ bosons have a charge of ± 1, and the Z^0, the gluons, the Higgs boson and the photon are electrically neutral. Knowing this, we can acknowledge that all fermions except the neutrinos, and only the $\mathrm{W}^\pm$ among the bosons, directly[11] feel the electromagnetic force.

[10] In a more informal and pictorial way of looking at it; which particles talk together and which are rather unsocial.

[11] In order for the other particles to participate in processes involving the electromagnetic force, they need to go through loops of other particles, which do directly couple to the photon.

Type	Name	Mass [GeV]	Spin	$Q/\lvert e\rvert$	Color charge	Y^W	I_3^W
Quark	u, c, t	$2.3{\cdot}10^{-3}$, 1.275, 174	1/2	+2/3	yes	See Table 2.2	
	d, s, b	$4.8{\cdot}10^{-3}$, 0.095, 4.18	1/2	−1/3	yes		
Lepton	e^-, μ^-, τ^-	$5.11{\cdot}10^{-4}$, 0.106, 1.78	1/2	−1	no	See Table 2.2	
	ν_e, ν_μ, ν_τ	all ≈ 0	1/2	0	no		
Boson	γ	0	1	0	no	0	0
	W^+, W^-, Z^0	80.4, 80.4, 91.2	1	+1, −1, 0	no	0	+1, −1, 0
	g	0	1	0	yes	0	0
	H	∼126	0	0	no	+1	-1/2

Table 2.1: Elementary particles of the Standard Model, and some of their quantum numbers. Q is electric charge, Y^W and I_3^W are weak hypercharge and third component of weak isospin as given in Eq. (2.3). The masses are taken from Ref. [11] – for uncertainties on the masses, see this reference. The masses of the neutrinos are non-zero, but small – believed to be less than 1 eV, with slightly different values.

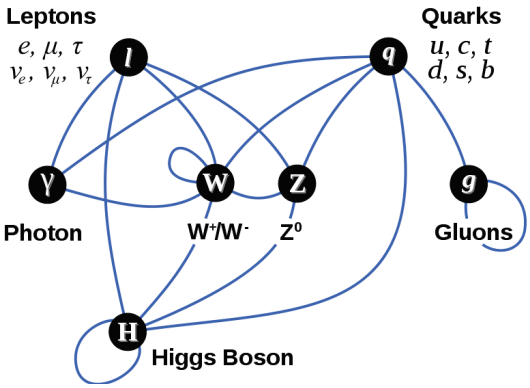

Figure 2.3: A sketch of the interactions between the particles of the Standard Model. The lines indicate that a direct interaction exists between two particles. Particles without such a line between them do not directly communicate.

The particles that feel the weak force, *i.e.* that interact with the $W^{\pm}$ and Z^0 bosons, are the ones that have weak charge (weak isospin and/or weak hypercharge). This involves all particles, except right-handed fermions (and left-handed anti-fermions), the gluons and the photon. The electric charge can, due to the unified description of weak and electromagnetic interactions, be broken down into a part containing the third component of weak isospin, I_3^W and the weak hypercharge, Y^W, as in the Gell-Mann-Nishijima relation

$$\frac{Q}{|e|} = \frac{1}{2}Y^W + I_3^W \ . \tag{2.3}$$

As the name indicates, this force is a weak one – the force carriers responsible for the interactions are so heavy, that at the energies we have around these days,

Chirality	*Generation* 1.	2.	3.	$Q/\lvert e\rvert$	I_3^W	Y^W
L	$\begin{pmatrix} \nu_e \\ e^- \end{pmatrix}_L$	$\begin{pmatrix} \nu_\mu \\ \mu^- \end{pmatrix}_L$	$\begin{pmatrix} \nu_\tau \\ \tau^- \end{pmatrix}_L$	0 -1	$\frac{1}{2}$ $-\frac{1}{2}$	-1 -1
	$\begin{pmatrix} u \\ d' \end{pmatrix}_L$	$\begin{pmatrix} c \\ s' \end{pmatrix}_L$	$\begin{pmatrix} t \\ b' \end{pmatrix}_L$	$\frac{2}{3}$ $-\frac{1}{3}$	$\frac{1}{2}$ $-\frac{1}{2}$	$\frac{1}{3}$ $\frac{1}{3}$
R	e_R^-	μ_R^-	τ_R^-	-1	0	-2
	u_R	c_R	t_R	$\frac{2}{3}$	0	$\frac{4}{3}$
	d_R	s_R	b_R	$-\frac{1}{3}$	0	$-\frac{2}{3}$

Table 2.2: The three generations of fermions in the Standard Model. The left-chiral (L) particles are grouped in weak isospin doublets and the right-chiral ones (R) are isosinglets of weak isospin. The quantum numbers Q, I_3^W and Y^W are respectively the electric charge, the third component of weak isospin and the weak hypercharge. Please note that no right-chiral neutrinos (singlets) are included as this is not part of the (minimal) Standard Model – in order to do so, it must be determined whether they are Dirac particles or Majorana particles (meaning that they are their own anti-particles).

they do not exist in a real state.[12] However, thanks to Heisenberg's uncertainty principle, $\Delta E\,\Delta t \geq \hbar/2$, they can "borrow" some energy from the vacuum, and exist in a virtual state for a very short time. Thus, this force is a short-ranged one. Albeit being a weak force, it is an extremely important one. The universe as we know it would not exist if not for this force. It is the only force that can transform one type of particle into another, through the exchange of a $\mathrm{W}^\pm$ boson, which changes the third component of the weak isospin, and thus the flavour and charge of the particle. Particles that feel the weak force and can be transformed in this manner can be arranged in doublets of weak isospin, and by a mutation of the third component, the upper part of the doublet can be transformed into the lower part and *vice versa* (see Table 2.2). This permits radioactive decays to take place – for instance the processes that make our Sun burn.

In observing decays like $K^+ \to \mu^+ + \nu_\mu$, where the kaon is a bound state of $u\bar{s}$, it became evident that the weak force (working within the isospin doublets as indicated in Table 2.2), rather than couping to the weak eigenstates, couples to 'rotated' quark mass eigenstates, in which the different generations of quarks

[12] Moving backwards in time, or equivalently, up in energy, the energies present a fraction of a second after the Big Bang were large enough for the $\mathrm{W}^\pm$ and Z^0 bosons to be naturally around – meaning, in a non-virtual state.

get mixed. This can be expressed through a 3×3 rotation matrix, called the Cabbibo-Kobayashi-Maskawa (CKM) matrix. Thus, the down-type quark mass eigenstates (d, s, b) are connected to the down-type gauge eigenstates (d', s', b') and the weak current can change between any flavour of quarks. Within the weak force, there is violation of charge-parity symmetry (CP-violation), resulting in a slight asymmetry between matter and anti-matter. This is, however, not sufficient to explain the much bigger matter−anti-matter asymmetry which is observed in the universe.

The particles which have color charge are affected by the strong force. Color charge is only carried by the quarks and the gluons. Gluons carry color charge in the form of a superposition of color and anti-color, such that an exchange of a gluon can change the color charge of a quark. The strong force would, as the electromagnetic force, have infinite range, due to the massless force carriers. However, it does not; the strong force is *confining*, meaning that the energy stored in the attractive interaction between the quarks increases rapidly with distance, so the quarks are bound to stay close together. Trying to pull them apart can be compared to pulling a rubber-band; the more force you put into it, the bigger is the opposite force. If you pull hard enough, the rubber-band breaks, creating two quark−anti-quark pairs, which each are connected by rubber bands. This happens because creating such a pair costs less energy than pulling the quarks further apart. This is the mechanism that causes showers of hadrons in our detector, which we call *jets*. Color is not observed directly in Nature – the quarks *dress* themselves into hadrons, and the same thing happens for gluons. At very high energies (or equivalently very small distances), the confinement gets less pronounced and the quarks act essentially as free particles – this is called *asymptotic freedom*. In these energy domains, the coupling constant of QCD, α_s, (luckily) becomes small and the theory thus is perturbative (calculable).

All massive particles interact directly with the BEH field. Thus, all particles except[13] the gluons and the photon interact with the Higgs boson. This also involves that the Higgs boson interacts with itself, the so-called self-coupling of the BEH field.

[13] In the (minimal) Standard Model also the massless neutrinos do not interact with the Higgs boson. However, there are strong indications that the neutrinos have a small, non-zero mass [19, 20].

2.2.3 The Dynamics of the Particles

Thus far, the particle content of the Standard Model, and the properties of the particles, have been presented. Also contained in the SM are the rules of *how* these particles can interact. These rules are contained in the Lagrangian equation of the Standard Model. At the heart of the Lagrangian are the symmetries of Nature. We will first address the importance of symmetry in the description of the physical world in general, before we move on to the specific symmetry group of the SM. In the section to come after this, the terms of the Lagrangian will systematically be addressed. This section, and the Higgs section, are based on Refs. [21–26], of which some are general references for the theory chapter.

2.2.3.1 Symmetries in Nature

The importance of symmetries in Nature was shown by Emmy Noether in 1918, when she demonstrated that for each symmetry, there is a conserved quantity. Conservation laws are extremely important when trying to understand the physical world; they decide which processes might or might not take place. Since quantities like charge, lepton number and spin are conserved, some processes are not allowed. This is important, because everything that is not forbidden, will eventually happen. Thus, symmetries are utterly fundamental. We call it a symmetry when something looks the same before and after some transformation. More specifically, this means invariance under transformations in space-time.

Invariance under transformations is essential: the laws of physics ought to be the same in all locations of the universe, at all times, for different configurations (at different speeds, rotations, or when using a ruler with different lengths between the ticks) in which one can perform a test – these are purely conventional, so making such changes to the system, should not alter the outcome. Thus, for instance, laws that are part our model of elementary particles must obey special relativity; they must be Lorentz invariant. Demanding invariance under rotation in space-time gives conservation of angular momentum (spin), while invariance under space translation yields conservation of momentum, and invariance under time displacement gives conservation of energy. Similarly, conservation of charge (electric or color) comes from invariance under a global (gauge) phase transformation. For a single symmetry group, this is defined as

$$U = e^{\alpha^a T_a} \ , \tag{2.4}$$

where α^a are the parameters of the transformation and T^a is a general expression for the symmetry group generators. Further demanding this invariance not only to

apply globally, but also locally, making $\alpha(x)^a$ a function of coordinates, involves going from the idea of free particles, to interaction of particle fields. In order to insure so-called local gauge invariance, we are forced to introduce new fields that carry forces, one for each generator of the symmetry group. This leads us to describe the physics in the framework of Quantum Field Theory (QFT). The symmetries mentioned need to be in place for the theory to make sense. The generators of the symmetry groups thus determine which vector fields must be introduced in order for these symmetries to be fulfilled.

The gauge symmetry group of the Standard Model is

$$\mathcal{SU}(3)_C \times \mathcal{SU}(2)_L \times \mathcal{U}(1)_Y \ . \tag{2.5}$$

This is chosen for no special reason, apart from that it is the smallest symmetry group sufficient to describe the particles and interactions observed in Nature. $\mathcal{SU}(3)$ has eight generators, corresponding to the eight gluon fields, $\mathcal{SU}(2)$ has three generators that give rise to the fields $W^{1,2,3}$, and $\mathcal{U}(1)$ has only one, connected to the B field. The $W^{1,2,3}$ and B fields are not the ones we observe in Nature; to arrive at the observed fields, the electroweak symmetry must be broken – this will soon be addressed.

For no obvious reason, Nature decided for electroweak interactions to be chiral.[14] Therefore, the fermionic fields are split in a left-chiral and a right-chiral representation; left-chiral fields transform as $\mathcal{SU}(2)$ doublets, and right-chiral as $\mathcal{SU}(2)$ singlets. The denotation, L, on the $\mathcal{SU}(2)$-group indicates that the $W^{1,2,3}$ gauge fields only couple to left-chiral particles and right-chiral anti-particles. Transformation between two chiral states, or equivalently; space inversion (reflection), is called *parity* transformation. The weak force is the only force that breaks this symmetry, as well as charge symmetry. Symmetry under charge-parity (CP) transformations seems to be fulfilled for all forces but the weak, which slightly violates this symmetry.

[14]The concept of chirality is related to, but not the same as helicity – unless the particle is massless, where they are identical. However, confusingly, the two terms are often used interchangeably. Helicity, also known as *handedness*, can be determined from the spin and direction of flight; if the two are in the same direction, the particle is right-handed – opposite directions: left-handed. This quantity, however, depends on the frame of reference for massive particles: one can boost the system, so as to overtake the particle's speed, thus changing the direction of flight. If the particle is massless, it is not possible to overtake it, meaning that boosting from one frame to another does not make any difference. Chirality on the other hand, is the same regardless of the frame. Chirality is more abstract, and has to do with whether the particle transforms into left-handed or right-handed representation of the Poincaré group. Figuratively, one can imagine chiral objects to be mirror images of each other. To illustrate the level at which the confusion is embedded in literature, sfermions in supersymmetry are called left-*handed* or right-*handed*, albeit them being scalar – not having any spin! The notation refers to whether they decay to left-*chiral* or right-*chiral* particles.

2.2.3.2 The Lagrangian of the Standard Model

The most central piece of the Standard Model is its Lagrangian (density), $\mathscr{L}_{SM}$, containing the full dynamics of the particles therein. The motion of the particles in any system can be derived from the Lagrangian of the system, both classically and in quantum mechanics, using the principle that particles take the path of least action through space-time. The action is defined as $S = \int \mathscr{L}\, \mathrm{d}t\, \mathrm{d}x\, \mathrm{d}y\, \mathrm{d}z$ – demanding $\partial S = 0$ gives the equation of motion (according to Hamilton's principle). For actions much greater than Planck's constant, quantum effects become negligible. The Lagrangian of the SM can be described by these main parts:

$$\mathscr{L}_{\mathrm{SM}} = \mathscr{L}_{\mathrm{matter}} + \mathscr{L}_{\mathrm{gauge}} + \mathscr{L}_{\mathrm{Higgs}} + \mathscr{L}_{\mathrm{Yukawa}} \ . \tag{2.6}$$

The matter part describes the kinetic energy of the fermions and their interaction with the gauge fields;

$$\mathscr{L}_{\mathrm{matter}} = i \sum_{f_L} \bar{f_L} \gamma^\mu (D_L)_\mu f_L + i \sum_{f_R} \bar{f_R} \gamma^\mu (D_R)_\mu f_R \ , \tag{2.7}$$

where the sums run over the different right and left-handed fermion fields f, and for the strong force also over the three color charges. The Dirac matrices, γ^μ, are a representation of Clifford algebra, $[\gamma_\mu, \gamma_\nu] = 2g_{\mu\nu}$. In one representation, these read

$$\gamma^0 = \begin{pmatrix} 1 & 0 \\ 0 & -1 \end{pmatrix} \qquad \gamma^k = \begin{pmatrix} 0 & \sigma^k \\ -\sigma^k & 0 \end{pmatrix} \ , \ k = \{1, 2, 3\}$$

where the Pauli matrices, σ^k, are as defined in (2.10).

The covariant derivatives are[15]

$$(D_L)_\mu = \partial_\mu + ig\frac{\sigma^a}{2} W_{a,\mu} + ig'\frac{Y^W}{2} B_\mu + ig_s \frac{Q_s \lambda^j}{2} G^j_\mu \ , \tag{2.8}$$

$$(D_R)_\mu = \partial_\mu + ig'\frac{Y^W}{2} B_\mu + ig_s \frac{Q_s \lambda^j}{2} G^j_\mu \ , \tag{2.9}$$

where the charge Q_s is one for fermions with color charge (the quarks), and zero

[15] These could have been gathered into one expression:

$$(D)_\mu = \partial_\mu + ig\frac{I_3^W \sigma^a}{2} W_{a,\mu} + ig'\frac{Y^W}{2} B_\mu + ig_s \frac{Q_s \lambda^j}{2} G^j_\mu \ .$$

By substituting for I_3^W, it is explicit that the weak force in the Standard Model distinguishes between right-chiral and left-chiral particles.

otherwise. From these equations it can be appreciated that the weak $W^{1,2,3}$ fields do not couple to right-chiral particles. Here, Y^W, weak hypercharge, is the generator of the single field in the $\mathcal{U}(1)$ group and σ^a with $a = \{1, 2, 3\}$ are the generators of the $\mathcal{SU}(2)$ group, spanning the weak isospin space (zero in case for $\mathcal{SU}(2)$ singlets); these are the 2×2 Pauli matrices

$$\sigma^1 = \begin{pmatrix} 0 & 1 \\ 1 & 0 \end{pmatrix} \qquad \sigma^2 = \begin{pmatrix} 0 & -i \\ i & 0 \end{pmatrix} \qquad \sigma^3 = \begin{pmatrix} 1 & 0 \\ 0 & -1 \end{pmatrix} . \tag{2.10}$$

For the strong force mediated by the G fields with coupling constant g_s, there are eight $\mathcal{SU}(3)$ group generators, as specified by the Gell-Mann matrices:

$$\lambda_1 = \begin{pmatrix} 0 & 1 & 0 \\ 1 & 0 & 0 \\ 0 & 0 & 0 \end{pmatrix} \qquad \lambda_2 = \begin{pmatrix} 0 & -i & 0 \\ i & 0 & 0 \\ 0 & 0 & 0 \end{pmatrix} \qquad \lambda_3 = \begin{pmatrix} 1 & 0 & 0 \\ 0 & -1 & 0 \\ 0 & 0 & 0 \end{pmatrix}$$

$$\lambda_4 = \begin{pmatrix} 0 & 0 & 1 \\ 0 & 0 & 0 \\ 1 & 0 & 0 \end{pmatrix} \qquad \lambda_5 = \begin{pmatrix} 0 & 0 & -i \\ 0 & 0 & 0 \\ i & 0 & 0 \end{pmatrix} \qquad \lambda_6 = \begin{pmatrix} 0 & 0 & 0 \\ 0 & 0 & 1 \\ 0 & 1 & 0 \end{pmatrix}$$

$$\lambda_7 = \begin{pmatrix} 0 & 0 & 0 \\ 0 & 0 & -i \\ 0 & i & 0 \end{pmatrix} \qquad \lambda_8 = \frac{1}{\sqrt{3}} \begin{pmatrix} 1 & 0 & 0 \\ 0 & 1 & 0 \\ 0 & 0 & -2 \end{pmatrix} . \tag{2.11}$$

Moving on to the next term, the one involving the gauge fields – their kinetic energy and self-coupling (the latter only for the non-abelian fields) can be described by

$$\mathscr{L}_{\text{gauge}} = -\frac{1}{4} B_{\mu\nu} B^{\mu\nu} - \frac{1}{4} W^i_{\mu\nu} W^{\mu\nu}_i - \frac{1}{4} G^i_{\mu\nu} G^{\mu\nu}_i \ , \tag{2.12}$$

where the field strength tensors are

$$B_{\mu\nu} = \partial_\mu B_\nu - \partial_\nu B_\mu \tag{2.13}$$

$$W^i_{\mu\nu} = \partial_\mu W^i_\nu - \partial_\nu W^i_\mu - g\, \epsilon^{ijk}\, W^j_\mu\, W^k_\nu \qquad i = \{1, 2, 3\} \tag{2.14}$$

$$G^i_{\mu\nu} = \partial_\mu G^i_\nu - \partial_\nu G^i_\mu - g_s\, f^{ijk}\, W^j_\mu\, W^k_\nu \qquad i \in (1, 8) \tag{2.15}$$

with ϵ^{ijk} being the Levi-Civita symbol; these are the structure constants of the $\mathcal{SU}(2)$ group, according to $[\sigma_i, \sigma_j] = 2i\epsilon^{ijk}\sigma_k$, yielding + if the indices are in cyclic order, − otherwise. The structure constants for the strong force, f^{ijk}, are defined by $[\lambda_i, \lambda_j] = 2if^{ijk}\lambda_k$, where λ are the Gell-Mann matrices as defined in

Eqs. (2.11). In the equations for the field strength tensors, it becomes apparent that the non-abelian groups $\mathcal{SU}(2)$ and $\mathcal{SU}(3)$ have a self-coupling term.

The motivation for constructing these equations was to have QED and weak interactions in a unified framework. However, the fields W_μ and B_μ are not the ones we observe in Nature – the physical fields are defined as

$$W_\mu^\pm = \frac{W_\mu^1 \mp W_\mu^2}{\sqrt{2}} \ , \qquad Z_\mu = \frac{gW_\mu^3 - g'B_\mu}{\sqrt{g^2+g'^2}} \ , \qquad A_\mu = \frac{g'W_\mu^3 + gB_\mu}{\sqrt{g^2+g'^2}} \ , \tag{2.16}$$

where A_μ is the electromagnetic field. The coupling constant of the $\mathcal{SU}(2)$ group (weak isospin coupling constant), g, and the coupling constant of the $\mathcal{U}(1)$ group (weak hypercharge coupling constant), g', are related to the electromagnetic coupling constant, e, via the Weinberg mixing angle, θ_W, as $e = g\sin\theta_W = g'\cos\theta_W$. Using the relations $\cos\theta_W = g/\sqrt{g^2+g'^2}$ and $\sin\theta_W = g'/\sqrt{g^2+g'^2}$ we can write the two latter fields as

$$Z_\mu = W_\mu^3\cos\theta_W - B_\mu\sin\theta_W \qquad A_\mu = W_\mu^3\sin\theta_W + B_\mu\cos\theta_W \ . \tag{2.17}$$

But the force carriers are observed to be massive bosons – so we need to address the mechanism that causes the mass. The idea of how to generate mass for elementary particles in the framework of QFT was developed, unknowingly, in parallel by several (groups of) persons in the mid-sixties. We will have a closer look at the field introduced in this theory and the mechanism of symmetry breaking in Section 2.3.1. For now, it suffices to say that the contribution of this sector can be written as

$$\mathscr{L}_{\text{Higgs}} = \left(D_\mu\phi^\dagger\right)\left(D^\mu\phi\right) - V(\phi^\dagger\phi) \ , \tag{2.18}$$

where the potential V is described by

$$V(\phi^\dagger\phi) = \mu^2\left(\phi^\dagger\phi\right) + \lambda\left(\phi^\dagger\phi\right)^2 \ , \tag{2.19}$$

μ^2 and λ being real parameters and $\phi(x)$ being a complex scalar field doublet,

$$\phi(x) = \begin{pmatrix} \phi_1(x) + i\phi_2(x) \\ \phi_3(x) + i\phi_4(x) \end{pmatrix} \ . \tag{2.20}$$

The field ϕ will also give rise to the mass of the fermions, via a direct coupling of

the fermions to the field:

$$\mathscr{L}_{\text{Yukawa}} = \sum_f g_f \bar{f}_L \phi f_R \tag{2.21}$$

where g_f are the arbitrary Yukawa couplings to the BEH field, determined experimentally.

For a schematic view of the processes taking place at the quantum mechanical level, we have the tool of Feynman diagrams – useful to keep track of terms in the Lagrangian and what processes they describe. In these diagrams, the particles are represented by lines. It is common[16] to indicate fermions by solid lines, photons and weak bosons by wiggly lines, gluons by curly lines and scalar particles such as the Higgs boson by a dashed line. Arrows on the lines indicates the flow of fermions, or the opposite flow of anti-fermions. The arrows of the fermion lines indicate the motion of the particle in space-time, and time has a certain direction in the diagram (upwards or to the right). Anti-particles are thought to travel backwards in time in this view. We will see several such diagrams in Chapter 6.

2.3 The Problem of Mass

As we have observed the weak force to be a short-range one, and its force carriers to be massive, we need the theory to include their masses. This is, however, not so straightforward. Simply adding mass terms for the weak bosons in the Lagrangian by brute force, terms like $\frac{1}{2} m_V^2 W_\mu W^\mu$ (m_V indicating the mass of the vector boson), the gauge invariance is spoiled – the $\mathcal{SU}(2)\times\mathcal{U}(1)$ symmetry is violated, and the theory no longer renormalizable.

One mechanism that can give rise to the masses of elementary particles while still keeping the invariance of the symmetry group, is *spontaneous symmetry breaking* (SSB). Spontaneous symmetry breaking can only occur when the ground state of a system is degenerate; when there are more than one lowest energy state. The symmetry is broken by choosing one, no matter which, of these many ground states, called the vacuum. This chosen state will not have the symmetry that the Lagrangian contains. In such a scenario – when the dynamical equations of a system is invariant under some transformation, but the solution to the system (the physical state) does not possess the same invariance; when the symmetry is not apparent in the ground state – we say that we have spontaneous symmetry breaking.

[16] There are deviations from this standard, like indicating weak bosons by dashed lines, causing quite some confusion.

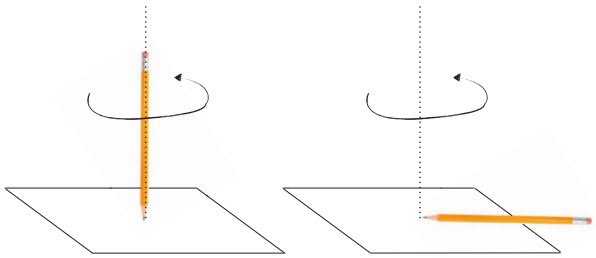

Figure 2.4: An illustration of spontaneous symmetry breaking; a pencil balancing on its tip and falling over, causing the system to no longer be invariant under the rotational transformation around the axis running orthogonal to the table, through the middle of the standing pencil.

To get a more tangible picture of spontaneous symmetry breaking, one can imagine a pencil, round with no pattern, balancing on its tip as shown in Fig. 2.4. Standing like this, it can rotate around the axis running through the middle of it, orthogonal to the table, and we would be none the wiser. The system is symmetric with respect to this rotational transformation. The pencil balancing on its tip is not a stable configuration, so sooner or later, it will fall over. Now, rotating the pencil around the same axis (orthogonal to the table) makes it very easy to tell that the system is being manipulated. The symmetry is not longer retained – it is broken. The pencil might have fallen in any direction; which direction it fell is not so important, the important point is that it fell, breaking the symmetry. We will see that, in the same manner, the $\mathcal{SU}(2)\times\mathcal{U}(1)$ symmetry is spontaneously broken when introducing the Higgs potential, having an unstable state of a local maximum for a vanishing field, causing the system to "fall" into a stable state of lower energy where the field is non-zero.

The idea of SSB first emerged in connection with superconductivity, and was introduced by Anderson in 1962, however, without a proper relativistic model incorporation. The mechanism lies in that the ground state of a ferromagnetic setup breaks the rotational symmetry of the Hamiltonian describing the system by choosing a (arbitrary) spatial direction for the spin to align along. When heating up this system, the orientation of the spins become random by thermal movement, and the rotational symmetry is restored. Similar to this, the weak isospin symmetry is expected to be restored after a certain critical temperature, and the weak bosons will be massless at this high energy.

2.3.1 The BEH Mechanism

The Standard Model solution to the problem of mass was unveiled in 1964, more or less simultaneously, by Brout & Englert, Higgs, and Hagen, Guralnik & Kibble [27–32]. It is called the Brout-Englert-Higgs (BEH) mechanism, or the Brout-Englert-Higgs-Hagen-Guralnik-Kibble-mechanism, or sometimes, simply the Higgs mechanism. As mentioned in Section 2.2.3.2, a complex scalar field, ϕ, has been introduced, which is called the BEH field. The equations are repeated here as a reminder: the potential energy density of the field is

$$V(\phi^\dagger\phi) = \mu^2\left(\phi^\dagger\phi\right) + \lambda\left(\phi^\dagger\phi\right)^2 \ , \tag{2.19}$$

where μ^2 and λ are real parameters, and $\phi(x)$ is

$$\phi(x) = \begin{pmatrix} \phi_1(x) + i\phi_2(x) \\ \phi_3(x) + i\phi_4(x) \end{pmatrix} \ . \tag{2.20}$$

In order for the potential to be bounded from below – meaning that it has a state of minimum energy such that it is stable, λ must be positive. Now, in order for spontaneous symmetry breaking to occur, the ground state (the vacuum) as mentioned cannot be unique. In order for this state of minimum energy to be degenerate, $\mu^2 < 0$ must be fulfilled. For such a constellation of the potential, one of the doublet components of the field has the 'Mexican hat' or 'champagne bottle' shape that is shown in Fig. 2.5.

To illustrate the mechanism through which the bosons gain mass from the SSB, we make use of the easiest scenario, the $\mathcal{U}(1)$ group, having only one force field, namely that of the photon. In this case, called the Goldstone model, the doublet of imaginary scalar fields is not needed; a singlet, $\phi(x) = \frac{1}{\sqrt{2}}\{\phi_1(x) + i\phi_2(x)\}$, is sufficient.

In order to find the non-zero vacuum expectation value (VEV) of the BEH field, $\langle 0|\phi|0\rangle = v/\sqrt{2}$, we can substitute $\phi^\dagger\phi$ with $v^2/2$ and minimize the potential;

$$\frac{\partial V}{\partial v} = \mu^2\frac{v^2}{2} + \lambda\frac{v^4}{4} = 0 \tag{2.22}$$

$$\Downarrow$$

$$v = \sqrt{\frac{-\mu^2}{\lambda}} \tag{2.23}$$

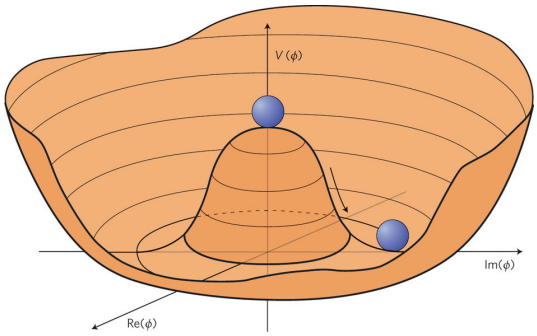

Figure 2.5: An illustration of the 'Mexican hat' shaped Higgs potential with $\lambda > 0$ and $\mu^2 < 0$. The local maximum gives a perfectly symmetric state, but is an unstable configuration – giving rise to spontaneous symmetry breaking, by the choice of one of the degenerate ground states in the ring of minima. Massless, spin-0 Nambu-Goldstone bosons are connected to movement along this ring - these get absorbed in massless spin-1 particles (like $W^{1,2,3}$) and give rise to the masses of these. The Higgs boson is connected to movement in the radial direction, oscillating up and down between the centre and the side of the hat (in the direction of the arrow) [33].

This is a ring of minima in the complex plane

$$\phi(x) = \sqrt{\frac{-\mu^2}{\lambda}} e^{i\theta} \qquad 0 \leq \theta \leq 2\pi \tag{2.24}$$

and the symmetry can be spontaneously broken by choosing one of the infinitely many ground states described by this ring of minima. Since gauge invariance is fulfilled,

$$\phi'(x) = e^{-iq\theta}\, \phi(x) \ , \tag{2.25}$$

we are in principle free to choose the gauge (perform a so-called gauge fixing). One choice is $\theta = 0$, such the ground state is at a real value. Since the VEV itself is not gauge invariant, the symmetry is spontaneously broken.

The Lagrangian density in this model is given by

$$\mathscr{L} = (D^\mu \phi(x))^\dagger \, (D_\mu \phi(x)) - V(\phi^\dagger \phi) - \frac{1}{4} F_{\mu\nu}(x) F^{\mu\nu}(x) \ , \tag{2.26}$$

where D_μ is the covariant derivative

$$D_\mu = \partial_\mu + ieA_\mu(x) \, . \tag{2.27}$$

The last term in Eq. (2.26) is the Lagrangian density of the free gauge field $A_\mu(x)$,

where

$$F_{\mu\nu}(x) = \partial_\nu A_\mu(x) - \partial_\mu A_\nu(x)\,. \tag{2.28}$$

The Lagrangian (2.26) is invariant under $\mathcal{U}(1)$ gauge transformations; thus the system is invariant under these transformations:

$$\phi(x) \to \phi(x)' = \phi(x)e^{-ie\theta(x)} \tag{2.29}$$

$$\phi^*(x) \to \phi^*(x)' = \phi^*(x)e^{ie\theta(x)} \tag{2.30}$$

$$A_\mu \to A'_\mu = A_\mu + \partial_\mu\theta(x) \tag{2.31}$$

The breaking of the $\mathcal{U}(1)$ symmetry will invalidate these equations.

Given that V has the shape needed for SSB to take place (that is $\lambda > 0$, $\mu^2 < 0$) such that there is a non-zero value of v, we are set to get massive bosons out – in this case, a massive photon. To demonstrate the mechanism behind the assignment of mass, the $\phi(x)$ field is expanded around its vacuum value by introducing two real fields $\sigma(x)$ and $\eta(x)$ according to the equation

$$\phi(x) = \frac{1}{\sqrt{2}}[\, v + \sigma(x) + i\eta(x)\,]\ , \tag{2.32}$$

where $\sigma(x)$ and $\eta(x)$ measure the deviation of the field $\phi(x)$ from the ground state, $\sigma(x)$ in the radial direction and $\eta(x)$ in the longitudinal direction. As we will see later, $\sigma(x)$ corresponds to the field of the Higgs particle and $\eta(x)$ is an unphysical field which gives rise to mass of the photon. When inserting this expansion of the field into the Lagrangian (2.26), it becomes

$$\begin{aligned}\mathscr{L} \;=\; & \frac{1}{2}[\,\partial^\mu\sigma(x)\,][\,\partial_\mu\sigma(x)\,] + \frac{1}{2}[\,\partial\eta^\mu(x)\,][\,\partial\eta_\mu(x)\,] \\ & - \frac{1}{4}F_{\mu\nu}(x)F^{\mu\nu}(x) + \frac{1}{2}(ev)^2 A_\mu(x)A^\mu \\ & -\frac{1}{2}(2\lambda v^2)\sigma^2(x) + evA^\mu(x)\partial_\mu\eta(x) + \text{'interaction terms'}\ ,\end{aligned} \tag{2.33}$$

where the 'interaction terms' are cubic and quartic in the fields, and a constant term has been discarded. It would seem the particle content of this equation is a massive scalar, σ, a massive vector, A_μ, and a massless boson, η.

However, this Lagrangian cannot yet be interpreted physically: the term off-diagonal in the fields, $evA^\mu(x)\partial_\mu\eta(x)$, would let the vector field A_μ change into the scalar field η – which is not physically permitted. Adding to that, when comparing with the Lagrangian before the expansion of the potential around the ground state

and counting degrees of freedom, it can be seen that Eq. (2.26) has four degrees of freedom, while Eq. (2.33) has five, due to the field A_μ getting another polarization degree. It seems there is an extra degree of freedom gained in the process. This is true – it stems from the field η, an unphysical field which is connected to a massless Nambu-Goldstone boson. But the Lagrangians describe the same physical system, so it must be possible to get rid of this field, in order for the representation to return to a physical scenario. The way to achieve this is to choose a certain gauge (we are free to do so, since the Lagrangian is gauge invariant). The apparent extra degree of freedom is thus spurious; it corresponds only to the freedom to do a gauge transformation. By the choice of unitary gauge, making the ϕ field real, the unphysical η field is gotten rid of;

$$\phi(x) = \frac{1}{\sqrt{2}}[\, v + \sigma(x)\,] \ , \tag{2.34}$$

Substituting this into the Lagrangian in Eq. (2.26) renders:

$$\begin{aligned} \mathcal{L} \ &= \ \frac{1}{2}[\, \partial^\mu \sigma(x)\,][\, \partial_\mu \sigma(x)\,] - \frac{1}{2}(2\lambda v^2)\sigma^2(x) \\ &\quad - \frac{1}{4}F_{\mu\nu}(x)F^{\mu\nu}(x) + \frac{1}{2}(ev)^2 A_\mu(x)A^\mu \\ &\quad + \text{'interaction terms'} \ . \end{aligned} \tag{2.35}$$

Since there no longer are any unphysical mixing terms, the last term may be interpreted as a massive vector field A_μ. Through this (unnecessary, but illustrative) expansion of the field in the radial and longitudinal direction, the mechanism is demonstrated; the component of the scalar potential in the longitudinal direction donates its degree of freedom to the vector field: the photon field has absorbed the scalar field, *i.e.* it has "eaten" the Nambu-Goldstone boson and taken its degree of freedom. Thus, the boson connected to the vector field now has "the freedom not to move at the speed of light": it has become massive. The second component of the field, in the radial direction, σ, remains – this is a physical field and the particle connected to it is a so-called Higgs boson.

This was the demonstration for the case of a massive photon. The photon, however, is massless, so this scenario is not realized in Nature. The mechanism remains the same, though, and it can be applied to the case of the weak fields, by introducing a complex scalar field doublet instead of a singlet. Conservation of electric charge must be retained (and thus the photon is massless). It is easy to appreciate that the gauge, the choice of ground state, in which the VEV is in the electrically neutral part of the doublet fulfils this. It can be seen from the Gell-Mann-Nishijima relation in Eq. (2.3) that the neutral part of the doublet is the lower component, given that

the weak hypercharge of the doublet is +1, knowing that the lower component of the doublet has $I_3^W = -1/2$. This unitary gauge, requiring $\phi_1 = \phi_2 = \phi_4 = 0$, yields the Higgs VEV

$$\langle\phi(x)\rangle_0 = \begin{pmatrix} 0 \\ v/\sqrt{2} \end{pmatrix} . \tag{2.36}$$

For this gauge, we can parametrize fluctuations of the real, neutral component of the field, $\phi_3(x)$, around the vacuum as

$$\langle\phi(x)\rangle_0 = \begin{pmatrix} 0 \\ \{v + \sigma(x)\}/\sqrt{2} \end{pmatrix} , \tag{2.37}$$

where the real field, σ, is the BEH field and the other (unphysical) fields, ϕ_1, ϕ_2, ϕ_4 give their degrees of freedom to the spin-1 bosons, causing them to be massive.

The weak and the electromagnetic forces are unified: the $\mathcal{SU}(3)_C \times \mathcal{SU}(2)_L \times \mathcal{U}(1)_Y$ symmetry group of the Standard Model is spontaneously broken – what remains is $\mathcal{SU}(3)_C \times \mathcal{U}(1)_{em}$. Since electroweak symmetry is broken, we expect weak isospin and weak hypercharge not to be conserved in some interactions. If it was, the masses of the pairs in the weak isospin doublets would have had identical mass, which from measurements is clearly not the case [23]. The breaking of the weak isospin and weak hypercharge symmetry compensates to keep electrical charge conserved. The masses of the physical fields are, as obtained by substituting Eq. (2.36) into the Lagrangian $\mathscr{L}_{\text{Higgs}}$ in Eq. (2.18) :

$$m_W = \frac{gv}{2} , \qquad m_Z = \frac{\sqrt{(g^2 + g'^2)}v}{2} = \frac{m_W}{\cos\theta_W} , \qquad m_\gamma = 0 . \tag{2.38}$$

With these relations and the measured values for the coupling constants, the vacuum energy expectation is determined to be $v \approx 246$ GeV. This does not only imply that the vacuum has a non-zero energy connected to it, it is also filled up with weak charge, which is a rather dramatic consequence of the BEH mechanism.

The masses of the fermions can be obtained by substituting Eq. (2.36) into the Lagrangian $\mathscr{L}_{\text{Yukawa}}$ in Eq. (2.21)

$$m_f = \frac{v}{\sqrt{2}} g_f , \quad f = u, d, e, \ldots \tag{2.39}$$

These mass terms are given by the coupling, g_f, of the fermion to the BEH field.

The couplings are not determined by the Standard Model, and the values for the masses of fermions are thus not predicted by the theory. But, since these masses are precisely measured in experiments, there are precise predictions of the couplings.

The mass of the quantum of the scalar field, the Higgs boson, can be found from the second derivative of the potential (the curvature) – it corresponds to quantum fluctuations in the radial direction, oscillations up and down the wall of the potential, in the direction of the arrow in Fig. 2.5 and is

$$m_H^2 = \frac{\partial^2 V}{\partial v^2} = \mu^2 + 3\lambda v^2 \tag{2.40}$$

$$= 2\lambda v^2 \ , \tag{2.41}$$

where we in the last step used the result in Eq. (2.23). This mass term can also be seen from the term in Eq. (2.35), which is quadratic in the real part of the scalar field, $\sigma(x)$. However, neither λ nor μ, the parameters of the Higgs potential, are possible to determine from relations such as in Eq. (2.38), so the mass of the Higgs boson – a function of these, as displayed in Eq. (2.40) – is undetermined, which is one of the reasons it took so long to find it.

It should be appreciated that in this framework, there is a complete knowledge of how the Higgs boson couples to all other particles, and a complete ignorance of the mass of the boson itself. What does exist, is a definite prediction of the relation of the mass of the Higgs boson to the self-coupling, λ. Some consider probing the self-coupling term of the field, $\lambda \left(\phi^\dagger \phi\right)^2$, the ultimate test of the theory. It is a tough test to perform, since the rate for self-coupling events (production of two Higgs bosons) is very low and separating them from the background difficult at the LHC, or even at a high-energy e^+e^- linear collider [34, 35].

2.4 The Shortcomings of the Standard Model

The SM has been tested to great precision in a multitude of experiments over several decades. It works astonishingly well, with the power to predict – as for instance the mass of the top quark several years before its discovery in 1995. The cross sections found from calculations within this model match to a large degree with the data taken by ATLAS at the LHC over many orders of magnitude, as can be appreciated from Fig. 2.6. But even though the SM is a extremely successful theory, it is still thought to be an *effective* theory. This means that at shorter distances (or equivalently, higher energies) than the ones we have probed up until today, the theory will not be sufficient to describe the phenomena taking place.

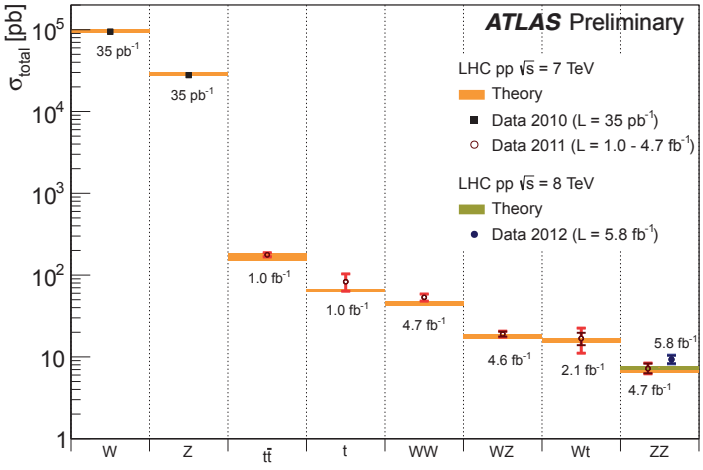

Figure 2.6: Cross sections for various Standard Model processes, as calculated from theory and measured in experiment [36]. The theoretical values with uncertainty are indicated in orange and green (for 7 and 8 TeV center of mass collision energies, respectively), whereas the data is indicated in circles (empty for 7 TeV center of mass collision energy, full for 8 TeV) and squares (for 2010 data, taken at 7 TeV center of mass energy), with error bars. The good agreement over several of orders of magnitude is an indication of the success of the Standard Model.

Equivalently, Newton's theory, an effective theory, is perfectly adequate to describe the movements of objects, until the velocities of the objects get close to the speed of light (giving the need for the Special theory of Relativity for a correct description), or at locations where space-time is sufficiently curved for an Euclidean description of geometry to fail (giving the need for the General theory of Relativity, GR), or at distances smaller than the size of an atom (giving the need for quantum mechanics).

In addition to being thought of as an effective theory, the SM has quite some shortcomings and troublesome features. This has succinctly been expressed by Peskin as: "The Standard Model is insulting to me as a theorist!" [37]. This includes both questions that are left completely unanswered by the theory, and solutions to problems that are not naturally emerging, but rather *ad hoc* and unsatisfactory. Let us address some of these features.

How does gravity fit into the world of the smallest constituents?

For starters, the Standard Model does not include the fourth known force in Nature; gravity. This is not grave in terms of the experimental consequences, because gravity becomes negligible at the scale of elementary particles. However, it is a force

of Nature, and to have a complete model, it should be included. Unfortunately, all attempts at describing gravity in the framework of QFT have failed – the postulated force carriers for gravity, *gravitons*, cannot be described in a coherent way, and the particles themselves have not been observed (a very difficult task, due to the weakness of the gravitational force).

Why the BEH mechanism?

The BEH field and the shape of its potential are added to the model *ad hoc*. Moreover, the lightness of the Higgs boson is problematic. Knowing that the masses of the particles the Higgs boson couples to contribute to the mass of the Higgs boson itself, together with the fact of the Higgs boson being a particle that couples to particles according to their mass (meaning, more strongly the heavier the particle), the idea of particles much heavier than the ones observed as of today becomes troublesome. Imagine particles with masses up towards the Planck scale, $M_p \sim 10^{19}$ GeV, where gravity becomes an important force at the quantum level. The contribution of these to the Higgs boson mass should be proportional to their own mass through radiative corrections from vacuum polarization. For new particles in Grand Unified Theories (GUTs), this is expected to be only around a factor thousand less than the Planck scale. However, if the Higgs boson would be measured to be rather light in this respect, there would be a factor of around 10^{14} between the 'natural' Higgs boson mass and the measured one. Merging this light Higgs boson mass with the theory of heavier particles requires extreme fine-tuning in cancellations between new particles, something physicists in general frown upon. This is called the *hierarchy problem* or the *naturalness problem*.

What is the dark matter we know around 25% of our universe consists of?
What is the dark energy we know around 70% of our universe consists of?

Cosmological measurements, such as studies of the cosmic microwave background radiation and the movement and distribution of galaxies have shown that the universe consists of around 5% baryonic matter, 25% dark matter and 70% dark energy. The SM only describes the baryonic matter.

What about the masses of neutrinos?

The SM assumes neutrinos to be massless particles. However, oscillations between different flavor eigenstates in for instance solar or atmospheric neutrinos have been observed (neutrino mixing), demonstrating that neutrinos must have mass, albeit a tiny one [19, 20].

What is the origin of the structure of the matter generations?

There is no reason given by the Standard Model as to why there are three generations of matter particles, or why they should be placed in chiral doublets. Their masses span an enormous scale: between the light down quark and the heavy top quark, there is a mass difference of nearly five orders of magnitude, for no apparent reason. In addition, the masses themselves, originating from the coupling to the BEH field, are put in by hand and must be measured. This seems too arbitrary for a solid theory, and gives rise to the question:

Are the parameters of the SM really independent?

A good theory should involve as little fiddling as possible – the beauty of physics is displayed most clearly when phenomena new to us come naturally out of the formulation we use in the attempt of capturing the workings of Nature. The contrary, having to make a lot of assumptions and physically unmotivated solutions, is thought to pollute a description. The belief is that the underlying structure of Nature is simple, but manifested in a rich spectra of diverse phenomena. We have seen this demonstrated a number of times, which makes us keep faith in this assumption. However, in the simplest version of the SM, without masses for the neutrinos, there are 19 arbitrary parameters: 9 fermion masses; 3 angles and one phase that specify the quark mixing matrix; 3 gauge coupling constants; 2 parameters to specify the Higgs potential; and an additional phase θ that characterizes the QCD vacuum state [38]. This does not sound much like a fundamental theory, which ought to have few free (unexplained) parameters.

Why is QCD confined?

Another feature of the SM is that QCD is confined, meaning that the strength of the force increases with distance, so the quarks are bound to stay close together – but the reason for it remains elusive.[17]

Is it possible to unify all the forces to one?

Along the lines of the belief of a simple, underlying structure, it is an alluring idea that the forces we have today are really only manifestations of *one* force. The thought would be that symmetries that are broken at the energy scale of today, might be restored at higher energies. The evolution of the coupling constants of the forces with energy further fires this hypothesis: they seem to close in on each other at higher energies. However, they do not meet in a single point with the

[17]This is even one of the seven so-called Millennium Prize Problems, announced by the Clay Mathematics Institute in 2000, recording some of the most difficult mathematical problems at the turn of the millennium [39].

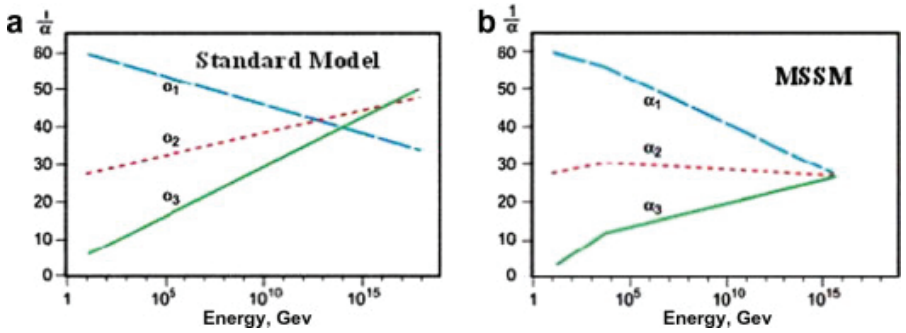

Figure 2.7: The coupling constants of the three forces as a function of energy, **a** in the SM and **b** in the Minimal Supersymmetric extension to the SM (MSSM) [41]. This illustrates that a unification of the forces is easier to achieve in the supersymmetric scenario than in the Standard Model.

evolution of the SM alone (*the unification problem*), but seem to come together much more nicely in more advanced theories, like supersymmetry (SUSY) [40], illustrated in Fig. 2.7.

Do the constituents themselves have an inner structure?

History has shown repeatedly that objects that were thought to be indivisible turned out to have some inner structure – so it is appropriate to display the humility of posing this question.

Why is there such a discrepancy between matter and antimatter?

There is a profound imbalance between the amount of baryonic and anti-baryonic matter in the universe. This asymmetry is a result of that there was matter left after the annihilation of the matter and anti-matter produced in the Big Bang (assumed to be produced in equal proportions). The physical process at the origin of this asymmetry, and thus the reason that we are here today, is called baryogenisis. The baryogenisis described in the SM is not large enough to explain the actual imbalance.

2.5 Models Beyond the Standard Model

To solve some of the problems of the SM, a great number of theoretical models for physics beyond the Standard Model have been proposed. These theories are more or less exotic, but they all have in common that they extend the content of the SM, either by expanding the minimal gauge symmetry group which is

contained in the SM or by only extending the particle content.[18] For an overview of some experimental limits by ATLAS on various exotic models other than supersymmetry, see Fig. 2.8. An exhaustive list of these would be far beyond the scope of this thesis. In the following sections, we will go into some detail for a few theories beyond the Standard Model, one of which incorporates the BEH mechanism (supersymmetry), and one which replaces the BEH mechanism with particle dynamics (technicolor).

2.5.1 Supersymmetry

Supersymmetry (SUSY) postulates that there exists a symmetry between bosons and fermions, making each spin-$\frac{1}{2}$ particle have a spin-1 sibling and *vice versa*. The symmetry group of this theory is the same as for the SM, but the particle content is doubled, and in order to give masses to both the right-chiral and left-chiral doublets, another BEH field must be introduced, resulting in five Higgs bosons instead of the one sufficient to do the job in the SM. It is interesting to note that the BEH mechanism is an integral part of supersymmetry, and the form of the BEH potential can be explained through radiative breaking of electroweak symmetry. Supersymmetry predicts that the mass of the lightest neutral Higgs boson, h, should be lighter than the mass of the Z^0 at tree level. Higher order radiative corrections can drive m_h up to around 130 GeV, but a higher mass than that is difficult to obtain [42]. Since supersymmetric particles have not yet been observed, this symmetry must be a broken one, such that the mass scales of our known elementary constituents and the supersymmetric ones are quite different. Imposing this symmetry is appealing, since it solves the hierarchy problem – the corrections to the mass of the Higgs boson by heavier particles are cancelled by the loops including the supersymmetric particles, contributing with the opposite sign (the fermionic and bosonic loops cancel each other). In addition, as mentioned earlier, the evolution of the coupling constants in SUSY seems to indicate that these come together quite nicely at some higher energy scale, giving aid to the idea of a GUT. Furthermore, if the lightest supersymmetric particle (LSP) is stable, it poses as an excellent candidate for the dark matter making up about 25% of our universe. The LSP is stable, when R-parity is conserved. R-parity is given by

$$P_R = (-1)^{2s+3B+L} \ , \tag{2.42}$$

[18] "Only" extending the particle content means to introduce new fields which obey the symmetry group already contained in the Standard Model. Extending the symmetry group of the SM also leads to new particles.

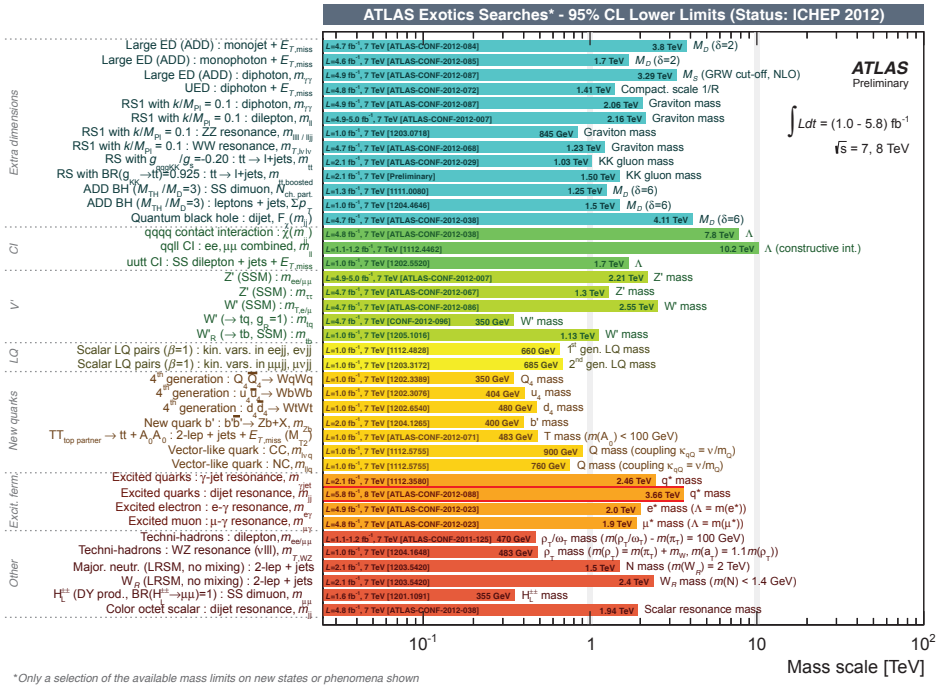

Figure 2.8: An overview of the limits of a selection of new physics (exotic) models in ATLAS, represented as the lowest allowed value at the 95% CL of one of the main variables of the theory (*e.g.* particle mass or energy scale). Several possibilities for the existence of more dimensions than the four we know are studied – see Section 2.5.3 for further discussion about extra dimensions. New physics at scales beyond the reach of the LHC can be modelled by contact interactions (CI), which are described by effective four-fermion point interactions, and not mediated by a gauge boson. This affects *e.g.* the invariant mass spectra of dileptons and high-p_T jet rates. Many possible extensions to the SM introduce additional, heavy gauge bosons, V', generally called W' for charged bosons and Z' for neutral ones. In the 'Sequential Standard Model' (SSM), these have the same couplings as the SM weak bosons. The similarities between leptons and quarks in the SM inspire the thought of a fundamental relationship between these at higher energies, leading to leptoquarks (LQ) – hypothesized particles that carry both lepton and baryon number. Searches for more quarks (among other as part of a fourth generation, since there is no reason in the SM why there should be only three generations), excited fermions (*i.e.* that the fermions are composite particles), techni-hadrons (see Section 2.5.2 for a brief introduction to the theory of technicolor), majorana neutrinos (where the neutrino is its own anti-particle) and many more phenomena are also performed.

where s is spin, B is baryon number and L is lepton number. Standard Model particles have R-parity 1, while supersymmetric particles have R-parity -1. Conservation of R-parity causes supersymmetric particles to be produced only in pairs; a supersymmetric particle *must* decay to an odd number of supersymmetric particles. Although very appealing, SUSY is not yet observed. The allowed parameter space is continuously being diminished by the measurements and searches performed at the LHC, and the simplest solutions are already almost completely ruled out. An overview of the limits on some of the various supersymmetric models, represented as the lowest allowed value at the 95% CL of one of the particle masses or energy scales of the theory is shown in Fig. 2.9.

2.5.2 Technicolor

An alternative to the BEH mechanism for assigning mass to elementary particles is to have the symmetry broken dynamically instead of introducing a scalar field. In dynamical symmetry breaking, the symmetry is broken by condensates of new (techni)particles, much like in superconductivity. The gauge bosons are given their masses through gauge interaction with these condensates. In order to give fermions masses, an additional new sector must be introduced, in which technifermions also interact with the fermions through new gauge bosons – this is called Extended Technicolor. The naturalness of technicolor is attractive, no fine-tuning is needed, and thus the hierarchy problem would be solved. Even with the presence of a BEH field, technicolor might also be realized in Nature. It is, however, difficult to construct such a theory that is in accordance with data [38, 43–47].

2.5.3 Extra Dimensions

One way of extending the theory is to introduce extra space-time dimensions, in addition to the four we know of today (three space and one time dimension). This was first proposed by Theodor Kaluza and Oscar Klein in the 1920's, in an attempt to unify electromagnetic and gravitational fields. Since these extra dimensions are not yet discovered, they must be by some means inaccessible at the scales we have probed until now. They could either be minuscule, called Kaluza-Klein compactification, as in universal extra dimension theories where the extra dimensions have been rolled up into compact circles [48], or large, but extremely warped as for instance in the Randal-Sundrum model [49]. Extra dimensions could be the reason why gravity is such a weak force compared to the ones incorporated in the SM. This could be explained for instance by gravity being spread also into additional, large dimensions and therefore being diluted, while the other forces are banned from dimensions other than our four known ones, as in the ADD (Arkani-

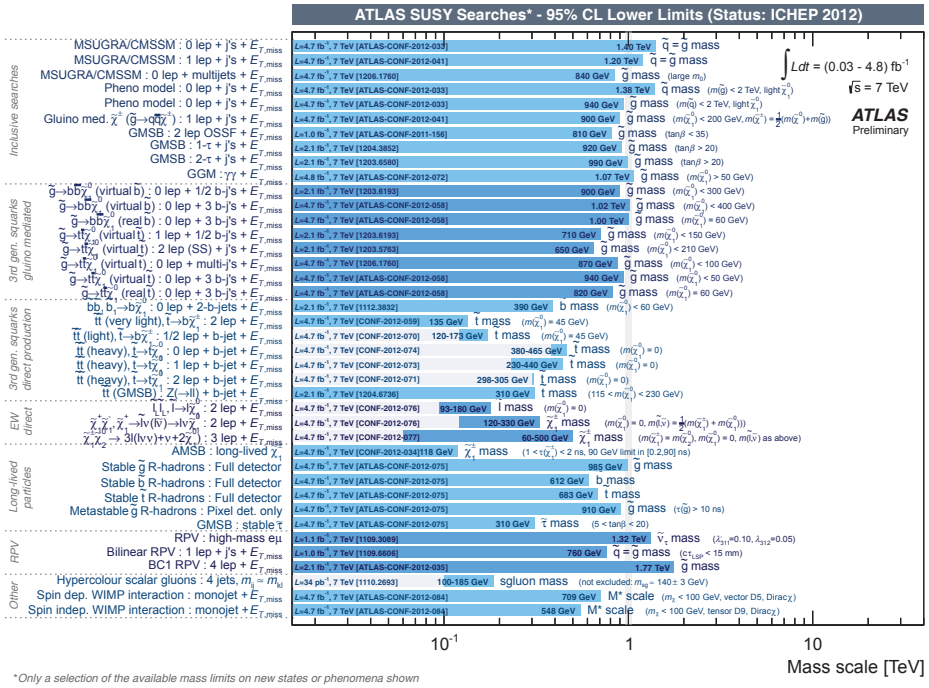

Figure 2.9: An overview of the limits on various supersymmetric models, represented as the lowest allowed mass of chosen supersymmetric particles at the 95% confidence level. There are many parameters that can be adjusted in SUSY, giving different signatures to search for. For instance, in the smallest extension of the SM that realizes SUSY, the Minimal Supersymmetric Standard Model (MSSM), more than 100 new parameters are introduced. There are several mechanisms, which can break the symmetry, in order to give the different mass scales to SM particles and SUSY particles. Limits on models based on these various symmetry breaking mechanisms, like gravity mediated symmetry breaking, the minimal supergravity model being mSUGRA, and Gauge Mediated Supersymmetry Breaking (GMSB), can be seen. Also general searches, with as little assumption as possible on the underlying mechanisms are performed, looking for fingerprints that occur within many SUSY models. Scenarios where R-parity conservation is violated (RPV) are also considered.

Hamed, Dimopoulos and Dvali) model [50]. This is not the case in universal extra dimensions, where all forces propagate universally in all dimensions (the closest option to the original idea of Kaluza-Klein). The quantized excitations in the compact dimensions are observed as new particles, so called KK-towers, in our four dimensional world. In such theories, unification of the SM forces is allowed, with the observed Planck scale only seeming large because of the extra dimensions.

We observe a "fake" Planck scale M_F given by

$$M_F^2 = M_p^{2+\delta} R^\delta, \tag{2.43}$$

where M_p is the real Planck scale, R is the size of the extra compact dimensions and δ is the number of such extra dimensions. In this way the Planck scale may well be of the order of the weak scale. Introducing extra dimensions may also make it possible to build GUTs, as for instance in string theory, requiring both extra dimensions and SUSY.

2.6 Concluding Remarks: the Way Forward

This very selective display of some exotic theories serves to show that theorists have been several steps ahead of experimentalists for the last half century. The way forward is not at all clear, and one tends to try in every possible (however plausible) direction. The BEH mechanism has long been the unproven theory in which physicists have believed the most (which also includes supersymmetry, having the BEH mechanism as an integral part). This, due to that it is woven so deeply into the tapestry of the Standard Model. The electroweak theory is based on the BEH mechanism being a reality. Renormalization of the theory was not achieved before the BEH mechanism was included in the description. The electroweak precision measurements are in great accordance with the prediction from theory, so if the BEH mechanism is not realized in Nature, something doing much of the same job must be present.

Thus, searching for and finding or disproving the Higgs boson is a very important step and points in which direction it may be profitable to proceed. This is, and has been, one of the highlights of LHC physics programme. Precision electroweak measurements, together with the hypothesis of the theory of the BEH mechanism, with its radiative corrections to these electroweak processes, give an indication of the mass of the Higgs boson, as displayed in Fig. 2.10. These yield a 95% CL that the mass of the Higgs is less than 152 GeV, including both experimental and theoretical uncertainty, and indicate 94^{+29}_{-24} GeV being the most likely value. The observed, new resonance, as declared in the Summer of 2012, reveals a particle at around 126 GeV – just at the border of the upper 68% CL value as obtained from this fit to precision EW data.

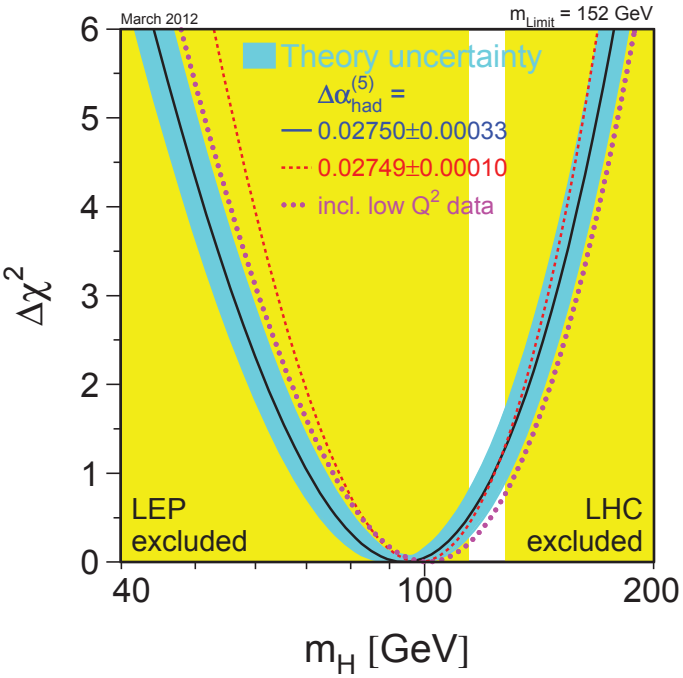

Figure 2.10: The status of a global fit to the Higgs boson mass, m_{H}, as of March 2012. Electroweak precision measurements performed at LEP, SLD, and by the CDF and D0 experiments at Tevatron, assuming the Standard Model to be the correct theory of Nature, give an indication of the Higgs boson mass, here as a $\Delta\chi^2$ of a fit to these. The most likely value of the Higgs boson mass is at the minimum of the curve, at 94 GeV. The experimental uncertainty is +29GeV and −24GeV (at $\Delta\chi^2 = 1$ of the black line). The yellow areas are excluded by direct searches for the Higgs boson; the lower masses by LEP, the higher masses by LHC and Tevatron at Fermilab. Theoretical uncertainty is given by the cyan band [51].

Chapter 3

The Experimental Setup

As mentioned in the previous chapter, there is a synergy between theory and experiment; they both rely on each other. To sustain the feedback between the two, a test of the theories that have been presented must be performed. In order to be able to do so, an experiment must be built. In this chapter, a few of the tools developed and built to test predictions of quantum field theories will be presented. We will briefly describe the Large Hadron Collider (LHC) and the ATLAS detector, both situated at the physics laboratory CERN.

3.1 CERN

CERN, Conseil Européen pour la Recherche Nucléaire – European Organization for Nuclear Research,[1] is situated at the border between France and Switzerland in the vicinity of Geneva, and is the world's largest particle physics laboratory. It was established in 1954 and has 20 member states and even more states with cooperation agreements and scientific contact. Scientists from 608 institutes and universities with 113 nationalities from around the world use CERN's facilities. These make up around 10 000 persons; half the world's particle physicists. The cooperation of humans with such different background, culture and language – all gathered with the common goal of unravelling the mysteries of the nature of fundamental physics, all speaking the language of mathematics – is something of beauty and can thus, in addition to being a scientific enterprise, be characterized as a global peace project. The variation in the work performed at CERN is

[1] At the time CERN was founded, nuclear research was the frontier. Today, a large fraction of the research done at CERN is the study of even smaller constituents of Nature, and CERN is often referred to as the European laboratory for particle physics.

substantial, from developing equipment, care for safety issues, human resources responsibilities, data treatment and storage, and innumerable different physics experiments and analyses.

Advanced technology is necessary to wring from Nature its secrets at the scale of elementary particles. This becomes apparent when considering that it took more than 20 years from the biggest accelerator, the Large Hadron Collider, and the experiments connected to it were first thought of, until they were commissioned – a planning process involving trust in that the technology needed, but not present at the time, would be developed in the course of time. Technologies such as the cooling down of huge magnets to obtain superconductivity, needed to produce the powerful magnetic field required to keep high-energy protons in circular orbit around the LHC, had to be developed. Indeed, they were. The CERN accelerator complex can be appreciated in Fig. 3.1.

3.2 The Large Hadron Collider at CERN

The Large Hadron Collider (LHC) [53–55] is not only the biggest particle accelerator at CERN, but also in the world. It started operation the 10^{th} of September 2008, before an accident[2] caused it to be shut down for somewhat more than a year [56]. After reopening in November 2009, it has been extremely successfully operated and delivered more collision data than dreamt of.

The accelerator lies approximately 100 meters underground, is about 27 kilometers in circumference, comprises around 9600 magnets cooled down by 130 tonnes of superfluid helium to a temperature of 1.9 K (colder than outer space), and holds an ultrahigh vacuum. The main dipoles produce a magnetic field of 8.3 T and are used to steer the protons. The other magnets are used to focus and tune the beam. To appreciate the size of LHC, and the complexity of the machine, see Fig. 3.2: an aerial view of the Geneva area with the LHC and SPS sketched in to the left, and the cross section of a dipole magnet to the right. When operated at design energy and intensity, the protons in the two beams circulating in opposite directions in the machine each has a kinetic energy of 7 TeV. The beams then consist of about 2800 proton bunches each, one bunch consisting of $1.1 \cdot 10^{11}$ protons, revolving more than 11 000 times around the ring each second (close to the speed of light). The total energy stored in two such LHC beams is about 700 MJ (and ca. 30 times more in the magnets), equivalent to around 170 kg of TNT explosives, enough to melt around 500 kg of copper. One such beam might circulate in the LHC for nearly 24 hours, putting a distance behind it large enough to reach the outskirts of

[2] A magnet quench (loss of superconductivity) due to an electrical connection fault resulted in 750 meters of damaged magnets and the loss of approximately six tonnes of helium.

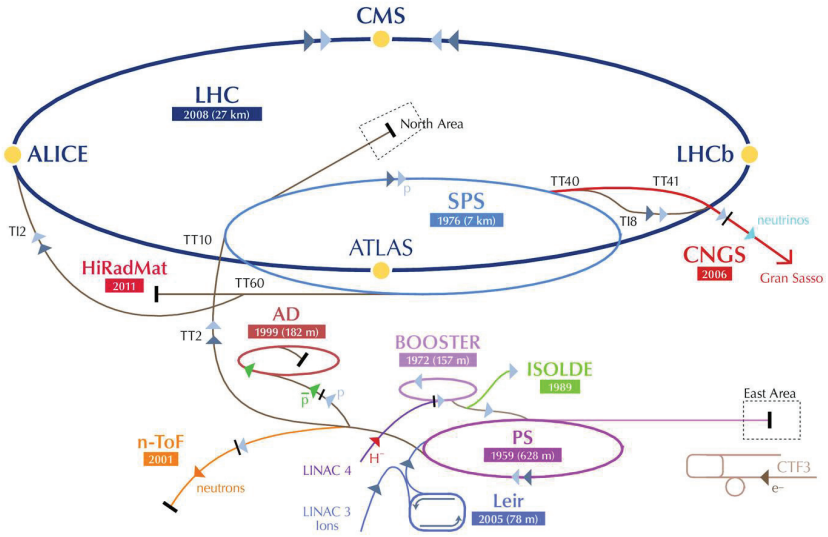

Figure 3.1: The CERN accelerator complex [52] – showing the path the particles travel before being collided head-on in the detectors (yellow dots) located around the LHC ring; protons from ionized hydrogen gas gain speed in a linear accelerator (LINAC2), before being injected at 50 MeV in the PS Booster (heavy ions also collided in the LHC start from LINAC3 and go through the Low Energy Ion Ring (LEIR) instead). When the beam has reached 1.4 GeV, it is fed to the PS (Proton Synchrotron), being further accelerated to 25 GeV and transferred to the SPS (Super Proton Synchrotron). In the SPS, the proton beam gains an energy of 450 GeV before finally being sent into the LHC, to be accelerated for ca. 20 minutes before reaching the final collision energy. Other experiments performed at CERN can also be seen, like the study of the gravity of anti-hydrogen at the Antiproton Decelerator (AD), numerous studies of the properties of nuclear and atomic matter at ISOLDE, neutron-induced reactions at n-TOF and neutrino flavor oscillations from the neutrino beam sent to Gran Sasso in Italy.

our solar system and back. The distance between the proton bunches is about 7 m (or 25 ns) at the design intensity. At this design configuration the machine will produce around 600 million proton-proton collisions per second. A measurement of intensity is *luminosity*, depending on the bunch crossing (BC) frequency, f, the transverse size of the beam, $4\pi\sigma_x\sigma_y$, and the number of protons in each of the two bunches, n_1 and n_2. Assuming complete overlap between the two colliding bunches, the luminosity is given by

$$\mathcal{L} = f\frac{n_1 n_2}{4\pi\sigma_x\sigma_y}\ , \tag{3.1}$$

and is of the order of $10^{34}\,\mathrm{cm}^{-2}\mathrm{s}^{-1}$ at the design configuration. Such extreme conditions are needed to reach the minuscule cross sections of the rare processes

(a) (b)

Figure 3.2: (a) Overview of the LHC and SPS tunnels from above [57]. The Geneva airport can be seen to the right in the picture. The main part of CERN is the triangle shaped cluster of buildings where the two rings meet. (b) Cross section of a dipole magnet [58], which steers the protons on a circular track. The actual magnets are the half-circle shaped metal coils around the beam pipes; the other structures are in place to keep the temperature down, the electricity running, the vacuum acceptable and the construction stable, counteracting the force the magnet sets up. The proton bunches are illustrated as bright lines emerging from the beam pipes.

which are being sought. The LHC also accelerates and collides heavy ions, such as lead, at 2.76 TeV per nucleon.

The accelerated particles collide head-on-head at various points located around the LHC ring. At these unprecedented high energies, which only existed a fraction of a nano-second after the Big Bang, particles never seen before might be produced and discovered. For the purpose of gathering the information about what happened in the collisions, four detectors are built at the collision points,[3] as illustrated in Fig. 3.3. These are ALICE (A Large Ion Collider Experiment), ATLAS (A Toroidal Lhc ApparatuS), LHCb (Large Hadron Collider beauty experiment) and CMS Compact Muon Spectrometer). ALICE is designed to primarily look at the heavy ion collisions that will take place in the LHC, to study the nature of quark-gluon plasma believed to exist in the very first fractions of time after the Big Bang. LHCb is specialized to look at hadrons containing the beauty (bottom) quark to unveil the nature of CP-violation, to close in on the answer to the riddle of why there is such an asymmetry between matter and anti-matter in the universe. The ATLAS and CMS detectors are general purpose detectors, built to be able to discover a broad spectrum of possible new physics. They were both designed in such a way that, given the existence of the Higgs boson, a discovery would be guaranteed. More details about the ATLAS detector, used in this thesis, will be given in the following section.

[3] There exists several other, smaller detectors around the ring of various purposes, but we will not address them here.

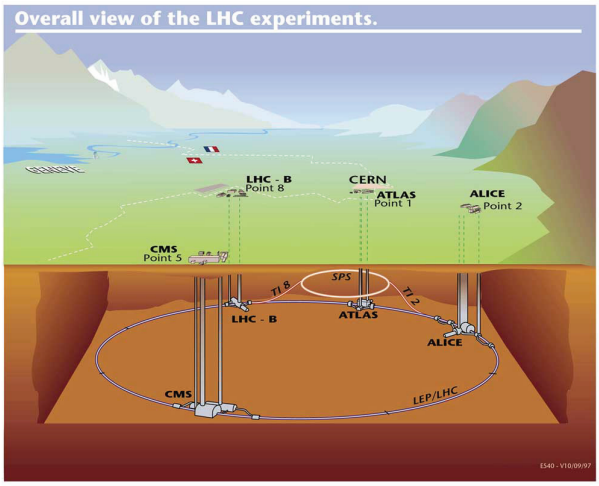

Figure 3.3: Overview of the LHC tunnel [drawing by CERN], approximately 100 meters underground, at the border of Switzerland and France. Four major detectors are connected to it: ALICE, ATLAS, LHCb and CMS.

3.3 The ATLAS Detector

The ATLAS (A Toroidal Lhc ApparatuS) detector [59–63] is one of the two general purpose detectors at the LHC, and is the biggest one in volume. It is 25 meters high, 44 meters long and weighs about 7000 tonnes (this is equal to the weight of approximately 40 empty 747-400 jumbo jets [64]). Its location along the LHC-ring is called *Point 1*, to which we will be referring later. This term includes both the physical buildings and structures (like the ATLAS control room and the computer farm next to the detector), as well as the software and monitoring implemented to run the detector and trigger the events.[4] ATLAS is not only a magnificent detector, it is also an experiment – around 3000 people work within ATLAS – which makes it one of the largest collaborative efforts ever attempted in the physical sciences. In this section, we will introduce the ATLAS detector and its structure.

The coordinate system of ATLAS, as illustrated in Fig. 3.4, is a right-handed one, in which the z-axis points along the beam-pipe in the counterclockwise direction seen from above, the y-axis points upwards to the earth's surface and the x-axis points towards the center of the LHC ring. The azimuthal angle, ϕ, runs in the transverse plane around the beam-line. The polar angle, θ, is measured from the

[4] An *event* is referred to as the resulting activity in the detector as a consequence of one bunch crossing.

beam-axis, but most commonly, the *pseudorapidity*, η, is used instead. This is defined as

$$\eta = -\ln\left[\tan\left(\frac{\theta}{2}\right)\right] . \tag{3.2}$$

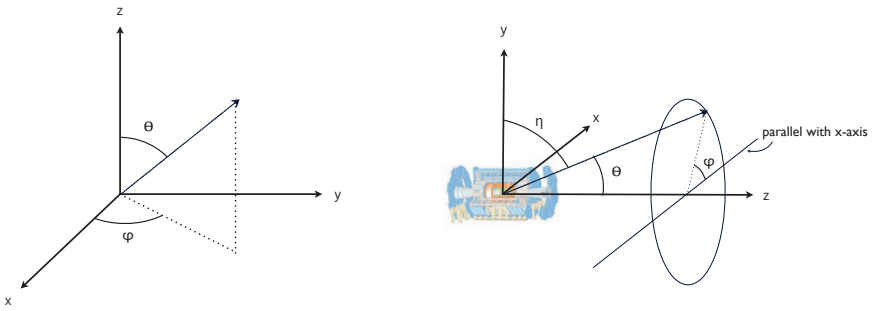

Figure 3.4: The coordinate system of ATLAS, illustrated from two different perspectives. The polar angle, θ, the azimuthal angle, ϕ, and the pseudorapidity, η, are indicated. The ATLAS detector is sketched in the rightmost view of the coordinate system.

The transverse momentum, $\vec{\mathrm{p}}_\mathrm{T}$, and the thereto belonging missing component, $\vec{\mathrm{p}}_\mathrm{T}^{\,miss}$ (also denoted $\not{\vec{p}}_\mathrm{T}$), are defined in the x-y plane. The scalar magnitudes of $\vec{\mathrm{p}}_\mathrm{T}$ and $\vec{\mathrm{p}}_\mathrm{T}^{\,miss}$ are often called $\mathrm{E_T}$ and $\mathrm{E_T}^{miss}$ (also denoted $\not{E}_\mathrm{T}$). The distance in pseudorapidity-azimuthal angle space is defined as $\Delta R = \sqrt{\Delta\eta^2 + \Delta\phi^2}$.

The ATLAS detector is built up of layers of various subdetectors, each with its own purpose. Each of the subdetectors are in three parts; one barrel and two end-caps. The ATLAS detector and its different components can be seen in Fig. 3.5. The 'general purpose' flavour of the detector means that it must be able to identify a large variety of possible new physics. Since the signature of new, weakly interacting particles will be that they escape detection – leave the detector unnoticed, taking some energy with them – they can only be reconstructed by missing energy. Thus, getting as close as possible to a hermetic detector covering the full 4π of solid angle is attempted, but this is complicated by cabling and supporting material.

3.3.1 Identifying Particles with the ATLAS Detector

ATLAS has an onion structure, with layers of different kinds of detectors. We will shortly describe the various subdetectors, but first we will address the motivation for such a structure. The purpose of the design is to be able to tell the different

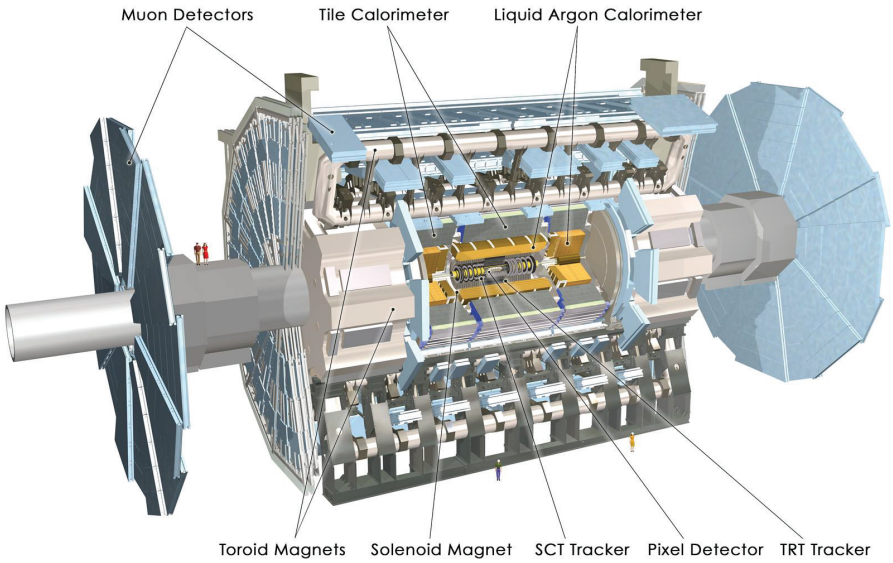

Figure 3.5: The ATLAS detector and its subdetectors [63]. At the core in grey is the inner detector, consisting of pixel layers, a semiconductor tracker (SCT) and a transition radiation tracker (TRT), all immersed in a magnetic field of 2T produced by the solenoid magnet. In yellow is the electromagnetic liquid argon calorimeter (ECAL), and in grey the hadronic tile calorimeter (HCAL). The blue structures are the muon spectrometer, for which the toroidal magnets in light grey produce a magnetic field aimed at determining the momentum of muons. Note the humans to the left and at the bottom of the detector to get a feeling of the vast size of the apparatus, which is 25 meters high and 44 meters long.

particles apart (as well as determine their properties like energy, momentum and charge). An illustration of the main idea of how to recognize the various particles can be seen in Fig. 3.6, in which a transverse cut of the ATLAS detector is displayed. The behaviors of the most frequently produced stable (with respect to detection in ATLAS) particles through the layers of the detector are depicted. Charged particles leave a track, curved by the magnetic field, in the inner detector, indicated by full lines. Dashed lines illustrate particles that do not interact with that part of the detector and are effectively invisible. Electrons and photons are fully stopped in the electromagnetic calorimeter, whereas hadrons, such as protons and neutrons, continue on through and deposit their energy only in the hadronic calorimeter. Muons, being minimum ionizing particles, leave a bit of their energy throughout the detector, and make it through to the muon spectrometer, where they are measured before they escape the detector. Some particles escape the detector leaving no trace behind, as neutrinos – they can only be inferred by conservation of energy and momentum and show up as missing energy in some part

of the detector. This is true also for many particles of new physics, like some of the postulated supersymmetric particles. To be able to use the law of conservation of energy to infer these particles, a close-to hermetic detector is crucial. Combining information from the different subdetectors makes it possible to interpret which kind of particle likely was observed. This simple illustration does not do justice to the complicated task of particle identification. The details of such an effort, for the case of the photon object, will be given in Section 4.2.

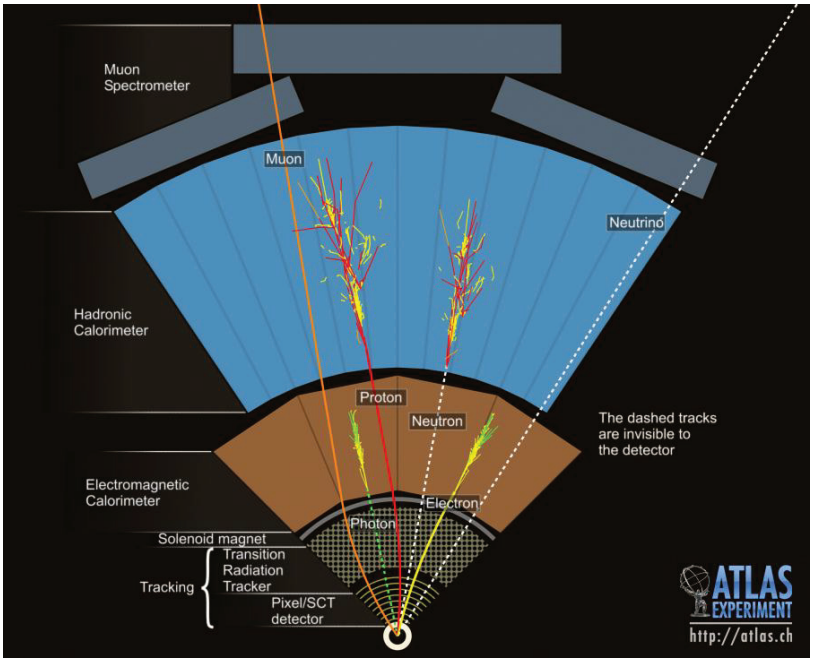

Figure 3.6: The identification of various particles with the use of the onion structure of the ATLAS detector. A transverse cut of the detector is shown; the beam pipe is indicated at the bottom by a small circle; it is followed by the different layers of subdetectors. The behaviour of the various particles through these layers is indicated. A dashed line illustrates particles that do not interact with that part of the detector. The bending of the muon tracks by the toroids cannot be seen in this transverse view.

3.3.2 The Inner Detector

The innermost part of ATLAS is called the inner detector (ID) and consists of three parts; the pixel detector, the semi-conductor tracker (SCT) and the transition radiation tracker (TRT). All these three subdetectors are immersed in

a 2T magnetic field produced by the solenoid magnet. To get a closer view of the ID structure, see Fig. 3.7. The ID must provide excellent resolution to render possible the reconstruction of the tracks and momentum of particles spanning a large energy domain. It must also be able to recover between the read-outs of different collisions/particle showers. The inner detector will be subject to large doses of highly energetic particles, and must be radiation-hard in order to survive such a harsh environment: at design luminosity, it will see around 40 billion charged particles per second. In addition, as little material as possible is wanted in the inner parts of the detector, to avoid inducing particle showers, causing the objects to loose energy before the calorimeters (whose job is to measure the energy of the particles). The resolution of the tracking parameter $\frac{1}{\mathrm{p_T}}$ is given by [11]

$$\sigma\left(\frac{1}{\mathrm{p_T}}\right) = a \oplus \frac{b}{\mathrm{p_T}} \ , \tag{3.3}$$

where $\oplus$ indicates addition in quadrature. Following this, it can be shown that

$$\frac{\sigma(\mathrm{p_T})}{\mathrm{p_T}} = a\,\mathrm{p_T} \oplus b \ , \tag{3.4}$$

where the constant a captures the intrinsic resolution of the detector, and b arises from multiple scattering, dominating the resolution at low momentum. The expected resolution of the tracking, with $\mathrm{p_T}$ given in GeV, is (depending on the position in the detector) around $\frac{\sigma_{\mathrm{p_T}}}{\mathrm{p_T}} = 0.05\%\,\mathrm{p_T} \oplus 1\%$ [65]; it is worse for larger momenta, since the bending of the track is smaller and thus harder to determine.

The pixel detector

Closest to the beam pipe are the three silicon pixel layers with double-sided processing, consisting together of 1744 pixel sensors of 250 μm thickness and dimensions 19×63 mm^2. Each sensor has 46 080 read-out channels, thus making up more than 80.4 million read-out channels in total. The layer closest to the beam-line, at a radius of 5.05 cm, is called the *b-layer*, and is important for recognizing particles with substantial lifetimes. Some particles, like those containing a b-quark, travel some short distance from the primary vertex (PV) before decaying – the b-layer makes it possible to resolve the secondary vertex of such decays. The other layers are at radii of 8.85 and 12.3 cm respectively. The end-cap disks are located at ±49.5, ±58.0 and ±65.0 cm along the z-axis. The pixel layers have an intrinsic accuracy of 10 μm in the $R-\phi$ plane orthogonal to the beam-axis ($z-\phi$ plane for the end-cap disks) and 115 μm along z (R for the end-cap disks).

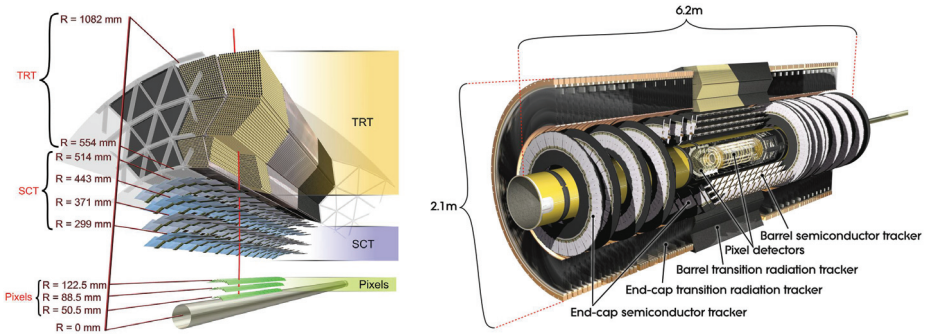

Figure 3.7: The inner detector of ATLAS [63]. To the left, the layers of the inner detector barrel at the different radial lengths from the beam pipe. To the right, both the barrel and end-cap parts of the inner detector.

The semi-conductor tracker (SCT)

Next in the onion-structure of the ATLAS detector is the silicon semi-conductor tracker. At larger radii, the particle density decreases, so the SCT is allowed a coarser granularity than the pixel detector. Four layers in the barrel and nine disks in each end-cap make up the SCT. For the radial distances at which the layers in the barrel are located, see Fig. 3.7. In the end-caps, the layers are located at ± 85.4, ± 93.4, ± 109.2, ± 123.0, ± 124.0, ± 117.1, ± 211.5, ± 250.5 and ± 272.0 cm along the z-axis. The SCT has 4088 modules (2112 in the barrel and 1976 in the end-caps) of length 128 mm, with two layers of 768 sensory strips of 12 cm per module. This comprises approximately 6.3 million read-out channels. The two sensors per module have a thickness of 285 μm, are glued back-to-back to the module spine and rotated by ± 20 mrad. With such a rotation, hits in two strips of the separate module layers provide a space-point. The SCT has an intrinsic accuracy of 17 μm in the $R - \phi$ plane ($z - \phi$ plane for the end-cap disks) and 580 μm along z (R for the end-cap disks).

The precision tracking of the pixel and SCT detectors are performed within $|\eta| < 2.5$. Both the pixel and SCT are operated in temperatures of -5 to -10 °C.

The transition radiation tracker (TRT)

The transition radiation tracker surrounds the SCT, at radii from 55.4 to 108.2 cm, with aluminized straw tubes of 4 mm diameter operating in room temperature. In

the middle of each straw is an anode made of 31 μm diameter tungsten wire plated with gold. The tubes are filled with a xenon/carbon dioxide/oxygen gas mixture, which is ionized when traversed by energetic, charged particles. The ions drift to the anode and the signal is read out at the end of the straw. The TRT has an intrinsic accuracy of 130 μm, and provides around 35 hits per track. In addition to tracking, the TRT is used for particle identification. It exploits the fact that particles radiate photons when they cross over from one material into another. The straw tubes are placed in plates of polypropylene fibers (foils in the end-cap) that serves as the transition radiation material. Low energy transition radiation photons are absorbed by the gas and yields a higher signal. How much transition radiation is induced, increases with the relativistic factor of the particle - thus, at a given momentum, a heavier particles radiate less than lighter ones, and the TRT information can be used to separate electrons from pions in the typical energy range of particles at the LHC. The TRT has about 350 000 read-out channels.

3.3.3 The Calorimeters

The calorimeters are built to measure the energy of particles emerging from the interaction point. The aim is to fully stop the particles by making them interact with matter in the calorimeters, scattering and producing so-called (electromagnetic or hadronic) showers. The calorimeter structure of ATLAS can be seen in Fig. 3.8. There are two calorimeters in the ATLAS detector: the electromagnetic calorimeter (ECAL) and the hadronic calorimeter (HCAL). As the ECAL is essential in the search for $H \to \gamma\gamma$, we will focus more on this part of the detector than the others. Electrons and photons are so to speak fully contained in the electromagnetic calorimeter and do not reach the hadronic calorimeter. The strongly interacting hadrons interact negligibly with the electromagnetic calorimeter and continue on to deposit nearly all their energy in the hadronic calorimeter. The liquid-argon calorimeters of both the ECAL and the HCAL reside in common cryostats, one for the barrel and two for the end-caps. The energy resolution of the calorimeters is the most important feature of the calorimetry and can be parametrized by [11]

$$\frac{\sigma_E}{E} = \frac{a}{\sqrt{E}} \oplus b \oplus \frac{c}{E} \ , \tag{3.5}$$

where a is the sampling term, a stochastic term indicating statistically related fluctuations due to, for instance, sampling differences, shower fluctuations and dead material in front of the calorimeter, b is the constant term, indicating non-uniformity of the calorimeter, calibration uncertainty and radiation damage of the active medium, and, finally, c is due to electronic noise. The higher the energy

deposited, the more accurate the measurement, up to high energies where the constant term, b, sets a limit.

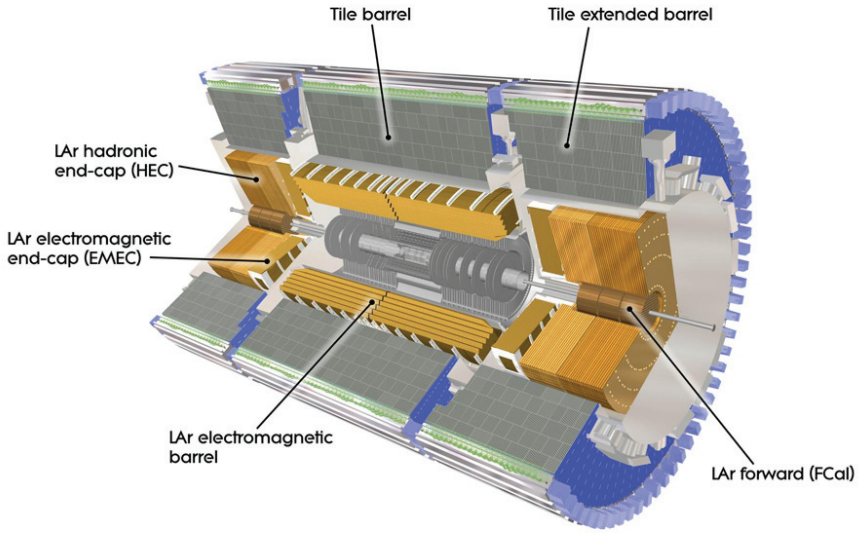

Figure 3.8: The ATLAS calorimeters [63]. The electromagnetic barrel and end-cap liquid-argon calorimeters (in yellow), along with the hadronic tile barrel and extended barrel (in grey) and hadronic liquid-argon end-cap and forward calorimeters (also in yellow).

The Electromagnetic Calorimeter (ECAL)

The lead-liquid argon (LAr) electromagnetic calorimeter of ATLAS has an accordion shape to maximize the material the particles traverses. The accordion shape also ensures full ϕ symmetry, without azimuthal cracks, and the features of this geometry give a very uniform performance in ϕ in terms of linearity and resolution. The passive (non-sensory) lead is in place to ensure a high rate of interactions. The thickness of the lead plates varies from 1.13 mm to 2.2 mm. The total thickness of the ECAL is more than 22 radiation lengths (X_0) in the barrel and more than 24 X_0 in the end-caps. The ECAL consists of a barrel, extending out to $|\eta| < 1.475$ and two end-caps, which cover $1.375 < |\eta| < 3.2$. Although the electromagnetic calorimeter covers a pseudorapidity range of $|\eta| < 3.2$, precision measurements are restricted to $|\eta| < 2.5$. In between the barrel and end-caps there is a section occupied mostly by cabling and cryostat walls that give poor performance in the region $1.37 < |\eta| < 1.52$. This is commonly referred to as the *crack region*. The barrel is divided into two parts separated by 4 mm at $z = 0$,

each weighing 57 tonnes, with a length of 3.2 m, an inner radius of 1.4 m and an outer radius of 2 m. Each half-barrel is divided into 16 modules, where one module covers a $\Delta\phi$ of 22.5°. In addition, to recover the energy lost by the photons and electrons upstream of the calorimeter, presamplers of thickness 1.1 (0.5) cm in the barrel (end-cap) are placed at $|\eta| < 1.8$. There are in total 3424 readout cells per module, including the ones in the presampler. The expected energy resolution of the ECAL is $\frac{\sigma_E}{E} = \frac{10\%}{\sqrt{E}} \oplus 0.7\%$ [65].

The ATLAS ECAL was designed with a sufficiently high granularity to render possible the resolution of a decay of the Higgs boson to two photons. In particular, being able to separate the two photons coming from the $\pi^0 \to \gamma\gamma$ decay instead of reconstructing them as a single photon is of uttermost importance. This is one of the most difficult and prominent backgrounds to the $H \to \gamma\gamma$ search. As can be seen from Fig. 3.9, the ECAL module is segmented in parts with different granularity. The first layer is called the strip layer, and is finely segmented in η; one strip is of width $\Delta\eta = 0.0031 \approx 4.7$ mm. This finely segmented region is an excellent tool to separate π^0s from photons and is made good use of in the shower shape discriminating variables for photon identification (see Section 4.2). The second layer captures most of the energy and the third layers collects only the tails of the energy distribution and is therefore less segmented in η. One cell, which is square only in the second layer of the ECAL, is approximately $\Delta\eta \times \Delta\phi = 0.025 \times 0.025 \approx 37$ mm $\times$ 37 mm.

The transformation of a photon into an electron-positron pair is called a *conversion*. Depending on pseudorapidity, around 25 – 60% of the photons will convert before they reach the face of the calorimeter. Recovering these photons is essential for the analysis, and we will learn more about photon conversions and recovery in Chapter 4.

The Hadronic Calorimeter (HCAL)

The hadronic calorimeter of ATLAS consists of a tile calorimeter in the barrel and LAr end-cap and forward calorimeters placed directly outside the electromagnetic calorimeter. The tile barrel extends to $|\eta| < 1.0$ and the extended barrel covers the region $0.8 < |\eta| < 1.7$. Radially, the barrel extends from 2.28 m to an outer radius of 4.25 m. It consists of steel plates as absorber material (19 mm in between each tile) and 3 mm scintillating tiles as the active medium, which together comprise around 9.7 hadronic interaction lengths (λ) of material at $\eta = 0$. Wavelength-shifters transform the ultraviolet light to visible light, to be detected by photomultipliers at each end of the scintillating tiles. In the end-caps, the absorber material is copper, and between the copper plates there are gaps of 8.5 mm filled with liquid argon (LAr) as the active material for this sampling calorimeter. This is true

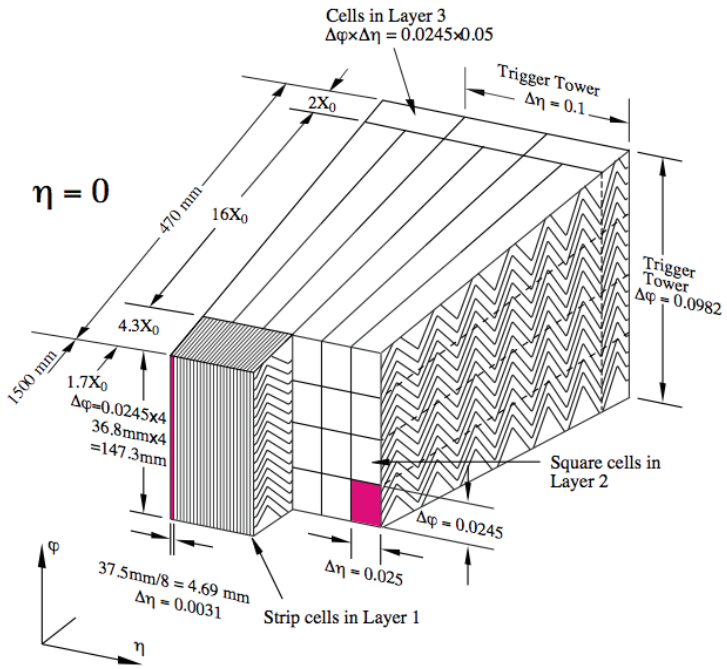

Figure 3.9: A barrel module of the ECAL [63], where the different granularity in η and ϕ of the three layers are shown.

(except for the use of different sized gaps) for one of the three modules of the forward calorimeter as well, the other two have tungsten as the absorber material. The expected energy resolution of the HCAL is $\frac{\sigma_E}{E} = \frac{50\%}{\sqrt{E}} \oplus 3\%$ in the barrel and end-caps and $\frac{\sigma_E}{E} = \frac{100\%}{\sqrt{E}} \oplus 10\%$ in the forward parts.

3.3.4 The Muon Spectrometer

The muon spectrometer (MS), as shown in Fig. 3.10, is built up of separate trigger and precision tracking layers. The resistive-plate chambers (RPC) in the barrel and the thin gap chambers (TGC) in the end-caps, covering the pseudorapidity range $|\eta| < 2.4$, are used for triggering events with muons. For precision tracking, chambers covering $|\eta| < 2.7$ are used. These are mainly monitored drift-tubes (MDT), in addition to the higher granularity cathode strip chambers (CSC) for the innermost layers at $2 < |\eta| < 2.7$. The expected momentum resolution in the muon spectrometer is $\frac{\sigma_{p_T}}{p_T} = 10\%$ for 1 TeV p_T muons, and about $\frac{\sigma_{p_T}}{p_T} = 3\%$ for 100 GeV p_T muons.

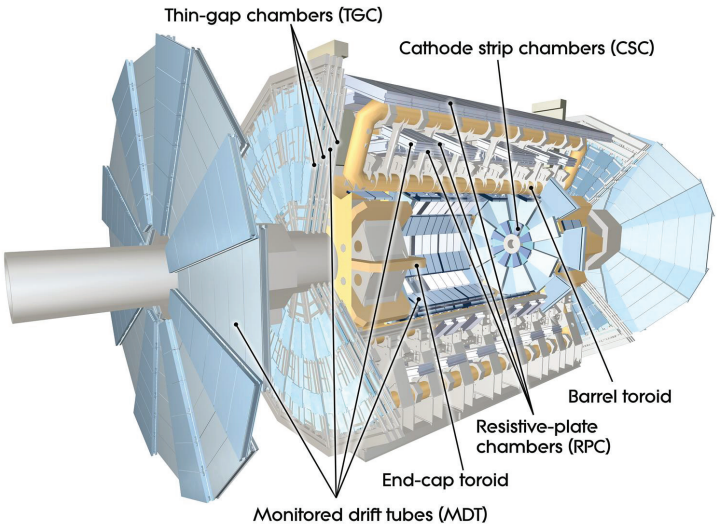

Figure 3.10: The ATLAS muon spectrometer uses resistive-plate chambers (RPC) and thin gap chambers (TGC) for triggering, and monitored drift-tubes (MDT) along with cathode strip chambers (CSC) for precision tracking [63].

3.3.5 The Forward Detectors

ATLAS has three smaller forward detector systems, two with the main purpose of measuring the luminosity delivered to ATLAS. These two are LUCID (LUminosity measurement using Cerenkov Integrating Detector) and ALFA (Absolute Luminosity For ATLAS), both of which detect p-p scattering in the forward direction. LUCID consists of gas-filled tubes around the beam pipe and is located at ± 17 m from the interaction point, before the last MDT layer of the MS. ALFA is located at ± 240 m and consists of scintillating fibers inside Roman pots, designed to approach the beam (once stable) to a proximity of 1 mm. In addition, the Zero-Degree Calorimeter (ZDC), located at ± 140 m from the interaction point, aims at measuring the centrality of heavy-ion collisions.

3.3.6 The Magnet System

The ATLAS detector has two distinct magnet systems – one for the inner detector; the solenoid, and one for the muon spectrometer; the toroids.

As mentioned earlier, the amount of material in the inner detector should be as small as possible, to avoid particle showers before the calorimeters. Therefore, the

solenoid is designed to be thin, and contributes with only 0.66 radiation lengths. Its job is to produce a magnetic field for the components of the inner detector, so the tracks of charged particles are bent, making it possible to measure their momenta from the curvature. For this purpose, the solenoid delivers a 2 T magnetic field. It operates at a temperature of 4.5 K and shares the vacuum vessel with the LAr calorimeter.

The superconducting air-core toroidal magnets are unique to ATLAS (as can be appreciated from the fingerprint they have put on the name of the detector). The toroidal magnets produce a magnetic field for the muon detectors of approximately 0.5 T in the central region and 1 T in the end-cap regions. There are eight toroid coils in the barrel and each of the end-caps. For the region $|\eta| < 1.4$, the barrel toroids provide magnetic bending of the muons, whereas for $1.6 < |\eta| < 2.7$, the smaller end-caps toroids perform the bending. For the transition region $1.4 < |\eta| < 1.6$, a combination of barrel and end-cap toroids is used. The toroid coils also operate at a temperature of 4.5 K.

3.3.7 The Trigger System

The trigger system is designed to cope with the immense amount of data produced in ATLAS, and has the task of filtering out which events are interesting, and which most likely stem from already-known processes. Storing detector data from all collisions can simply not be afforded, except under very low-luminosity conditions. The unknown physics that is sought for is taking place at an extremely low rate compared to the well-known physics; the cross sections are several orders of magnitudes smaller. Thus, the trigger must be able to make fast and correct decisions. In order to make the right decision, a large amount of information is needed. However, reading out this much information for each and every event is not feasible. It is for this reason that the trigger system of ATLAS is partitioned into three: Level-1 (L1), Level-2 (L2) and Event-Filter (EF), where L2 and EF are commonly referred to as the High-Level Trigger (HLT). The different levels process increasingly detailed information from the detector, which naturally leads to a longer latency. This does, however, not pose a bottleneck for the read-out of the detector; the higher levels can afford to spend a longer time making their decision, processing the more detailed information, because they receive a reduced data rate from the lower levels. Different chains of triggers are constructed, dedicated to recognizing physical objects like electrons, photons, jets and tau leptons, as well as large missing transverse energies, to accommodate for various models beyond the SM. The bunch crossing rate in ATLAS will at the design be around 40 MHz – the trigger will reduce this to around 200 Hz of interesting events to be permanently stored. The structure, data-flow, rates and latencies of the ATLAS trigger system

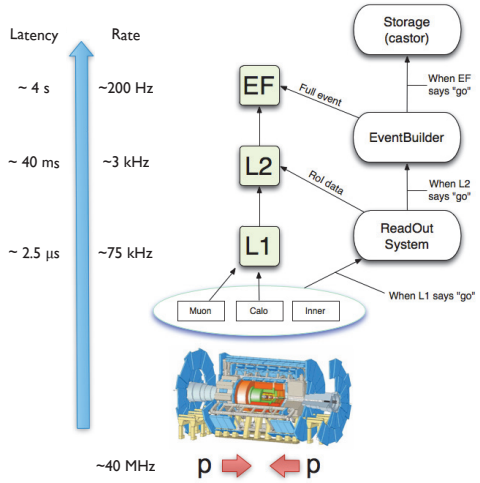

Figure 3.11: The trigger system of ATLAS, with the three levels (L1, L2 and EF), the corresponding latencies and rates, along with the flow of information. A coarse read-out of the muon system and the calorimeters are used for the L1 decision. If the event is accepted by L1, proper read-out (also of the inner detector) is temporarily stored in the ReadOut System (ROS), and Regions of Interest (RoIs) are passed on to L2, containing more detailed information. If the event is accepted also by L2, the EventBuilder passes the fully reconstructed event to the EF. If the event finally passes the EF, it is sent to permanent data storage.

can be appreciated in Fig. 3.11. Details on the trigger system can be found in [66].

L1 uses a very coarse read-out of subsets of the detector. For the decision to be taken by L1, the muon spectrometer and the calorimeters are used to search for highly energetic particles or missing transverse energy. From this information, Regions of Interest (RoIs) are built up, later to be passed to L2. The rate of acceptance from the L1 trigger is aimed to be around 75 kHz and the latency is about 2.5 micro-seconds; during this time, read-out information resides in the pipe-lines of the detector. Once L1 has accepted the event, the information is read out to computer sub-farms in a rack-room next to the detector. The L2 uses the RoI information as created by L1, but at full precision and granularity within these, which is approximately 2% of the full event data. This level is designed to reduce the rate of data to approximately 3 kHz, at a latency of less than 40 ms. If L2 accepts the event, the fully reconstructed event is passed to the EF. At a latency of around 4 seconds, it makes its decision and finally reduces the data rate to about 200 Hz, which are permanently stored for physics analysis.

3.3.8 Pile-up in ATLAS

As mentioned earlier, the proton bunches circulated in the LHC consist of hundred billion particles. Therefore, when they collide, the probability of interaction between several of the protons is rather high. One event may therefore contain the outcome of several (hard) interactions of the protons in the bunches. Multiple interactions per bunch-crossings are generally referred to as *pile-up*. To be more precise, this is called *in-time pile-up*. Overlapping information from different interactions can also come from previous or following BCs, before the detector had time to recover from the action and corresponding read-out. This is called *out-of-time pile-up*. Pile-up presents a great challenge to an analysis, working out what occurred in one single interaction.

An example event in ATLAS after the September 2011 shutdown, in which the β^* was reduced to one meter from 1.5 meters,[5] can be seen in Fig. 3.12. In this event, 20 vertices are reconstructed, one of them containing a candidate $Z \to \mu\mu$ event. In 2012, ATLAS saw at the maximum instantaneous luminosity 72 events in one BC.

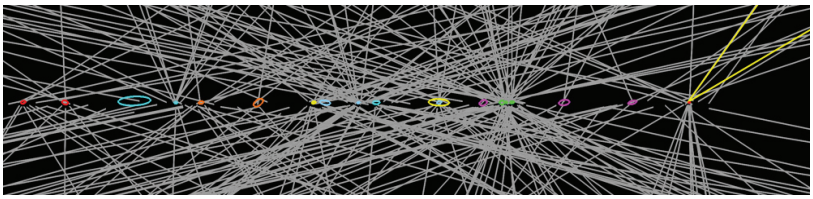

Figure 3.12: An event recorded by ATLAS the 14^{th} of September 2011, in which 20 vertices can be seen [67]. This is a zoom inside the vacuum-pipe, such that no detector elements are visible. Reconstructed tracks (in grey) extrapolated back to the vertices (colored ellipses) are shown. The vertex error ellipses are blown up by a factor of 20, in order to make them visible. To the rightmost, a candidate for a $Z \to \mu\mu$ decay is highlighted, with the muon tracks marked by thicker, yellow lines.

Some examples of the response in the detector depending on the pile-up can be seen in Figs. 3.13 and 3.14. In Fig. 3.13, the dependence of the calorimeter pointing (extrapolation to the beam from position and tilt of the reconstructed showers, see section 7.6 for more information) on pile-up is illustrated. The difference, Δz, in the estimated z-position of the vertex from each of the photons, as found from calorimeter pointing for photons passing the $H \to \gamma\gamma$ selection, with both photons

[5]The beam parameter β^* is the distance from the beam crossing to the position where the beam is twice as wide. The larger β^*, the less "squeezed" is the beam – the larger the cross section of the beam at the interaction point (with respect to the beam size outside the collision point). A small cross section of the beam at the interaction point is desirable to increase the probability of a hard scattering.

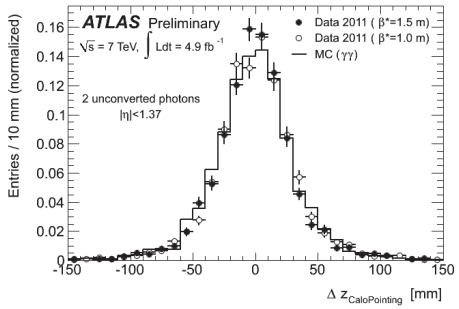

Figure 3.13: The difference, Δz, in the estimated z-position of the vertex from each of the photons, as found from calorimeter pointing (see section 7.6 for more information), for photons passing the $H \to \gamma\gamma$ selection, with both photons being unconverted and in the ECAL barrel ($|\eta| < 1.37$). The two different β^* configurations used in 2011 are shown, along with the expectation from Monte Carlo simulations. No impact on the increased pile-up (a consequence of the diminished β^*) is observed [68].

being unconverted and in the ECAL barrel ($|\eta| < 1.37$) is shown. The difference between the two β^* configurations, involving different amounts of pile-up, does not seem to have an impact on the resolution. This indicates that the ECAL can cope with the increased activity.

In Fig. 3.14, the dependence of the isolation on the out-of-time pile-up can be seen. The isolation as a function of which BC the event belongs to in the bunch train structure used in the LHC (in which there are groups of proton bunches, with some spacing in between) are plotted for two different isolation variables. The isolation variable based on a fixed area of calorimeter cells shows dependence on the BC. This is due to how the ECAL responds to energy deposits, where the resulting pulse shape has a large negative tail, specially designed to cancel out the contribution of underlying energy deposited in earlier bunch crossings. It takes approximately 12 BCs for this designed effect to fully take place, approximately as much as the ECAL readout window. This dependence disappears when using topological clusters, including only calorimeter cells above a certain threshold for the isolation variable, both for the raw isolation and for the ambient energy density corrections. The latter variable is the isolation used in this thesis. For more information about isolation, see Section 7.3. We will return to the issue of pile-up later in this thesis.

3.3.9 Performance and Data Harvesting

The detector has proven to work exceedingly well. The ATLAS data taking efficiency in 2011 was in total 93.5%, with a total recorded luminosity of 5.25 fb^{-1}, out of a total delivered amount of 5.61 fb^{-1}. However, there was a problem in the electromagnetic calorimeter, especially relevant for the $H \to \gamma\gamma$ search. In around 17% of the data taken in 2011, six Front End Boards (FEBs), devices for reading out the energy information of the calorimeter, were dead. These FEBs covered the region $0 < |\eta| < 1.475\,, -0.791 < \phi < 0.595$, of which four were in the second layer

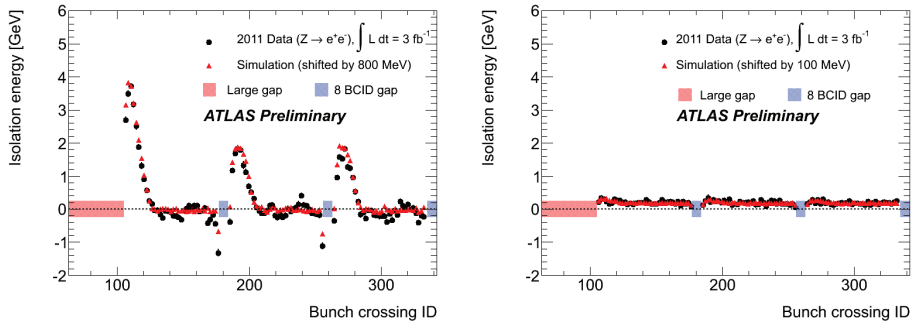

Figure 3.14: Dependence of photon isolation on out-of-time pile-up [68]. To the left is the isolation based on a fixed area of calorimeter cells, used by HSG1 for the Physical Review Letter (PRL) article in February 2012. This isolation variable showed dependence on which BC the event belonged to in the bunch-train structure in the LHC. The dependence is due to the ECAL pulse shape, having a long negative energy tail, designed to cancel the remaining energy activity from previous BCs. It takes approximately 12 bunches into the bunch train (corresponding to the ECAL readout window) for the pile-up energy contributions from previous BCs to cancel out. This dependence was gotten rid of, as illustrated in the figure on the right, with a new isolation variable based on topological clusters. The latter variable is the isolation used in this thesis. For more information about isolation, see Section 7.3.

of the ECAL, and two in the third layer. The four boards located in the second layer were repaired during a short technical stop in July.

The total integrated luminosity as a function of time can be seen in Fig. 3.15 on the left, and the peak luminosity can be seen to the right, increasing steadily throughout the data-taking period, reaching a maximum of $3.65 \cdot 10^{33}\text{cm}^{-2}\text{s}^{-1}$. The ratio of good data quality delivered by the detector subsystems after reprocessing was at an average 99.2%, ranging from 97.5% for the ECAL up to 99.8% for the solenoid magnet and the pixel detector [69]. The number of colliding bunches increased steadily until July 2011, at which time it reached nearly 1400. It was kept at this level for the rest of the data-taking. Data was collected from 21^{st} of March to 30^{th} of October 2011. The mean number of interactions per BC in 2011 was 9.1, with a maximum of 32 number of events in one BC. As can be appreciated from Fig. 3.16, the pile-up increased when β^* was diminished from 1.5 m to 1 m, which happened the 7^{th} of September, after a technical stop that started the 21^{st} of August [70]. Before this squeeze of the beam, the mean number of interactions per BC was 6.3, whereas after, it was 11.6.

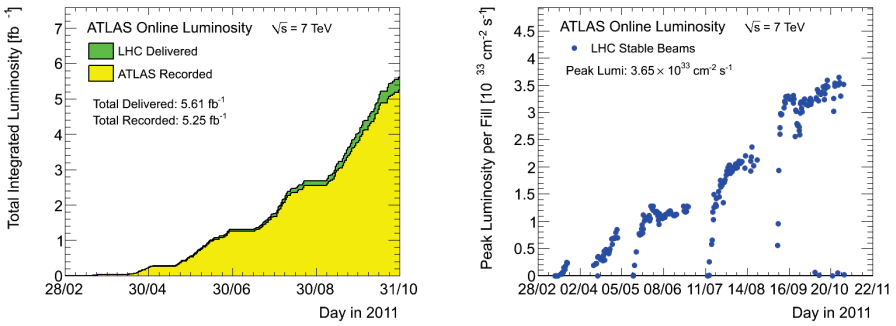

(a) The total integrated luminosity delivered by LHC and recorded by ATLAS, as a function of the date in 2011.

(b) The peak luminosity as a function of the date in 2011.

Figure 3.15: Data-taking with ATLAS in 2011 [71].

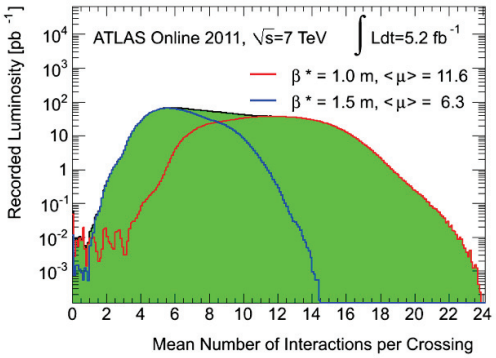

Figure 3.16: The mean number of interactions per bunch crossing in 2011 [71], for $\beta^* = 1.5$ and $\beta^* = 1.0$. It is apparent that squeezing the beam, indicated by a smaller β^*, increased the amount of pile-up.

3.4 Simulation of Collisions in the Detector

In order to know what in principle could be achieved with the data, simulations of the processes that take place in the collisions are made. These Monte Carlo (MC) samples must, to as large a degree as possible, resemble the data. Various MC generators are utilized for the purpose of simulating the hard scatterings of the protons, or more specifically the gluons and (sea or valence) quarks inside the protons, as well as the following process of hadronization. The interaction of the particles with the detector is of great importance for the similarity between the simulations and the data. A good knowledge about the material in the detector and its response to particles is needed. For simulating the passage of particles through matter, Geant4 (GEometry ANd Tracking) is used [72, 73]. These interactions

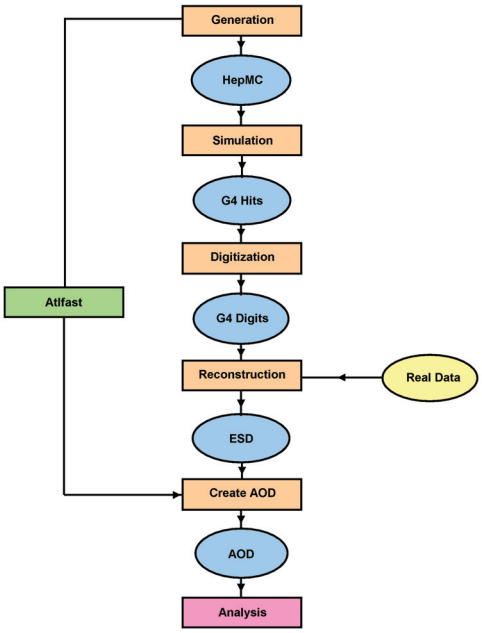

Figure 3.17: The chain of MC simulations in ATLAS [74]. The generation of hard scattering processes is done by various High Energy Physics (HEP) MC generators, in the form of EVNT files. The simulation of the particles passage through the detector is performed by Geant4 (G4), providing the HITS data format. Digitization of the interaction of the particles with the detector is made, yielding RDO files, looking like the data format files (RAW). At this stage, the simulation is treated exactly the same way as real data. Reconstruction of physical objects are done from these files. Several data formats are subsequently made, like ESD and AOD files, with different levels of information used for the numerous analyses. In fast simulation, denoted Atlfast, the interaction of the particles with the detector is skipped, and an average behaviour is applied. This is naturally less precise, but the production of the files is more rapid, such that sufficient statistics is reached faster.

then need to be digitized, like they would have been in a real collision in the detector.

Through the process of simulation, as illustrated in Fig. 3.17, different file formats, involving various amounts of information, are provided [74]. Geant4 receives EVNT files from the MC generators and produces HITS files, which are in terms digitized, converting energy deposits to detector responses, stored in RDO (Raw Data Output) files. These RDO files look the same as what the detector delivers, which is in the RAW data format, basically a byte-stream format of approximately 1.5 MB/event. From this stream, objects are reconstructed. The full information of these is available in ESD (Event Summary Data) files, with a typical size of around 1 MB/event. In the next step, AODs (Analysis Object Data) are made, focusing on "physical objects", like electrons and jets. Information about the track hits are for instance discarded for this data format. The typical size of AOD files is of the order of 200 kB/event. DPD (Derived Physics Data) files, nominally amounting to around 10 kB/event, are used for most end-analyses, for which the events have been through a filtering prosess, aimed at selecting interesting events for the specific analyses. For the $H \rightarrow \gamma\gamma$ analysis, this involves for instance choosing events that contain two photons with p_T greater than 20 GeV.

Chapter 4

Photons in the ATLAS Detector

At the base of any analysis lies the identification of the physics object(s) studied, the particle(s) upon which the analysis is built. For the analysis considered in this thesis, a search for $H \to \gamma\gamma$, that is the photon object. The reconstruction and identification of photons is thus an extremely important prerequisite for the analysis. In this chapter, we will address the task of identifying photons. We will have a look at the reconstruction and recovering of photons, as well as the discriminating variables describing the shape of the electromagnetic showers deposited by the particles in the calorimeter. These are used for selection of the photons and are constructed to give good separation from fake photons. First, we will introduce photon conversions; $\gamma \to e^+e^-$.

4.1 Photon Conversions

The rate of conversions of photons into electron-positron pairs depends on the amount of material. The probability for a conversion to take place in a layer is linearly dependent on the amount of material in that layer. In regions with higher $|\eta|$, the probability is larger, due to that the particle has to traverse more material. The fraction of photons converting inside a radius of 80 cm and 115 cm respectively as a function of $|\eta|$ can be seen in Fig. 4.1(a). Depending on $|\eta|$, between 10 to 50% of photons have converted before they leave the SCT, and between 25 and 70% of the photons convert below a radius of 115 cm. The probability for a photon to convert as a function of the radius, for four different pseudorapidities, can be

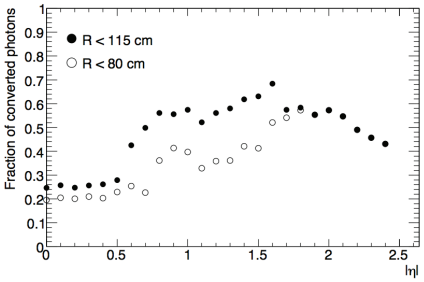

(a) Fraction of photons converting as a function of $|\eta|$, at a radius under 80 cm (115 cm) in open (full) circles.

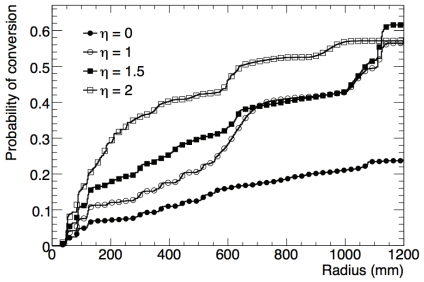

(b) The probability of conversion for photons in minimum-bias events with $p_T > 1$ GeV as a function of $|\eta|$.

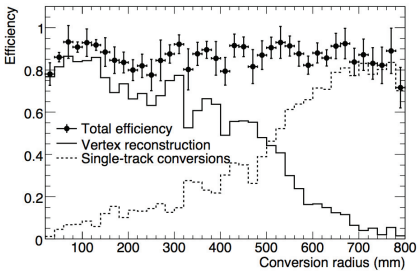

(c) The total efficiency for reconstruction photon conversions for photons with $p_T = 20$ GeV and $|\eta| < 2.1$ as a function of conversion radius, including single-track conversions.

Figure 4.1: Conversions of photons into electron-positron pairs in ATLAS [63].

seen in Fig. 4.1(b). Overall, as many as 60% of the photons will convert into an electron-positron pair before reaching the calorimeter [65]. The probability of conversion is fairly independent of the energy of the photon for $p_T > 1$ GeV.

If the conversion radius is within 80 cm, converted photons can be reconstructed efficiently [75], with a rather flat efficiency as can be appreciated from Fig. 4.1(c). This is, however, only the case if single-track conversions also are taken into account, in which the track of one of the electrons cannot be reconstructed. As can be seen in this figure, the efficiency for reconstructing conversions of photons with $p_T = 20$ GeV and $|\eta| < 2.1$ is about 90% [63].

4.2 Photon Identification

As mentioned earlier, the reconstruction and identification of photons is crucial for the $H \to \gamma\gamma$ search. We shall now see what demands and restrictions are put as a foundation for identifying photons. The material in this section come mainly from Ref. [76].

4.2.1 Reconstruction and Recovery of Photons

The starting point of finding a photon in the detector, is a cluster with energy exceeding 2.5 GeV found in a sliding 3×5 cells tower in $\eta \times \phi$ in the second layer of the electromagnetic calorimeter (to be reminded of the structure of the ECAL, see Fig. 3.9). Energy depositions in the finely segmented first layer in front and the coarsely segmented third layer in back are associated to this seed.

There are two classes of photons: converted or unconverted. If there is no track matched[1] to the photon, it is treated as an unconverted photon candidate. For the case of the converted photon, there is at least one track associated with it. For one track conversions, the track emerges at some radial distance from the primary vertex, and for double-track conversions, a secondary vertex within the tracker volume is identified. There is a large overlap between converted photons and electrons – almost all converted photons are also classified as electron candidates. In addition, a significant fraction (around 9% in the $H \to \gamma\gamma$ simulated sample) of unconverted photons are reconstructed as electrons, and need to be recovered after electron reconstruction. The innermost layer of the pixel detector, called the *b-layer*, because of its aim of identifying the secondary vertices of particles like B-hadrons, is important in separating electrons from photons.

To increase the efficiency for reconstruction, a recovery of photons that have converted is done. This is crucial, since a large fraction of the photons undergo a conversion. A search is made for tracks that originated in the inner detector (from the conversion vertex), which match the cluster when extrapolated to the calorimeter. When the second track is not expected to be found, one-track conversions are also included in the photon collection.

Comparison of the best-matched track of the cluster to the track candidate of the best conversion vertex is performed. If they coincide, the candidate is taken out of the electron collection, unless the p_T is smaller than that of the converted photon candidate. Electrons with only TRT-hits with $p_T < 2$ GeV and $E/p > 10$ are also recovered. Approximately 6 out of 7 converted photons erroneously classified as

[1] A *match* means a small distance in (η, ϕ) between the extrapolation of the last track measurement to the cluster center in the second sampling layer of the calorimeter.

electrons are recovered. For photons from $H \to \gamma\gamma$ with a $p_T > 20$ GeV, the efficiency before recovery is around 57% (6% for converted photons and 86% for unconverted photons), whereas after recovery it is substantially increased to about 98% (94% for converted photons and close to 100% for unconverted photons).

The energy of the object is calculated using the calorimeter. The size of the cluster considered depends on the classification of the particle. In the end-caps, 3×5 cells are used for unconverted photon clusters, 3×7 for converted. In the barrel, the cluster size is the same in both cases, namely 5×5 cells [75].

4.2.2 The Discriminating Shower Shape Variables

To identify a photon, calorimeter variables describing the shape of the electromagnetic shower are utilized. Combining these variables give good separation between isolated photons and fake photons from QCD jets, the most dominant source being π^0 (which decays to $\gamma\gamma$). Cuts are applied to the shower shape variables, and two different sets of cuts are constructed to make up the levels of photon identification: the so-called loose and tight definitions. The values for the cuts can be seen in Appendix D.

The tight selection gives an efficiency of about 85% for photon candidates with transverse energy larger than 20 GeV, and a corresponding background rejection factor of about 5000. For the same transverse energy, the loose selection gives an efficiency of about 95%, and a corresponding background rejection factor of about 1000. The reconstruction efficiency for a tight selection of photons coming from a $H \to \gamma\gamma$ decay is about 89% for photons with $p_T > 20$ GeV and 90% for photons with $p_T > 40$ GeV. For a detailed description of the efficiency of identifying photons in the 2011 data, see Ref. [77]. During 2012, a multivariate technique was employed for the tight classification, increasing the photon identification efficiency for a given background rejection. This gave an improvement of approximately 5% in the performance of the $H \to \gamma\gamma$ analysis [78].

After the loose (tight) selection, the composition of the sample for objects passing the shower shape cuts and having $E_T > 20$ GeV is expected from MC to be around 70 (48) % photons coming from π^0 decays, 10 (8) % from η, η' or ω decays into two photons and 6 (3) % from hadrons with complex decay processes and particles interacting with the material in the tracker. Approximately 8 (25) % of the photons in the loose (tight) samples at this energy are expected to be prompt[2] photons, and around 6 (17) % from initial or final state radiation of quarks.

[2] Prompt, "without delay", particles are produced directly in the proton-proton collision.

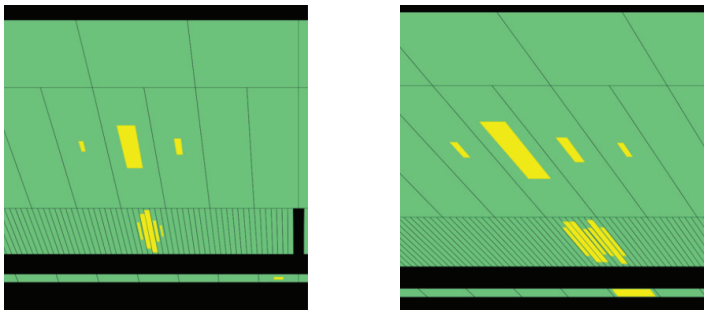

Figure 4.2: Illustration of the use of the finely segmented strip layer of the ECAL to separate photons from π^0s. The active calorimeter layers are indicated by the colored areas; the presampler can be seen at the bottom of the figures, followed by the finely segmented strip layer, the middle layer and the back layer of the calorimeter. The energy depositions of the photon candidates are indicated by the brighter areas. To the left is a tightly identified, isolated (the isolation energy is 178 MeV) photon with a p_T of 32 GeV. To the right is a non-isolated (6.2 GeV) π^0 with a p_T of 21 GeV passing the 2^{nd} layer identification criteria, but failing the strip layer criteria.

The fine granularity of the ECAL strip layer is vital for photon identification and position measurement. The strips extend to an $|\eta|$ of 2.4 [63]. Since the electromagnetic shower will have some extension, some strips on each side of the barycenter of the shower is required for a precise measurement. Thus, as a natural choice, clusters with barycenters in the last tower with strips are rejected. As can be seen in Fig. 3.9, a tower consists of $\Delta\eta \times \Delta\phi \approx 0.025 \times 0.025$. Ergo, the fiducial region extends to 2.4 - 0.025 $\approx$ 2.37.

Converted and unconverted photons are separated only in the tight selection. The variables used for the loose selection shows relatively small differences for unconverted and converted classifications; for trigger purposes, common cuts and thresholds are used for electrons and photons. The tight cuts are specially designed to give good γ - π^0 separation, by exploiting the finely segmented strip layer – therefore, the photons are required to lie within the pseudorapidity region covered by the strip layer. Together with excluding the crack region, this thus defines the fiducial detector acceptance region, defined by $|\eta| < 1.37$ and $1.52 < |\eta| < 2.37$.

The discriminating (shower shape) variables can be categorized in three: hadronic leakage, variables using the second (middle) longitudinal layer of the ECAL, and the ones using the finely segmented first (strip) layer. The strip layer cuts are designed to recognize second maxima, for instance to separate the two photons from the $\pi^0 \to \gamma\gamma$ decay, as illustrated in Fig. 4.2. For all variables, the cuts are independent of the photon transverse energy, but dependent on the position in η. The discriminating variables are as follows [79]:

- **Leakage in the hadronic calorimeter**

  The following discriminating variable is defined, based on the energy deposited by the photon candidate in the hadronic calorimeter:

  – *Normalized hadronic leakage*

  $$R_{\text{had}} = \frac{E_T^{\text{had}}}{E_T} \tag{4.1}$$

  is the total transverse energy, E_T^{had}, deposited in the hadronic calorimeter behind the electromagnetic cluster, normalized to the total transverse energy, E_T, of the photon candidate.

  In the $|\eta|$ interval between 0.8 and 1.37 the energy deposited in the whole hadronic calorimeter behind the electromagnetic cluster is used, while in the other pseudorapidity intervals only the leakage in the first compartment of the hadronic calorimeter is used (then called R_{had_1} – albeit the different names, the value is stored in one variable).

- **Variables using the second layer of the electromagnetic calorimeter**

  The discriminating variables based on the energy deposited in the middle layer of the electromagnetic calorimeter are the following:

  – *Middle η energy ratio*

  $$R_\eta = \frac{E_{3\times7}^{S2}}{E_{7\times7}^{S2}} \tag{4.2}$$

  is the ratio between the sum, $E_{3\times7}^{S2}$, of the energies of the second layer cells of the electromagnetic calorimeter contained in a 3×7 rectangle in $\eta \times \phi$ (measured in cell units), and the sum, $E_{7\times7}^{S2}$, of the energies in a 7×7 rectangle, both centered around the cluster seed.

  – *Middle ϕ energy ratio*

  $$R_\phi = \frac{E_{3\times3}^{S2}}{E_{3\times7}^{S2}} \tag{4.3}$$

  is defined similarly to R_η. R_ϕ behaves very differently for unconverted and converted photons, since the electrons and positrons generated by the latter bend in different directions in ϕ because of the solenoid magnetic field, producing larger showers in the ϕ direction than the unconverted photons.

See Fig. 4.3 on page 71 for an illustration of these two variables.

– *Middle lateral width*

$$w_{\eta_2} = \sqrt{\frac{\sum E_i \eta_i^2}{\sum E_i} - \left(\frac{\sum E_i \eta_i}{\sum E_i}\right)^2} \tag{4.4}$$

measures the shower lateral width in the second layer of the electromagnetic calorimeter, using all cells in a window $\eta \times \phi = 3 \times 5$ measured in cell units.

◦ **Variables using the first layer of the electromagnetic calorimeter**

The discriminating variables based on the energy deposited in the strip layer of the electromagnetic calorimeter are the following (the naming convention is "front", indicating that this is measured in the first layer of the ECAL):

– *Front side energy ratio*

$$F_{\text{side}} = \frac{E(\pm 3) - E(\pm 1)}{E(\pm 1)} \tag{4.5}$$

measures the lateral containment of the shower, along the η direction. $E(\pm n)$ is the energy in the $\pm n$ strip cells around the one with the largest energy.

– *Front lateral width (3 strips)*

$$w_{s\,3} = \sqrt{\frac{\sum E_i (i - i_{\max})^2}{\sum E_i}} \tag{4.6}$$

measures the shower width along η in the first layer of the electromagnetic calorimeter, using two strip cells around the maximal energy deposit. The index, i, is the strip identification number, $i_{\max}$ identifies the strip cells with the greatest energy, E_i is the energy deposit in each strip cell.

– *Front lateral width (total)*

$w_{s\,\mathrm{tot}}$ measures the shower width along η in the first layer of the electromagnetic calorimeter using all cells in a window $\Delta\eta \times \Delta\phi = 0.0625 \times 0.2$, corresponding approximately to 20×2 strip cells in $\eta \times \phi$, and is computed as $w_{s\,3}$.

– *Front second maximum difference.*

$$\Delta E = \left[E^{S1}_{2^{\mathrm{nd}}\mathrm{max}} - E^{S1}_{\mathrm{min}}\right] \tag{4.7}$$

is the difference between the energy of the strip cell with the second greatest energy, $E^{S1}_{2^{\mathrm{nd}}\mathrm{max}}$, and the energy in the strip cell with the least energy found between the greatest and the second greatest energy, E^{S1}_{min} ($\Delta E = 0$ when there is no second maximum).

– *Front maxima relative ratio*

$$E_{\mathrm{ratio}} = \frac{E^{S1}_{1^{\mathrm{st}}\,\mathrm{max}} - E^{S1}_{2^{\mathrm{nd}}\,\mathrm{max}}}{E^{S1}_{1^{\mathrm{st}}\,\mathrm{max}} + E^{S1}_{2^{\mathrm{nd}}\,\mathrm{max}}} \tag{4.8}$$

measures the relative difference between the energy of the strip cell with the greatest energy, $E^{S1}_{1^{\mathrm{st}}\,\mathrm{max}}$, and the energy in the strip cell with second greatest energy, $E^{S1}_{2^{\mathrm{nd}}\,\mathrm{max}}$ (E_{ratio} is 1 when there is no second maximum).

For a schematic overview of the discriminating variables, along with which variables are required to be fulfilled for the loose and tight classifications, see Table 4.1.[3] Generally, for the loose definition, three discriminating variables are considered: the hadronic leakage of the shower in the hadronic calorimeter (R_{had} or $R_{\mathrm{had_1}}$), the middle η energy ratio (R_η), and the lateral width in the second ECAL layer (w_{η_2}). For the tight definition, six more variables are used, in addition to the fiducial acceptance cut.

The efficiency for (tightly) identifying converted photons as a function of transverse energy in the full 2011 dataset can be seen in Fig. 4.4. To obtain the estimates, three different data-driven methods have been constructed. Four different pseudorapidity regions are shown, the least central of these being the one in which photons are least efficiently reconstructed. The identification efficiency increases with photon transverse momentum; at around 60 GeV, it is about 90% for unconverted photons and around 95% for converted photons.

[3] I have spent some time understanding the photon identification discriminating variables: Commenting on CDS and private communication with the convener of the Standard Model Direct Photon (SMDP) group led to alteration of the description of the shower shape variables in this table. The ranges in $R_{\mathrm{had_1}}$ were wrong, "lateral" was added for clarity for $w_{s\,3}$ and several sentences were rephrased (http://cdsweb.cern.ch/record/1296263/comments).

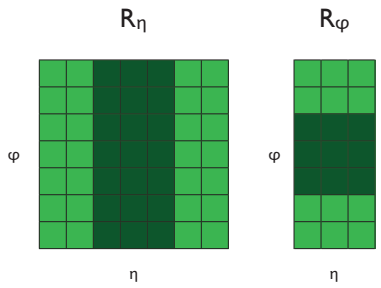

Figure 4.3: Illustration of the R_η and R_ϕ variables. The energy in the dark colored cells are considered for the numerator, while the energy in all the cells are considered for the denominator.

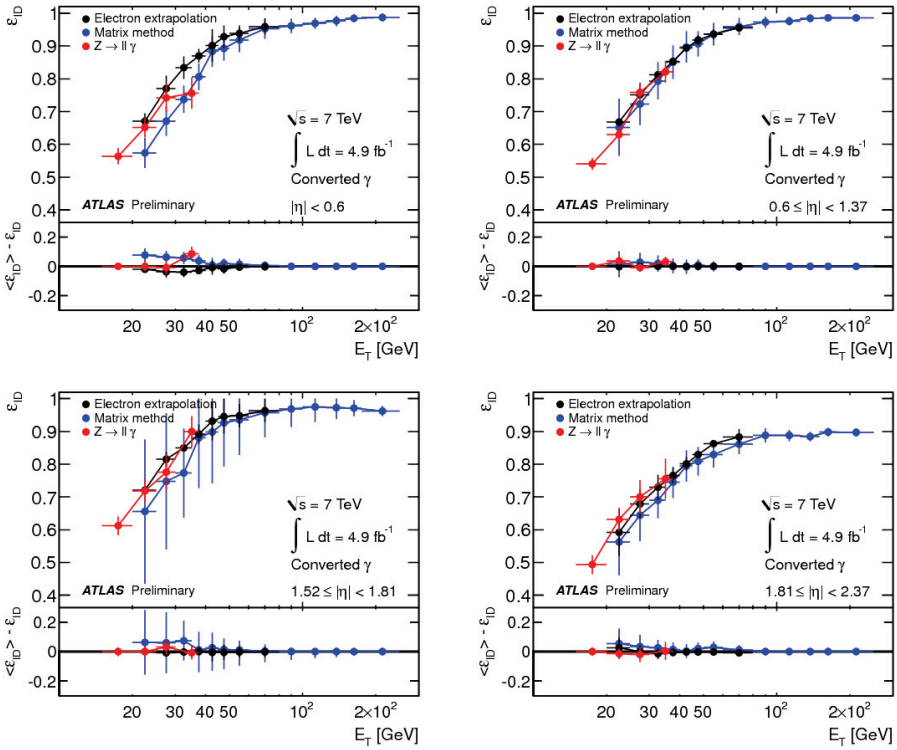

Figure 4.4: Efficiency for identifying converted photons as a function of the transverse energy in the 2011 data for four different pseudorapidity regions [77]. Three different data-driven methods have been used to obtain the estimates, and the comparison of each of the methods to the weighted mean is indicated in the lower pad. The error bars are the quadratic sum of statistical and systematic uncertainties.

Category	Description	Name	loose	tight
Acceptance	$\|\eta\| < 2.37$, $1.37 < \|\eta\| < 1.52$ excluded (crack region)	–		✓
Hadronic leakage	Ratio of E_T in all compartments of the hadronic calorimeter behind the electromagnetic cluster to E_T of the cluster; used over the range $0.8 < \|\eta\| < 1.37$ (R_{had}). In the ranges $\|\eta\| < 0.8$ and $\|\eta\| > 1.37$, E_T in the first sampling of the hadronic calorimeter behind the electromagnetic cluster is used for the numerator (R_{had_1})	R_{had} or R_{had_1}	✓	✓
ECAL middle layer	Ratio between the sum, $E^{S2}_{3\times7}$, of the energies of the cells contained in a 3×7 $\eta\times\phi$ rectangle (measured in cell units), and the sum, $E^{S2}_{7\times7}$, of the cell energies in a 7×7 rectangle, both centered around the cluster seed	R_η	✓	✓
	Lateral width of the shower in the η direction (in a 3×5 $\eta\times\phi$ rectangle)	w_{η_2}	✓	✓
	Ratio between the sum, $E^{S2}_{3\times3}$, of the energies of the cells contained in a 3×3 $\eta\times\phi$ rectangle, and the sum, $E^{S2}_{3\times7}$, of the cell energies in a 3×7 rectangle, both centered around the cluster seed	R_ϕ		✓
ECAL strip layer	Lateral shower width for maximum strip and two neighbouring strips	$w_{s\,3}$		✓
	Total lateral shower width in $\Delta\eta\times\Delta\phi = 0.0625\times0.2$	$w_{s\,\text{tot}}$		✓
	Fraction of energy outside core of three central strips but within seven strips to the energy within the core three central strips	F_{side}		✓
	Difference between the energy of the second largest energy deposit strip and the least deposit energy strip between the two leading strips	ΔE		✓
	Ratio of the difference of the largest and the second largest energy deposits over the sum of these two energies	E_{ratio}		✓

Table 4.1: Acceptance and discriminating (shower shape) variables used for loose and tight photon identification cuts.

Chapter 5

Corrections to Data and Simulation Samples

In this chapter, the corrections that were made to data and Monte Carlo signal samples used for the analysis will be presented. Background decomposition studies were done using exclusively data-driven methods, as described in Section 7.2, the shape and normalization of the background were taken from unconstrained fits to data, whereas the background bias studies were performed on high-statistics MC samples produced internally by HSG1, as described in Section 8.3. The Monte Carlo samples mentioned in this chapter, however, are solely signal simulations. Some of the corrections apply only to data, some only to MC and some to both. We will go into a little detail for a few of these corrections.

The data files used were of the p868 group production tag, which means they were reconstructed using the ATLAS software release AtlasPhysics_17.0.6.4.1. The runs used were as specified from the Good Runs List (GRL) 'data11_7TeV.periodAllYear_DetStatus-v36-pro10_CoolRunQuery-00-04-08_Eg_standard.xml', which includes runs with good detector data for electrons and photons, out of the runs ranging from run number 177986 – 191933, collected in the period from 21^{st} of March to 30^{th} of October 2011. This corresponds to an integrated luminosity of 4.9 fb^{-1}.

The Monte Carlo files used in this thesis came from the so-called MC11c campaign, also belonging to the p868 group production tag. The Pythia MC generator [80, 81] was used for associated production with W, Z and $\text{t}\bar{\text{t}}$, whereas the PowHeg MC generator [82] was used for the gluon-gluon fusion and vector boson fusion production mechanisms (see Section 6.1 for the various production mechanisms). Monte Carlo samples were made for eleven mass points; from 110 GeV to 150 GeV in steps of 5 GeV.

For the full list of files, both for data and Monte Carlo, see Appendix E.

5.1 Corrections of the Monte Carlo Samples

To make reliable predictions with the simulations, they must mimic data as closely as possible. In order for the MC to closer resemble the data, some corrections were carried out. In addition to corrections applied with the aim of mimicking conditions in data, some corrections due to theoretical knowledge were also made; these are the latter two in the list to follow. The following corrections of the MC samples were carried out:

- the average number of interactions per beam-crossing was adjusted (see Section 5.1.1);
- the spread in the beam spot was reweighted (see section 5.1.2);
- the photon energy was smeared to account for resolution differences between data and MC. In addition, an extra correction of the photon energy for converted photons was applied (see Section 5.3.1);
- the position in z of the photon for unconverted photons in the end-cap was corrected for a small oscillation as a function of pseudorapidity (see Section 5.3.2);
- the means of the shower shape variables were shifted, according to the differences of these between data and MC;
- the p_T spectra of the photons for the gluon-gluon signal samples were modified;
- the signal cross section was corrected for, due to destructive interference between the $gg \to H \to \gamma\gamma$ and $gg \to \gamma\gamma$ processes.

For the four first bullets in the list, we will go into some detail in the indicated sections. The remaining bullet points will be briefly mentioned in the following paragraphs.

Corrections to variables describing the shape of the showers created by photons in the electromagnetic calorimeter (introduced in Section 4.2.2) were applied to amend for the difference of these in data and MC. The correction consisted of simple shifts (known as *fudge factors*), based on the difference in the means of the shower shape variable in data and MC [83]. The fudging changes the variable typically by 2 – 4%. These shower shape variables are used for discriminating real photons from fake ones, and the corrected Monte Carlo variables yield a more realistic efficiency. The shift in efficiency due to the fudging of the shower shapes is typically 1 – 4%, smaller at higher E_T. For more details on photons reconstruction and identification, see Chapter 4.

For Monte Carlo samples of the gluon-gluon fusion process, the p_T distribution of the Higgs boson was adjusted to fit the spectrum obtained with the HQT package [84], due to it being a more precise simulation. This was done with the ggFReweighting[1] software package [85]. For all mass points, the correction is approximately a 50% increase for low p_T, falling off to 40% decrease at around 100 GeV, from which point it is slowly falling for the rest of the p_T spectrum out to about 600 GeV. At around 30 GeV, no correction is applied.

Due to destructive interference of the $gg \to H \to \gamma\gamma$ and $gg \to \gamma\gamma$ processes, the signal yield was adjusted, depending on the position of the photons in the detector. The correction is of the order of a few percent of the expected Higgs boson signal. The size of the interference increases with θ; it is smallest centrally in the detector ($\eta \simeq 0$), and largest close to the beam-pipe. The shape of the size of the interference (for a specific θ) as a function of the Higgs boson mass is a negative parabola, with the smallest interference at around 125 GeV. In newer MC samples than the ones used for this thesis, this correction was applied already in the production.

5.1.1 Pile-up Reweighting of the Monte Carlo Simulations

As mentioned in Section 3.3.8, the number of interactions per bunch-crossing is commonly called (in-time) pile-up, and this is denoted by μ. A large pile-up results in many primary vertices in one event. This of course needs to be incorporated in the simulations, in order for them to give a realistic picture of what to expect in data. Niels Bohr stated: "prediction is very difficult, especially if it's about the future". This is also true when producing MC simulations before the data-taking has come to an end. In order to be flexible with regards to which changes might take place in the run configuration, the MC was produced with a quite broad distribution of mean number of interactions per bunch-crossing, $\langle\mu\rangle$. This way, it is possible to reweight the simulations, such that they fit the conditions during data-taking.

An illustration of different $\langle\mu\rangle$-distributions in MC and data is shown in Fig. 5.1, along with the corresponding weights, w, assigned to the MC simulation for different values of pile-up. Regions in the $\langle\mu\rangle$-distribution populated by MC, but not by data, will be weighted by zero (and those events will have been simulated in vain) – the leftmost, hashed area in the figure. For values of $\langle\mu\rangle$ populated by data, but not by MC, it is impossible to reproduce the data with the MC – the rightmost, hashed area in the figure. Thus, a broad MC spectrum covering the data is desired. For values of $\langle\mu\rangle$ where there are more MC events than data

[1] For this thesis, the software package tag ggFReweighting-00-00-07 was used.

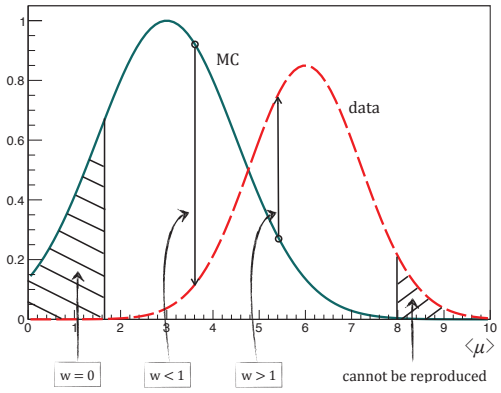

Figure 5.1: An illustration of pile-up reweighting, in order for the distribution of the mean number of interactions per bunch-crossing, $\langle\mu\rangle$, in Monte Carlo to fit the one in data. The idea is to weight the MC (full line) up or down to the data (dashed line). The weight, w, assigned to the MC simulation for some areas or values of $\langle\mu\rangle$ are indicated. Regions uncovered by data will have been simulated in vain, and regions covered by data, but unpopulated by MC can not be reproduced in Monte Carlo (hashed areas). The separation of the two distributions is exaggerated for the purpose of illustration.

events, the weight will be less than one, and if it is *vice versa*, the weight will be larger than one – each illustrated by the two lines in between the hashed areas in the figure.

Also as part of the pile-up reweighting, the fraction of events representing a particular pile-up condition needs to be taken into account. In order for the MC to represent the data, this fraction might have to be adjusted, by multiplying the simulations by

$$\frac{\mathcal{L}_{pile-up\,condition,\,data}}{\mathcal{L}_{pile-up\,condition,\,MC}} \quad , \tag{5.1}$$

where $\mathcal{L}_{pile-up\,condition,\,data}$ represents the luminosity of a certain pile-up condition in data and $\mathcal{L}_{pile-up\,condition,\,MC}$ represents the luminosity of a certain pile-up condition in Monte Carlo. Thus, the following manipulation of the MC (where $w_{\langle\mu\rangle}$ is found as illustrated in Fig. 5.1) is performed:

$$w_{pile-up,\,MC} = \frac{\mathcal{L}_{pile-up\,condition,\,data}}{\mathcal{L}_{pile-up\,condition,\,MC}} \cdot w_{\langle\mu\rangle} \ . \tag{5.2}$$

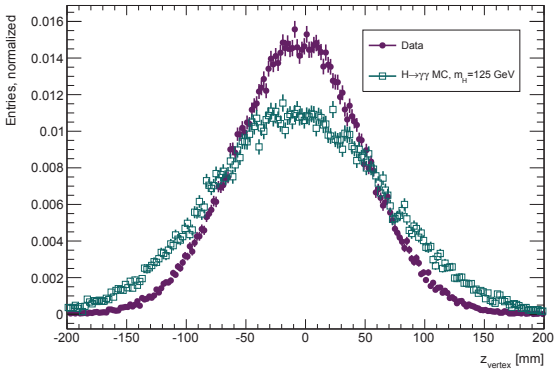

Figure 5.2: The distribution of the z-position of the vertex in Monte Carlo (open squares) and data (full circles).

5.1.2 Reweighting the z-Position of the Vertex

The distribution of the z-position of the vertex is Gaussian. However, the means and RMS (Root Mean Square) of the data and Monte Carlo are not identical. A reweighting of the Monte Carlo distribution must be made in order to reproduce the condition in data. The HSG1 group decided to use a simplified version when comparing the Gaussian in data with the Gaussian in Monte Carlo. The simplification consists of assuming that the mean vertex position in z is the same in MC as in data. The mean in data and MC are similar, albeit not identical – we will shortly address the impact of this simplification.

The distributions of the z-position of the vertex in MC and data can be seen in Fig. 5.2, where the mean of the MC distribution is statistically in agreement with the input value for the MC production of around -6.11 mm. In particular, the z-vertex distribution in MC is too broad with respect to the one in data, and purposely so. This is both due to the fact that a transformation (in terms of reweighting events) to a smaller mean is unproblematic, whilst a transition into a broader mean is undesirable, because the statistical fluctuations in the tails will be larger – as well as that the conditions in data changed after the MC production was started. The mean in the data differs from the mean in MC by 0.52 mm.

The ratio of the Gaussian in data to the Gaussian in MC, used for the reweighting of the simulation samples, is

$$\frac{\sigma_{MC}}{\sigma_{data}} \, e^{-\frac{1}{2}\left(\frac{(z-z_{0_{data}})^2}{\sigma^2_{data}} - \frac{(z-z_{0_{MC}})^2}{\sigma^2_{MC}}\right)} , \tag{5.3}$$

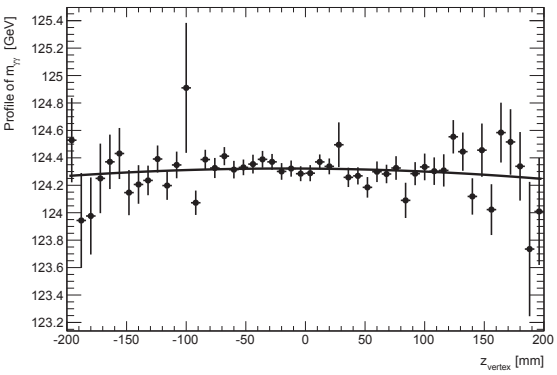

Figure 5.3: Profile plot of $m_{\gamma\gamma}$ versus the z-position of the vertex as obtained in gluon-gluon fusion signal MC for $m_{\mathrm{H}} = 125$ GeV, fitted with a second order polynomial. The parameter values of the fit are compatible with a straight line.

whereas the simplification used in HSG1 is

$$\frac{\sigma_{MC}}{\sigma_{data}} \, e^{-\frac{1}{2}(z-z_0)^2\left(\frac{1}{\sigma^2_{data}} - \frac{1}{\sigma^2_{MC}}\right)} \, . \tag{5.4}$$

The difference of the weights as obtained from Eq. (5.4) with respect to Eq. (5.3) is less than 4%.

To study the dependence of the invariant mass on the z-position of the vertex, a profile plot of $m_{\gamma\gamma}$ versus z_{vertex} was made for a gluon-gluon fusion signal Monte Carlo sample with $m_{\mathrm{H}} = 125$ GeV. This plot can be seen in Fig. 5.3, fitted with a second order polynomial. The fit yielded a result which was statistically compatible with a straight line. It is safe to state that there seems to be no significant effect on the invariant mass from the position in z of the vertex. Reweighting or not would have very little impact on $m_{\gamma\gamma}$, thus, reweighting with the simplified Eq. (5.4) with respect to the full Eq. (5.3), would have a minuscule impact on the invariant mass.

5.2 Corrections Applied to Data

Some adjustments of the data were also made, based on knowledge about the performance of the detector, and due to artifacts not observed in the MC.

- the position in z of the photon for unconverted photons in the end-caps was corrected for a periodic, large amplitude oscillation as a function of pseudorapidity (see Section 5.3.2);
- the photon energy was adjusted by scale factors obtained from $\mathrm{Z} \to e^+e^-$

decays. In addition, an extra energy correction for converted photons were applied (see Section 5.3.1).

In addition, the isolation and the choosing of the common diphoton vertex are special variables in this analysis – we will come back to them in Chapter 7.

5.3 Corrections Applied Both to Monte Carlo Samples and Data

In the following two sections, we will address the corrections that were applied both to data and Monte Carlo simulations. These involve correction of the energy based on knowledge about the detector response, and correction of an oscillation pattern observed in z-position of the vertex as a function of pseudorapidity.

5.3.1 Correction of the Energy

The energy of the photons were corrected in data and smeared in MC. Depending on the position (η and ϕ) of the photon in the detector, the photon energy was corrected using scale factors obtained from $Z \to e^+e^-$ decays [86]. For this, the EnergyRescaler tool [87] was used,[2] which also takes into account systematic uncertainties; these were different for converted and unconverted photons. The shift in energy is around 3% near the crack regions, and generally less than 2% over the $|\eta|$ acceptance range. Furthermore, the energy resolution in data and MC were not identical, and the simulations were smeared in order to closer resemble data. In addition to the EnergyRescaler tool, the ConvertedPhotonScaleTool was also used both for data and MC. This tool applies an extra energy correction, based on MC, of the energy for converted photons only (these are the most difficult ones to calibrate), taking into account the radial information about the conversion point. The radial position reflects how much material the electron pair has traversed and therefore affects how much energy the converted photon has lost, both in front of the calorimeter and out of the cluster [88]. The tool returns a multiplicative factor close to one, and results in a better linearity of the energy of the converted photons, and improves the RMS spread of the diphoton invariant mass by around 3% for the inclusive sample.

[2]The version of the tool used in this analysis was EnergyRescaler-00-02-07, as part of egammaAnalysisUtils-00-02-76.

5.3.2 Correction of the z-Position of the Photon

A periodic oscillation pattern was found in data, when looking at the difference of the z-position of the primary vertex (as obtained from the inner detector) and z-position as found from the pointing method (see Section 7.6) as a function of η^{γ} in the 2^{nd} layer of the calorimeter. The pattern was seen only in the end-caps and only for unconverted photons. This large-amplitude oscillation could not be reproduced in the Monte Carlo simulation, however, an oscillation with much smaller amplitude was seen in MC. A convincing reason for the oscillation is yet to be found, but meanwhile, a correction of varying magnitude, damping the oscillation, was applied both to data and MC. This decreased the standard deviation of the Δz distribution in data by approximately 8%, gave an excellent agreement between MC and data and improved the mass resolution by about 1% [89].

Chapter 6

The $H \to \gamma\gamma$ Signal

In this chapter the production of the Higgs boson at the LHC is presented, as well as the various ways the (highly unstable) Higgs boson is transformed into other particles; the so-called *decay channels*. The descriptions of the production and decay of the Higgs boson in this chapter are mainly from Refs. [90, 91]. We will give special attention to the $H \to \gamma\gamma$ decay. Throughout this thesis, to label the two photons in this decay, we will use the nomenclature "leading" for the photon with the largest p_T (the *hardest* photon), and "subleading" for the photon with the smallest p_T (the *softest* photon).

6.1 Production of the Higgs Boson at the LHC

The dominant production mechanism of the Higgs boson, when colliding protons against protons as is done at the LHC, is through the fusion of two gluons residing inside the protons, illustrated in Fig. 6.1(a). This differs from the production at the Tevatron (a particle accelerator in Illinois, which ended its operation in 2011), where protons were collided against anti-protons. At the Tevatron, the dominant way of producing the Higgs boson was through the quark−anti-quark interaction of the (valence) quarks inside the proton and anti-proton. This production mechanism is called vector boson fusion (VBF) and illustrated in Fig. 6.1(b). Producing the Higgs boson this way at the LHC requires the anti-quark to arise from the sea-constituents of the proton. Sea-constituents have a much smaller probability of carrying a significant fraction of the proton's momentum, so reaching sufficient collision energy to make a Higgs boson happens more seldom this way at the LHC than in gluon-gluon fusion. Nevertheless, it is the second most important production mechanism at the LHC. The so-called associated processes

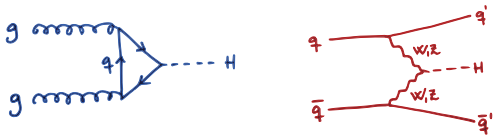

(a) Gluon-gluon fusion (b) Vector boson fusion (VBF)

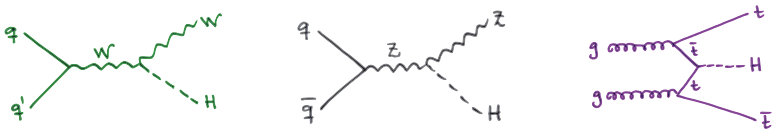

(c) W-strahlung (d) Z-strahlung (e) $t\bar{t}$ fusion

Figure 6.1: Feynman diagrams of the various production mechanisms of the Higgs boson. The colors of the diagrams correspond to the relevant cross section in Fig. 6.2.

follow in importance. Of these, the third and fourth most important production mechanisms of the Higgs boson at the LHC are W- and Z-strahlung, in which a Higgs boson is radiated from a W or a Z boson. The last notable production mechanism is the fusion of a top and anti-top quark. For a Higgs boson with $m_H = 120$ GeV, the fractions of gluon-fusion, VBF, WH, ZH and $t\bar{t}H$ production are approximately 87%, 7%, 3%, 2% and 1%, respectively. The Feynman diagrams for all these production mechanisms can be seen in Fig. 6.1 and the corresponding cross sections, as a function of the Higgs boson mass, in Fig. 6.2.

6.2 The Decay of the Higgs Boson

The Higgs boson is a highly unstable particle: a light Higgs boson would have a life-time of around 10^{-23} seconds. The width, Γ, of the Higgs boson (which is inversely proportional to the life-time, τ) can be seen in Fig. 6.3. It increases with the Higgs boson mass – when approaching a mass of 1 TeV, the width of the particle becomes comparable to its mass, and whether it should still be called a particle is questionable. At the mass where it is likely observed, around 126 GeV, the width is so small that the detector resolution dominates the observed width. Since it is very unstable, very shortly after the Higgs boson is produced, it is transformed

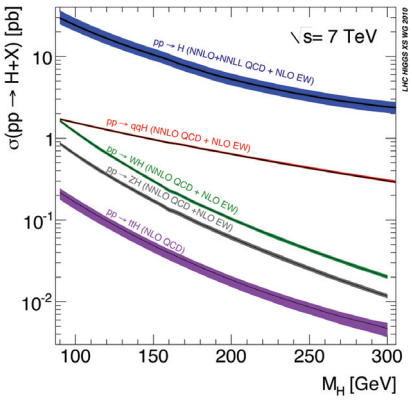

Figure 6.2: The predicted cross sections of the different production mechanisms of the Higgs boson at the LHC, as a function of the Higgs boson mass. The values are for a center of mass energy of 7 TeV [90]. For the corresponding Feynman diagrams of the processes, see Fig. 6.1.

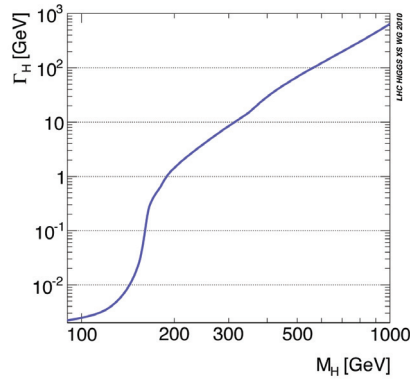

Figure 6.3: The predicted width of the SM Higgs boson as a function of its mass [90]. The dependence of the width on the mass is strong, and at around 1 TeV, the width approaches the mass of the particle, washing out a resonance feature.

into other particles. Which particles the Higgs boson preferably decays to is also a function of its mass. The branching ratios (BRs), the probability of the decay into different pairs of SM particles, can be seen in Fig. 6.4.

As can be seen from Fig. 6.4, the H $\rightarrow \gamma\gamma$ decay, relevant for this thesis, is a rare one: the probability of the Higgs boson to be transformed into two photons is less than 0.2%. However, at low Higgs boson masses, due to having an experimentally clean signature, it is still one of the most sensitive channels. At the LHC, backgrounds arising from QCD interactions are overwhelming. Thus, separating the other dominant decay channels at low masses, such as $H \rightarrow \tau\tau$ and $H \rightarrow b\bar{b}$, from the background is very difficult – these channels have a poor signal-to-background ratio. When learning that the signal-to-background ratio of the H $\rightarrow \gamma\gamma$ decay is not much more than one percent for the inclusive case, it becomes clear that finding the Higgs boson is a challenging task. Luckily, at the

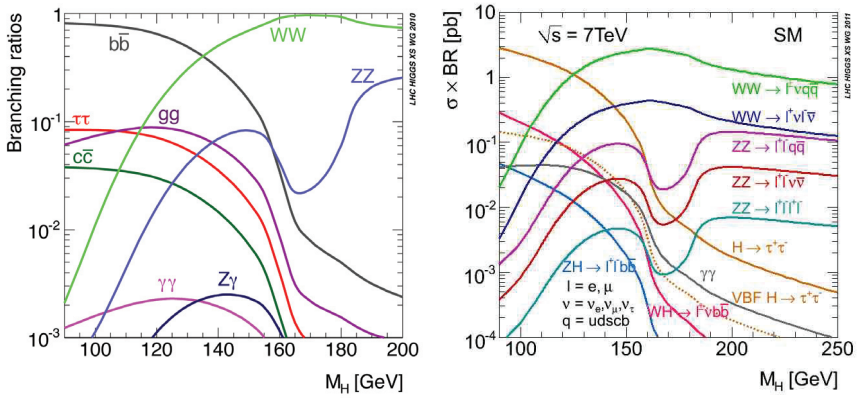

Figure 6.4: The branching ratio of the SM Higgs boson as a function of its mass is shown to the left. The H $\to \gamma\gamma$ decay has only a probability of ∼0.2%, but is still one of the most sensitive decay channels. To the right, the branching ratio times cross section for the different decay channels, further separated according to the decay products is displayed.

mass where a 'Higgs boson'-like particle is found, there is a variety of different decay channels available, as can be appreciated in Fig. 6.4. This makes it possible to retrieve a great deal of information about how this particle behaves, making the job of pin-pointing whether this truly is in accordance with the Standard Model behaviour easier. There is another reason to search specifically for the decay of the Higgs boson into two photons: the observation disfavors the spin-1 hypothesis, as a spin-1 particle cannot decay into two massless spin-1 particles (like photons), according to the Landau-Yang theorem [92, 93].

The leading Feynman diagrams for the H $\to \gamma\gamma$ signal can be seen in Fig. 6.5. This decay must go through a loop of massive particles, since the Higgs boson couples to mass and the photons are massless. The coupling of the Higgs boson to a particle is in general proportional to the mass of the particle. Therefore, the heaviest of the fermions and bosons allowed in the loop, the top-quark and the W boson, will be dominating. The next-heaviest fermion, the bottom quark, is so much lighter that it can be discarded in this process. In the boson loop, the only contributor is the W boson, as a $ZZ\gamma$-vertex is forbidden. The boson loop is dominant over the fermion loop [94].

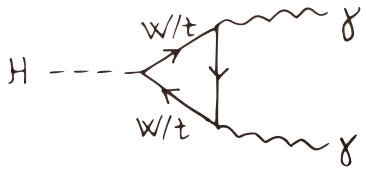

Figure 6.5: The main Feynman diagrams for the H $\rightarrow \gamma\gamma$ signal. Since the Higgs boson couples to mass and the photons are massless, the decay to two photons must go through loops of massive, charged particles. The triangle loop of W bosons is dominant, together with the triangle loop of top quarks.

6.3 The Diphoton Invariant Mass Spectrum

The main observable in the H $\rightarrow \gamma\gamma$ analysis is the invariant mass of the diphoton pair. The signal is expected to be a narrow resonance on top of a smoothly falling background spectrum, and it is through this distinguishing characteristic a discovery of the Higgs boson may be claimed. The invariant mass of a particle system is the rest mass of the system, invariant under Lorentz transformations. It depends on the total energy and momentum of a system of particles and is described by[1]

$$m^2 = E^2 - |\,\vec{p}\,|^{\,2} \ . \tag{6.1}$$

For a two-particle system as the one addressed here, this becomes

$$\begin{aligned} m^2 &= (E_1 + E_2)^2 - |\,\vec{p}_1 + \vec{p}_2\,|^2 && (6.2)\\ &= m_1^2 + m_2^2 + 2(E_1E_2 - \vec{p}_1 \cdot \vec{p}_2) \ , && (6.3) \end{aligned}$$

and for the case of massless particles, as the photons, simply

$$m^2 = 2p_1p_2(1 - \cos\theta) \ , \tag{6.4}$$

where θ is the angle between the two photons in the laboratory reference frame.

The position of the diphoton primary vertex affects the pseudorapidity of the photons, and thus also the transverse momentum of the photons. The determination of the diphoton primary vertex is therefore important for the invariant mass calculation, and was done as described in Section 7.6. The pseudorapidity of unconverted photons in the end-cap was further corrected for an oscillation pattern, as described in Section 5.3.2. The energy of the photons was corrected using scale factors from Z $\rightarrow e^+e^-$ events, differently for converted

[1] Remember that we are using natural units. Otherwise, the complete formula would read: $E^2 = m^2c^4 + |\,\vec{p}\,|^{\,2}\,c^2$.

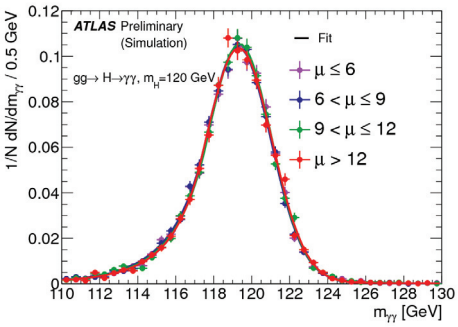

Figure 6.6: Simulation results show that the invariant mass distribution of the $\gamma\gamma$-pair is quite robust against pile-up; $m_{\gamma\gamma}$ in four different pile-up conditions. From Ref. [95].

and unconverted photons, as described in Section 5.3.1. The invariant mass was calculated based on the corrected transverse momentum, corrected pseudorapidity, corrected energy and the cluster azimuthal angle.

The invariant mass is fortunately robust against pile-up. This can be seen in Fig. 6.6, where the reconstructed invariant mass of photons of a $m_{\mathrm{H}} = 120$ GeV $\mathrm{H} \to \gamma\gamma$ signal from the gluon-gluon fusion process is shown for four different pile-up conditions. The mean number of interactions per bunch-crossing was, as already mentioned in Section 3.3.8, 6.3 before the 2011 September shutdown, and 11.6 after. The reconstructed invariant mass separated for some different pile-up conditions can hardly be distinguished.

6.3.1 Signal Distributions

In this section, we will have a look at some basic distributions that characterize the $\mathrm{H} \to \gamma\gamma$ signal. A simulated signal with $m_{\mathrm{H}} = 125$ GeV was chosen for this purpose, and the sample used for the plots were the events passing the thesis selection, as will be described in Section 7.7. To indicate the background, the full sample of 2011 data was used. The entries in both samples were normalized to one, in order to compare their shapes.

In Fig. 6.7, the azimuthal angle of the leading and the subleading photons of the $\mathrm{H} \to \gamma\gamma$ signal can be seen. The trend is rather flat, as expected, since the calorimeter is designed to be uniform in this angle. As described in section 3.3.9, the calorimeter was suffering under some dead FEBs in the region covering $0 < |\eta| < 1.475\,, -0.791 < \phi < 0.595$ for a period of time. This was also simulated in Monte Carlo and can be recognized in these distributions.

The difference in azimuthal angle between the two photons can be seen in Fig. 6.8. From this figure, it can be appreciated that the photons of the Higgs boson decay

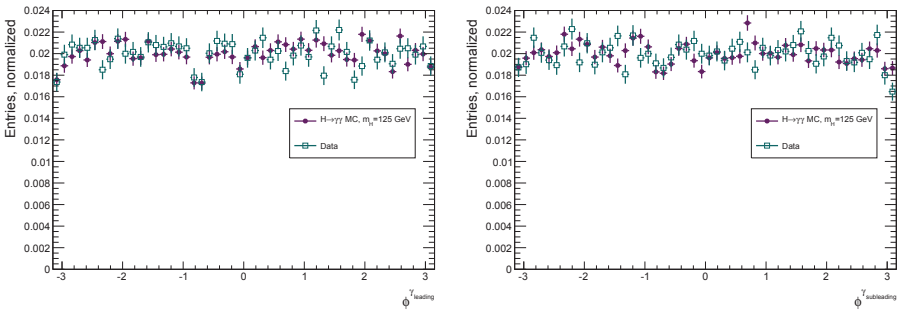

Figure 6.7: The azimuthal angle, ϕ, of the leading (left) and the subleading (right) photons of a $H \to \gamma\gamma$ signal with $m_H = 125$ GeV (full circles) and 2011 data (open squares). The dip corresponds to the dead FEBs in the region $0 < |\eta| < 1.475\,, -0.791 < \phi < 0.595$, as described in Section 3.3.9, also simulated in Monte Carlo.

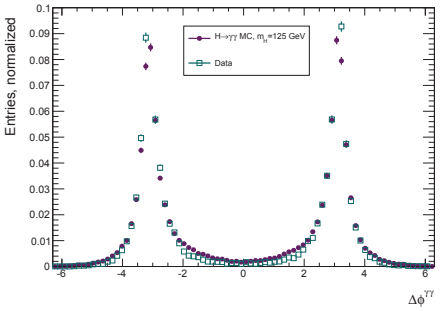

Figure 6.8: The difference in azimuthal angle, $\Delta\phi^{\gamma\gamma}$, between the leading and subleading photon of a $H \to \gamma\gamma$ signal with $m_H = 125$ GeV (full circles) and 2011 data (open squares).

are preferrably in a back-to-back fashion (separated by $\pm\pi$) in the transverse plane. This indicates that the Higgs boson was produced without much boost orthogonal to the beam axis, reflecting that the motion of the protons and their constituents is to a large degree restricted to the z-axis. The data, consisting after the selection mostly of two promptly produced photons, as will be described in Section 7.2, also displays the same preferred back-to-back constellation of the photons.

The distributions of the transverse momentum of the leading and the subleading photons can be seen in Fig. 6.9. For the signal, the distributions are quite peaked at $p_T \simeq m_H/2$, the leading photon naturally being the somewhat harder one when they are not balanced. The tail of the leading photon is also larger than that of the subleading photon, but does not extend much further than m_H. The background has generally lower p_T, especially for the leading photon, with a somewhat broader

distribution. The p_T cuts of 40(25) GeV for the leading(subleading) photon can be clearly recognized in the data distributions.

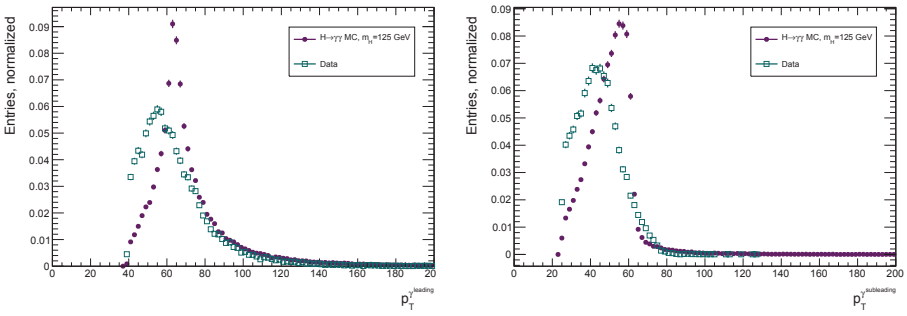

Figure 6.9: The p_T distribution of the leading (left) and the subleading (right) photons of a $H \to \gamma\gamma$ signal with $m_H = 125$ GeV (full circles) and 2011 data (open squares).

The distribution of the pseudorapidity the leading and the subleading photons can be seen in Fig. 6.10, showing that most Higgs bosons decay centrally in the detector ($\eta \simeq 0$), *i.e.* orthogonal to the beam-pipe. The crack regions between the barrel and the end-caps, left out of the analysis, can clearly be seen. The background is less peaked than the signal; more photon pairs are produced in a forward direction, closer to the beam-pipe.

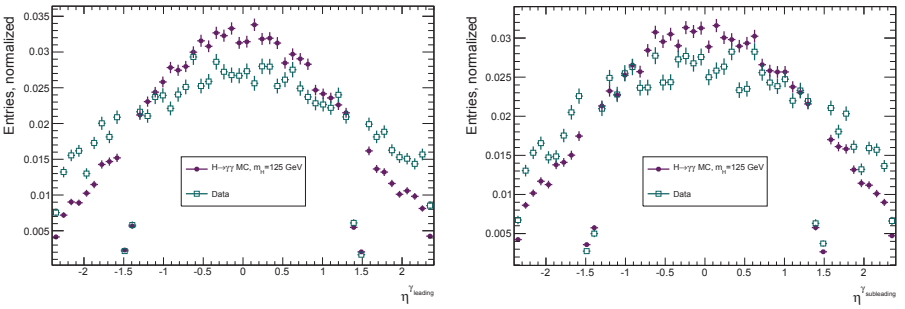

Figure 6.10: The distributions of η for the leading (left) and the subleading (right) photons of a $H \to \gamma\gamma$ signal with $m_H = 125$ GeV (full circles) and 2011 data (open squares).

Chapter 7

Background Rejection and Event Selection

In this chapter, the backgrounds to the $H \to \gamma\gamma$ signal, separated in irreducible and reducible parts, will be described. The methods utilized by HSG1 to decompose the background to the $H \to \gamma\gamma$ search into the $\gamma\gamma$, γ-jet, jet-γ and jet-jet parts will be introduced. Various means of rejecting as much as possible of the reducible background (identified photon candidates which are fake) while still keeping the signal will be presented. As means to reach this goal, isolation of the photon candidate (cutting on jet activity around the photon candidate) will be presented, as well as the triggering of events with diphotons. Cutting on the transverse momenta of the photon pair is an important way to reduce the background. These cuts have not been revised since the 1990's; here, a study of the p_T cuts has been made. How to choose the diphoton vertex, crucial for the calculation of invariant mass through the impact it has on the angle of the photons, will be detailed, along with the development in the technique for doing so. The selection of the diphoton events, as well as how the events are categorized, are addressed. At the end, the invariant mass distributions in the categories, both for standard and variable p_T cuts will be shown, before a rough estimation of the performance under the two sets of p_T cuts will be presented.

7.1 The $H \to \gamma\gamma$ Background

The background to the search for the $H \to \gamma\gamma$ decay can be divided into two parts: the *irreducible* and the *reducible* background. We will be having a brief look at these backgrounds in this section. Due to the large rejection factor of jets faking

photons, necessary to resolve the signal, samples of full Monte Carlo simulation with sufficient statistics is not possible to obtain. Therefore, the background to the $H \to \gamma\gamma$ search is taken solely from data. The data-driven decomposition of the $H \to \gamma\gamma$ background into $\gamma\gamma$, γ-jet, jet-γ and jet-jet components (not directly used in the results of the analysis, but a valuable cross-check), is described in Section 7.2. The modeling of the background received a lot of attention in the HSG1 group. The background normalization and shape of the invariant mass distribution was estimated exclusively from data, but the choice of background parametrization was made based on studies using high-statistics fast simulations. This is described in detail in Section 8.3.

7.1.1 The Irreducible Background

As the name indicates, the irreducible background is impossible to separate from the signal: it consists of two real photons, promptly produced. This will be the main background remaining after cuts have been applied to get rid of most of the reducible background. Of the irreducible backgrounds, of which some are illustrated in Fig. 7.1, the Born and the box contributions are the dominant ones. These are respectively quark−anti-quark annihilation and gluon annihilation (through a loop of quarks) processes. The process including radiation of a photon off a quark (bremsstrahlung) is semi-irreducible, as it may to some extent be diminished by isolation requirements on the photon. After isolation requirements, it is shown to contribute about 50% of the sum of the Born and box processes [62]. To learn more about the irreducible background, the reader is referred to Refs. [96–99].

After the cuts, the irreducible background, made up of true diphotons, is about 70% of the total background. This is shown in Section 7.2.

7.1.2 The Reducible Background

The reducible backgrounds include all cases with fake photons – the most common being the ones where one or several jets were misidentified as photons. The QCD background most commonly misidentified as photons, is, as already mentioned, π^0 mesons, which decay into two photons. Separating the photons from the $\pi^0 \to \gamma\gamma$ decay, recognizing that it is not one true photon, is one of the most challenging tasks of the ECAL. The backgrounds involving jets misidentified photons are commonly noted as γ-jet, with one real and one fake photon, and jet-jet, where both jets were misidentified as photons. A small background also arises from the Drell-Yan process, in which a quark−anti-quark annihilate to a $Z^{(*)}$ or γ, which

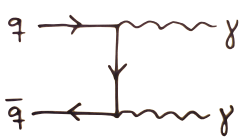

(a) The Born diagram (irreducible)

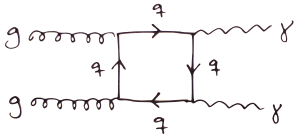

(b) The box diagram (irreducible)

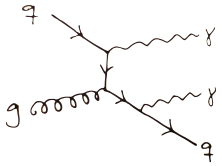

(c) Semi-reducible background – the bremsstrahlung process

Figure 7.1: The Feynman diagrams for the irreducible H → γγ background.

subsequently decays to two electrons, where both of the electrons are misidentified as photons. This process contributes mostly at the lower end of the invariant mass spectrum in the range used for the H → γγ search, not too far away from the Z-resonance.

These processes, in particular QCD processes, have a far larger cross section than that of the signal. For events with two clusters in the calorimeter passing the kinematic cuts, the ratios of the jet-jet and γ-jet to the γγ processes are around (with large uncertainties) 10^6 and 10^2 respectively. To eliminate the reducible background as much as possible, a large rejection of jets must be obtained. In order to be able to resolve the signal, jet rejection factors of around 10^7 and 10^3 are needed [62]. This is achieved through the photon identification, as presented in Section 4.2, and isolation of the photon candidate, presented in the next section.

After the cuts, the reducible background comprises about 30% of the background, and is dominated by γ-jet, as shown in Section 7.2.

7.2 Background Composition

The reduction of the reducible backgrounds γ-jet, jet-γ and jet-jet is of vital importance in order to have sensitivity to a signal. The cross sections of these processes are much greater than that of the signal, and the selection for the analysis must reduce the rate of these by several orders of magnitude. Because of this reduction in rate, it is not feasible to simulate the background to sufficient precision; only every millionth or so of the generated events would pass the selection criteria for the $H \to \gamma\gamma$ analysis; gathering enough statistics would require tremendous computing time. Therefore, Monte Carlo simulations of the background are abandoned, and data-driven methods, studying side-band regions to the signal in data, have been developed to learn about the composition of the background.

To evaluate the composition of the background spectrum of the $H \to \gamma\gamma$ search, four different methods were developed by HSG1; the 2×2D sideband method, the 1×2D sideband method, the template fit method and the 4×4 matrix method. The 2×2D sideband method was used as the baseline method for the final statement of the decomposition, but the different methods served as cross-checks and gave comparable results. The results from these studies were not used in the final computation of limits, but gave confidence in that the background spectrum was coherently understood in a satisfactory manner. The different methods will be described briefly here, for which the main reference is [100].

The decomposition of the $H \to \gamma\gamma$ candidates in the 2011 data can be seen in Fig. 7.2, 7.2(a) showing the invariant mass spectrum partitioned in jet-jet, jet-γ and $\gamma\gamma$ + DY components stacked on top of each other, and 7.2(b) showing a comparison of the data-driven estimates to the ones obtained from simulation. Both figures are made using the double two-dimensional sideband method, soon to be explained. The results of each of the methods can be seen in Table 7.1. It can be appreciated that the background rejection leaves mostly true diphotons: around 70% of the remaining candidate events are events with two real photons. This is reassuring; since the event selection keeps diphoton events, we should be able to see a $H \to \gamma\gamma$ signal.

7.2.1 The 2×2D Sideband Method

The 2×2D sideband method was first used by the SMDP group for the measurement of the inclusive photon cross section, and was later adopted by HSG1. A detailed description of the recursive 2×2D sideband method can be found in Refs. [101, 102].

	2x2D	1x2D	2D Template Fit	4×4 Matrix
$\gamma\gamma + DY$	16 139 ± 203 ± 1 106	14 814 ± 152 ± 3 033	16 184 ± 165 ± 1 202	13425 ± 192 ± 1692
$\gamma j + j\gamma$	5 232 ± 127 ± 878	6 369 ± 30 ± 2 517	5 277 ± 76 ± 759	7529 ± 113 ± 1030
jj	1 118 ± 50 ± 602	1 306 ± 20 ± 516	1 036 ± 21 ± 706	1535 ± 36 ± 534
DY	165 ± 2 ± 8			
$\gamma\gamma$ Purity	71%	65%	71%	59%

Table 7.1: Results of the background decomposition in the inclusive analysis at the time of the Council, using the four different methods described in the text. The first error denotes the statistical uncertainty, the second the systematic uncertainty. The results are compatible within the uncertainties. In the 2x2D and 1x2D sideband methods, the number of events is constrained to the number of candidates observed in the tight-isolated photon pairs sample. This is not the case in the 2D template fit where the number of events is constrained to the number of tight photon pair candidates before applying the isolation cut. The 4×4 Matrix method conserves the numbers of events both before and after the isolation cut [100].

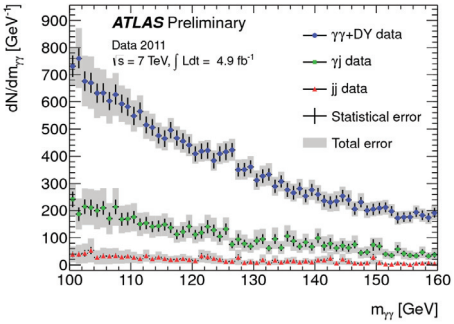

(a) The jet-jet, jet-γ and $\gamma\gamma$ + DY components stacked on top of each other. Error bars indicate statistical uncertainty, whereas the grey area indicates the total statistical and systematic uncertainty.

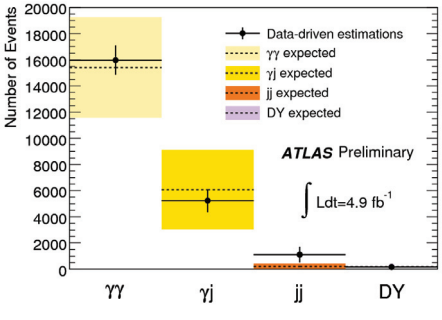

(b) The jet-jet, jet-γ, $\gamma\gamma$ and DY estimates from data (points) compared to the estimates from simulation (colored areas).

Figure 7.2: Background decomposition of the H $\rightarrow \gamma\gamma$ candidates for the 2011 data using the double two-dimensional sideband method [95].

The basic idea of the method is to estimate the purity of tight, isolated photons in the signal region by extrapolating from background regions. The starting sample used for the estimation was called *Loose′*, and consisted of loosely identified photons which also passed a constructed "tight-relaxed" criterion; the tight definition with the $\{w_{s\,3}, F_{\text{side}}, \Delta E, E_{\text{ratio}}\}$ cuts omitted. These shower shape variables were chosen since they have a negligible correlation with isolation (as they are all evaluated in the strip layer). Due to this definition of the sample, I find it more logical to refer to the superset as *TightRelaxed* instead of the official name *Loose′*, and will use this naming in the following.

In this method, a two-dimensional parameter plane is constructed, consisting of tight photon identification (pass/fail) and isolation of less than 4 GeV (pass/fail). Thus, there are four regions in which the photons can be classified: tight and isolated (signal region A); tight, but not isolated (region B); not tight, but isolated (region C) and finally not tight and not isolated (region D). Sorting the events is done recursively: after the leading photon is classified following this scheme, only events with the leading photon in the signal region (A) are further evaluated, sorting the events after the label of the subleading photon; see Fig. 7.3 for illustration. In the improved 2×2D sideband method later introduced, the photons were sorted simultaneously, leading to 4×4 = 16 classifications of the photon pair (where it is distinguished between the leading and the subleading photon).

The validity of this method relies on some assumptions:

- the ratios of the background (jet) and the signal (γ) yields are respectively preserved between the vertically and horizontally linked regions (implying that the different regions are uncorrelated – in this case, isolation and tight γ-ID):

$$\frac{N^A_{jet,\gamma}}{N^B_{jet,\gamma}} = \frac{N^C_{jet,\gamma}}{N^D_{jet,\gamma}} ,$$

- most of the signal (true, direct photons) is in the signal region (A).

The main systematic uncertainties of this method were the definition of the *TightRelaxed* sample (estimated by variating the omitted variables of the tight identification), correlation between the isolation and the identification, and leakage of the signal into the background regions. The total systematic uncertainty on the $\gamma\gamma$ yield was 7%. The result of the decomposition for the $H \to \gamma\gamma$ search at the time of the Council can be seen in Table 7.2.

Composition	$\gamma\gamma$	γj	jj	Drell-Yan
Events	$16000 \pm 200 \pm 1100$	$5230 \pm 130 \pm 880$	$1130 \pm 50 \pm 600$	$165 \pm 2 \pm 8$
Fraction	$(71 \pm 5)\,\%$	$(23 \pm 4)\,\%$	$(5 \pm 3)\,\%$	$(0.7 \pm 0.1)\,\%$

Table 7.2: Composition of the 22 489 selected candidate events in the inclusive sample for the $H \to \gamma\gamma$ search for the Council, as found by the 2×2D sideband method. The first uncertainty is statistical, the second is systematical [95].

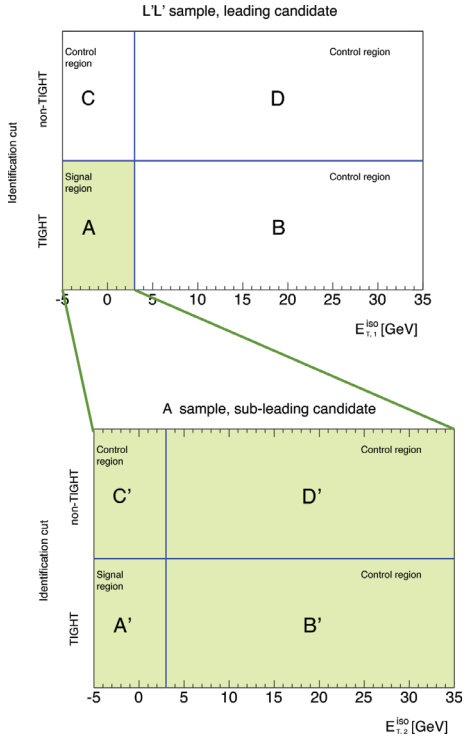

Figure 7.3: Illustration of the recursive 2×2D sideband method [101]. Only events with the leading photon in the signal region (A) are further evaluated (colored area) and classified based on the subleading photon.

7.2.2 The 1×2D Sideband Method

In the 1×2D sideband method, data is used to measure the fake rate of jets being identified as photons, in order to extrapolate the background components into the signal region. A detailed description of the method is given in Ref. [100]. First, the fake rate, with which jets pass all photon criteria for tight identification and isolation, was measured from W($\rightarrow$ eν)+jets events. To estimate the fraction of the γ-jet and jet-jet components, a sample enriched in reducible background was created, by selecting isolated and tightly identified leading photons, but demanding the subleading photon only to pass the loose identification criteria. These events were sorted in the same manner as in the 2×2D sideband method, according to photon identification and isolation. The contribution of the reducible backgrounds in the signal region (where both photons are isolated and tightly identified) of this sample was found by multiplying the fake rate obtained in the W($\rightarrow$ eν)+jets

sample to the subleading photon. To get the number of true diphoton events, this reducible background component was subtracted from the signal region events. The main systematic uncertainties on this method were:

- the purity of the W$\rightarrow$ eν+jets sample;
- the bias induced from the p_T cut of 40 GeV on the leading photon, leading to a suppression of the fake rate for the subleading photon in the region of $p_T < 40$ GeV;
- the fake rate dependence on the jet composition – quark-induced jets and gluon-induced jets have different profiles, therefore also fake rates, and the composition of these jets might differ in the control and signal samples;
- the fraction of jet-γ events in both the control and the signal sample, which is assumed to be negligible (due to the selection of the sample);
- the fraction of $\gamma\gamma$ events in the control sample, which is also assumed to be negligible.

7.2.3 The Template Fit Method

The isolation template fit method was first used in the measurement of the (di)photon cross section as described in Refs. [101, 103]. In this method, an extended two-dimensional maximum-likelihood fit to the isolation profile of the diphoton pair was performed. The probability density functions (the templates) for the isolation of fake and real photons, used in the likelihood, were taken from fits to control regions in data. The starting sample for obtaining the templates was the same *TightRelaxed* one used in the 2×2D sideband method. The fake photon isolation template was obtained from the candidates in data that fail the tight identification (this isolation distribution is unbiased with respect to the background candidates that pass the identification). To get the isolation template for the real photons, the fake photon isolation distribution was subtracted off the candidates passing the identification. Before the subtraction is done, the two isolation distributions are normalized, in such a manner that the number of events in the tails above 10 GeV are equal (above an isolation of 10 GeV, the contribution of real photons in the *TightRelaxed* is negligible; fake photons fully dominate). The total likelihood consists of four 2D likelihood contributions, one for each of the combinations of jet or γ flavor of the two photons. The two-dimensional likelihood fit was performed on a sample consisting of tightly identified photons, but without applying any isolation requirement, and provides the yields of (and systematic uncertainties on) $N_{\gamma\gamma}$, $N_{\gamma\text{-jet}}$, $N_{\text{jet-}\gamma}$ and $N_{\text{jet-jet}}$. The isolation distribution in the first 1.08 fb^{-1} of 2011 data, for the leading and subleading photon separately, fitted

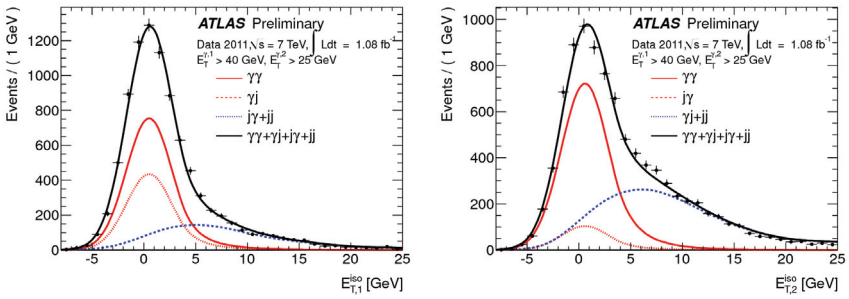

Figure 7.4: Isolation distribution of the first 1.08 fb^{-1} of 2011 data (black points), fitted with the isolation templates of the $\gamma\gamma$, γ-jet and jet-jet components [104]. The leading photon can be seen to the left, the subleading photon to the right. The true diphoton component can be seen as clearly the most isolated one, separated from the reducible backgrounds.

with the isolation templates of the $\gamma\gamma$, γ-jet and jet-jet components can be seen in Fig. 7.4. The true diphoton component can be seen as clearly the most isolated one. The main systematics come from the definition of the control sample used to get the fake photon template. In addition, correlation between isolation and identification variables, as well as real photons failing the identification might bias the fake template.

7.2.4 The 4×4 Matrix Method

In the 4×4 matrix method, the starting sample is diphoton events with both photons passing the tight identification [100]. Each event is categorized into four regions, depending on whether the (sub)leading photon passed (P) or failed (F) isolation. In the following notation, the first index represents the leading photon and the second index represents the subleading photon. The four pass/fail statuses $(S_{PP}, S_{PF}, S_{FP}, S_{FF})$ of events are represented by four event weights $(W_{\gamma\gamma}, W_{\gamma\text{-jet}}, W_{\text{jet-}\gamma}, W_{\text{jet-jet}})$ and a 4×4 matrix. The 4×4 matrix is based on how probable it is for a certain configuration of the two photon candidates to give the corresponding pass/fail status. This can be written as

$$\begin{pmatrix} S_{PP} \\ S_{PF} \\ S_{FP} \\ S_{FF} \end{pmatrix} = \mathbf{E} \begin{pmatrix} W_{\gamma\gamma} \\ W_{\gamma\text{-jet}} \\ W_{\text{jet-}\gamma} \\ W_{\text{jet-jet}} \end{pmatrix} , \tag{7.1}$$

where $\mathbf{E}$ is the 4×4 matrix. If there were no correlation between the isolation

energies of the two photons, it would have the form

$$\begin{pmatrix} \epsilon_1\epsilon_2 & \epsilon_1 f_2 & f_1\epsilon_2 & f_1 f_2 \\ \epsilon_1(1-\epsilon_2) & \epsilon_1(1-f_2) & f_1(1-\epsilon_2) & f_1(1-f_2) \\ (1-\epsilon_1)\epsilon_2 & (1-\epsilon_1)f_2 & (1-f_1)\epsilon_2 & (1-f_1)f_2 \\ (1-\epsilon_1)(1-\epsilon_2) & (1-\epsilon_1)(1-f_2) & (1-f_1)(1-\epsilon_2) & (1-f_1)(1-f_2) \end{pmatrix}, \quad (7.2)$$

where ϵ is the probability for a real photon to pass the isolation requirement, and f the probability for a fake photon to do so ($i = 1, 2$ indicates the leading/subleading candidate). However, there is a correlation between the isolation energies of the two photons, and thus a conditional probability is used, in which the status of the other photon is taken into consideration. The probabilities are extracted from data by looking at the probability density functions (pdfs) of the isolation of the candidates. The fake photon isolation template is taken from the photons in the *TightRelaxed* sample failing the tight identification cut (called the non-tight sample). For the real photon isolation template, photons passing the tight requirements are used, after subtracting the fake photon isolation template. Before the subtraction is done, the two templates are normalized to have the same number of events in the tail above 10 GeV, as in the 1×2D Template method.

Whether or not the prompt/fake photon is tightly identified is assumed to be uncorrelated with whether or not the photon is isolated (this correlation turns out to be non-negligible for prompt photons), and the anti-isolated region is assumed not to contain any real photons. The diphoton yield, $N_{\gamma\gamma}$, in the analysis sample can be found by a sum of event weights, where $W_{\gamma\gamma}$ is multiplied with ϵ_1 and ϵ_2. Similar expressions also hold for $N_{\gamma\text{-jet}}$, $N_{\text{jet-}\gamma}$ and $N_{\text{jet-jet}}$, exchanging ϵ_1 and ϵ_2 with the relevant probabilities. The main sources of systematic uncertainties are the definition of the non-tight sample, the statistics used for the isolation distributions and the choice of the region in which the fake and real photon templates are normalized.

7.2.5 Estimation of the Z-Background

A small background comes from the decay of the Z boson to two electrons (e^+e^-), where both electrons are misidentified as photons. Its contribution is largest in the lower end of the invariant mass window used for the H $\to \gamma\gamma$ analysis (100 – 160 GeV), and due to its resonance nature, it is not described well by an exponential distribution, which can be appreciated from Fig. 7.5. The estimation of the background from this Drell-Yan (DY) process is mainly performed in data.

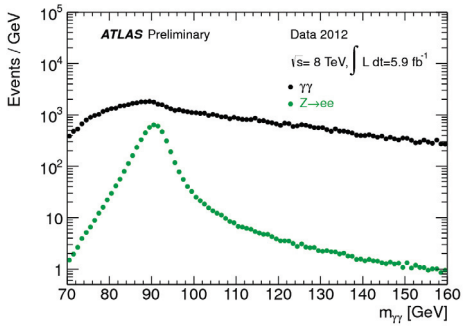

Figure 7.5: Invariant mass distribution after applying the ICHEP diphoton selection: Data and estimated contribution of $Z \to e^+e^-$ events to the diphoton invariant mass distribution for a sample of 5.9 fb^{-1} of $\sqrt{s}$ = 8 TeV data. This background contribution is obtained from reconstructed $Z \to e^+e^-$ events in data [105].

The contribution from this background can be represented by

$$N_{\gamma\gamma}^{DY} = \rho_{12} N_{ee}^{DY} = \alpha\rho_1\rho_2 N_{ee}^{DY} \ , \tag{7.3}$$

where ρ_{12} is the rate with which dielectrons are misidentified as diphotons, $\rho_{1(2)}$ is the misidentification rate of the (sub)leading electron and α the correlation between their misidentification rates. This latter parameter is found using Monte Carlo simulations, as the only ingredient in the method not extracted from data; the value is found to be $\alpha = 1.14 \pm 0.01\%$. A fit in the region 80 – 100 GeV of a Crystal-Ball + Gaussian (see Section 8.2 for a description of this pdf) to the invariant mass peak of the Z boson in e^+e^- and eγ events is used to infer ρ_1 and ρ_2. To avoid distorting the Z peak shape by the nominal asymmetric p_T cuts used in the $H \to \gamma\gamma$ analysis, the electrons are both chosen to have a transverse momentum exceeding 30 GeV. The values obtained are $\rho_1 = (8.59 \pm 0.04)\%$ and $\rho_2 = (10.00 \pm 0.04)\%$. The main systematic uncertainties are the effect of the asymmetric cuts (found to be about 5% on the correlation factor, 2% on the rates), the fit region bias: finding the misidentification rates in 80 – 100 GeV and applying them to 100 – 160 GeV (found to be about 5% on the correlation factor), and the fit bias: whether the number of dielectron events found by the fit disagrees with the true number of events (found to be 0.04% – negligible).

The DY background was added to the Monte Carlo simulation samples used to select the background functions, as detailed in Section 8.3. It made it especially difficult to describe the high-statistics categories with a single exponential. It also inspired the idea of a function with a turn-on at the low-mass end of the spectrum, which later got discarded due to fit instabilities.

7.2.6 The W+γ -Background

Another possible background to the search is $W + \gamma$, where the electron from the decay of the W boson is misidentified as a photon. A quick evaluation of this background is performed on Monte Carlo. After applying the diphoton selection, even with a K-factor[1] of 1.5, the contribution is found to be smaller than, or comparable to, that of the DY background. However, in contrast to the DY background, this background is fitted well by the exponential function, and will thus not distort the invariant mass spectrum to any significant degree. Due to its small contribution and exponential distribution, this background would not have a significant impact on the spectrum, and was therefore not added into the background templates used to determine the background parametrizations.

7.3 Isolation of the Photon Candidate

The isolation energy is a powerful tool for separating prompt photons from the background photons stemming from jets. It is estimated by looking at the transverse energy, E_T, deposited in a cone around the photon candidate. For real photons, there is very little energy collected in this cone, apart from the underlying event deposits, pile-up activity and electronic noise. For fake photons, there is more activity around the candidate, from the additional particles accompanying the photon candidate. For the calorimeter isolation variable, the transverse energy of the calorimeter cells within a cone of $\Delta R < 0.4$ around the photon candidate is summed, excluding a core of 5×7 (in cells units), containing most of the photon energy. However, some of the photon energy leaks outside this core – how much depends on the E_T of the photon; in general, the leakage increases as a function of E_T. Leakage outside the 5×7 core is taken into consideration, as well as the energy from pile-up (both in-time and out-of-time) and underlying event (UE) activity. The ambient (surrounding) energy and underlying event activity are found on an event-by-event basis, through the methods developed in Refs. [106, 107]. The jets are reconstructed using topological clusters with a k_T clustering algorithm, and the energy with which they contribute is corrected for in the photon energy. The elements in this paragraph is what the $E_T^{cone40,\,corrected}$ variable comprises.

As the $E_T^{cone40,\,corrected}$ variable showed dependence on the event activity and the bunch crossing ID, as illustrated in Fig. 3.14, a pile-up robust isolation variable was developed later on by people contributing to both the HSG1 and the e/gamma

[1] K-factors are used to capture the level of (lack of) knowledge about theoretical cross-sections, and is generally a reference for the ratio of the cross-section found by leading-order calculation, to the cross section found when including next-to-leading order processes, $K = \frac{\sigma_{NLO}}{\sigma_{LO}}$.

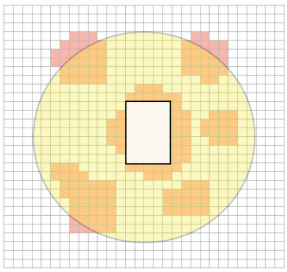

Figure 7.6: Illustration of isolation computation [109]. The grid represents the ECAL cell size in the second layer. The isolation area cone of $\Delta R < 0.4$ is depicted by the circle. The empty, rectangular area indicates the 5×7 cells that are removed for the isolation calculation, containing most of the energy of a candidate photon. For topological cluster isolation, only the topological clusters (colored areas) are used, whereas for the calorimeter cell-based isolation, all cells within the isolation area are used.

performance groups. This new isolation variable, as illustrated in Fig. 7.6, uses topological clusters instead of the energy measured in a fixed area of calorimeter cells. For the topological clusters, only neighbouring calorimeter cells with an energy above a certain threshold, defined as a function of the expected noise, are used. For more information about the two different clustering algorithms, see Ref. [108]. The clustering algorithm in this method works as noise suppression, because it only takes the (positive) energy of the candidate if it is spread coherently among the neighbouring cells. These same clusters are used as input to the jet software, from which the ambient energy and underlying event activity is obtained and corrected for in the photon energy [106, 107]. The isolation is still calculated in a cone of $\Delta R < 0.4$ around the photon candidate after subtracting the photon cluster core defined by a 5×7 cell rectangle; however, only the energy of topological clusters within the isolation cone is considered. The energy is corrected for leakage outside the core; the leakage is determined with photon Monte Carlo simulation. For more details about the new isolation variable, see Ref. [109], and for the technical implementation of it, see Ref. [110].

7.4 Triggering Events Containing Two Photons

The diphoton trigger used to select the events for the analysis is called `2g20_loose`. In this trigger, transverse energies of 20 GeV or more are required for both of the photon candidates. The efficiency of the trigger was found to be 98.9±0.2% for the 2011 dataset, and was obtained using a bootstrap method, from an ensemble in which the L1 trigger is fully efficient, as described in Ref. [111]. It was verified

using tag-and-probe on $Z \to e^+e^-\gamma$ events, in which a photon was radiated off one of the electrons. The difference of the tag-and-probe approach and the bootstrap approach resulted in a systematic uncertainty of less than one percent. The trigger had an efficiency greater than 99% for events passing the final selection [105].

I took part in monitoring the stability and performance of e/gamma triggers, which included the base trigger `g20_loose`. This work is described in Appendix B.

7.5 Study of the p_T Cuts on the Photons

Cutting on the transverse momenta of the two photon candidates is an effective way of reducing background in the search, as most of the noise is rather soft. Too hard p_T cuts, on the other hand, would be unfortunate, as it would also reduce or remove the signal. The balance between reducing the background while keeping most of the signal should be sought. A study of the cuts on the transverse momenta of the two photon candidates was made in order to see whether something could be gained in sensitivity to a possible signal with respect to the standard p_T cuts of 40(25) GeV for the leading(subleading) photon. An effort of optimizing the cuts on p_T had not been made since the 1990's [112]. In this section, the density of the signal and background in the $p_T^{\gamma_{subleading}}$ versus $p_T^{\gamma_{leading}}$ plane will be presented. A rough evaluation of which p_T cuts would yield the best significance is made, using the log-likelihood ratio of an Asimov dataset (defined in Chapter 8). Variable cuts on the transverse momenta are proposed, following a linear evolution with the invariant mass of the hypothesized Higgs boson.

For this study, the full dataset of 2011 itself was used as the background. In case there is a signal contribution therein, this would give slightly pessimistic results. Only candidates in a mass window of $\pm$ 2 GeV around the respective Higgs boson mass were considered. The raw simulated signal and background (data) distributions can be seen in Fig. 7.7. The aggregation of events at $m_H/2$ in the background is merely a reflection of the mass window cut. The same distributions, only integrated from the p_T cut in question and up (to a p_T of 100 GeV), can be seen in Fig. 7.8.

As an estimate of the significance squared obtained by cutting at a specific p_T, the Asimov log-likelihood ratio for discovery was used; assuming the signal hypothesis. The number of events were assumed to follow the Poisson distribution, thus the log-likelihood ratio for n number of events is given by [113].

$$2\ln\frac{\mathcal{L}(s+b)}{\mathcal{L}(b)} = 2\ln\left(\frac{\frac{(s+b)^n}{n!}\,e^{-(s+b)}}{\frac{b^n}{n!}\,e^{-b}}\right) \tag{7.4}$$

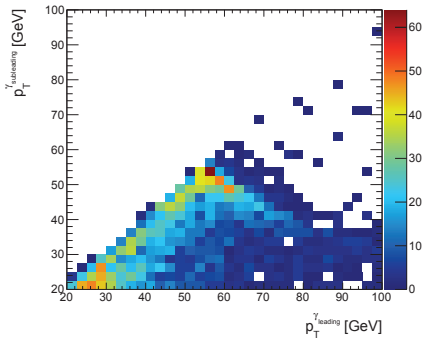

(a) Background (data) for $m_H = 110$ GeV

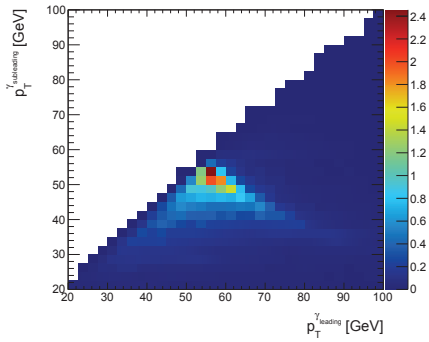

(b) Signal $m_H = 110$ GeV

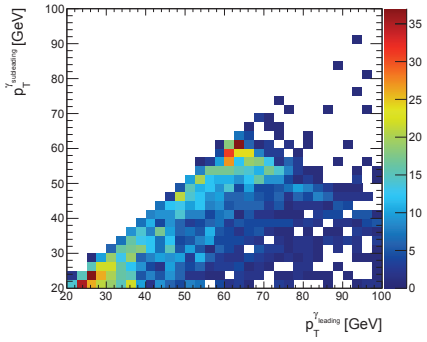

(c) Background (data) for $m_H = 125$ GeV

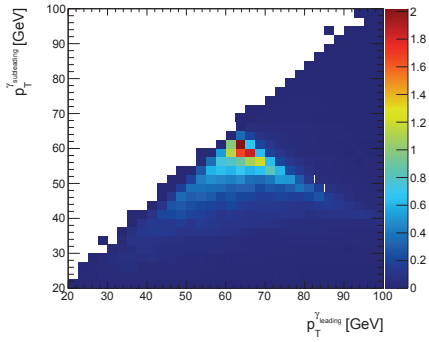

(d) Signal $m_H = 125$ GeV

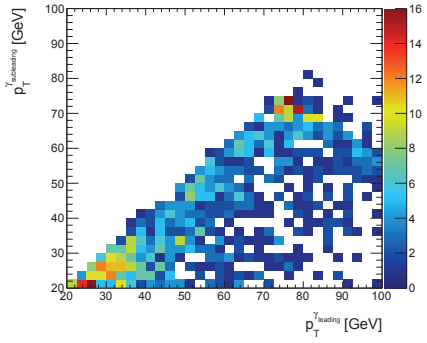

(e) Background (data) for $m_H = 150$ GeV

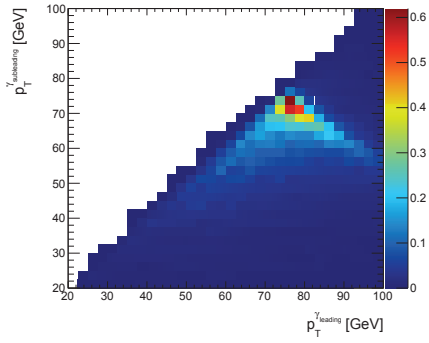

(f) Signal $m_H = 150$ GeV

Figure 7.7: The raw signal and background $p_T^{\gamma_{subleading}}$ vs $p_T^{\gamma_{leading}}$ distributions, cut in a mass window ± 2 GeV around the respective Higgs boson mass, for $m_H \in (110, 125, 150)$ GeV. The background (data) and signal correspond to 4.9 fb^{-1}.

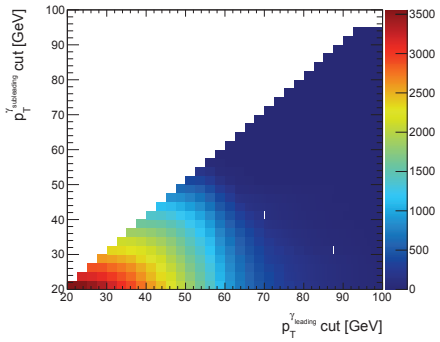

(a) Background (data) for $m_{\mathrm{H}} = 110$ GeV

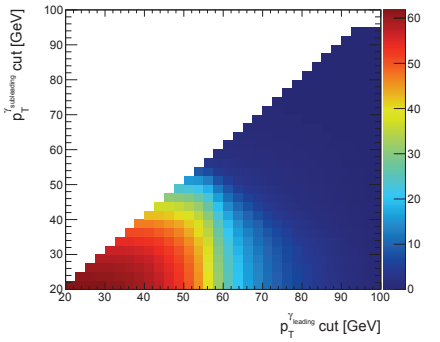

(b) Signal $m_{\mathrm{H}} = 110$ GeV

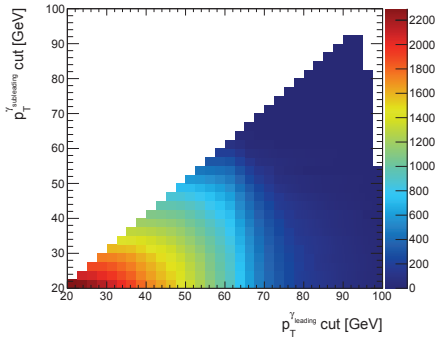

(c) Background (data) for $m_{\mathrm{H}} = 125$ GeV

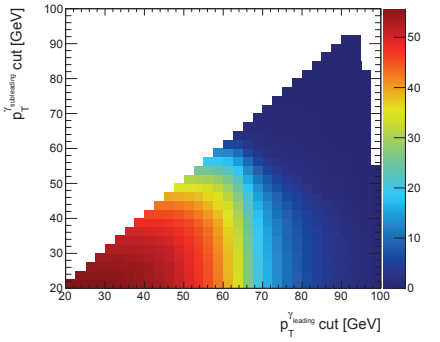

(d) Signal $m_{\mathrm{H}} = 125$ GeV

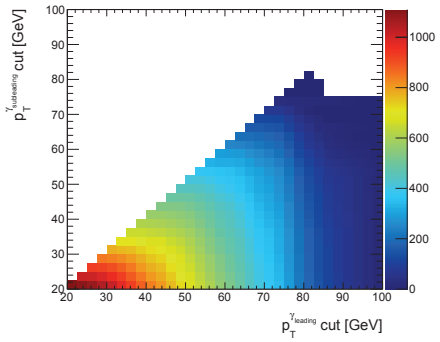

(e) Background (data) for $m_{\mathrm{H}} = 150$ GeV

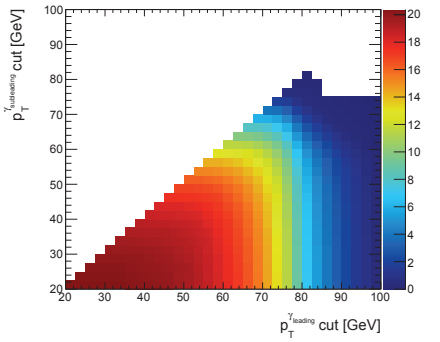

(f) Signal $m_{\mathrm{H}} = 150$ GeV

Figure 7.8: The signal and background $\mathrm{p_T}^{\gamma_{subleading}}$ vs $\mathrm{p_T}^{\gamma_{leading}}$ distributions, integrated from the $\mathrm{p_T}$ cut in question and up, cut in a mass window $\pm$ 2 GeV around the respective Higgs boson mass, for $m_{\mathrm{H}} \in (110, 125, 150)$ GeV. The background (data) and signal correspond to 4.9 fb^{-1}.

$$= 2\,\{n\ln(s+b) - n\ln(b) - s\} \tag{7.5}$$

$$= 2\left\{n\ln\left(1+\frac{s}{b}\right) - s\right\}\,, \tag{7.6}$$

where s is the signal and b the background, and $n = s + b$ for the Asimov dataset. The predicted signal and background were found taking the integral from the p_T cut in question and up. If the bin in question had zero background entries, it was skipped. The results of this "cut-and-count" approach can be seen in Fig. 7.9.

From these plots, a rough estimate was made of the optimal cut on p_T as a function of the Higgs boson mass. This was done by finding the bin with the largest log-likelihood ratio for the expected results – the corresponding $p_T^{\gamma_{leading}}$ and $p_T^{\gamma_{subleading}}$ cuts were taken as estimates of the best cuts. The uncertainties on the best estimate p_T cuts were taken by the first bin falling under 90% of the maximal log-likelihood ratio value. This corresponds roughly to the extension of the red/dark orange areas.[2] These points were then fitted with a straight line, constrained to pass through origo;

$$p_T^{\gamma}\,\text{cut} = \alpha \cdot m_{\gamma\gamma}\,. \tag{7.7}$$

The result can be seen in Fig. 7.10, in which also the p_T dependent cuts used by CMS [114] are illustrated by the dashed lines. The fit to the points rendered

$$\alpha^{\gamma_{leading}} = 0.4022 \pm 0.040 \tag{7.8}$$

$$\alpha^{\gamma_{subleading}} = 0.2978 \pm 0.041\,, \tag{7.9}$$

corresponding to

$$p_T^{\gamma_{leading}}\,\text{cut} = \frac{m_{\gamma\gamma}}{2.5} \tag{7.10}$$

$$p_T^{\gamma_{subleading}}\,\text{cut} = \frac{m_{\gamma\gamma}}{3.4}\,. \tag{7.11}$$

These are the cuts to be used throughout the rest of this thesis, whenever it is referred to "variable p_T cuts". We will come back to the performance of the p_T cuts versus the performance of the standard p_T cuts after we have presented the selection of the photon pairs and the categorization of these.

[2] This estimate, although crude, is not likely to change significantly if found by a more formal method. The likelihood function is visibly flat over an extensive area, indicating low sensitivity to the choice of p_T cuts.

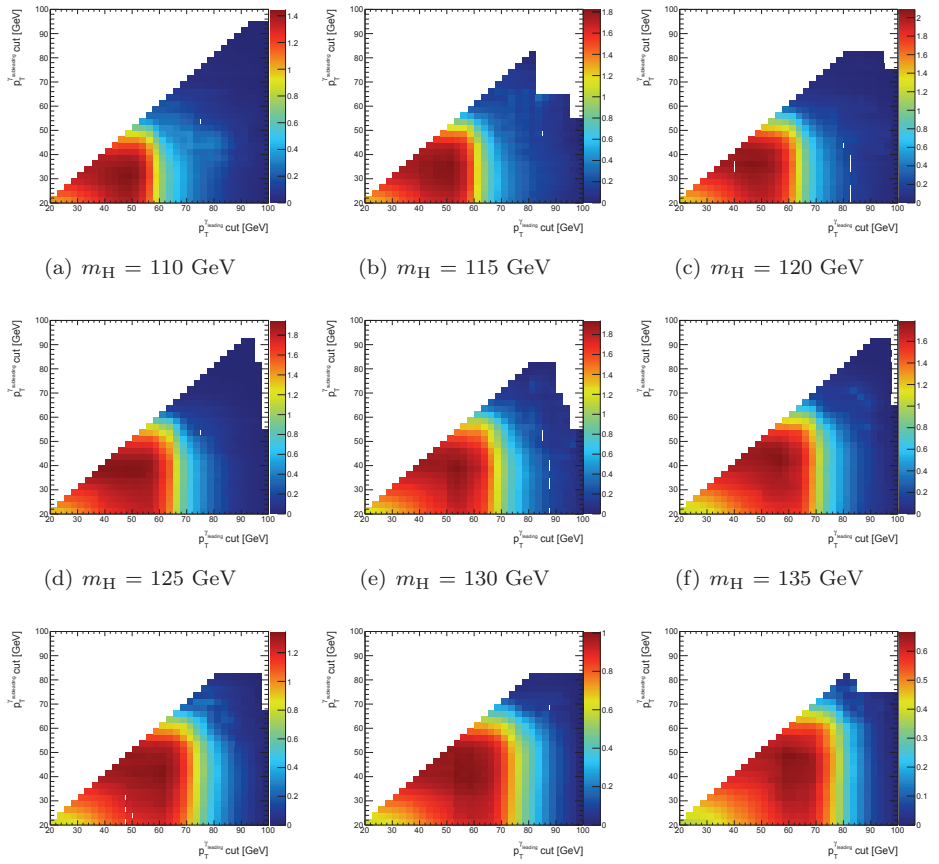

(a) $m_{\mathrm{H}} = 110$ GeV (b) $m_{\mathrm{H}} = 115$ GeV (c) $m_{\mathrm{H}} = 120$ GeV

(d) $m_{\mathrm{H}} = 125$ GeV (e) $m_{\mathrm{H}} = 130$ GeV (f) $m_{\mathrm{H}} = 135$ GeV

(g) $m_{\mathrm{H}} = 140$ GeV (h) $m_{\mathrm{H}} = 145$ GeV (i) $m_{\mathrm{H}} = 150$ GeV

Figure 7.9: Log-likelihood ratio following the Asimov formula in Eq. (7.6) in the $\mathrm{p_T}^{\gamma_{subleading}}$ versus $\mathrm{p_T}^{\gamma_{leading}}$ plane, for the integrated signal and background from the $\mathrm{p_T}^{\gamma_{subleading}}$ versus $\mathrm{p_T}^{\gamma_{leading}}$ bin in question and up. The background (data) and signal correspond to 4.9 fb^{-1}.

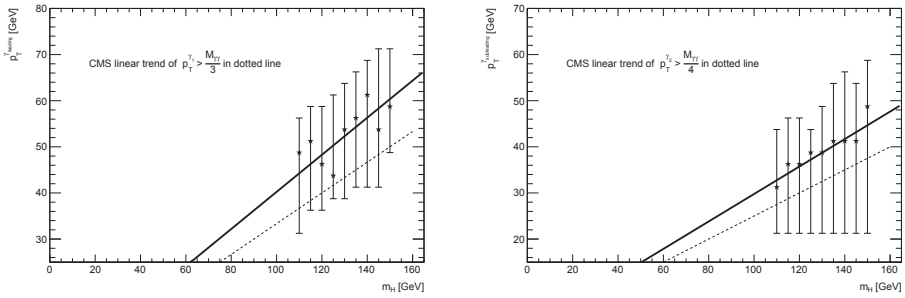

(a) $p_T^{\gamma leading}$ cut

(b) $p_T^{\gamma subleading}$ cut

Figure 7.10: Linear fit of the optimized cut on p_T as a function of Higgs boson mass. The points are obtained from Fig. 7.9, the error bars indicate a p_T range where the expected significance is within 90% of its maximum value, roughly corresponding to the extension of the red/deep orange areas. The p_T dependent cuts previously used by CMS [114] are illustrated by the dashed lines. The background (data) and signal correspond to 4.9 fb^{-1}.

7.6 Choosing the Diphoton Primary Vertex

An evolution has taken place in the analysis with regards to the method used for choosing the position in z of the common vertex of the diphoton pair. The position of this primary vertex, and thereby the angles of the photons, greatly influences the resolution of the invariant mass distribution. To obtain a better significance of a possible signal on top of the large, exponential-like background distribution, a narrow mass peak is desired. The significance of an excess is roughly inversely proportional to the width of the mass peak, so this is a crucial point. Being such, estimating the common diphoton z-vertex in data has received quite some attention in HSG1. This evolution and the different methods utilized will be presented here.

For the paper for the Moriond 2011 conference [115, 116], simply the vertex with the largest sum of p_T^2 of the tracks associated to it was chosen. This procedure is coming from the Inner Detector group. An improvement was done in the next paper for the EPS conference [117, 118], for which the photon pointing method was first introduced. The method of photon pointing is the following:

- for unconverted photons, and TRT StandAlone converted photons, take the first (front/strip) and the second (middle) layer deposit in the ECAL (called calorimeter pointing),
- for converted photons, take the conversion point, and the deposition in the

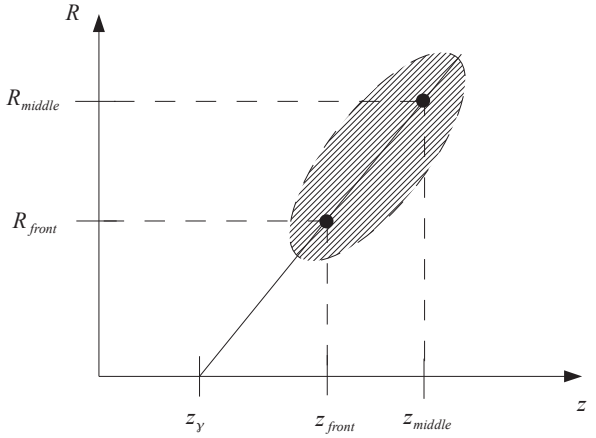

Figure 7.11: Illustration that shows how calorimeter pointing works. The electromagnetic shower is indicated, as well as the barycenters of the readouts in the first and second sampling layers of the ECAL, where z is the position along the beam-axis and R is the radial position in the detector. The vertex position in z given by this one photon, z_γ, is found from the intersection of the line between these two points and the beam axis. The formula for finding z_γ is given in Eq. (7.13).

first layer of the ECAL,

and extrapolate the straight line made by these points back to the beam axis, to find the position in z of the vertex. Thus, the high resolution of the first layer of the ECAL is exploited, as well as the precision of the position measurement of the inner detector when converted photons result in reconstructed tracks also before they reach the TRT.

The photon calorimeter pointing technique is illustrated in Fig. 7.11. The z-position of the vertex as given by pointing of one photon, z_γ, will only roughly coincide with the origin of the coordinate system of the detector. The RMS spread of the beam-spot is about 5.6 cm. Furthermore, the z_γ obtained with photon pointing will be more precisely determined than taking the information from the inner detector alone (that is, using the $\sum \mathrm{p}_\mathrm{T}^2$ approach). The resulting z-position of the vertex when taking the pointing of both photons into consideration is used, and the angles of the photons are adjusted based on this vertex position. For finding z_γ of each of the two photons, we take advantage of that the slope made by the points $\{(z_\gamma, 0), (z_{front}, R_{front})\}$ and $\{(z_{front}, R_{front}), (z_{middle}, R_{middle})\}$ is the same. Thus, we get

$$\frac{R_{middle} - R_{front}}{z_{middle} - z_{front}} = \frac{R_{front} - 0}{z_{front} - z_\gamma} \ , \tag{7.12}$$

which gives

$$z_\gamma = \frac{z_{front}\, R_{middle} - R_{front}\, z_{middle}}{R_{middle} - R_{front}} \ . \tag{7.13}$$

To read more about the reconstruction of the z-vertex and direction of the photon, see Ref. [119].

To find the common vertex position in z of the diphoton pair, a weighted mean[3] is used, taking into account the origin estimates of the two photons, $z_{\gamma_{1,2}}$ (found by photon pointing), as well as the beam-spot, z_{BS}, and their respective uncertainties, $\sigma_{\gamma_{1,2},\,BS}$, as given in Eq. (7.14):

$$z_{\gamma\gamma} = \frac{\frac{z_{\gamma_1}}{\sigma^2_{\gamma_1}} + \frac{z_{\gamma_2}}{\sigma^2_{\gamma_2}} + \frac{z_{BS}}{\sigma^2_{BS}}}{\frac{1}{\sigma^2_{\gamma_1}} + \frac{1}{\sigma^2_{\gamma_2}} + \frac{1}{\sigma^2_{BS}}} \ . \tag{7.14}$$

As a further improvement, for the Council Note[4] [95, 120], a correction of photons which are candidates for calorimeter-only pointing and located in the end-cap was applied. This correction was meant to take into account the oscillation structure in the end-cap observed in the data, but not seen in MC. Further explanation can be found in Appendix A of Ref. [120].

In Fig. 7.12, the fit of the signal (see Section 8.2 for description of the signal function) using the different methods described for determining the position of the vertex is shown. Also shown in green is the resolution obtained when using the truth information in MC. One can appreciate that the photon pointing method does nearly as good a job as using the truth vertex position. Thus, pointing is practically the best one can do; the possibility for improvement is rather small. The improvement of the mass resolution when moving from the $\sum \mathrm{p}_\mathrm{T}^2$ approach to the photon pointing is of the order of 5-20%, depending on the pile-up conditions [95]. With calorimeter pointing only, the resolution obtained is $\sigma_z = 15$ mm; for two converted photons with silicon hits, when utilizing the conversion vertex information, it is 6 mm.

In March 2012, the tactic was changed, to taking the primary vertex that was closest to the one found by calorimeter pointing of the two photons. Using a specific

[3] The formula for weighted mean can be derived maximizing the likelihood of several Gaussian measurements (or equivalently, minimizing the negative log-likelihood).

[4] This note was made for the CERN Council. The preliminary results from the searches for a Standard Model Higgs boson performed by the ATLAS and CMS experiments were presented in the CERN Open Seminar the 13$^{\mathrm{th}}$ of December 2011. The selection of the photon pair events for this note will be presented in Section 7.7.1.

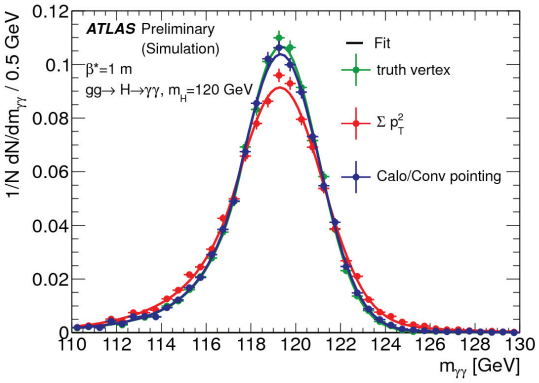

Figure 7.12: The invariant mass distribution of $gg \rightarrow \mathrm{H} \rightarrow \gamma\gamma$ with $m_{\mathrm{H}} = 120$ GeV, using different methods for finding the primary vertex position [95]. It can be appreciated that using calorimeter pointing (in blue) gives nearly as good a resolution at using truth information for MC (in green).

reconstructed vertex was adopted in connection to selecting jets from the hard scattering process for the extra category introduced, aimed at VBF production. As already shown, choosing a specific primary vertex of the inner detector is not necessary for the invariant mass resolution. Later, for the International Conference on High Energy Physics (ICHEP) July 2012, a likelihood with the information from tracking; $\sum \mathrm{p}_{\mathrm{T}}^2$, was also added to the pointing information to find the most probable primary vertex [105].

7.7 Photon Pair Selection

In this section, the criteria for selecting photon pairs for the main analysis – a search for the SM Higgs boson via the $\mathrm{H} \rightarrow \gamma\gamma$ decay – will be described. Since comparisons will be made with the official selections, both prior to the one used for this thesis, the so-called *PRL selection*, and posterior to the one used for this thesis, the so-called *ICHEP selection*, these will also be detailed. For all selections, corrections as detailed in Chapter 5 were carried out.

7.7.1 The PRL Selection

The so-called PRL (Physical Review Letters) selection was used in the paper published therein [121]. This was also the selection used for the CERN Council in December 2011, when the first serious hints of a Higgs boson was to be seen in the data of ATLAS and CMS. For the event to be accepted for the final analysis, the following criteria were enforced [122]:

- The event had to be within a run and luminosity block contained in the

Good Runs List (GRL) `data11_7TeV.periodAllYear_DetStatus-v35-pro09-03_CoolRunQuery-00-04-00_Eg_standard.xml`. The e/γ GRL assures of good inner detector and calorimeter data quality.

- It had to be triggered by the `2g20_loose` trigger.
- The event had to contain a primary vertex (PV) with at least three tracks (to reject background from non-collision events).
- The photons to be considered had to be within the fiducial acceptance region of the detector, $|\eta^{\gamma}| < 1.37$ or $1.52 \leq |\eta^{\gamma}| < 2.37$, excluding the crack region between the barrel and the end-cap.
- Photons were required to have a good object quality in the LAr detector; the cluster was not to contain bad calorimeter cells (this is ensured of via the ph_OQ variable, containing information about *e.g.* the High Voltage (HV) and read-out of the cells).
- Photons that have bad timing with respect to the BC or a large amount of energy within bad cells of the calorimeter, likely being noise, were rejected (*photon cleaning* [123, 124]).
- Photons had to pass the loose identification criteria.
- A transverse momentum of at least 25 GeV was demanded of each photon.
- The photon candidates had to pass the Ambiguity Resolver (AR) bit. This only affects converted photon candidates, and makes sure the track is not extrapolated back to a faulty cell of the innermost pixel layer. Demanding the b-layer to work properly in this manner strongly reduces the amount of electrons falsely reconstructed as converted photons.

The above selections regarding the photon candidates is called the *preselection*, named so because it is done before treating the two photons differently. After this preselection, the two leading (meaning highest-p_T) photon candidates had to

- be of tight identification quality,
- be isolated, meaning $E_T^{cone40,corrected} < 5$ GeV (for information about the isolation, see Section 7.3),
- have $p_T > 40$ GeV for the leading candidate and $p_T > 25$ GeV for the subleading candidate,
- have a reconstructed invariant mass within the mass window 100 – 160 GeV.

The azimuthal angle, ϕ, was taken from the second layer of the calorimeter and η was as measured in the first layer of the calorimeter, corrected based on the common diphoton vertex. Finally, the event

- must not have indications of a noise burst or data integrity problems (like a faulty layer) in the Liquid-Argon calorimeter, given by the the larError-flag.

With this selection, 20 894 events were found in the mass range of 100 – 160 GeV.

7.7.2 The Thesis Selection

The selection used in this thesis resides somewhere between the PRL and the ICHEP selection (described in the next section). The changes in the selection with respect to the PRL selection were as follows:

- The event had to belong to the `data11_7TeV.periodAllYear_DetStatus-v36-pro10_CoolRunQuery-00-04-08_Eg_standard.xml` GRL and have a larError-flag[5] not indicating problems.
- It had to contain at least one primary vertex with at least two associated tracks (which is the minimal requirement for PV reconstruction).
- Both photons had to pass the tight identification requirement based on a Neural Network (NN), instead of the `tight` requirement based on cuts on the shower shape variables [125].
- The photons had to have topological cluster based isolation less than 4 GeV (for information about the isolation, see Section 7.3).
- The chosen PV was the reconstructed ID vertex closest to the common diphoton vertex found by the photon pointing.
- In addition to the energy correction based on $Z \to e^+e^-$ events, an extra MC-based energy correction for converted photons only was applied.
- For the invariant mass calculation, ϕ was taken from the cluster.
- In between the PRL selection and the one used for this thesis, the packages used (like GoodRunsLists, egammaAnalysisUtils, PileupReweighting, PhotonAnalysisUtils and ggFReweighting) were updated. The package tags used in this analysis are the same or newer than the ones used for the ICHEP selection.

With this selection, 23 611 events are observed for the full 2011 data sample in the mass range 100 – 160 GeV. The number of events passing the different stages of the selection, the so-called *cutflow*, can be seen in Table 7.3. In the same table, the cutflow for a $m_H = 125$ GeV $H \to \gamma\gamma$ simulation can also be seen, both the raw

[5]Having the LarError flag in the beginning of the selection ensures that one does not process events that would in the end either way be discarded. On the other hand, having it in the beginning instead of at the end, one cannot report the impact of the variable to the e/gamma working group.

number of entries, and the entries when scaled to the integrated luminosity of 2011 data. In this amount of data, the expectation for a $m_{\mathrm{H}} = 125$ GeV signal is close to 80 events. In the last column, the efficiency of the selection can be seen, where the final efficiency for selecting the signal is 40%. The expected signal yield for this selection in the 2011 data, partitioned into the separate production mechanisms, can be seen in Table 7.4. Here it can be appreciated that gluon-gluon fusion is the dominant production process, and that associated production with two top-quarks is minuscule in comparison. In Table 7.5, the expected signal yield at different masses of a SM Higgs boson, ranging from $m_{\mathrm{H}} = 110$ GeV to $m_{\mathrm{H}} = 150$ GeV in steps of 5 GeV can be seen. The maximum yield is around $m_{\mathrm{H}} = 120$ GeV.

Selection	**Data**	**Monte Carlo simulation**		
		Unscaled	Scaled	Eff. [%]
Initial	7 630 458	220 000	199	100
$\gamma\gamma$-trigger	6 424 212	160 197	145	72.8
GRL	6 105 095	160 197	145	72.8
PV	6 104 453	160 192	145	72.8
Preselection	1 211 591	122 038	110	55.5
Kinematics	627 032	119 771	108	54.4
Photon-ID	123 543	100 756	91.1	45.8
Isolation	73 300	88 077	79.6	40.0
Mass window	23 611	88 077	79.6	40.0

Table 7.3: Cutflow of the selection; number of events remaining after the different stages of the thesis selection, both for 2011 data and for Monte Carlo simulations. The number of entries for a $m_{\mathrm{H}} = 125$ GeV $\mathrm{H} \to \gamma\gamma$ signal simulation are both given "as is" and scaled to the integrated luminosity of the data. In the last column the efficiency of the MC selection with respect to the initial sample can be seen. The mass window is 100 – 160 GeV.

Production mechanism	ggF	VBF	WH	ZH	ttH
Entries	69.4	6.03	2.45	1.36	0.36

Table 7.4: Expected signal yield of the thesis selection for a $m_{\mathrm{H}} = 125$ GeV SM Higgs boson, separated into the different production mechanisms, for an integrated luminosity of 4.9 fb^{-1}.

Mass [GeV]	110	115	120	125	130	135	140	145	150
Entries	78.6	81.9	82.2	79.6	74.3	67.2	57.3	47.0	35.9

Table 7.5: Expected signal yield of the thesis selection for Standard Model Higgs bosons of $m_{\mathrm{H}} \in \{110, 150\}$ GeV in steps of 5 GeV, for an integrated luminosity of 4.9 fb^{-1}.

7.7.3 The ICHEP Selection

The changes in the so-called ICHEP selection [126] with respect to the selection used for this thesis are:

- The event had to belong to the `data11_7TeV.periodAllYear_DetStatus-v36-pro10_CoolRunQuery-00-04-08_GammaJet.xml` GRL for the 2011 data and `data12_8TeV.periodAllYear_DetStatus-v47-pro13-01_CoolRunQuery-00-04-08_GammaJet.xml` GRL for the 2012 data.
- For the 2012 data, the `g35_loose_g25_loose` trigger chain was used (for 2011, the `2g20_loose` was still used).
- The loose identification criteria cuts for 2012 were changed, to a looser selection to adapt to the relaxed cuts in the loose trigger, changed due to the increased pile-up.
- The kinematic cut on the subleading photon was raised from $\mathrm{p_T} > 25$ GeV to $\mathrm{p_T} > 30$ GeV
- The $\sum \mathrm{p_T^2}$ information was added to the likelihood for finding the common diphoton vertex, which already included the pointing of each photon and the beam spot.
- For the 2012 data, the tight identification was cut-based, re-tuned to be more robust against the increased pile-up.
- Jet selection and jet calibration was performed, in which $\mathrm{p_{T}}_{jet} > 25$ GeV, and $|\eta|_{jet} > 4.5$, quality cuts on the jets had to be passed, and the jet could not be matched to either of the two photons. A Jet Vertex Fraction (JVF), being the momentum fraction of tracks belonging to the jet which were matched to the chosen PV, of 0.75 or more was enforced.
- An extra category was added, aimed at the VBF production mechanism. The cuts for the VBF category, in which two forward jets were sought for, were $|\Delta\eta_{\text{jet-jet}}| > 2.8, M_{\text{jet-jet}} > 400$ GeV, $\Delta\phi(\gamma\gamma - \text{jet-jet}) > 2.6$.

With this selection, 23 788 diphoton candidates were found in the invariant mass range between 100 and 160 GeV in the 2011 data.

The cumulative expected improvement with respect to the PRL analysis can be seen in Table 7.6. For more details of the improvements from the PRL to the ICHEP selection, see Ref. [125].

Source	Cumulative improvement
Subleading photon $p_T > 30$ GeV	1.0%
Topological cluster-based isolation	6.0%
Neural net photon identification	11%
p_{Tt} reoptimization	13%
2-jets category	15%

Table 7.6: Expected improvement from changes in the diphoton selection from PRL to ICHEP [127].

7.8 The Categories

Now that the selection of the diphoton events has been described, it is time to move on to categorization of the events. Similar to taking the mean of two measurements with very different uncertainties, unless the results are weighted according to their inverse squares of the uncertainties, the poor resolution measurement will wash out the good one [113]. Thus, for the optimal sensitivity to a possible signal, it is wise to separate these Higgs boson candidate events into different categories. The categories would be defined depending on their mass resolution, given that the mass is the final discriminant in a discovery/exclusion of a SM Higgs boson signal in the diphoton channel.

For the categorization of events, the p_{Tt} of the diphoton system was used as a discriminating variable, as suggested in Ref. [128]. This variable is less sensitive to the momentum resolution of photons, less correlated to the invariant mass and yields a greater discriminating power that the transverse momentum of the diphoton pair. The p_{Tt} is defined as the component of the photon pair's transverse momentum that is orthogonal to the vectorial difference of the leading photon's

p_T and the subleading photon's p_T.[6] This can be seen illustrated in Fig. 7.13. The distribution of p_{Tt} in reducible background, and for signal separated in gluon-gluon fusion and VBF can be seen in Fig. 7.14. From this figure it can be appreciated that signal coming from the VBF production mechanism generally has harder p_{Tt} than the signal stemming from gluon-gluon fusion. For the categorization in the PRL selection, the p_{Tt} cut was at 40 GeV, whereas for the ICHEP selection, it was moved to 60 GeV.

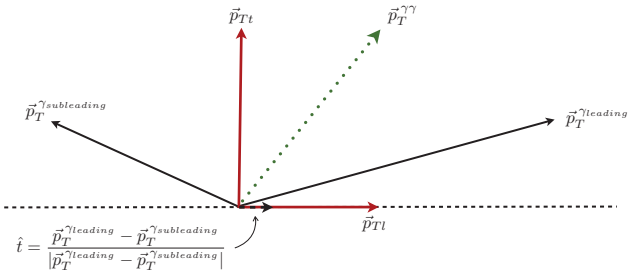

Figure 7.13: Illustration of the p_{Tt} definition used in categorization of diphoton events for the $H \to \gamma\gamma$ search.

[6] HSG1 misleadingly called this vectorial difference the "thrust axis". Thrust is defined as $\hat{T} = \max_{\hat{n}} \frac{\sum_i |\vec{p}_i \times \hat{n}|}{\sum_i |\vec{p}_i|}$, where the $\hat{n}$ which maximizes the expression is the thrust axis, $\hat{T}$. This is thus the axis for which the sum of the components of the vectors projected onto this axis is the largest. The HSG1 definition (called $\hat{t}$) is equivalent to thrust in the case where the p_T of the leading and the subleading photon have the same absolute size and the momentum vectors are more than 90° apart – but **not** in general.

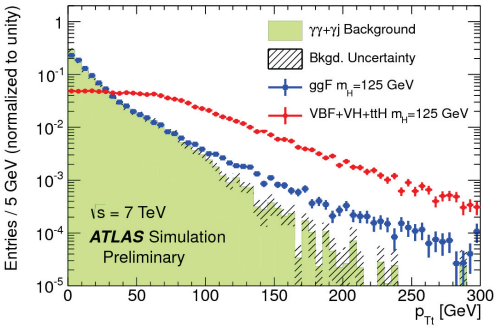

Figure 7.14: The p_{Tt} distribution, for background and signal separated in gluon-gluon fusion and VBF [105], where the background is obtained from SM $\gamma\gamma$ MC simulated with Sherpa [129] and γ-jet MC simulated with Alpgen [130]. The smaller jet-jet and DY components have been neglected. The distributions are normalized to unity.

For the 2011 analysis, nine categories were used, as summarized in Table 7.7. The events were sorted into the categories based on:

- e^+e^- conversion status of the photons,
- positions of the photons in the detector (discriminating on $|\eta|$),
- p_{Tt} of the diphoton system.

The events go into "unconverted" categories only when *both* photons are unconverted. For the categorization with respect to $|\eta|$, three regions are chosen, based on the detector resolution in those regions:

- "central" – both photons have $|\eta| < 0.75$ (best resolution);
- "transition" – at least one photon has $1.3 < |\eta| < 1.75$ (poor resolution);
- "non-central" or "rest" – all other constellations.

Name	Criteria		
CP1	unconverted	central	low p_{Tt}
CP2	unconverted	central	high p_{Tt}
CP3	unconverted	non-central	low p_{Tt}
CP4	unconverted	non-central	high p_{Tt}
CP5	converted	central	low p_{Tt}
CP6	converted	central	high p_{Tt}
CP7	converted	non-central	low p_{Tt}
CP8	converted	non-central	high p_{Tt}
CP9	converted	transition	

Table 7.7: The nine categories: based on the photons conversion statuses and positions in the detector, as well as the size of p_{Tt} of the diphoton system. Both photons have to be unconverted for the diphoton pair to end up in the "unconverted" categories. "Central" means $|\eta| < 0.75$ for both candidates, while "transition" corresponds to at least one photon in $1.3 < |\eta| < 1.75$. "Non-central" are all other cases (this is often called "rest"). The border for the p_{Tt} is at 60 GeV.

In Fig. 7.15, the display of an event of the CP4 category from the 2012 data-taking can be seen. The photon pair has a reconstructed mass of 126.9 GeV.

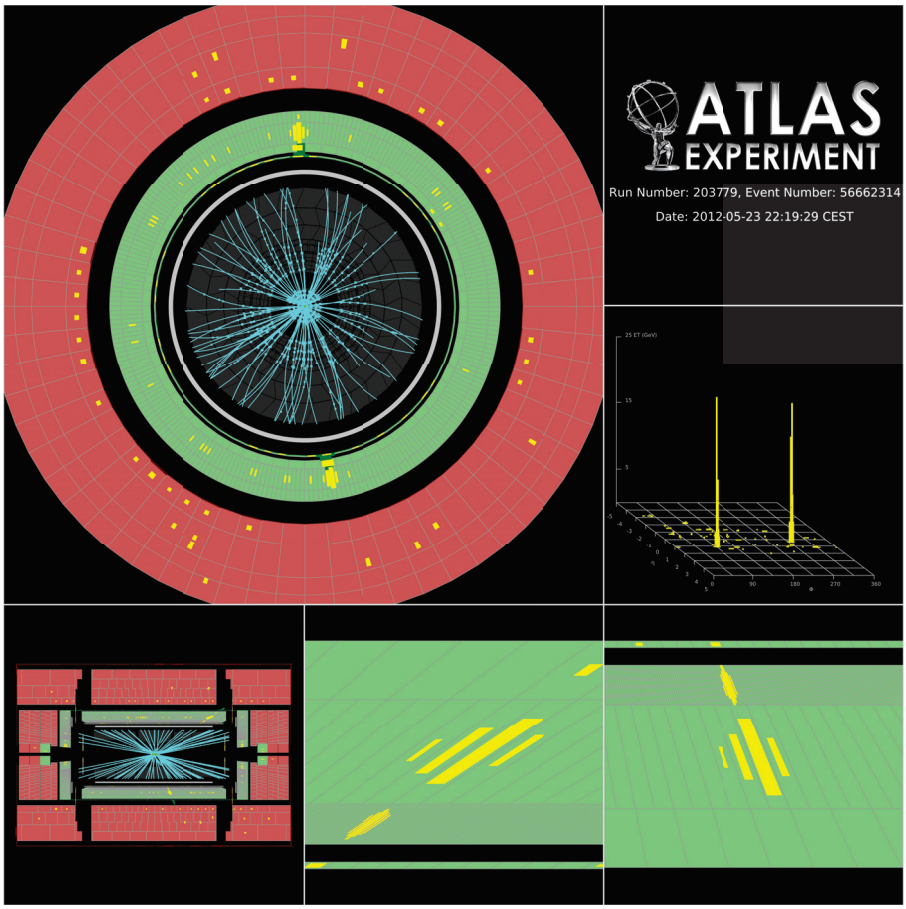

Figure 7.15: Event display of a diphoton event candidate in which both photon candidates are unconverted. The event number is 56662314 and it was recorded during run 203779 at $\sqrt{s} = 8$ TeV. The leading photon has $E_T = 62.2$ GeV and $\eta = 0.39$. The subleading photon has $E_T = 55.5$ GeV and $\eta = 1.18$. The measured diphoton mass is 126.9 GeV. The p_T and p_{Tt} of the diphoton are 9.3 GeV and 6.5 GeV, respectively. This Higgs boson candidate event is thus sorted into the CP4 category; unconverted, non-central, low p_{Tt}. Only reconstructed tracks with $p_T > 1$ GeV, hits in the pixel and SCT layers and TRT hits with a high threshold are shown [131].

7.9 Invariant Mass Distributions

As already mentioned, the invariant mass distribution of the photon pair is the main variable of the $H \to \gamma\gamma$ search. In Fig. 7.16, the invariant mass distributions in the 2011 data for the categories, both for standard and variable p_T cuts are shown. In these plots, the lower pad contains the ratio of the entries in the variable p_T cuts distribution to the entries in the standard p_T cuts distribution. The variable p_T cuts (open squares) are generally more aggressive than the standard p_T cuts (full circles). The difference between the two distributions is biggest for the low-p_{Tt}, high statistics categories CP3 and CP7, along with CP9. Both distributions have been fitted with an exponential function for all of the categories. In Fig. 7.17, the same invariant mass distributions and the exponential fits are shown on a logarithmic scale, only for the category with highest statistics, CP7. The distributions seem to at least not get less exponential when applying the variable p_T cuts.

7.10 Performance of the Standard and Variable p_T Cuts

With the selection and categorization presented, the remaining number of events in the 2011 data when using the standard p_T cuts, as well as using the variable p_T cuts can be seen in Table 7.8. The variable p_T cuts are more aggressive and are designed to remove more of the background. In Table 7.9, a coarse comparison of the performance using standard and variable p_T cuts on the 2011 data and a corresponding Monte Carlo simulation of $H \to \gamma\gamma$ with $m_H = 125$ GeV is given. For data, the entries, N_D, within ± 4 GeV around 125 GeV, an interval which covers approximately 90% of a signal at $m_H = 125$ GeV, is shown. The number of signal entries, N_S, is also given, along with the approximate significance, as given by $\frac{S}{\sqrt{B}}$, where the data entries are used as background. The change in data, signal and sensitivity when moving from standard p_T cuts to variable p_T cuts is given in the last three columns. An improvement of around 3.2% in the sensitivity is expected in the inclusive sample when moving from standard p_T cuts to variable p_T cuts. For some of the categories, the reduction in signal is not compensated by the reduction in background, thus the sensitivity is lower.

Using variable p_T cuts could be a direction to go in the future, with the net expected gain in sensitivity. More studies are needed to be sure of the effect on the categories and the overall sensitivity. In addition, implementing variable p_T cuts would require a new round of selection of background functions, as will be described in Chapter 8.3. The invariant mass distributions of the categories when using variable p_T cuts follow an exponential function seemingly to at least as good

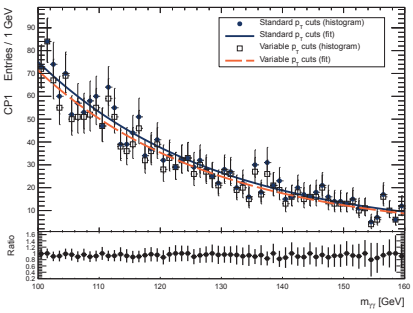

(a) CP1

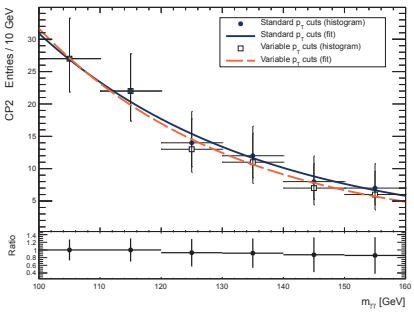

(b) CP2

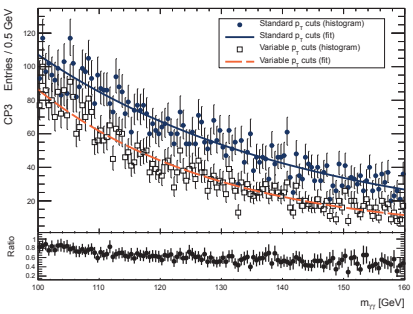

(c) CP3

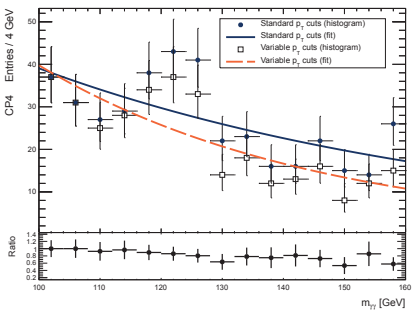

(d) CP4

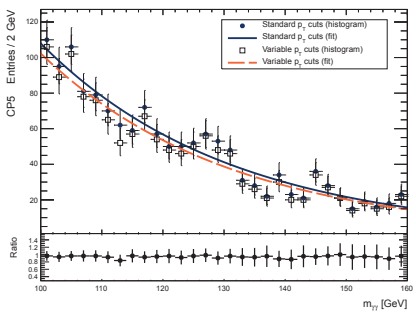

(e) CP5

Figure 7.16: Invariant mass distributions of the first five of the nine categories for the 2011 data, using standard p_T cuts of $p_T^{\gamma_{leading}} > 40$ GeV and $p_T^{\gamma_{subleading}} > 25$ GeV (full circles) and variable p_T cuts of $p_T^{\gamma_{leading}} > \frac{m_{\gamma\gamma}}{2.5}$ GeV and $p_T^{\gamma_{subleading}} > \frac{m_{\gamma\gamma}}{3.4}$ GeV (open squares). The lower pad displays the ratio of entries in the variable p_T cuts distribution to entries in the standard p_T cuts distribution. The distributions are fitted with a single exponential, displayed in full line for standard cuts and in dashed for variable cuts. The figure continues on page 121.

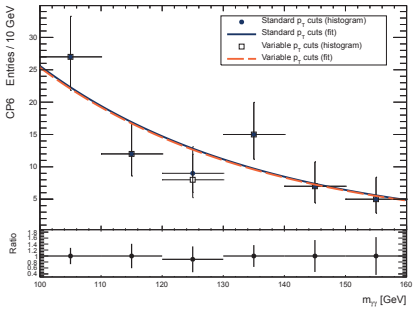

(a) CP6

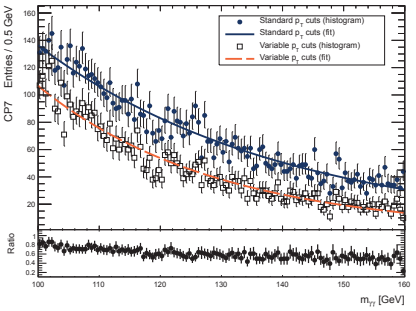

(b) CP7

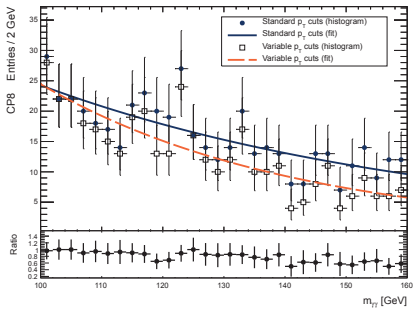

(c) CP8

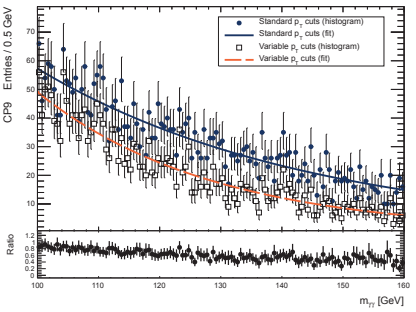

(d) CP9

Figure 7.16: (continued figure) Invariant mass distributions of the last four of the nine categories for the 2011 data, using standard p_T cuts of $p_T^{\gamma_{leading}} > 40$ GeV and $p_T^{\gamma_{subleading}} > 25$ GeV (full circles) and variable p_T cuts of $p_T^{\gamma_{leading}} > \frac{m_{\gamma\gamma}}{2.5}$ GeV and $p_T^{\gamma_{subleading}} > \frac{m_{\gamma\gamma}}{3.4}$ GeV (open squares). The lower pad displays the ratio of entries in the variable p_T cuts distribution to entries in the standard p_T cuts distribution. The distributions are fitted with a single exponential, displayed in full line for standard cuts and in dashed for variable cuts.

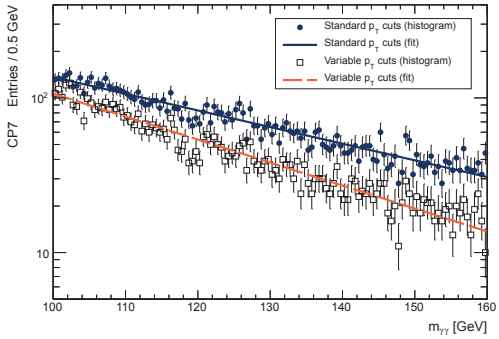

Figure 7.17: Invariant mass distribution of the high-statistics category CP7 on a logarithmic y-axis, for the full 2011 data of 4.9 fb^{-1} using standard p_T cuts of $p_T^{\gamma_{leading}} > 40$ GeV and $p_T^{\gamma_{subleading}} > 25$ GeV (full circles) and variable p_T cuts of $p_T^{\gamma_{leading}} > \frac{m_{\gamma\gamma}}{2.5}$ GeV and $p_T^{\gamma_{subleading}} > \frac{m_{\gamma\gamma}}{3.4}$ GeV (open squares). Both distributions are fitted with a single exponential.

Category	Standard p_T cuts	Variable p_T cuts
CP1	1898	1785
CP2	90	86
CP3	6951	4449
CP4	400	333
CP5	1436	1353
CP6	75	74
CP7	8511	5431
CP8	475	388
CP9	3775	2462
Inclusive	23611	16361

Table 7.8: Numbers of events in the nine categories and in the inclusive sample for standard and variable p_T cuts, for the 4.9 fb^{-1} of 2011 data.

a degree as when using fixed p_T cuts, as can be appreciated from Fig. 7.16. If the variable p_T cuts make the distributions more exponential, for which further studies are required to confirm or disprove, more categories would pass the simple exponential function, with an according gain in sensitivity. However, with the reduction of sensitivity in several categories, it seems not to be worth the effort. The categorization, with the exploitation of the p_{Tt} of the diphoton system, possibly absorbs some of the effect of the variable p_T cuts.

7.11 Changes in the Analysis Beyond the Scope of this Thesis

The HSG1 group has moved on since the studies performed in this thesis. Among other things, the p_T cuts were changed to 40(30) GeV for the leading(subleading) photon, another category aimed at singling out the VBF process was added, and the method of finding the primary vertex now includes taking the sum of p_T from the PV into consideration in the likelihood function, in addition to the pointing of each photon and the beam spot. This was added after jets were considered, due to the included VBF category. In addition, a different GRL was applied, also ensuring good quality of the hadronic calorimeter, needed for the jets in the VBF category.

Category	Standard p_T cuts			Variable p_T cuts			Change [%]		
	N_D	N_S	$\frac{S}{\sqrt{B}}$	N_D	N_S	$\frac{S}{\sqrt{B}}$	N_D	N_S	$\frac{S}{\sqrt{B}}$
CP1	251	10.1	0.64	243	9.7	0.62	-3.2	-4.5	-2.8
CP2	13	1.67	0.46	12	1.6	0.47	-7.7	-1.5	2.2
CP3	1027	21.9	0.68	622	16.8	0.67	-39	-23	-1.3
CP4	88	2.94	0.31	72	2.7	0.32	-18	-6.6	3.2
CP5	225	6.82	0.46	214	6.5	0.45	-4.9	-4.5	-2.2
CP6	7	1.1	0.42	7	1.1	0.41	0	-1.3	-1.9
CP7	1274	21.9	0.61	764	17.0	0.62	-40	-22	0.2
CP8	75	3.06	0.35	66	2.8	0.35	-12	-7	-0.9
CP9	573	10.2	0.43	354	8.4	0.44	-38	-18	4.2
Inclusive	3726	74.1	1.21	2472	62.3	1.25	-34	-16	3.2

Table 7.9: Number of events for standard and variable p_T cuts for 4.9 fb^{-1}. The number of events, N_D, within ± 4 GeV around 125 GeV in data, an interval which covers approximately 90% of a signal at $m_H = 125$ GeV, is shown, together with the number of signal events, N_S, of $m_H = 125$ GeV, and the approximate significance, as given by $\frac{S}{\sqrt{B}}$, where the data events are used as background. The change in data, signal and sensitivity when moving from standard p_T cuts to variable p_T cuts are given in the last three columns. Here it can be appreciated that the variable p_T cuts are more sensitive than the standard p_T cuts in the inclusive sample, by around 3.2%.

Chapter 8

Statistical Procedure and Modeling

For interpreting the results of the analysis, statistical tools are utilized. In this chapter, the statistical procedure in ATLAS used for exclusion and discovery will be described. We will here focus on the likelihood used by HSG1 and parameters therein which are necessary, but not of direct interest; so-called *nuisance parameters*. The signal model used to describe the $H \to \gamma\gamma$ signal will also be introduced, followed by a more thorough description of the background modeling.

8.1 The Statistical Procedure

In this section, the statistical procedure for deriving statements about the compatibility of the data with the signal and background hypotheses used by Higgs working groups in ATLAS, and in particular the one used by HSG1, will be described. For a description of the general statistical modeling used in the search for the SM Higgs boson, see Refs. [132, 133], which addresses the combined search for the Standard Model Higgs boson in the 2011 data. The statistical procedure is based on a profile likelihood method, where the test-statistic is a likelihood ratio, defined depending on the hypothesis that is being tested. The statistical treatment is in accordance with the ATLAS statistical recommendations [134].

The parameter μ is used to denote the signal strength in comparison to the one expected from the SM Higgs boson:

$$\mu = \frac{N_{signal}}{N_{signal}^{SM}} = \frac{\sigma_{signal}}{\sigma_{signal}^{SM}} \ . \tag{8.1}$$

In general, the test-statistic is called t_μ and is a log-likelihood ratio;

$$t_\mu = -2 \ln \frac{\mathcal{L}(\mu, \hat{\boldsymbol{\theta}}_\mu)}{\mathcal{L}(\hat{\mu}, \hat{\boldsymbol{\theta}})} \ , \tag{8.2}$$

where the likelihood, $\mathcal{L}$, will be defined later. Whenever a variable is marked with a hat, it indicates that this has been fitted. The nuisance parameters of the fit are described by $\boldsymbol{\theta}$. As the name indicates, these are parameters that are not of direct interest in the test, but which nonetheless affect the fit – like the integrated luminosity, the photon identification efficiency, the branching ratio of $\mathrm{H} \to \gamma\gamma$, the background normalization and shape and so forth.

In general, one can classify the nuisance parameters in two genres. The first class is nuisance parameters that are measured in other data than the search data, such as the luminosity and the photon identification efficiency. Their default values and uncertainties are input values and implemented into the likelihood function. Constraint terms for these external nuisance parameters, which represent the external measurements, indicate how much the nuisance parameters are allowed to vary, as a sort of penalty in the likelihood function; they are most commonly described by a Gauss function or a log-normal function (for more information about the log-normal constraint term, see Appendix C). The second class of nuisance parameters are variables that are fitted without constraint. The values of these internal nuisance parameters are found solely from the fit to the search data. This is for example the case for the background parametrization in the $\mathrm{H} \to \gamma\gamma$ search.

The indexed version of the nuisance parameters, $\hat{\boldsymbol{\theta}}_\mu$, represents the fitted value of the nuisance parameters at this particular value of μ. The numerator of the likelihood ratio is called the *conditional fit*, in which the signal strength, μ, is set to a particular value, and the rest of the parameters are fit under this condition. The denominator is the so-called *unconditional fit*, in which the parameters are left free. This provides the largest likelihood possible; the maximum likelihood. Thus, $\hat{\mu}$ and $\hat{\boldsymbol{\theta}}$ are the best fitted values possible for the signal strength and nuisance parameters. When scanning (profiling) the data over μ, fitting and finding the value of the likelihood ratio, this renders a parabola-like distribution of t_μ. An illustration can be seen in Fig. 8.1. The minimum of the parabola indicates the

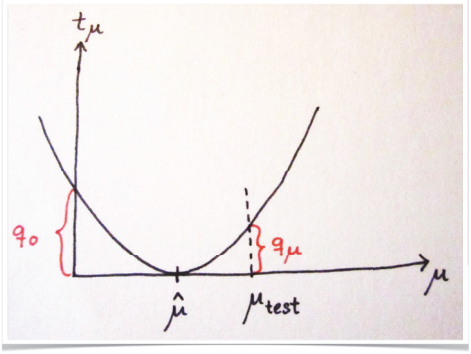

Figure 8.1: An illustration of the profile log-likelihood ratio test-statistic t_μ, according to Eq. (8.2). The value of the test-statistic for the background-only hypothesis is q_0, whereas q_μ is the value of the test-statistic for a signal hypothesis with signal strength μ_{test}. The best-fitted signal strength is given by $\hat{\mu}$, at the minimum of t_μ.

maximum likelihood, corresponding to the best fitted signal strength, $\hat{\mu}$. When moving away from this point, the likelihood of the conditional fits gets smaller (than the maximum likelihood), which makes the natural logarithm of the ratio more negative and the test-statistic larger.

In Fig. 8.1, values of t_μ at two points of interest are illustrated: q_0 and q_μ. We will shortly go into more detail of these parameters, as they are the test-statistics used. Suffice to say for now that the value of t_μ under the background-only hypothesis is called q_0 and is used for discovery, while the value of t_μ under the signal hypothesis with signal strength μ is called q_μ and is used for exclusion.

The distribution of the test-statistic can be obtained from Monte Carlo experiments, called *toys*.[1] In this approach, a random dataset is generated from a model of the experiment with the nuisance parameters fixed to their default values. Each toy is fitted with the full prescription to be used for data, *i.e.* including new fitted values of the nuisance parameters. The procedure is repeated a number of times until the test-statistic distribution is sufficiently populated. However, using this method to populate the distribution all the way out in the tails, which is necessary, for instance, to model the minuscule probability required for a discovery, requires a lot of computing power and is a time-consuming task. Therefore, whenever possible, asymptotic formulae [135] are used – after their validity is confirmed using toys. In the asymptotic limit, the distribution of q_0 is a χ^2 distribution under the background-only hypothesis, the distribution of q_μ is a χ^2 distribution under the

[1] A 'toy' is a nickname for a Monte Carlo experiment. "Throwing a toy" is a way of generating a MC experiment, which involves randomly picking out events from a template (typically a MC sample) a number of times corresponding to the number of entries in the template, in order to get the same expected statistical variation as in the template. The nuisance parameters are fixed to their default values in the template. This toy is then taken through the same profile likelihood ratio evaluation as the real data.

signal+background hypothesis, and t_μ versus μ is a perfect parabola.

In the coming, "observed" results are the ones obtained from the real data, while "expected" results are the outcome when using an Asimov[2] dataset generated with $\mu = 1$ for q_0 (disproving the background-only hypothesis) and $\mu = 0$ for the semi-frequentist variable $\mathrm{CL_s}$ (disproving the signal hypothesis), which will be described in the next section. The expected results are, however, not completely independent of data. The expected results for discovery are made from signal+background toys based on a data template, in which the nuisance parameters are fixed to the values obtained in a constrained $\mu = 1$ signal+background fit to data. Taking $\mathrm{H} \to \gamma\gamma$ as an example, an excess in data which is higher than the Standard Model signal can in such a fit be accommodated by for instance a higher photon identification. Thus, in regions of data with an excess exceeding the SM signal, the nuisance parameter for photon identification will likely have a higher value than elsewhere, and the expected result at that region will be more sensitive. This slightly unphysical behaviour of the expected results does not impact the observed results.

8.1.1 Exclusion Limits

When setting exclusion limits, the null hypothesis is the signal+background assumption, and a compatibility-test of this hypothesis with the data is performed. If the hypothesis is rejected, there is little reason to believe in a presence of signal in the data. The limit for certainty about a lack of signal is traditionally set at a confidence level of 95% – if there is less than 5% chance for signal+background data to produce the lack of signal seen, one claims this point to be excluded. This test is quantified by $\mathrm{CL_s}$ [136], a hybrid-frequentist variable, given by the ratio:

$$\mathrm{CL_s} = \frac{p_{s+b}}{1 - p_\mathrm{b}} \,, \tag{8.3}$$

where p_{s+b} is the tail-probability integral (from the observation and out) of the signal+background hypothesis distribution, and $1 - p_\mathrm{b}$ is the tail-probability integral of the background-only hypothesis distribution, as illustrated in Fig. 8.2.

This variable is designed such that exclusion of a signal would not be claimed when there is no sensitivity to a signal. If no signal is observed, but one does not

[2] The term 'Asimov' stems from the science fiction short story 'Franchise' by Isaac Asimov. In this story, the outcome of an election is decided by the sole vote of a global supercomputer (Multivac) – the view of the supercomputer is taken as representative for the whole population. The term first showed up in the paper 'Asymptotic formulae for likelihood-based tests of new physics' [135]. In this context, the Asimov dataset, representing the median of all statistically possible experiments, means a 'perfect' statistical distribution: the statistical uncertainty in a histogram bin is the square root of the content of the bin and the content is the expectation in that bin.

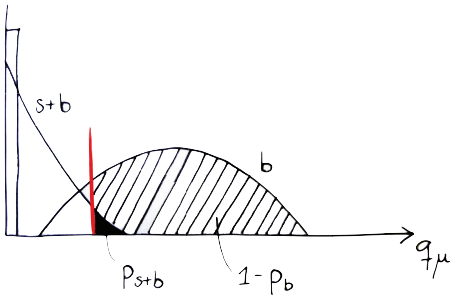

Figure 8.2: Illustration of the elements of CL_s as in Eq. (8.3). The observation is indicated by the vertical, thick line. When the ratio of the p-value of the signal+background hypothesis, p_{s+b} (black area), to the complement of the p-value of the background-only hypothesis, $1 - p_b$ (hashed area), falls under 5%, an exclusion of the signal hypothesis at that mass is claimed.

expect to be able to see any signal either, it would not make sense to rule out the signal hypothesis. This is taken into account by "punishing" the confidence level whenever the background and signal+background hypotheses both give similar numbers. CL_s can be thought of as an approximate and conservative "confidence in a signal" and whenever this falls under 5%, an exclusion of the signal hypothesis at that mass is claimed.

The p-value for the signal+background hypothesis is extracted using the test-statistic $\tilde{q}_\mu$;

$$\tilde{q}_\mu = \begin{cases} -2\ln \frac{\mathcal{L}(\mu,\hat{\hat{\boldsymbol{\theta}}}_\mu)}{\mathcal{L}(\hat{\mu},\hat{\boldsymbol{\theta}})} & \text{if } 0 \leq \hat{\mu} \leq \mu \\ 0 & \text{if } \hat{\mu} > \mu \\ -2\ln \frac{\mathcal{L}(0,\hat{\hat{\boldsymbol{\theta}}}_0)}{\mathcal{L}(\hat{\mu},\hat{\boldsymbol{\theta}})} & \text{if } \hat{\mu} < 0\ . \end{cases} \tag{8.4}$$

As can be seen, in the cases of a stronger observed signal than currently being tested, the test-statistic is set to zero – it is undesirable to exclude the signal hypothesis because *more* signal than expected was observed. If the fitted signal strength is lower than that expected for background ($\mu = 0$), $\mu = 0$ is used in the conditional fit to avoid technical and conceptual problems with negative pdfs.

8.1.2 Discovery

For discovery, a test of the compatibility of the data with the background-only hypothesis is made. This is quantified by the p-value p_0, which indicates the probability of the data for being in compliance with the background hypothesis; it is the probability for the background to have given the observed amount of data or even more than the observed amount. Thus, a large p-value indicates a good agreement with the background-only hypothesis, while a small p-value indicates a poor agreement with the background-only hypothesis – favouring a signal hypothesis. The p_0 is calculated from the test-statistic q_0 as illustrated in Fig. 8.3, following the formula;

$$q_0 = \begin{cases} -2\ln\frac{\mathcal{L}(0,\hat{\hat{\boldsymbol{\theta}}}_0)}{\mathcal{L}(\hat{\mu},\hat{\boldsymbol{\theta}})} & \text{if } \hat{\mu} \geq 0 \\ +2\ln\frac{\mathcal{L}(0,\hat{\hat{\boldsymbol{\theta}}}_0)}{\mathcal{L}(\hat{\mu},\hat{\boldsymbol{\theta}})} & \text{if } \hat{\mu} < 0\ . \end{cases} \tag{8.5}$$

The signal strength, μ, is set to zero in the conditional fit for this test of the background hypothesis. In datasets where there is a presence of a signal, the unconditional fit will render a much larger likelihood than the conditional background-only fit – so q_0 will be big, and p_0 small. Earlier, the p_0 was "capped", meaning that for negative fluctuations, $\hat{\mu} < 0$, q_0 was set to zero. This led to that whenever the data gave a smaller yield than predicted by the background hypothesis, p_0 would be 0.5. Negative fluctuations thus led to a "roof" in the p_0 plot. This way, one could not get a feeling for how big the negative fluctuation was. With the uncapped version, this becomes possible, as p_0 values just above 0.5 mean small negative fluctuations, and p_0 values close to 1 mean large negative fluctuations.

In making discoveries, excesses above the expected background are being searched for. Such an excess could, for example, be due to a new mass resonance on top a known background spectrum, but it could also be due to a random fluctuation of the background. A random fluctuation of the background can occur anywhere in the search area. The wider the range that is being searched, the more probable it is that a fluctuation will take place. Thus, this must be taken into account when evaluating how unlikely it is that a deviation is due to a background fluctuation. The effect is called the *look elsewhere* effect, and the size of the effect is described by a *trials factor* [137]. The trials factor is the ratio between the probability of finding an excess at a certain value of the search parameter, over the probability of finding such an excess anywhere in the search parameter range (for instance mass range, when mass is the search parameter, as in the $H \to \gamma\gamma$ search). Finding the trials factor involves counting how many times the curve q_0 as a function of

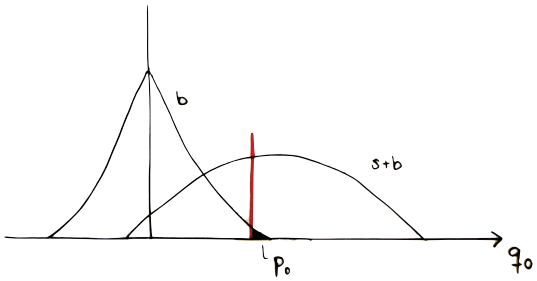

Figure 8.3: Illustration of the distributions of the test-statistic q_0 in background-only, and signal+background samples. The observation is given as a thick vertical line. The probability, p_0 (black area), of obtaining the observed value, or an even more extreme value, under the background-only hypothesis is used to reject this hypothesis.

the search parameter for background toys crosses some certain (arbitrary) level of probability – the average number of up-crossings, $\langle N_{up} \rangle$, gives an indication of how likely fluctuations are. The trials factor, f, can be written

$$f \simeq \langle N_{up} \rangle \cdot e^{-\frac{q-q_{ref}}{2}} \quad , \tag{8.6}$$

where q is the observed value of the test-statistic, and $\langle N_{up} \rangle$ is the average number of up-crossings with respect to the (freely chosen) limit q_{ref}. This approximation is excellent when $q - q_{ref} > 9$, decent for $q - q_{ref} > 4$, and poor for $q - q_{ref} > 1$ (corresponding roughly to 3, 2 and 1 standard deviations). In the absence of MC-toys statistics, it is possible to use data to get a rough estimate of $\langle N_{up} \rangle$.

8.1.3 The Likelihood function

The results of the search for $H \to \gamma\gamma$ by the HSG1 group were found using an unbinned maximum likelihood. The hypothesized Standard Model Higgs boson invariant mass, m_H, was the search parameter, thus the invariant mass of the diphotons in data was evaluated in the likelihood. The search was done as a scan over m_H in the mass region 110 – 150 GeV, in which a simultaneous fit to the individual mass spectra of the nine categories described in Section 7.8 was performed. For each m_H, the amplitude of a resonance was fitted in the $m_{\gamma\gamma}$ spectra of data. The signal strength, μ, was left free in the fit, but correlated

across the categories. The full likelihood that was used for this reads

$$\mathcal{L} = \prod_{i=1}^{n_{nuis}} \rho(\theta_i) \prod_{c=1}^{n_{cat}} \mathcal{L}_c(\mu, \boldsymbol{\theta}_c) \ , \tag{8.7}$$

where there are n_{cat} categories, $\mathcal{L}_c$ is the likelihood for one category, and $\boldsymbol{\theta}_c$ describes the nuisance parameters for category c. The constraint terms, ρ, one for each of the constrained nuisance parameters, $\theta_1, \cdots, \theta_{n_{nuis}}$, are parametrized as

$$\rho(\theta_i) = \frac{1}{\sqrt{2\pi}} e^{-\theta_i^2/2} \ . \tag{8.8}$$

These terms are penalty terms, constraining the fitted nuisance parameters from moving too far away from the estimated values; the deviation from the estimate is centered at zero, which is the default value of θ_i. If the search data contains information that pulls the parameter away from its estimated value, θ_i will be different from zero. We will shortly come back to the implementation of the size of the constraint on θ_i. The likelihood for one category is

$$\mathcal{L}_c(\mu, \boldsymbol{\theta}_c) = e^{-N_c} \prod_{n=1}^{N_c} \mathcal{L}_{c,n}(m_{\gamma\gamma}(n); \mu, \boldsymbol{\theta}_c) \ , \tag{8.9}$$

where N_c is the number of events observed in category c. The likelihood of the category is a product of the single likelihood for each event n. The event likelihood for category c itself, $\mathcal{L}_{c,n}$, consists of a signal part (s) and a background part (bkg):

$$\begin{aligned} \mathcal{L}_{c,n}(m_{\gamma\gamma}(n); \mu, \boldsymbol{\theta}_c) = \ & N_{s,c}(\mu, \boldsymbol{\theta}_c^{norm}) f_{s,c}(m_{\gamma\gamma}; \boldsymbol{\theta}_c^{shape}) \\ & + N_{bkg,c} \, f_{bkg,c}(m_{\gamma\gamma}; \boldsymbol{\theta}_c^{bkg}) \ , \end{aligned} \tag{8.10}$$

where $f_{s,c}$ is the signal probability distribution of reconstructed mass $m_{\gamma\gamma}$, and $f_{bkg,c}$ is the background probability distribution for the same mass. The pdf of the signal depends on the nuisance parameters that describe the shape of the signal, $\boldsymbol{\theta}_c^{shape}$, while the pdf of the background depends on the nuisance parameters that go into the background parametrization, $\boldsymbol{\theta}_c^{bkg}$. The fitted number of signal events, $N_{s,c}$, depends on the signal normalization part of the nuisance parameters, $\boldsymbol{\theta}_c^{norm}$. This signal normalization consists of a signal part and a so-called spurious signal part as detailed in the next paragraph. Finally, $N_{bkg,c}$ is the fitted number of background events. The complete set of nuisance parameters are thus given

by

$$\boldsymbol{\theta}_c = \boldsymbol{\theta}_c^{norm} \cup \boldsymbol{\theta}_c^{shape} \cup \boldsymbol{\theta}_c^{bkg} \cup \{N_{bkg,c}\} \ . \tag{8.11}$$

The signal normalization is split in the different production mechanisms, and also consists of a part taking into account a "spurious signal" term. More information about this term can be found in Section 8.3.2, but for now it is worth noting that, albeit in essence being an element intended to absorb the uncertainty on the background, it is described by a signal distribution. It is assigned the same mass probability density function as the hypothesized signal, an approach meant to give conservative results when attempting to reject the background hypothesis. The fitted number of signal events can be parametrized as

$$\begin{aligned} N_{s,c}\,(\mu, \boldsymbol{\theta}_c^{norm}) \ = \ & \mu\,[N_c^{ggH,SM}(\boldsymbol{\theta}_c^{ggH}) + N_c^{VBF,SM}(\boldsymbol{\theta}_c^{VBF}) \\ & + N_c^{WH,SM}(\boldsymbol{\theta}_c^{WH}) + N_c^{ZH,SM}(\boldsymbol{\theta}_c^{ZH}) + N_c^{ttH,SM}(\boldsymbol{\theta}_c^{ttH})] \\ & \cdot K_{BR}(\theta_{BR})\, K_{lumi}(\theta_{lumi})\, K_{eff}(\theta_{eff})\, K_{isol}(\theta_{isol}) \\ & \ K_{pile-up}(\theta_{pile-up}) K_{EScale}(\theta_{EScale}) \\ & \ K_{pile-up,c}(\theta_{pile-up,c}) K_{mat,c}(\theta_{mat}) \\ & + \sigma_{spurious,c}\,\theta_{spurious,c} \ . \end{aligned} \tag{8.12}$$

The normalization terms, $N_c^{X,SM}(\boldsymbol{\theta}_c^X)$, are the number of events per category expected from the SM split into the different production mechanisms (see Section 6.1), including selection efficiency. The normalization terms are modified with correction factors from the systematic uncertainties, which each represent a nuisance parameter, summarized in $\boldsymbol{\theta}_c^X$. These are factors like the uncertainty on the production cross-sections due to scale variations, and uncertainties on the gg and $q\bar{q}$ parton distribution functions (PDFs), taken from Refs. [90, 91]. On the gluon-gluon fusion yield alone, an uncertainty on the Higgs $\mathrm{p_T}$ distribution is applied, differently in the low- and high-$\mathrm{p_{Tt}}$ categories, including an uncertainty on the migration between these. In addition to correction factors on the normalization terms, there are factors $K_X(\theta_X)$, which affect the signal yield. Depending on the implementation, these can be written as

$$K(\theta) = 1 + \sigma\theta \qquad \text{for Gaussian,} \tag{8.13}$$

$$K(\theta) = e^{\sqrt{\ln(1+\sigma^2)}\theta} \qquad \text{for log-normal,} \tag{8.14}$$

where σ is the value of the constraint (the relative width of the Gaussian distribution), and θ is, as already indicated, distributed according to a unit Gaussian. Thus, looking at Eq. (8.8), it can be appreciated that σ represents

a one standard deviation fluctuation away from the estimated value of the nuisance parameter. For more information about the log-normal distribution, see Appendix C. In the case of nuisance parameters following the asymmetric log-normal distribution, θ follows a bifurcated Gaussian, *i.e.* for $\theta \geq 0$, σ has one value, whereas it has a different value for $\theta < 0$.

These factors adjusting the overall yield cover uncertainties on the branching ratio of $H \rightarrow \gamma\gamma$, the integrated luminosity, the efficiency (including photon identification and trigger efficiency), the isolation, the effect of pile-up on the photon identification and acceptance differences originating from the photon energy scale. In addition, there are uncertainties on the relative yield in the categories, taking into account migration between and out of the categories, such as the pile-up (applied differently to the conversion and non-conversion categories) and the imperfect knowledge of material in front of the calorimeter (also applied differently to the conversion and non-conversion categories). The uncertainty due to pile-up was estimated comparing simulations with a mean number proton-proton interactions per BC of less than 10, to those with more than 10.[3] The migration between the low-p_{Tt} and high-p_{Tt} categories due to uncertainty in the energy scale of photons was found to be negligible.

Several systematic uncertainties affecting the mass resolution, incorporated in $\boldsymbol{\theta}_c^{shape}$, were considered: the constant term in the ECAL energy resolution in Eq. (3.5), as evaluated using $Z \rightarrow e^+e^-$ events, amounting to 1% in the barrel, and from 1.2% to 2.1% in the end-caps, was varied within uncertainties as given in Ref. [140], and lead to an overall uncertainty on the mass resolution of 12%. The lack of knowledge about how well the properties of electrons can be extrapolated to those of photons, leads to 6% uncertainty on the mass resolution, whereas the effect from pile-up on the energy resolution is found to worsen the resolution by 3%.[4] The systematic uncertainty from the primary vertex selection is found to be negligible; smaller than 0.2%. This lead to an overall uncertainty on the mass resolution of nearly 14%. The uncertainty on the signal mass position, due to uncertainty on the photon energy scale, was estimated to be 0.5%.[5]

The unconstrained background normalization and shape nuisance parameters, N_{bkg} and $\boldsymbol{\theta}^{bkg}$, are taken from the fit to data. For a closer description of the background parametrization, the remaining systematic uncertainty described by the spurious signal term and its constraint values $\sigma_{spurious,c}$, see Section 8.3. In particular

[3] The numbers quoted in Refs. [138, 139] are the difference between the two samples normalized to the nominal sample, whereas the numbers quoted in Table 8.1, consistent with Refs. [105, 127], are simply the differences between the two samples.

[4] This number, correctly reported in Ref. [138], is erroneously reported to be 4% in Refs. [105, 127].

[5] This number is erroneously reported to be 0.6% in Refs. [105, 127], and not directly reported elsewhere.

Table 8.8 shows the chosen background parametrizations in grey for the different categories. For more detailed information about the systematic uncertainties and the implementation of these, see Refs. [138, 139, 141]. A summary of the systematic uncertainties can be seen in Table 8.1. Including all these gives 60 nuisance parameters for the signal+background model, and the one parameter of interest: the signal strength, μ.

8.2 The Signal Model

We will now turn to the description of a hypothesized $\mathrm{H} \to \gamma\gamma$ signal. The signal description consisted of a sum of a Crystal Ball function (CB) [142–144] and a wide Gaussian (G) with a small amplitude – the latter to model the outliers of the signal distribution at the high-mass end of the fitted range. The Crystal Ball function was adopted to account for the sizable low-mass tail, coming from photon energy losses before the electromagnetic calorimeter, which does not follow a Gaussian form. This function of the invariant mass of the diphoton pair reads

$$CB(t) = N_s \cdot \begin{cases} e^{-t^2/2} & \text{for } t > -\alpha, \\ \left(\frac{n}{|\alpha|}\right)^n \cdot \left(\frac{n}{|\alpha|} - |\alpha| - t\right)^{-n} \cdot e^{-|\alpha|^2/2} & \text{otherwise} \end{cases} \tag{8.15}$$

where $t = \frac{m_{\gamma\gamma} - m_{\mathrm{CB}}}{\sigma}$. In case of a binned fit, the bin width, $\Delta m_{\gamma\gamma}$, was multiplied to the function. The parameters to be fitted were $N_s, m_{\mathrm{CB}}, \sigma, n$ and α. Here, N_s represents the normalization parameter, m_{CB} is the mean of the distribution (the mass of the SM Higgs boson), σ is the diphoton invariant mass resolution (a function of the mass), α indicates where the transition from a Gaussian distribution to a non-Gaussian tail is and n impacts how broad the non-Gaussian tail is.

The parameters of the Crystal Ball function will in the following sections be denoted by a CB-suffix. Instead of fitting the yield, N_s, the fraction of events belonging to the Crystal Ball function, f_{CB}, was used. Thus, the full signal function reads

$$f_{CB}\, CB(m_{\gamma\gamma}, m_{\mathrm{CB}}, \alpha_{CB}, n_{CB}, \sigma_{CB}, f_{CB}) + (1 - f_{CB})\, G(m_{\gamma\gamma}, m_{\mathrm{G}}, \sigma_G)\ . \tag{8.16}$$

In the framework of HSG1, the simulated signal invariant mass resolution was found to develop smoothly as a function of the Higgs boson mass. This involves the parameters of the function describing the signal also evolving rather continuously as a function of m_{H}. Taking advantage of this, all simulated mass-points (eleven in total; from 110 GeV to 150 GeV in steps of 5 GeV) and categories were fitted simultaneously in a *global fit*. The continuous development made it possible

Systematic	Value[%]			Constraint form
Signal event yield				
Theory		Scale		
	ggH: $^{+11.9}_{-7.9}$		VBF: $^{+0.3}_{-0.4}$	Asymmetric
	WH: $^{+0.7}_{-0.4}$	ZH: $^{+1.5}_{-1.2}$	ttH: $^{+3.4}_{-9.4}$	Log-normal
		PDF+α_s		
	ggH: $^{+7.8}_{-7.2}$		VBF: $^{+2.4}_{-2.1}$	Asymmetric
	WH: $\pm$3.4	ZH: $\pm$3.5	ttH: $\pm$8.4	Log-normal
		BR: $\pm$5		Log-normal
Luminosity		$\pm$3.9		Log-normal
Efficiency		$\pm$8.5		Log-normal
Photon isolation		$\pm$0.4		Log-normal
Pile-up (photon-ID)		$\pm$4		Gaussian
Photon energy scale		$\pm$0.3		Log-normal
Signal category migration				
Pile-up mismodeling	Unconv: $\pm$3		Conv: $\mp$2	Log-normal
Material mismodeling	Unconv: $\pm$4.0		Conv: $\mp$3.5	Gaussian
Higgs p_T modeling	Low p_{Tt} : $\pm$1.1		High p_{Tt} : $\mp$12.5	Gaussian
Photon energy scale		negligible		
Signal mass resolution				
ECAL energy resolution		$\pm$12		Log-normal
$e \to \gamma$ extrapolation		$\pm$6		Log-normal
Pile-up (σ_E/E)		$\pm$3		Log-normal
Primary vertex		negligible		
Signal mass position				
Photon energy scale		$\pm$0.5		Gaussian
Background modeling				
Spurious signal		CP1 $\pm$2.1 events		Gaussian
		CP2 $\pm$0.2 events		
		CP3 $\pm$2.2 events		
		CP4 $\pm$0.5 events		
		CP5 $\pm$1.6 events		
		CP6 $\pm$0.3 events		
		CP7 $\pm$4.6 events		
		CP8 $\pm$0.5 events		
		CP9 $\pm$3.2 events		

Table 8.1: Summary of systematic uncertainties [105, 138, 141]. See the text for details.

to smoothly interpolate between the simulated mass-points. Some parameters were seen to have a linear dependence on the mass, namely the parameters: $m_{\mathrm{CB}}, \sigma_{CB}, \alpha_{CB}$. The linear trend was exploited in the fit, *e.g.* in m_{CB}, through the relation

$$m_{\mathrm{CB}} = m_{\mathrm{H}} + \delta^{125} + \Delta_m \cdot (m_{\mathrm{H}} - 125) \ , \tag{8.17}$$

where Δ_m was the fitted parameter and δ^{125} was the offset of the distribution from a mean value of the Higgs boson mass to be tested. This offset was taken at $m_{\mathrm{H}} = 125$ GeV, and assumed to be similar for all other masses. Similar relations were used for σ_{CB} and α_{CB};

$$\sigma_{CB} = \sigma^{125} + \Delta_\sigma \cdot (m_{\mathrm{H}} - 125) \ , \tag{8.18}$$

$$\alpha_{CB} = \alpha^{125} + \Delta_\alpha \cdot (m_{\mathrm{H}} - 125) \ . \tag{8.19}$$

The goal of these linear functions was to map the distributions of all different mass points to one that would be similar for the various masses, so that this one distribution could be fitted. In the following paragraphs, we will appreciate the train of thoughts. First, the distribution is centered around origo, taking into account that the mean of the distribution is slightly displaced from the true value of the Higgs boson mass,

$$m'_{\gamma\gamma} = m_{\gamma\gamma} - m_{\mathrm{H}} - \delta^{125} \ . \tag{8.20}$$

If tested at $m_{\mathrm{H}} = 125$ GeV, this would correctly place the distribution of $m_{\mathrm{H}} = 125$ GeV close to $m'_{\gamma\gamma} = 0$, but the other mass point distributions would be displaced to either side. Thus, the invariant mass is further corrected, for the mass difference to 125 GeV, to map the different masses onto the same distribution. However, how large the effect of this mass shift is, is allowed to vary from mass to mass, represented by the variable Δ_m:

$$m''_{\gamma\gamma} = m'_{\gamma\gamma} - \Delta_m \cdot (m_{\mathrm{H}} - 125) \ . \tag{8.21}$$

Furthermore, it needs to be taken into account that the resolution of the invariant mass distribution at the various masses differs. Adjusting also for the difference in widths provides

$$t = \frac{m'_{\gamma\gamma}}{\sigma'} \ , \tag{8.22}$$

where σ' is according to Eq. (8.18). At this stage, the variable t, as fitted in Eq. (8.15) has been reached. Still, the differences in the non-Gaussian tail of

m_{H}	110 GeV		125 GeV		150 GeV	
Analysis	Official	Thesis	Official	Thesis	Official	Thesis
α_{CB}	1.28	1.36	1.31 ± 0.0016	1.34 ± 0.36	1.35	1.48
σ_{CB}	1.57 GeV	1.66 GeV	1.73 ± 0.001 GeV	1.77 ± 0.21 GeV	2.00 GeV	2.05 GeV
f_{CB}	96.85 %	98.41 %	96.85 ± 0.025 %	97.26 ± 5.2 %	96.85 %	97.46 %
$\mu_{CB} = \mu_G$	109.6 GeV	109.6 GeV	124.6 GeV	124.6 GeV±0.2	149.5 GeV	149.5 GeV
κ	3.32	4.38	3.32 ± 0.01	3.96 ± 6.14	3.32	4.82

Table 8.2: Parameter values of the Crystal Ball+Gaussian fit, fitting MC signal at $m_{\mathrm{H}} \in \{110, 125, 150\}$ GeV. The results are from a global fitting procedure as in Ref. [138] (official) and from fitting using a non-global approach (thesis). The parameters f_{CB} and κ are global, and have thus the same value for all mass points in the official framework. The errors are only given for $m_{\mathrm{H}} = 125$ GeV, but are comparable at the other mass points.

the distribution at the different mass points needs to be accounted for, as in Eq. (8.19).

The parameters n_{CB} and f_{CB} were found to only mildly depend on the Higgs boson mass. While $n_{CB} = 10$ was fixed for all categories and mass points, f_{CB} was fitted in the categories as a single, global value for all mass points. It varied for the different categories and ranged from $f_{CB} = 88.6\%$ (CP9) to $f_{CB} = 99.7\%$ (CP2/CP5).

For the outlier function (the Gaussian), the mean was constrained to be equal to the mean of the Crystal Ball function; $m_{\mathrm{G}} = m_{\mathrm{CB}}$, and the width was parametrized as $\sigma_G = \kappa\,\sigma_{CB}$, with a single, fitted κ per category, valid for all mass points. Thus, in a single fit to the available MC samples, 8 parameters per category are extracted (three shape parameters with linear dependence on the Higgs boson mass, with 3 corresponding offsets and 2 global parameters). Due to limitations in time, such a global fitting procedure was not feasible to implement for this thesis, but I did check the signal model fit to separate mass points.

In Table 8.2, both the result from the official, global fitting procedure, and the result with the non-global fitting approach used for this thesis can be seen, for masses $m_{\mathrm{H}} \in \{110, 125, 150\}$ GeV. The results are statistically in agreement. The uncertainties for the other mass points than the default $m_{\mathrm{H}} = 125$ GeV are not stated, but comparable. Naturally, the uncertainties of the global fit are much smaller than the fit only performed at one mass point, due to a much larger sample. The fit to the simulated sample for $m_{\mathrm{H}} = 125$ GeV can be seen in Fig. 8.4, clearly displaying the non-Gaussian low-mass tail of the Crystal Ball function at the low end and the broad, low amplitude Gaussian at the high end. In Fig. 8.5, an official signal model fit to a simulated $\mathrm{H} \to \gamma\gamma$ signal with $m_{\mathrm{H}} = 120$ GeV can be seen.

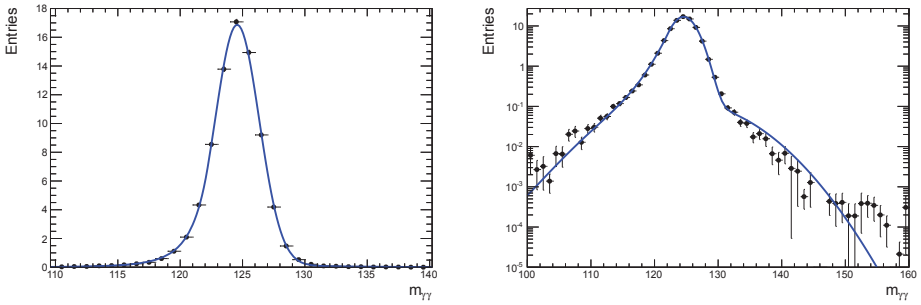

Figure 8.4: The inclusive invariant mass distribution of a simulated H $\rightarrow \gamma\gamma$ signal with $m_{\mathrm{H}} = 125$ GeV, superimposed with a Crystal Ball + Gaussian fit as described in the text. The plot is displayed on a non-logarithmic scale to the left, and on a logarithmic scale to the right. The parameters of the fit can be seen in Table 8.2.

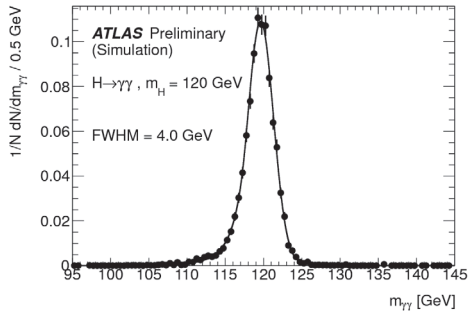

Figure 8.5: The inclusive invariant mass distribution of a simulated H $\rightarrow \gamma\gamma$ signal $m_{\mathrm{H}} = 120$ GeV, superimposed with a simultaneous fit to all mass points. The width of the Crystal Ball function is 1.7 GeV, and the FWHM is 4.0 GeV [95].

Fig. 8.6 shows a Crystal Ball + Gaussian fit of a $m_{\mathrm{H}} = 125$ GeV signal, both for standard and variable $\mathrm{p_T}$ cuts, in each of the categories. The respective widths of the distributions, both in σ_{CB} and the Full Width at Half Max (FWHM) are given in Table 8.3. The distributions for variable $\mathrm{p_T}$ cuts seem to have slightly smaller widths. A good resolution is preferred in order to have better sensitivity for a given category. For a summary of the signal and background characteristics, detailed in the categories, see Section 8.4.

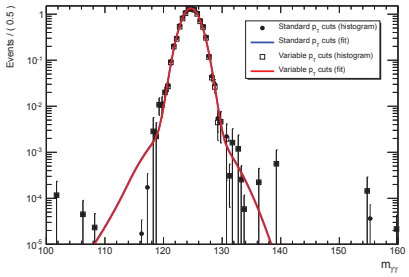

(a) CP1

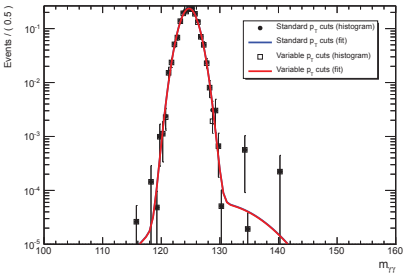

(b) CP2

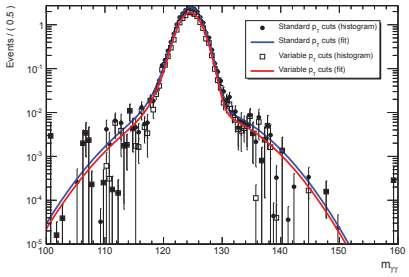

(c) CP3

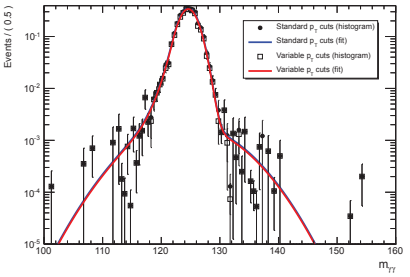

(d) CP4

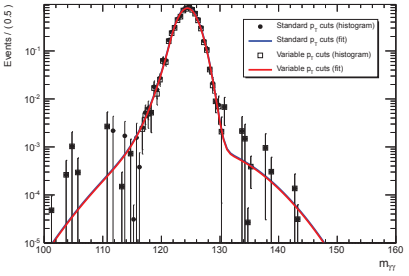

(e) CP5

Figure 8.6: Invariant mass distributions of the first five of the nine categories, for Monte Carlo simulation of $m_{\mathrm{H}} = 125$ GeV corresponding to 4.9 fb^{-1}, fitted with a Crystal Ball + Gaussian, using standard $\mathrm{p_T}$ cuts of $\mathrm{p_T^{\gamma_{leading}}} > 40$ GeV and $\mathrm{p_T^{\gamma_{subleading}}} > 25$ GeV (full circles) and variable $\mathrm{p_T}$ cuts of $\mathrm{p_T^{\gamma_{leading}}} > \frac{m_{\gamma\gamma}}{2.5}$ GeV and $\mathrm{p_T^{\gamma_{subleading}}} > \frac{m_{\gamma\gamma}}{3.4}$ GeV (open squares). The widths of the distributions are given in Table 8.3. The figure continues on page 141.

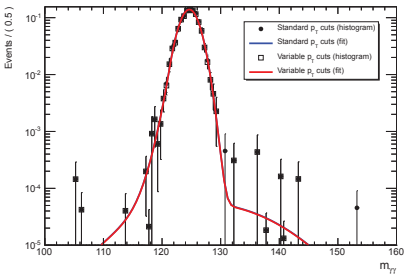

(a) CP6

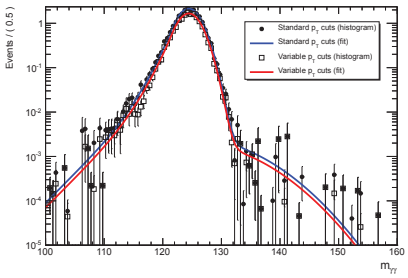

(b) CP7

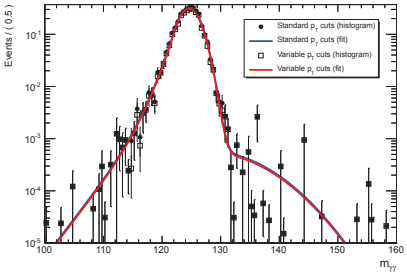

(c) CP8

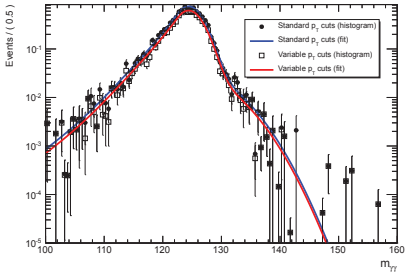

(d) CP9

Figure 8.6: (continued figure) Invariant mass distributions of the last four of the nine categories, for Monte Carlo simulation of $m_{\mathrm{H}} = 125$ GeV corresponding to 4.9 fb^{-1}, fitted with a Crystal Ball + Gaussian, using standard $\mathrm{p_T}$ cuts of $\mathrm{p_T^{\gamma_{leading}}} > 40$ GeV and $\mathrm{p_T^{\gamma_{subleading}}} > 25$ GeV (full circles) and variable $\mathrm{p_T}$ cuts of $\mathrm{p_T^{\gamma_{leading}}} > \frac{m_{\gamma\gamma}}{2.5}$ GeV and $\mathrm{p_T^{\gamma_{subleading}}} > \frac{m_{\gamma\gamma}}{3.4}$ GeV (open squares). The widths of the distributions are given in Table 8.3.

Category	Standard p_T cuts		Variable p_T cuts	
	σ_{CB}	FWHM	σ_{CB}	FWHM
CP1	1.44	3.40	1.44	3.39
CP2	1.39	3.27	1.39	3.27
CP3	1.71	4.05	1.71	4.05
CP4	1.57	3.72	1.56	3.69
CP5	1.64	3.87	1.64	3.86
CP6	1.55	3.66	1.55	3.64
CP7	1.99	4.70	1.97	4.63
CP8	1.75	4.13	1.74	4.11
CP9	2.24	5.56	2.22	5.49

Table 8.3: Widths of the Crystal Ball + Gaussian fits in Fig. 8.6, given in σ_{CB} and FWHM both for standard and variable p_T cuts, for each of the nine categories.

8.3 The Background Model

Even though the background to the $H \to \gamma\gamma$ search has a smooth shape and is well populated, it is a delicate matter to get a sufficiently good description of it. Even small systematic deviations from the true background shape to the model used to describe it can have a large impact on the observed signal, due to the tiny signal-to-background ratio. For the PRL paper published on the 2011 data, the simple exponential function was used for all categories. For larger data samples, this had to be revised. In order to stay unaffected by what the new data might contain, a group decision was made to stay "blind" – that is; not to look at the data, until which background model to use for the different categories was decided. Making a choice of background models before looking at the 2012 data was a major effort of HSG1 during Spring 2012, an effort to which I contributed. The decision was based on simulations of the 2011 data. With this blinded approach, it was assured that the choice of background models was based on fair criteria – expectations obtained from studies of Monte Carlo samples – and not (even subconsciously) influenced by Higgs hunters' hopes for what the data might contain. The unblinding of the 2012 data took place the 31st of May 2012.

The aim was to find parametrized functions describing the background distributions. These parametrized functions should have enough flexibility to accurately describe the background, but with as few degrees of freedom as possible, to ensure sensitivity to a signal. Once the function was decided, the actual background was taken purely from data; the fit was left unconstrained in the likelihood. This data-

driven approach reduces the uncertainty from using event generators and detector simulations of backgrounds with very large rejection factors and large theoretical uncertainties.

As already mentioned, in the $H \to \gamma\gamma$ channel, the signal is a small resonance on top of a big background. Using a background model that does not properly describe the background, has an unfortunate effect on the ability to make a discovery or exclusion. The worry was to give a false statement about seeing, or not seeing, a signal. If the true background at some mass point were in reality larger than the assumed background, too much observed signal would be claimed. On the other hand, if the true background were in reality smaller than the assumed background, an overly strong exclusion would be stated; one would claim to see less signal than there in reality was. Even small differences in the assumed and the true background shape could have a dramatic impact.

This additional or subtractive false signal was called *spurious signal*, and a corresponding term in the likelihood was introduced to accommodate for the uncertainty on the background knowledge. An illustration of the spurious signal arising from an incorrect background description can be seen in Fig. 8.7. For this illustrative example, it can be appreciated that where the background model undershoots the true distribution (in the middle of the figure), one would assume to have too much signal: the contribution from the true background distribution above the background model is taken as signal events. To each of the sides, the opposite effect occurs; the background model overshoots the true background distribution, and one would believe to see less signal than there in reality is: some of the signal would be taken as background (the signal needed to add to the real background distribution in order to reach up to the background model).

The implementation of the spurious signal is further explained in Section 8.3.2. The goal was to find a parametrization in which the spurious signal had an acceptable size. This meant that the spurious signal should not be larger than *either* 10% of the expected signal *or* 20% of the background uncertainty at 10 fb^{-1} for the background model to be accepted as unbiased. Since the scenario of a positive bias is the most threatening, meaning that more signal is thought to be seen than there is in reality, leading to an overly optimistic discovery (or pessimistic exclusion), this case will be addressed in more detail in Section 8.3.4.

In the following, when referring to "background model", the full background model is meant. This includes both the spurious signal term and the *basic* background model, which is the part of the background model before the spurious signal term is added, simple functions like exponentials and polynomials.

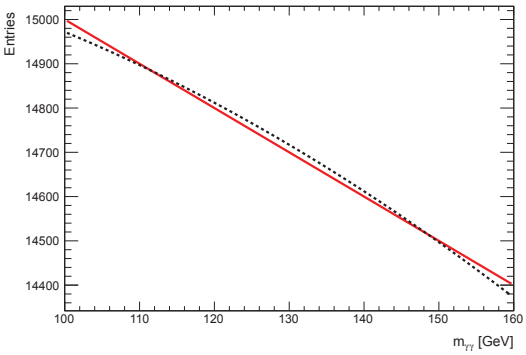

Figure 8.7: Illustration of the *spurious signal* arising from an incorrect background description. The true background distribution, indicated by the dashed line, is not properly described by the fitted background parametrization, indicated by the full line. In this case, it would lead to an overestimation of the observed signal in the middle of the mass range, and an underestimation of the observed signal at both ends of the mass range.

8.3.1 Monte Carlo Samples for Background Modeling

The samples of MC that were available for these studies were all based on fast simulation[6] produced by the HSG1 group – having sufficient statistics to study the potential bias in full simulation was simply unfeasible. This infeasibility was due to the high rejection of jets faking photons, and the staggering number of jet events that are produced by the LHC. Taking these two effects into account, one would have to simulate an enormous number of events to keep even one that contained one (or two) jet(s) passing the photon requirements. Thus, the fully simulated sample would have a larger statistical uncertainty than the data, due to the large weights the few events passing the requirements would have to be assigned, to be scaled up to the respective cross-section.

The simulation of the true diphoton part of the background spectrum was done using DIPHOX [97, 145], ResBos [96, 146] and Sherpa [129, 147]. For the DIPHOX sample, 8 billion events in total were generated, with a minimum p_T of 25 GeV for both photons, in the diphoton mass range 80 – 180 GeV – 6 billion for the direct process, 2 billion for each of the one and two fragmentation processes, in which one (or both, for the two fragmentation process) photon(s) is radiated off a directly produced quark. This resulted in about 2.6 billion events for the standard p_T cuts in the relevant fitted mass range 100 – 160 GeV. For the ResBos sample, 9 billion events were generated in the mass range 80 - 200 GeV, resulting in about 4.8 billion events in the relevant mass range of 100 – 160 GeV. For the Sherpa sample, 16 million $\gamma\gamma$ events and 4 million γ-jet events remained in the mass range 100 – 160 GeV after selection and efficiency corrections, described below, had been made. For the jet-jet component, officially produced (full) simulation samples were

[6] Fast simulation, as explained in Section 3.4, means simulation stopping at the generator level (EVGEN).

used, leaving 1.8 million events in the relevant mass range.

To all three sets of generated diphoton events, contributions to the spectrum from Drell-Yan, γ-jet and jet-jet processes were added. Whenever it is referred to DIPHOX+ , ResBos+ or Sherpa+, the full set of reducible and irreducible backgrounds are meant. The Drell-Yan contribution was estimated using a data-driven technique as explained in Section 7.2.5. While the inclusive estimation was done in a fully data-driven manner, because of lack of statistics, the fraction of DY in each of the categories was estimated from a simulated sample of $Z \to e^+e^-$ events. The γ-jet contribution was estimated using the Sherpa generator and the jet-jet component using Pythia [80]. The normalization of the background components were adjusted such that the total background consisted of 77.1% $\gamma\gamma$ (including DY), 21.3% γ-jet and 1.6% jet-jet, where the fractions were obtained from data-driven estimates using the 2D isolation template fit method at the time of the internal production.

Neglecting detector effects in fast simulation is bound to degrade the level at which it represents the real data. Some corrections were made in order to produce a more realistic background sample, within the strict frame of time (the background model decision had to be taken such that time was left to analyse the data before the ICHEP conference). In particular, for all samples, a correction of the photon identification efficiency as a function of p_T and $|\eta|$ was performed. For the Sherpa+ sample, additional detector effects were taken into account: an event-weighting based on photon isolation as a function of energy, location in the detector and conversion status was applied; $\epsilon(p_{T\,lead}, \eta_{lead}, conv_{lead}) \cdot \epsilon(p_{T\,sublead}, \eta_{sublead}, conv_{sublead})$. Furthermore, a smearing of the photon energy was performed, according to distributions of the ratio of the true energy to the reconstructed energy, also in $(p_T, \eta, conv)$-bins. The γ-jet and dijet samples were scaled with the rate of jets faking photons to estimate the number of such events passing the selection criteria. The p_T of the jets was adjusted by taking into account the effect of miscalibration when considering the jet to be a photon. For more information about the fast MC simulation samples, see Ref. [141].

8.3.2 The Implementation of a 'Spurious Signal'

Because of the limitations of MC background simulation, not to mention the limited statistics in the data, we could never be sure what the Standard Model background in reality looked like. This problematic fact is at the heart of the discussion to follow. The lack of certain knowledge about the background had to be transferred into the results – how certain we were about the correctness of the

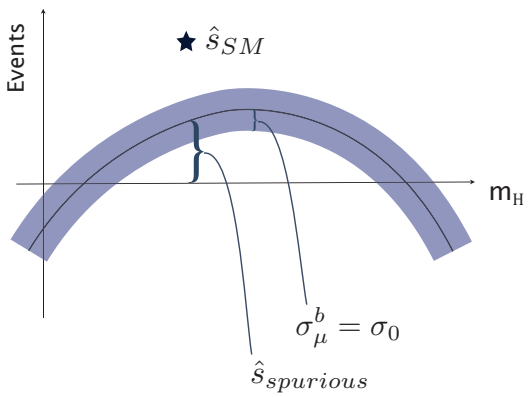

Figure 8.8: Illustration of the background+signal fit to the background-only MC sample, indicating a bias (a slowly evolving trend deviating from zero discrepancy) in the background modeling. The star indicates the expected number of signal events from a SM Higgs at some specific m_H, $\hat{s}_{spurious}$ illustrates how many events are due to the incorrect modeling of the background and σ_0 is the uncertainty on the background+signal fit predicted for the statistics in data (assuming no signal).

background description had to affect how strong statements could be made about what signal was seen, or not seen. Most of the shape uncertainty was accounted for in the statistical uncertainty on the basic background nuisance parameters. Thus, the estimation of the background normalization and shape was data-driven. The residual uncertainty was covered by the spurious signal: the uncertainty on the background, described as a spurious signal, was implemented as an exact copy of the signal model added to the likelihood function (see Eq. 8.12). All parameters of this spurious signal term were fixed to the signal model for each evaluated mass point, except the amplitude. The size of the constraint on the spurious signal amplitude in the limit procedure was taken from fits to the fast MC simulations previously described. This constraint value will in the following be called the spurious signal.

For evaluating the spurious signal, the sum of the background and spurious signal models was fitted to the background-only MC sample. The fitted spurious signal amplitude indicates the residual of the description of the background to the sample at hand. This amplitude *is* the spurious signal. In Fig. 8.8, an illustration is given of how such a fit could look, for the case that the background model does not to a satisfactory degree describe the background sample.

The largest absolute deviation of the fit in the mass range 110 – 150 GeV was used to set the Gaussian constraint value, $\sigma_{spurious}$. This turned out to be found in the Sherpa+ sample. This maximum deviation was taken to be a 1σ deviation (as already mentioned, the constraint value represents 1σ for all constrained nuisance parameters). In reality, what order of magnitude this largest discrepancy represented was not known, but calling it 1σ instead of for instance 3σ was the more conservative approach, and hence was the approach chosen. This discrepancy

was implemented as a systematic uncertainty, and was constrained in the fit to data.

The spurious signal can be looked upon as an uncertainty on the signal, instead of as an uncertainty on the background, because it has the same shape as the signal. There is no reason to believe that a deviation from a given background model would have the exact shape of a signal – there are no physical processes, except the signal, that give a peak in an otherwise smoothly falling distribution. Thus, this approach of accommodating an uncertainty on the background parametrization can be looked upon as a 'worst case scenario', and is an attempt at being conservative when trying to discover a signal. However, it has been shown that the way the spurious signal was implemented in the limit setting machinery of HSG1, that is, as a systematic uncertainty, was *not* recovering a bias of the size of the constraint, should it really be there. This can also be suspected from the fact that doubling the size of the spurious signal in the limit setting procedure had next to no impact on the result, as shown in Ref. [100]. If there *were* a true bias, the approach of treating the discrepancy as an uncertainty would not be sufficient to reach an unbiased significance – a correction would be needed. This is studied in more detail in Section 8.3.4.

The spurious signal term contributes both to the conditional background-only ($\mu = 0$) and the conditional signal+background ($\mu \neq 0$) maximum likelihood fits. It is thus neither solely part of the background modeling, nor only part of the signal modeling. In the unconditional fit ($\mu = \hat{\mu}$), on the other hand, an excess will be completely described by the Higgs boson signal model; that does not cost anything in the likelihood function, whereas allowing the spurious signal to accommodate some of the excess has a penalty. In Fig. 8.9, the unconstrained signal+background and the (constrained) background-only fits under the presence of a signal are illustrated. In the latter, the effect of the spurious signal can be appreciated, trying to accommodate some of the excess. If there were no spurious signal term, the (flat) background fit would be pulled up even higher across the invariant mass spectrum, balancing between the data points in the sideband and those of the signal.

Fitting a possible signal-like excess or deviation from the assumed background model with and without constraint is crucial for the outcome. Without the constraint on the spurious signal, as given from the largest discrepancy seen in the MC studies, any excess would be fully eaten up by the spurious term. This is of course very undesirable for the ability to make a discovery. The uncertainty on the background description should be accommodated for in such a manner that one believes to give enough flexibility for the real discrepancy of the background from the model to be accounted for, while still keeping some statistical power

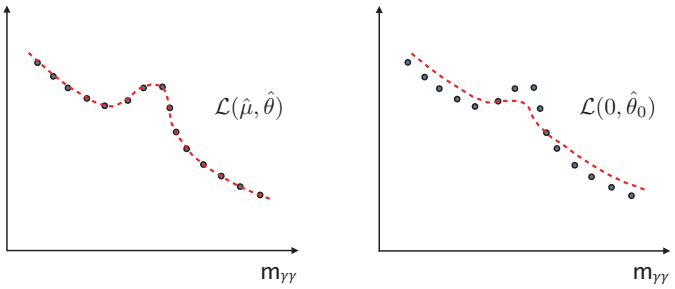

Figure 8.9: Illustration of the unconditional fit to the left, close to perfectly accommodating the data-points, and the conditional background fit to the right, where the signal strength is set to zero. The effect of the constrained spurious signal term included in the likelihood function can be seen – in which there is a compromise between moving away from the data-points in the sideband and fitting the excess. The effect is exaggerated for the purpose of illustration.

for a true signal. The number of parameters in the background function has a tight correlation with the statistical power of the model, because having more free parameters in the fit increases the statistical uncertainty. Given an excess in data, when having a function with too many degrees of freedom – allowing the background to be flexible enough to take a shape similar to a resonance – too much of the signal would be eaten up by the background model. Using a function with too few degrees of freedom could lead to an underestimation of how many events belong to the background, and thus an exaggerated statement about the significance of the observation. The balance between these two effects is what was the concern in the procedure of defining the background function, having the optimal compromise the final aim.

8.3.3 The Selection Criteria for Background Models

To evaluate whether a background model should be considered as unbiased or not, a limit for the spurious signal had to be decided. As a quantification of how small the deviation should be, the HSG1 group adopted this requirement for 10 fb^{-1}:

The spurious signal should not be larger than *either*

- 10% of the expected signal
  or
- 20% of the background uncertainty.

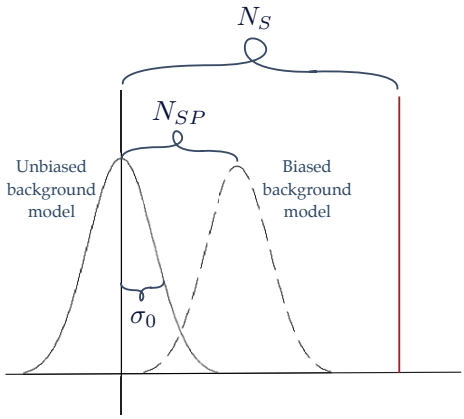

Figure 8.10: Illustration of the effect that using a biased background model, while believing one uses an unbiased model, can have. The graphs illustrate the fitted spurious signal, N_{SP}; the spread indicates the uncertainty on the fitted spurious signal (in the background-only case, this is σ_0). It can be appreciated that the integral of the tail above the expected number of signal events, N_S, is smaller for the (assumed) unbiased model, than for the biased one – thus, the p_0 is more extreme than it should have been.

This was called 'Criterion A' – passing either the signal, or the background requirement, led to the model passing Criterion A. As this was not always sufficient to assure a non-biased background parametrization, a second, qualitative, criterion B was introduced. This criterion stated that if, even after Criterion A was satisfied, there still was a clear trend of the spurious signal in all MC samples, indicating that there still existed a real bias, the model should also be discarded.

If there were evidence for such a clear bias, the model was rejected. Also, stability of the fit was demanded, where "stability" means that 100% of the fits to several hundred MC toys converged with good accuracy.

8.3.4 Accommodating for the Effect of a Bias

Making an unrealistically strong statement about seeing a signal was, as already mentioned, the biggest worry of the group. In this scenario, there is a positive bias of the background description; the true background is larger than the one modelled. From the scheme displayed in Fig. 8.10, it can be appreciated that having a positive bias will lead to a smaller integral in the tail beyond the observed number of events, N_S, for the unbiased model that is assumed, than for the biased model that one in reality has. Thus, the p_0 will be unrealistically extreme (small), leading to an unrealistically large significance for the observation. Such over-optimistic statements about what is observed is something that by all means should be avoided.

One way to compensate for such an unfortunate effect could be to smear the unbiased background model which is applied, to match the integral with the biased

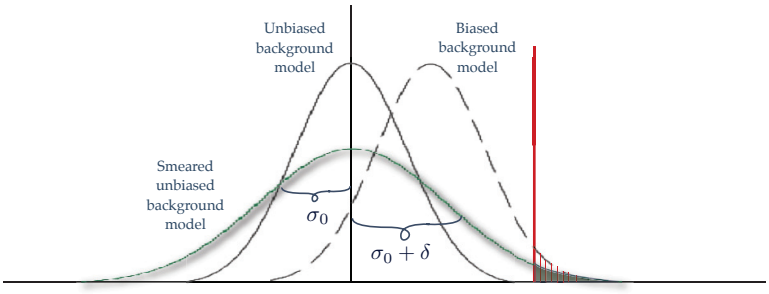

Figure 8.11: Illustration of one possibility to compensate, for a certain number of signal events only, for a biased description. Note that the integrals of the tails of the unbiased, smeared distribution (diffuse, full graph) and the biased distribution (dashed graph) are only the same at the point of the vertical line to the right (by construction).

background model at a certain number of observed events. One choice of such a point could be the median expected number of signal events. To retrieve the unbiased significance, as given by the right hand-side of Eq. (8.23), the uncertainty on the unbiased background model would need to be increased by δ, as given in Eq. (8.24).

$$\frac{\hat{s}_{SM} + \hat{s}_{spurious}}{\sqrt{{\sigma_0}^2 + \delta^2}} = \frac{\hat{s}_{SM}}{\sigma_0} \tag{8.23}$$

$$\delta = \sigma_0 \sqrt{\left(1 + \frac{\hat{s}_{spurious}}{\hat{s}_{SM}}\right)^2 - 1} \tag{8.24}$$

The corresponding schematic picture of what this approach implies can be seen in Fig. 8.11. The compensation of a biased description by smearing the background is conservative above the point at which the smeared and the biased background descriptions are matched; the thick, vertical line to the right in the figure. Below, on the other hand, is it aggressive: it does not compensate enough, and gives a smaller p_0 than the biased (true) model. That being said, the smeared unbiased model is less aggressive than the unsmeared (applied) unbiased model.

However, if one is convinced that there really *is* a bias in the background model being used, the bias should be reduced properly, by correcting for the bias. One way of correcting for the bias is simply to change the background model to one that

displays an acceptable level of deviation from the background-only MC sample. 'Acceptable' means that the deviation can be believed to be an uncertainty, and not a real bias: the size of the deviation should be small with respect to the statistical uncertainty on the amplitude fitted to the data (the opposite of what is illustrated in Fig. 8.10, which is exaggerated for the purpose of illustration).

8.3.5 The Background Parametrizations

The spurious signal was evaluated using different background parametrizations. Many functions were proposed to serve as such background models, but due to fit instabilities, were many of these rejected. For instance, the double exponential $(n_1 e^{-\beta_1 m_{\gamma\gamma}} + n_2 e^{-\beta_2 m_{\gamma\gamma}})$, as well as the exponential to the power of a third degree polynomial and functions with a turn-on at the low end of the invariant mass spectrum were found to be unstable. The exponential function, the exponentiated second degree polynomial and the Bernstein polynomials [148] were found to be stable in the fits and thus used for evaluation of the spurious signal. The decision to not consider the exponentiated third degree polynomial was taken after the studies presented here were performed – we did not see instabilities with this function (using a different framework than the rest of the group) and reported our findings, as given here, in Ref. [141]. The functional forms are:

- the exponential function

$$N e^{-\beta m_{\gamma\gamma}} \ , \tag{8.25}$$

  where N and β were the fitted parameters – the normalization and slope of the exponential, respectively;

- the exponential polynomial of order n (orders 2 and 3 were used)

$$e^{\sum_{i=0}^{n} \beta_i m_{\gamma\gamma}^i} \ , \tag{8.26}$$

  where β_i were the fitted parameters. Note that the latter i is the power $m_{\gamma\gamma}$ is raised to. The normalization, N, is described by the first term, e^{β_0};

- the Bernstein polynomial of order n (orders 3 – 7 were used)

$$b_n(t) = \sum_{i=0}^{n} \beta_i \binom{n}{i} t^i (1-t)^{n-i} \ , \tag{8.27}$$

where $t = \frac{m_{\gamma\gamma}[GeV]-100}{60}$, and where β_i were fitted parameters.

The exponential function will in the following sections sometimes be aliased by "exp" or "expDist", exponential polynomials by "epoly$N$" and Bernstein polynomials by "bern$N$", where N is a number indicating the order.

8.3.6 Study of the Spurious Signal

The bias performance of the background models presented in the previous section was tested on the DIPHOX+, ResBos+ and Sherpa+ MC samples described in Section 8.3.1. The signal model is the one described in Section 8.2. For the results in this section, the TF1 class of Root was used, providing a simple access to the Minuit minimization and fitting package. Minuit is what is working behind the scenes for the RooFit and RooStats classes, which were used for the other background bias studies performed by HSG1.

Binned fits were made, which for most of the categories does not pose problems due to the high statistics. The base results were obtained using an Asimov dataset of the high-statistics Monte Carlo samples, *i.e.* replacing the errors of the MC histograms with the statistical uncertainties corresponding to the number of entries per bin normalized to the luminosity being tested. For the high-statistics Monte Carlo samples, chi-squared fits were performed, whereas for the cross-checks using toys, log-likelihood fits were used.

The spurious signal was evaluated in the nine categories already presented. In Fig. 8.12, an illustrative sketch can be seen, explaining the elements of the (rather busy) plots that illustrate the results of the background bias study as a function of the diphoton invariant mass, $m_{\gamma\gamma}$, for the residuals, or as a function of the hypothesized Higgs boson invariant mass, m_{H}, for remaining entries. The elements of the plot are the following:

- ⋆ The black, thin histogram is the residual between the high-statistics MC sample and the background-only fit, $\mathrm{fit_b}$. This residual is nearly impossible to see: due to the fine binning, this line wiggles with a very low amplitude around the line indicating zero events.
- ⋆ This same residual, integrated in 10 GeV bins, can be seen as a red, thicker histogram. Earlier studies showed this was a rough estimate of the spurious signal amplitude.
- ⋆ The fitted spurious signal amplitude to the MC sample is shown in dark blue points. The error bars on these points are too small to see.
- ⋆ In smaller black points is the same, only fitted to an Asimov dataset based on the MC sample. The corresponding error bars (grey, filled area) represent

σ_0 ; the expected uncertainty on the fitted amplitude for the data sample. This error on the Asimov dataset representative of the luminosity in question, is comparable to the background taken in a mass window containing 90% of the signal (corresponding to a mass window of roughly ± 4 GeV around the signal mass), B_{sub90}.

- ⋆ $\pm 20\%$ of the error of the Asimov fit (σ_0) is indicated by the green area, which is centered at zero. That the spurious signal amplitude is within this area for the full mass range is part of Criterion A.
- ⋆ The spurious amplitude as found in a fit to toys at that mass point is shown as a big black point, with point error in thick red. For the cross-check of the Asimov results with toys, three mass-points within the search range of 110 – 150 GeV were looked at: the one with the maximal positive spurious signal, the one with the maximum negative spurious signal, and the one with the smallest spurious signal.
- ⋆ The corresponding error bar (the RMS of the amplitude distribution) to the fitted toys is displayed by blue, thin, vertical lines. These should, and do, correspond reasonably well to the Asimov fit errors.
- ⋆ Finally, the dark green lines (here within the green $\pm 20\%\,\sigma_0$ area) indicate $\pm 10\%$ of the expected signal. That the spurious signal amplitude is within these lines for the full mass range is part of Criterion A.

Since deviations from a simple exponential form tend to be small, the candidate parametrizations should all be able to approximate an exponential distribution reasonably well. In Fig. 8.13, the result of fitting the respective functions to an Asimov dataset based on a fitted exponential to the high-statistics MC histogram can be seen. This figure illustrates that, as expected, since the exponential is a subset of the epoly-functions, the exponential of a second order polynomial can perfectly describe the true exponential nature of the sample. While fourth and higher order Bernstein polynomials are good approximations to exponential distributions typical of this search, the third order Bernstein polynomial introduces a clear systematic bias. For this reason the third order Bernstein polynomial was not considered as a candidate even if it technically passed Criterion A.

The performance of the various background functions are compiled in tables showing the results for all three MC samples. In these tables, the maximal absolute spurious amplitude (and at which mass it manifests itself), Max $|N_{SP}|$ (mass[GeV]), is given, as well as the percentage of the expected signal this amounts to (and what the expected signal yield N_S is), $r^S_{SP}[\%]\,(N_S)$, along with the percentage of the background uncertainty it corresponds to (and what σ_0 is), $r^{\sigma_0}_{SP}[\%]\,(\sigma_0)$. In addition, the unbiased significance, $\sigma^{N_S} = \frac{N_S}{\sigma_0}$, and the significance bias due to the spurious term, $\sigma^{N_{SP}} = \frac{N_{SP}}{\sigma_0}$, are stated. Finally, whether Criterion A was passed

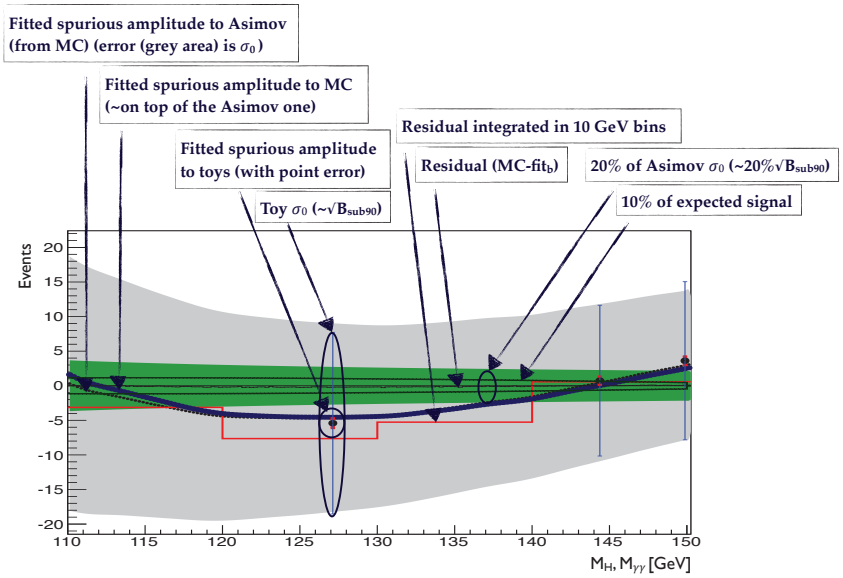

Figure 8.12: Explanation of the entries in the background bias plots. The elements are explained in detail in the text. Please note that, while in the plots to follow, the x-axis is denoted by $M_{\gamma\gamma}$ only, although the residuals are a function of the diphoton mass, while the other variables are a function of the hypothesized Higgs boson mass.

or not is indicated. The background criterion, $N_{SP}(m_H^{\max}) < 20\%\,\sigma_0(m_H^{\max})$ for 10 fb^{-1} is transformed into $\sim 20\%/\sqrt{2} \approx 14\%$ for an integrated luminosity of 4.9 fb^{-1} – the check-mark in this table is evaluated using this latter criterion, since the numbers are compiled for an integrated luminosity of 4.9 fb^{-1}.

An overview over the bias performance of the exponential background function in all three MC samples can be seen in Table 8.4. The visualization of these results can be seen in Fig. 8.14 – in the interest of not using too much space, only for the Sherpa+MC sample. Earlier studies showed that the integrated residual in 10 GeV bins was a rough estimate of the spurious signal amplitude, this is confirmed here. Also for the sake of saving space, the high-p_{Tt} categories (even number categories) are all represented by CP2 in this figure. This is done although the uncertainty (σ_0) varies slightly between the high-p_{Tt} categories, because the others also have a vanishing spurious signal. The high-p_{Tt} categories all pass the background criterion for this baseline background model that was used for the PRL publication. For the other categories, the exponential function has too few degrees of freedom to accommodate the behaviour of the background distributions: it can be seen that the other categories show an unacceptably large spurious signal amplitude (being

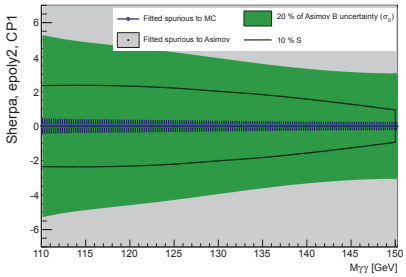

(a) Epoly2

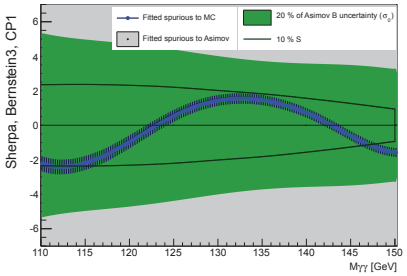

(b) Bern3

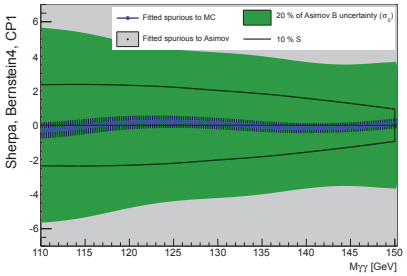

(c) Bern4

Figure 8.13: Illustration of the spurious signal amplitudes produced by the exponential of a second order polynomial, as well as third and fourth order Bernstein polynomial background models when the true distribution is exponential (the distribution is an Asimov dataset based on the result of a simple exponential fit to CP1 in the Sherpa+ sample corresponding to 10 fb^{-1}).

outside the green area of $\pm 20\%\,\sigma_0$). To illustrate the level of consistency between the different MC samples, the performance of the simple exponential for CP1 in all three MC samples is shown in Fig. 8.15.

The performance of the exponential of a second order polynomial background function can be seen in Table 8.5. The high-p_{Tt} categories are naturally also well described by this more advanced function, and in addition, the background distributions of categories CP1, CP5 and CP9 are also satisfactorily described by this background model. Nonetheless, there are still two categories, CP3 and CP7, for which the spurious signal is too large, so an increase in the function complexity is still necessary to describe these.

Exponential						
Category	Max $\lvert N_{SP}\rvert$ (m_H[GeV])	r_{SP}^{S}[%] (N_S)	$r_{SP}^{\sigma_0}$[%] (σ_0)	σ^{N_S}	$\sigma^{N_{SP}}$	Criterion A
DIPHOX+						
CP0	-15 (139)	-25 (60)	-28 (52)	1.2	-0.28	
CP1	-4.6 (127)	-44 (10)	-34 (14)	0.77	-0.34	
CP2	0.11 (112)	6.9 (1.5)	3.2 (3.3)	0.46	0.032	✓
CP3	14 (117)	60 (23)	43 (32)	0.71	0.43	
CP4	0.41 (120)	14 (2.9)	5.6 (7.3)	0.39	0.056	✓
CP5	-4.5 (124)	-65 (7.0)	-34 (13)	0.53	-0.34	
CP6	0.072 (134)	8.3 (0.87)	2.7 (2.7)	0.32	0.027	✓
CP7	13 (119)	59 (22)	35 (38)	0.59	0.35	
CP8	0.91 (127)	33 (2.8)	11 (8.1)	0.34	0.11	✓
CP9	-8.3 (124)	-84 (9.9)	-28 (30)	0.34	-0.28	
ResBos+						
CP0	-20 (130)	-27 (75)	-37 (55)	1.4	-0.37	
CP1	-4.8 (124)	-44 (11)	-34 (14)	0.77	-0.34	
CP2	0.13 (113)	8.3 (1.5)	3.9 (3.3)	0.47	0.039	✓
CP3	11 (116)	49 (23)	34 (33)	0.70	0.34	
CP4	0.67 (131)	25 (2.6)	9.5 (7.0)	0.38	0.095	✓
CP5	-4.8 (124)	-68 (7.0)	-36 (13)	0.53	-0.36	
CP6	-0.079 (130)	-8.4 (0.94)	-2.9 (2.7)	0.35	-0.029	✓
CP7	8.4 (115)	37 (22)	21 (40)	0.55	0.21	
CP8	-0.52 (110)	-20 (2.7)	-5.8 (9.0)	0.30	-0.058	✓
CP9	-12 (124)	-119 (9.9)	-40 (29)	0.34	-0.40	
Sherpa+						
CP0	-21 (134)	-31 (68)	-40 (53)	1.3	-0.40	
CP1	-4.7 (126)	-45 (11)	-35 (14)	0.78	-0.35	
CP2	-0.23 (110)	-15 (1.5)	-6.4 (3.5)	0.43	-0.064	✓
CP3	12 (117)	50 (23)	35 (33)	0.71	0.35	
CP4	0.50 (132)	19 (2.6)	7.2 (6.9)	0.38	0.072	✓
CP5	-4.4 (126)	-64 (6.8)	-34 (13)	0.54	-0.34	
CP6	-0.27 (110)	-27 (0.98)	-8.0 (3.4)	0.29	-0.080	✓
CP7	6.5 (122)	29 (22)	18 (37)	0.60	0.17	
CP8	0.45 (134)	18 (2.5)	5.7 (7.9)	0.32	0.057	✓
CP9	-16 (130)	-179 (9.1)	-59 (28)	0.33	-0.59	

Table 8.4: Overview of the spurious signal performance for the exponential background function using all three MC samples. See the text for explanation of the entries. Results are compiled for an integrated luminosity of 4.9 fb^{-1}.

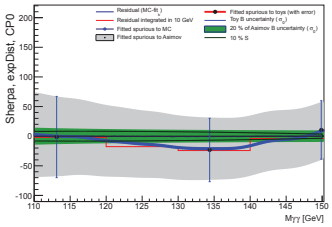

(a) CP0

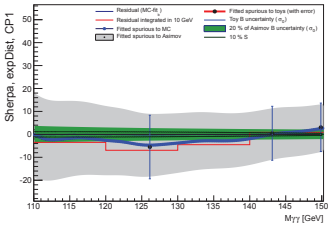

(b) CP1

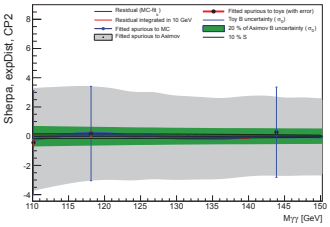

(c) CP2

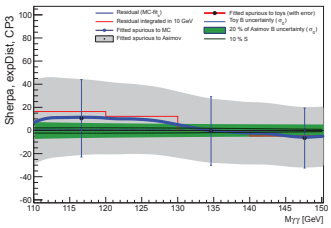

(d) CP3

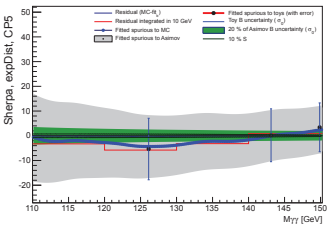

(e) CP5

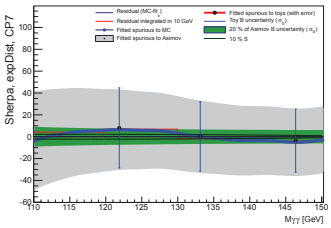

(f) CP7

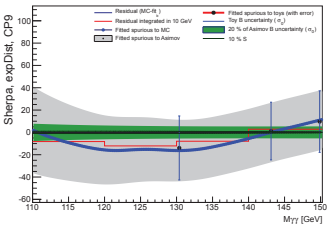

(g) CP9

Figure 8.14: Background bias performance for the exponential function for the categories in the Sherpa+ MC sample, for an integrated luminosity of 4.9 fb^{-1}. The high-p_{Tt} categories are all represented by CP2, as the other categories also have a vanishing spurious signal.

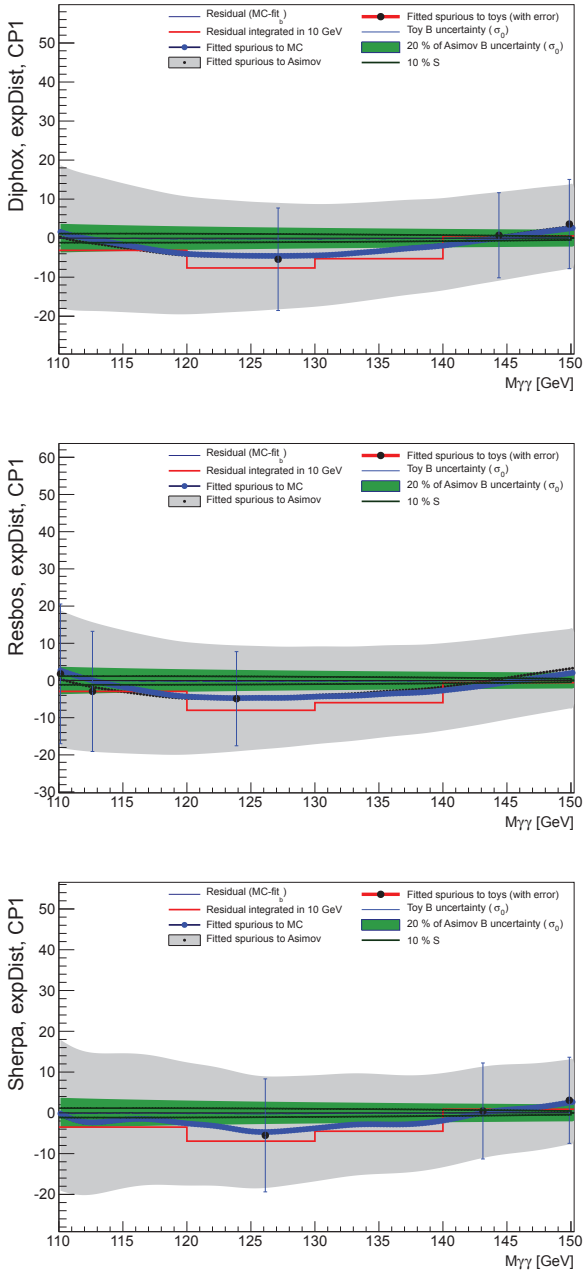

Figure 8.15: Background bias performance for the exponential function in the three MC samples (DIPHOX+, ResBos+, Sherpa+), in category CP1 for an integrated luminosity of 4.9 fb^{-1}.

Exponential of a second order polynomial

Category	Max $\lvert N_{SP}\rvert$ (m_H[GeV])	r_{SP}^{S}[%] (N_S)	$r_{SP}^{\sigma_0}$[%] (σ_0)	σ^{N_S}	$\sigma^{N_{SP}}$	Criterion A
		DIPHOX+				
CP1	1.1 (114)	9.4 (12)	6.4 (17)	0.68	0.064	✓
CP2	0.11 (112)	6.9 (1.5)	3.2 (3.3)	0.46	0.032	✓
CP3	9.0 (112)	40 (23)	26 (35)	0.65	0.26	
CP4	0.13 (119)	4.6 (2.9)	1.7 (7.6)	0.38	0.017	✓
CP5	0.70 (115)	9.4 (7.4)	4.4 (16)	0.47	0.044	✓
CP6	0.081 (134)	9.3 (0.87)	2.9 (2.8)	0.31	0.029	✓
CP7	8.4 (115)	38 (22)	20 (42)	0.54	0.20	
CP8	0.34 (115)	12 (2.8)	3.8 (8.8)	0.32	0.038	✓
CP9	-1.8 (110)	-19 (9.9)	-4.8 (38)	0.26	-0.048	✓
		ResBos+				
CP1	0.83 (110)	7.2 (12)	4.5 (18)	0.62	0.045	✓
CP2	0.13 (113)	8.3 (1.5)	3.9 (3.3)	0.47	0.038	✓
CP3	8.4 (112)	37 (23)	24 (35)	0.64	0.24	
CP4	0.24 (132)	9.2 (2.6)	3.2 (7.5)	0.35	0.032	✓
CP5	0.42 (115)	5.6 (7.4)	2.6 (16)	0.47	0.026	✓
CP6	0.087 (134)	10 (0.87)	3.1 (2.8)	0.31	0.031	✓
CP7	6.9 (115)	31 (22)	17 (42)	0.54	0.17	
CP8	-0.43 (110)	-16 (2.7)	-4.7 (9.1)	0.30	-0.047	✓
CP9	-3.1 (110)	-31 (9.9)	-7.9 (39)	0.26	-0.079	✓
		Sherpa+				
CP1	2.1 (117)	18 (12)	13 (16)	0.70	0.13	✓
CP2	0.23 (118)	14 (1.6)	6.8 (3.3)	0.47	0.068	✓
CP3	9.2 (112)	41 (23)	26 (36)	0.64	0.26	
CP4	-0.4 (127)	-14 (2.8)	-5.3 (7.5)	0.37	-0.053	✓
CP5	1.6 (117)	22 (7.4)	10 (16)	0.47	0.10	✓
CP6	-0.28 (110)	-28 (0.98)	-8.2 (3.4)	0.29	-0.082	✓
CP7	5.8 (122)	26 (22)	14 (40)	0.56	0.14	
CP8	0.54 (134)	21 (2.5)	6.4 (8.5)	0.30	0.064	✓
CP9	-3.2 (110)	-33 (9.9)	-8.3 (39)	0.26	-0.083	✓

Table 8.5: Overview of the spurious signal performance for the exponential of a second order polynomial background function using all three MC samples. See the text for explanation of the entries. Results are compiled for an integrated luminosity of 4.9 fb^{-1}.

The results for the exponential of a third order polynomial background function are displayed in Table 8.6. In the framework used here, this function was flexible enough to adequately describe all the categories. However, as already mentioned, other parts of HSG1, using different fitting frameworks, had problems with the stability of the function, so it was not considered for the final decision. Generally, it was seen that the Bernstein polynomials of order n described the distributions approximately at the same level as the exponentiated polynomials of order $n-1$. Finally, the results for the Bernstein polynomial of fourth order are compiled in Table 8.7. The categories CP3 and CP7 are both modelled at an acceptable level by this function.

The results, steadily increasing the degrees of freedom until a satisfactory model is reached, are compiled in Table 8.8 for the Sherpa+ sample only, since it gave the largest spurious signal of any of the three background templates. Showing the bias results for all functions, categories and MC samples would take excessive space. However, the performance plots for the chosen background functions for the respective categories for the three MC samples are shown in Figs. 8.16 – 8.24.

Exponential of a third order polynomial

Category	Max $\lvert N_{SP}\rvert$ (m_H[GeV])	r_{SP}^{S}[%] (N_S)	$r_{SP}^{\sigma_0}$[%] (σ_0)	σ^{N_S}	$\sigma^{N_{SP}}$	Criterion A
			DIPHOX+			
CP1	0.46 (114)	3.9 (12)	2.5 (18)	0.63	0.025	✓
CP2	-0.075 (129)	-5.2 (1.4)	-2.4 (3.1)	0.47	-0.024	✓
CP3	2.8 (111)	12 (22)	7.3 (38)	0.59	0.073	✓
CP4	-0.26 (127)	-9.5 (2.8)	-3.5 (7.6)	0.36	-0.035	✓
CP5	0.51 (115)	6.8 (7.4)	2.9 (18)	0.42	0.029	✓
CP6	-0.079 (129)	-8.4 (0.94)	-2.7 (2.9)	0.32	-0.027	✓
CP7	1.4 (115)	6.2 (22)	3.0 (47)	0.48	0.029	✓
CP8	-0.27 (133)	-10 (2.6)	-3.0 (8.8)	0.29	-0.03	✓
CP9	1.7 (118)	16 (10)	4.1 (41)	0.25	0.041	✓
			ResBos+			
CP1	-0.41 (139)	-5.2 (7.9)	-3.2 (13)	0.62	-0.032	✓
CP2	0.092 (113)	6.0 (1.5)	2.6 (3.5)	0.44	0.026	✓
CP3	2.8 (110)	12 (22)	7.4 (38)	0.59	0.074	✓
CP4	0.25 (132)	9.4 (2.6)	3.2 (7.7)	0.34	0.033	✓
CP5	0.33 (115)	4.5 (7.4)	1.9 (18)	0.43	0.019	✓
CP6	-0.073 (130)	-7.8 (0.94)	-2.5 (2.9)	0.32	-0.025	✓
CP7	2.0 (128)	9.8 (21)	5.3 (38)	0.55	0.053	✓
CP8	-0.4 (110)	-15 (2.7)	-4.2 (9.4)	0.29	-0.042	✓
CP9	-2.1 (110)	-22 (9.9)	-5.2 (41)	0.24	-0.052	✓
			Sherpa+			
CP1	-1.9 (112)	-17 (12)	-10 (19)	0.60	-0.10	✓
CP2	-0.3 (110)	-19 (1.5)	-8.1 (3.7)	0.42	-0.081	✓
CP3	3.4 (111)	15 (22)	8.8 (38)	0.59	0.088	✓
CP4	-0.38 (127)	-14 (2.8)	-5.1 (7.5)	0.37	-0.051	✓
CP5	-1.3 (111)	-18 (7.4)	-7.1 (19)	0.40	-0.071	✓
CP6	-0.27 (110)	-27 (0.98)	-7.6 (3.5)	0.28	-0.076	✓
CP7	-6.3 (110)	-29 (22)	-13 (48)	0.46	-0.13	✓
CP8	0.47 (134)	19 (2.5)	5.4 (8.7)	0.29	0.054	✓
CP9	-3.0 (133)	-35 (8.6)	-9.5 (32)	0.27	-0.095	✓

Table 8.6: Overview of the spurious signal performance for exponential of a third order polynomial background function using all three MC samples. See the text for explanation of the entries. Results are compiled for an integrated luminosity of 4.9 fb^{-1}.

Bernstein polynomial of fourth order

Category	Max $\lvert N_{SP}\rvert$ (m_H[GeV])	r_{SP}^{S}[%] (N_S)	$r_{SP}^{\sigma_0}$[%] (σ_0)	σ^{N_S}	$\sigma^{N_{SP}}$	Criterion A
			DIPHOX+			
CP1	-0.41 (111)	-3.6 (12)	-2.1 (20)	0.59	-0.021	✓
CP2	-0.095 (115)	-6.1 (1.6)	-2.6 (3.6)	0.44	-0.026	✓
CP3	-2.5 (122)	-11 (23)	-7.4 (34)	0.66	-0.074	✓
CP4	-0.23 (127)	-8.4 (2.8)	-2.9 (8.1)	0.34	-0.029	✓
CP5	-0.64 (110)	-8.6 (7.4)	-3.3 (19)	0.39	-0.033	✓
CP6	-0.090 (129)	-9.6 (0.94)	-2.9 (3.1)	0.30	-0.029	✓
CP7	1.3 (114)	5.8 (22)	2.6 (49)	0.45	0.026	✓
CP8	-0.38 (133)	-15 (2.6)	-4.0 (9.6)	0.27	-0.040	✓
CP9	1.9 (118)	19 (10)	4.7 (42)	0.24	0.046	✓
			ResBos+			
CP1	0.49 (130)	5.0 (9.9)	3.3 (15)	0.67	0.033	✓
CP2	-0.086 (116)	-5.5 (1.6)	-2.4 (3.5)	0.44	-0.024	✓
CP3	-3.1 (121)	-14 (23)	-8.9 (35)	0.66	-0.089	✓
CP4	0.32 (132)	12 (2.6)	3.9 (8.2)	0.32	0.039	✓
CP5	-0.60 (110)	-8.1 (7.4)	-3.1 (19)	0.39	-0.031	✓
CP6	-0.088 (130)	-9.5 (0.93)	-2.9 (3.1)	0.30	-0.029	✓
CP7	2.9 (115)	13 (22)	6.0 (49)	0.45	0.060	✓
CP8	-0.33 (132)	-13 (2.6)	-3.5 (9.6)	0.27	-0.035	✓
CP9	-2.5 (110)	-25 (9.9)	-5.6 (44)	0.22	-0.056	✓
			Sherpa+			
CP1	-2.2 (112)	-19 (12)	-11 (20)	0.59	-0.11	✓
CP2	-0.30 (110)	-20 (1.5)	-7.9 (3.8)	0.40	-0.079	✓
CP3	2.8 (111)	13 (22)	7.1 (40)	0.56	0.071	✓
CP4	-0.66 (146)	-38 (1.7)	-8.1 (8.1)	0.21	-0.081	✓
CP5	-1.6 (111)	-21 (7.4)	-8.2 (19)	0.39	-0.082	✓
CP6	-0.25 (110)	-25 (0.98)	-6.8 (3.7)	0.27	-0.068	✓
CP7	-4.5 (110)	-20 (22)	-8.8 (50)	0.43	-0.088	✓
CP8	0.38 (134)	15 (2.5)	4.0 (9.5)	0.27	0.040	✓
CP9	-3.9 (133)	-46 (8.6)	-11 (37)	0.23	-0.11	✓

Table 8.7: Overview of the spurious signal performance for Bernstein polynomial of fourth order background function using all three MC samples. See the text for explanation of the entries. Results are compiled for an integrated luminosity of 4.9 fb^{-1}.

Category	Function	Max $\lvert N_{SP} \rvert$ (m_H[GeV])	r_{SP}^{S}[%] (N_S)	$r_{SP}^{\sigma_0}$[%] (σ_0)	σ^{N_S}	$\sigma^{N_{SP}}$	Pass	Pass$_{all}$
CP1	Exp	-4.7 (126)	-45 (11)	-35 (14)	0.78	-0.35		
CP1	Epoly2	2.1 (117)	18 (12)	13 (16)	0.70	0.13	✓	✓
CP2	Exp	-0.23 (110)	-15 (1.5)	-6.4 (3.5)	0.43	-0.064	✓	✓
CP3	Exp	12 (117)	50 (23)	35 (33)	0.71	0.35		
CP3	Epoly2	9.2 (112)	41 (23)	26 (36)	0.64	0.26		
CP3	Epoly3	3.4 (111)	15 (22)	8.8 (38)	0.59	0.088	✓	✓
CP3	Bern3	5.8 (111)	26 (22)	16 (36)	0.62	0.16		
CP3	Bern4	2.8 (111)	13 (22)	7.1 (40)	0.56	0.071	✓	✓
CP4	Exp	0.5 (132)	19 (2.6)	7.2 (6.9)	0.38	0.072	✓	✓
CP5	Exp	-4.4 (126)	-64 (6.8)	-34 (13)	0.54	-0.34		
CP5	Epoly2	1.6 (117)	22 (7.4)	10 (16)	0.47	0.10	✓	✓
CP6	Exp	-0.27 (110)	-27 (0.98)	-8.0 (3.4)	0.29	-0.080	✓	✓
CP7	Exp	6.5 (122)	29 (22)	18 (37)	0.60	0.17		
CP7	Epoly2	5.8 (122)	26 (22)	14 (40)	0.56	0.14		
CP7	Epoly3	-6.3 (110)	-29 (22)	-13 (48)	0.46	-0.13	✓	✓
CP7	Bern3	-6.3 (110)	-29 (22)	-14 (46)	0.47	-0.14	✓	✓
CP7	Bern4	-4.5 (110)	-20 (22)	-8.8 (50)	0.43	-0.088	✓	✓
CP8	Exp	0.45 (134)	18 (2.5)	5.7 (7.9)	0.32	0.057	✓	✓
CP9	Exp	-16 (130)	-179 (9.1)	-59 (28)	0.33	-0.59		
CP9	Epoly2	-3.2 (110)	-33 (9.9)	-8.3 (39)	0.26	-0.083	✓	✓

Table 8.8: Overview of the spurious signal performance for different background functions using the Sherpa+ MC sample. The rightmost column is the result which takes all three MC generators into consideration (although numbers for the other two are not shown). See the text for explanation of the entries. Be aware that the criteria applies to all three MC generators, whereas the numbers in this table are only for the Sherpa+ sample, and might not be the most extreme ones, although they tend to be. The chosen functions are shown in grey. Results are compiled for an integrated luminosity of 4.9 fb^{-1}.

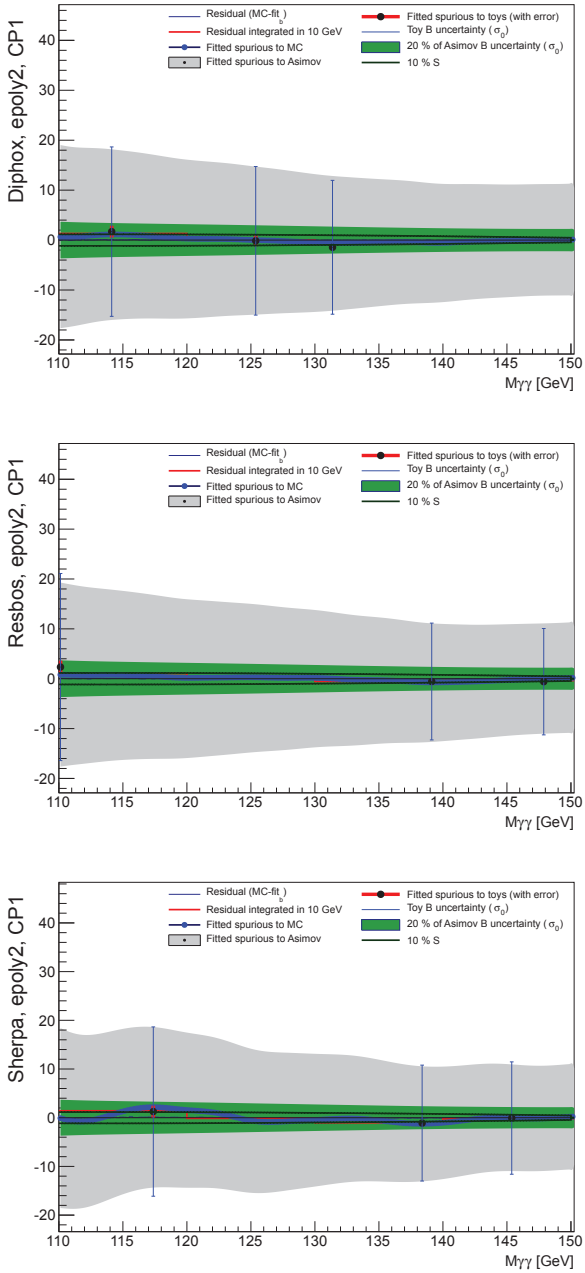

Figure 8.16: Background bias performance for the exponential of a second order polynomial in the three MC samples (DIPHOX+, ResBos+, Sherpa+), in category CP1 for an integrated luminosity of 4.9 fb^{-1}.

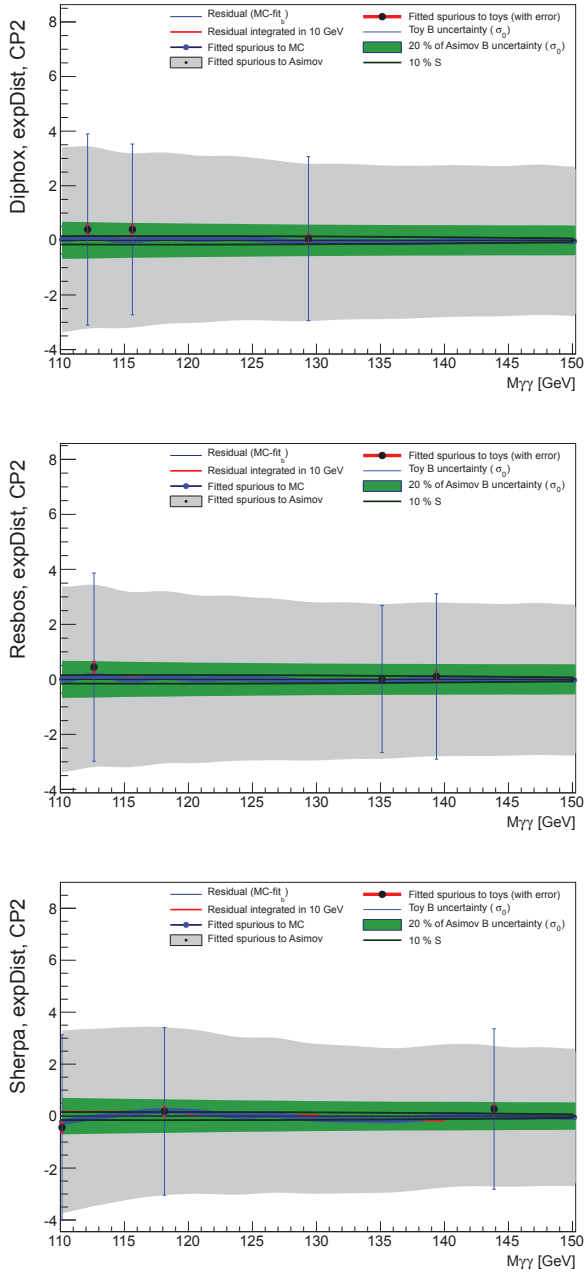

Figure 8.17: Background bias performance for the exponential function in the three MC samples (DIPHOX+, ResBos+, Sherpa+), in category CP2 for an integrated luminosity of 4.9 fb^{-1}.

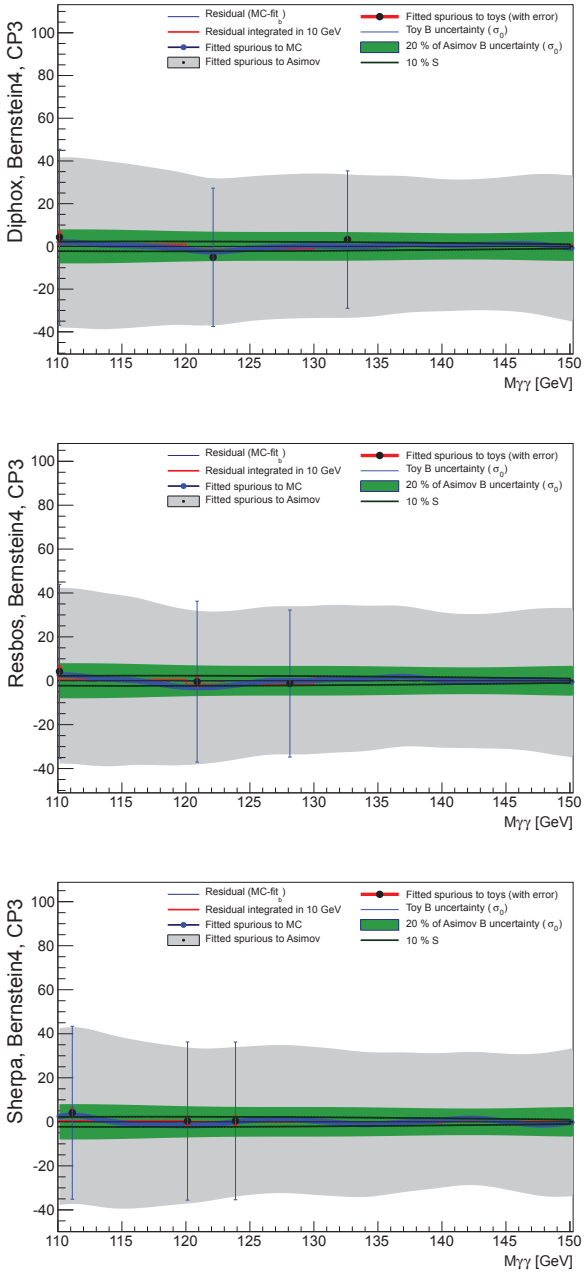

Figure 8.18: Background bias performance for the Bernstein polynomial of fourth order in the three MC samples (DIPHOX+, ResBos+, Sherpa+), in category CP3 for an integrated luminosity of 4.9 fb^{-1}.

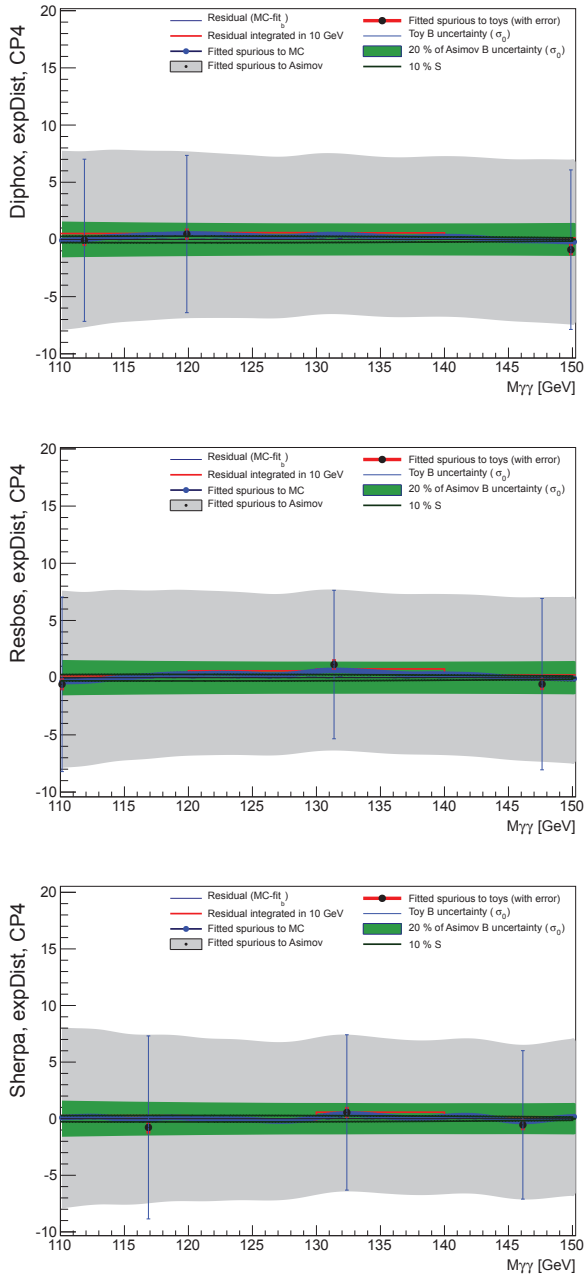

Figure 8.19: Background bias performance for the exponential function in the three MC samples (DIPHOX+, ResBos+, Sherpa+), in category CP4 for an integrated luminosity of 4.9 fb^{-1}.

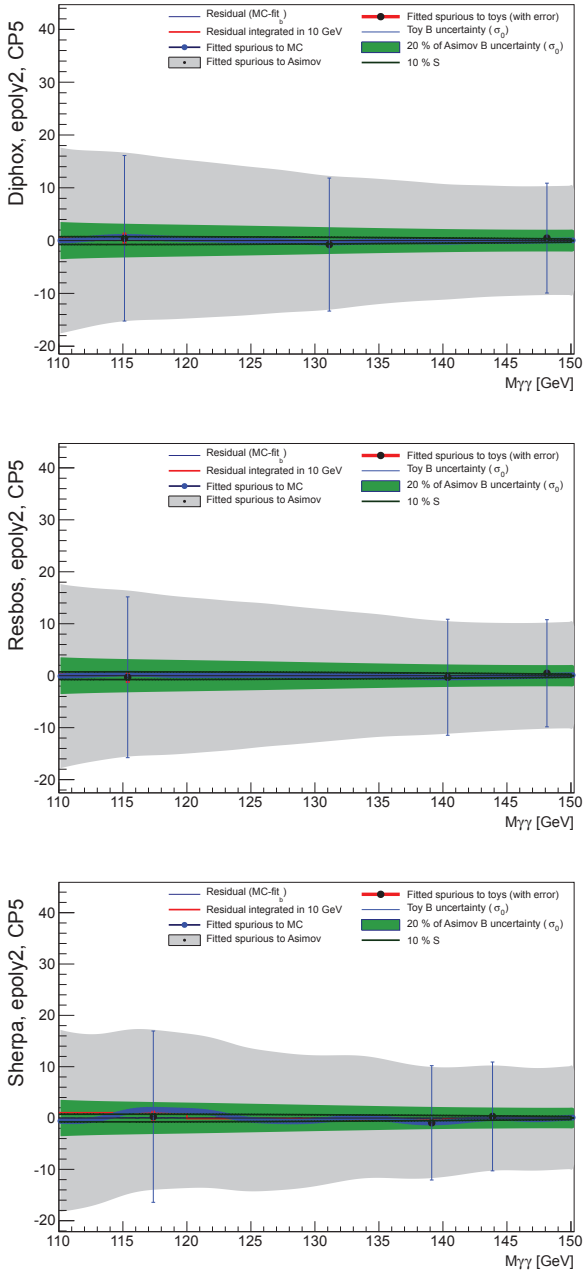

Figure 8.20: Background bias performance for the exponential of a second order polynomial in the three MC samples (DIPHOX+, ResBos+, Sherpa+), in category CP5 for an integrated luminosity of 4.9 fb^{-1}.

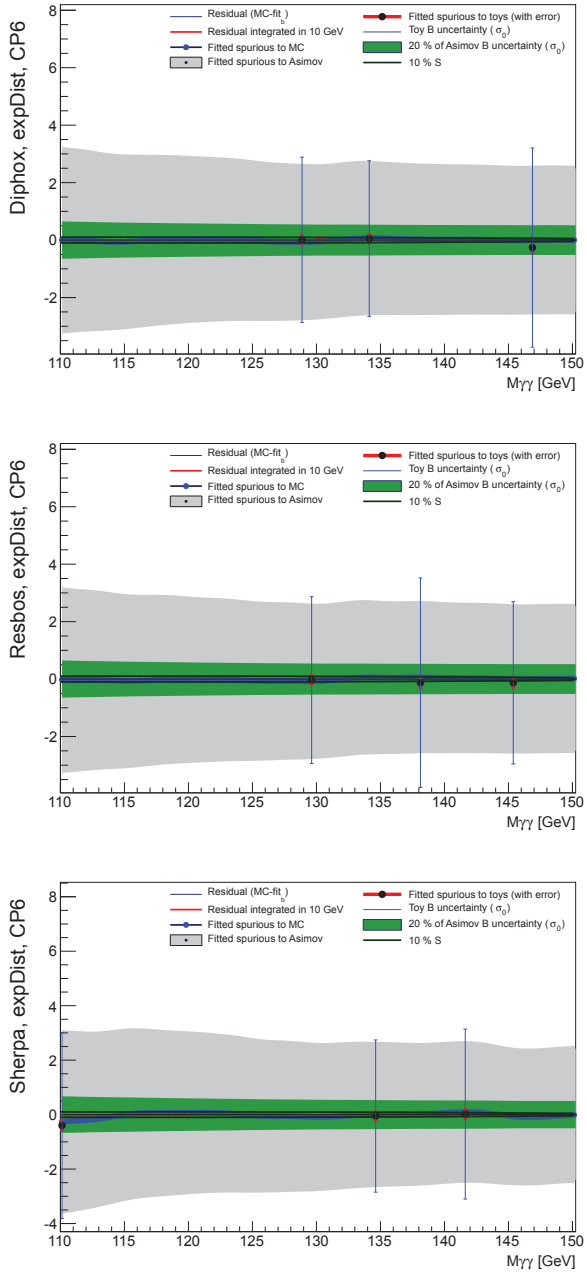

Figure 8.21: Background bias performance for the exponential function in the three MC samples (DIPHOX+, ResBos+, Sherpa+), in category CP6 for an integrated luminosity of 4.9 fb^{-1}.

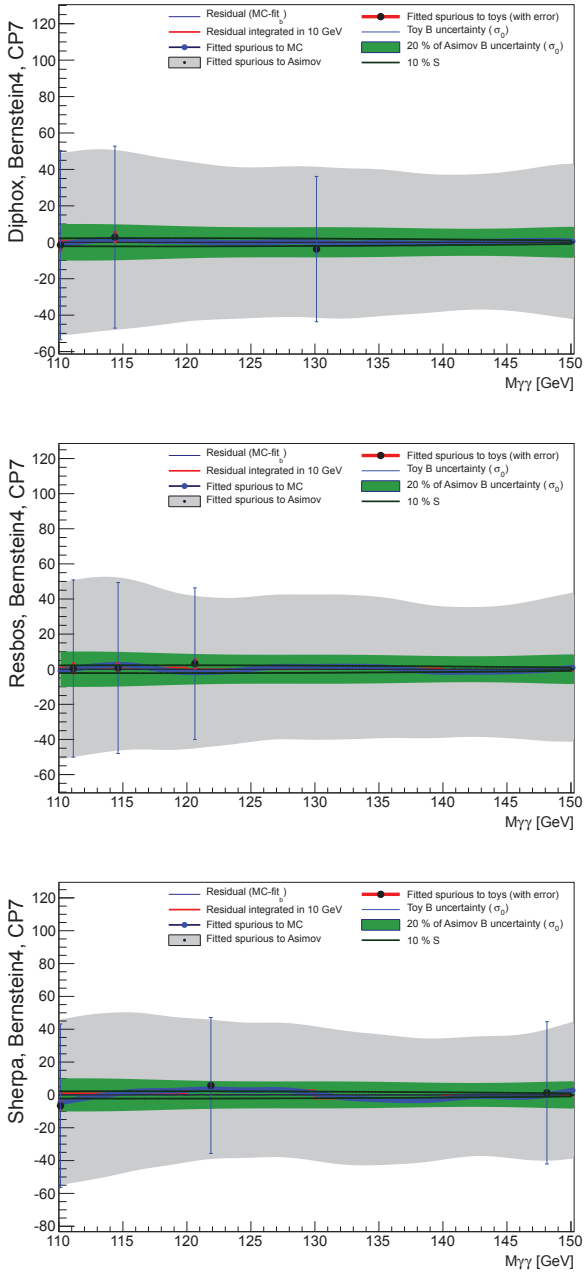

Figure 8.22: Background bias performance for the Bernstein polynomial of fourth order in the three MC samples (DIPHOX+, ResBos+, Sherpa+), in category CP7 for an integrated luminosity of 4.9 fb^{-1}.

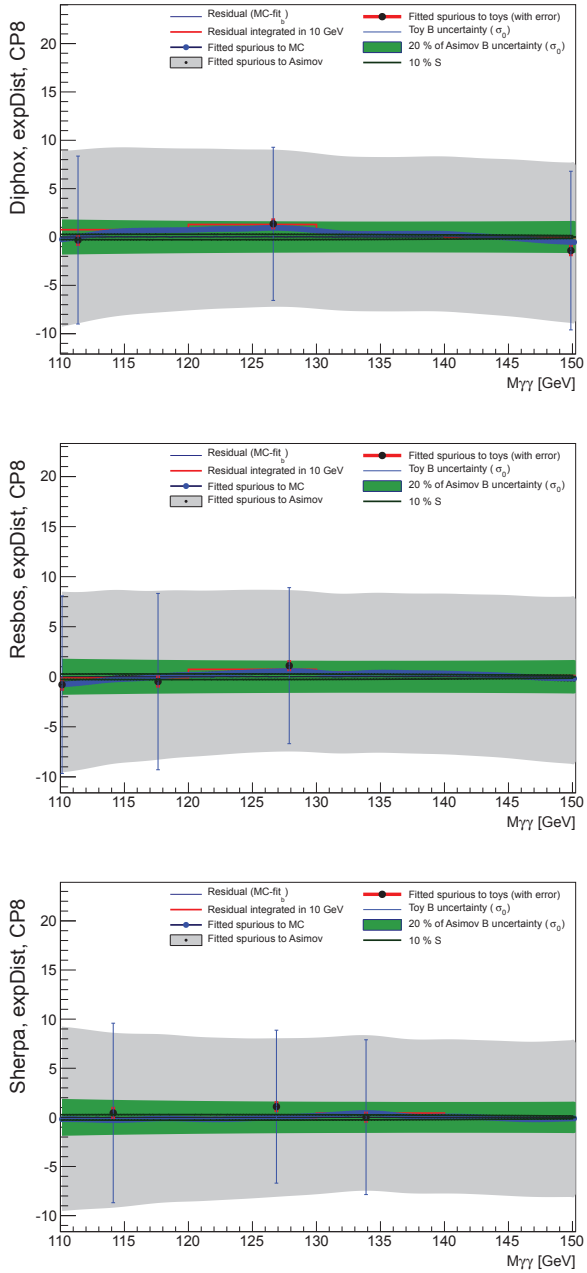

Figure 8.23: Background bias performance for the exponential function in the three MC samples (DIPHOX+, ResBos+, Sherpa+), in category CP8 for an integrated luminosity of 4.9 fb^{-1}.

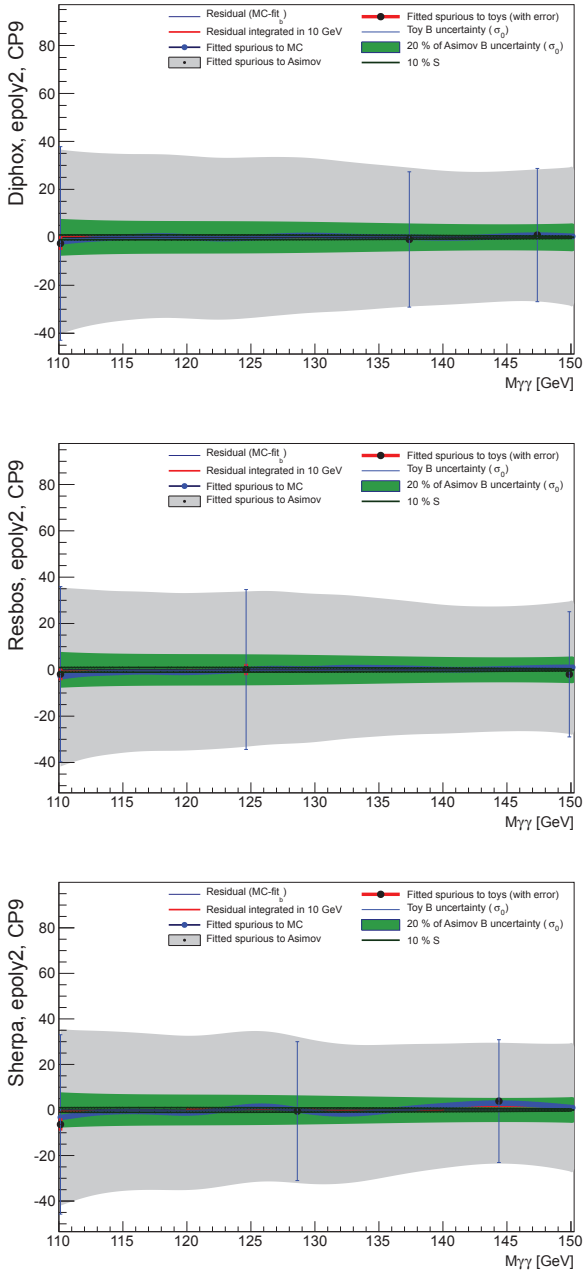

Figure 8.24: Background bias performance for the exponential of a second order polynomial in the three MC samples (DIPHOX+, ResBos+, Sherpa+), in category CP9 for an integrated luminosity of 4.9 fb^{-1}.

8.4 Signal and Background Characteristics

A summary of the main characteristics of the signal and the background, for each of the categories can be seen in Table 8.9. The width of a $m_{\mathrm{H}} = 125$ GeV signal, given in σ_{CB} as well as FWHM, is displayed, along with the expected yield. The background yield in a ± 4 GeV window around the Higgs boson mass, as estimated using the ResBos+ histograms is also indicated. The resulting signal fraction, $f_S = \frac{S}{S+B}$, and a rough estimate of the sensitivity, given by $S/\sqrt{B}$, based on these estimates of the signal and background are displayed. The sensitivity, as can be appreciated from this table, is a balance between invariant mass resolution and statistics.

Category	σ_{CB}	FWHM	S	B	f_S	$S/\sqrt{B}$
CP1	1.44	3.40	10.1	279	0.04	0.6
CP2	1.39	3.27	1.67	13.5	0.11	0.5
CP3	1.71	4.05	21.9	1028	0.02	0.7
CP4	1.57	3.72	2.94	64.2	0.04	0.4
CP5	1.64	3.87	6.82	202	0.03	0.5
CP6	1.55	3.66	1.10	10.6	0.09	0.3
CP7	1.99	4.70	21.9	1198	0.02	0.6
CP8	1.75	4.13	3.06	71.6	0.04	0.4
CP9	2.24	5.56	10.2	508	0.02	0.5
Inclusive	1.77	4.18	79.6	3388	0.02	1.37

Table 8.9: Characteristics of the signal and background in the categories, for a $m_{\mathrm{H}} = 125$ GeV signal. The width of the signal model fit to the simulated sample, given both in σ_{CB} and FWHM, can be seen. The estimated background, B, is found from ResBos+ histograms, in a mass window of ± 4 GeV around the signal mass. The fraction of signal in the total number or events, $f_S = \frac{S}{S+B}$, and a rough estimate of the sensitivity, given by $S/\sqrt{B}$, are displayed.

The background, $B_{data} = \sigma_0^2$, as estimated from the uncertainty on fits to data histograms of the chosen background functions in Table 8.8, and a Bernstein polynomial of fourth order for the inclusive spectrum, can be seen in Table 8.10. These numbers are roughly in agreement with the estimates from ResBos+, but most likely less precise, as the statistical fluctuations in data are much larger than in the simulated high-statistics ResBos+ sample.

Category	B_{data}
CP1	201
CP2	6.00
CP3	1112
CP4	79.7
CP5	216
CP6	4.95
CP7	1779
CP8	70.4
CP9	1203
Inclusive	4338

Table 8.10: The estimated effective background under a signal peak at $m_{\mathrm{H}} = 125$ GeV, as obtained from the background fit uncertainty, $B_{data} = \sigma_0^2$, in fits to data histograms. The background functions are indicated in Table 8.8, and for the inclusive spectrum, a Bernstein polynomial of fourth order was used.

Chapter 9

Results Obtained with a Weighted Approach

Instead of taking the resulting invariant mass distributions of the categories through the full statistical procedure, as explained in Chapter 8, to obtain results, an alternative approach would be to weight the events. In this approach, each event is given a weight based on the expected sensitivity of the category it belongs to. The more sensitive the category, the higher the weight. Thus, the events in which a signal is easier seen would be given higher importance. This is more or less equivalent to assessing the log-likelihood ratio, as we soon will see. The invariant mass distribution of the weighted events could be used, on the same level as the full-blown, intricate statistical approach of HSG1, to obtain results, as *e.g.* the significance of an excess above the expected background.

Moreover, when looking at an inclusive invariant mass spectrum, the resulting p_0 as obtained from the statistical procedure can be quite surprising. A non-impressive looking excess can correspond to a rather small p_0. The fact that the categorization of the events is taken advantage of in the statistical procedure of HSG1 gives great power to the analysis. The different signal-to-background ratios of the categories increases the sensitivity to a signal. The size of p_0 is impossible to predict by looking at the inclusive invariant mass distribution, and difficult to appreciate from looking at the numerous invariant mass distributions of the categories. The weighting of the categories produce an inclusive invariant mass distribution which gives a result easier to interpret visually.

To find the weights, the log-likelihood ratio, being the best thing possible to do to separate two distinct hypotheses, according to the Neyman-Pearson lemma [149], is taken as a starting point. The number of events, n, is assumed to be distributed

according to a Poisson distribution. This yields a log-likelihood ratio as in Eq. (7.6). If several channels, i, are combined, the resulting likelihood will be

$$\mathcal{L} = \prod_i \mathcal{L}_i \tag{9.1}$$

$$-2\ln\mathcal{L} = -2\sum_i \ln\mathcal{L}_i \tag{9.2}$$

and the resulting test-statistic will be

$$t = \sum_i \left\{ 2s_i - 2n_i \ln\left(1 + \frac{s_i}{b_i}\right) \right\} \tag{9.3}$$

$$= 2\,S - 2\sum_i n_i w_i \ , \tag{9.4}$$

where $S = \sum_i s_i$ and the event weights are $w_i = \ln\left(1 + \frac{s_i}{b_i}\right)$.

The normalization of the weights is a matter of choice. We felt the natural choice was to conserve the signal on the average, such that if a signal was present in the data, the weights would give an unbiased estimate of the number of signal events. An estimation of the number of signal events, $\hat{s}$, is gotten from subtracting the expected background, b, from the total number of events, n, $\hat{s} = n - b$. The normalization, α, can be found by demanding that this signal estimate should be equal to the total expected signal, S;

$$\alpha \cdot \sum_i \langle \hat{s}_i \rangle w_i \equiv S \ . \tag{9.5}$$

Since the expectation of the signal per channel under the signal hypotheses is equal to the average number of signal events per channel, $\langle \hat{s}_i \rangle = s_i$, this provides the normalization

$$\alpha = \frac{S}{\sum_i s_i w_i} \ . \tag{9.6}$$

The normalized estimate of the number of signal events is thus

$$\hat{S} = \frac{S}{\sum_i s_i w_i} \sum_c \hat{s}_c w_c \ , \tag{9.7}$$

where both sums run over the categories. This will on the average give S under the signal hypothesis, zero under the background hypothesis, and some other number

if the signal is distributed differently in the categories than the SM signal.

The weight applied to all the events in category c is thus

$$w_c = \frac{S \ln(1 + \frac{s_c}{b_c})}{\sum_i s_i \ln(1 + \frac{s_i}{b_i})} , \tag{9.8}$$

where the sum runs over the categories, and $S = \sum_i s_i$. For each category, the signal, s_c, is the expectation from a SM Higgs boson and the expected background, b_c, is estimated from MC (for the weights). In particular, these weights were chosen to preserve the number of signal events of a 125 GeV SM Higgs on the average.[1] The weights will not be wrong, but simply suboptimal if the signal is not distributed like the SM signal, and/or the background differs from the estimated one. The expected background is taken as the square of the uncertainty on the background fit at a specific invariant mass; σ_0^2. This specific invariant mass is determined by the relevant signal peak position – the background of interest is the one under the signal peak. However, σ_0^2 must naturally be gotten from a distribution not containing signal. For the weights, the effective background rates, $b = \sigma_0^2$, obtained from DIPHOX+ histograms were applied. We will have a closer look at the different options for σ_0 and consistency checks in Section 9.1.

In order to be able to extract information about the statistical power of the analysis, and the results when analysing real data, the signal model used in the calculation must also be a weighted one. This indicates merging the signal model of each of the categories, $S_c(m_{\gamma\gamma})$, adding them with their respective weights and signal yields to a common pdf, as

$$S(m_{\gamma\gamma}) = \sum_c \frac{s_c w_c \, S_c(m_{\gamma\gamma})}{\sum_i s_i w_i} , \tag{9.9}$$

where both sums run over the categories, c and i. The normalization of this inclusive,[2] weighted signal distribution is simply set to the expected number of signal events, as the weights are constructed to reproduce the number of signal events, when such is present. The inclusive (unweighted) and the weighted signal models can be seen in Fig. 9.1. Here it becomes apparent that the weighted

[1] For the official weights, only used in an illustrative plot so far, 90% of the expected signal was used, along with the estimated background in a mass window containing 90% of the signal. This background was shown to correspond well to the square of the uncertainty on the background under the signal top, σ_0^2. The impact on the expected significance of a signal at 125 GeV using the background uncertainty together with 90% of the signal and 100% of the signal was checked. This had the miniscule impact on the significance of 0.07% for the DIPHOX+ sample.

[2] Please note that whenever a weighted distribution is in question, using the term 'inclusive' is superfluous – a weighted spectrum only makes sense for the inclusive case.

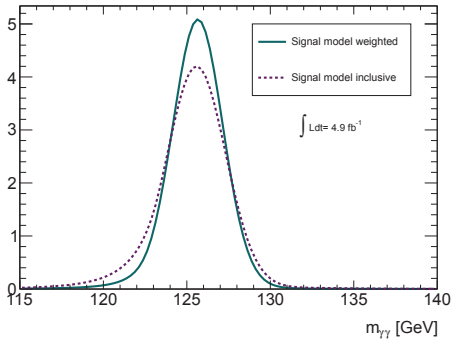

Figure 9.1: The inclusive (dashed) and the weighted (full) signal models for $m_{\mathrm{H}} = 125$ GeV. It can be appreciated that the weighted signal model is more sensitive.

approach is more sensitive; the resolution of the weighted signal model is much better.

The background is naturally also weighted (there is no way of separating the background and the signal on an event-by-event basis). The normalization is not to be worried about, since this is taken purely from data. It will be lower than the actual number of events – as the weights are designed to give a better signal-to-background ratio, but keep the signal events on average intact, the background must thereby be reduced. However, the uncertainty on the weighted spectrum requires some thought. Combining the weighted histograms of the categories according to their weight does not retain the correct uncertainty. This error propagation must be assured of manually, and the correct uncertainty can be expressed by

$$\sigma^2 = \sum_c w_c^2 \, n_c \ , \tag{9.10}$$

where c runs over the categories, and w_c and n_c are the weight and number of events for this category, respectively.

Throughout this section, when nothing else is stated, a Bernstein polynomial of the fourth order is used as the background function for the weighted approach.

9.1 Consistency in σ_0 between Toys, diphox+ and Data

The consistency in the uncertainty on the signal amplitude fitted to the background, σ_0, in the categories when using diphox+ histograms and histograms

from data was checked. To evaluate whether differences could be due to natural fluctuations, the uncertainty on the uncertainty needed to be evaluated. This was done by throwing toys, based on the DIPHOX+ histograms. The uncertainty could then be retrieved from the variance of the σ_0-distribution.

The yields in the DIPHOX+ histograms were found to be somewhat different from the ones in data, by -4.2% to $+13\%$, as indicated in Table 9.1. The corresponding invariant mass distributions can be seen in Fig. 9.2. The category with the biggest discrepancy, CP4, has a very unlikely distribution in data; it is not expected to be reproduced by simulation (see Fig. 9.2 or Fig. 7.16).

Category	Yield data	Yield DIPHOX+	Difference [%]
CP1	1898	2069	9
CP2	90	94	4.4
CP3	6951	7156	2.9
CP4	400	451	13
CP5	1436	1504	4.7
CP6	75	75	0
CP7	8511	8372	−1.6
CP8	475	501	5.5
CP9	3775	3615	−4.2

Table 9.1: The difference in normalization between the DIPHOX+ sample and the data for each of the categories.

The weights were obtained from the raw DIPHOX+ distributions. A test was made to evaluate the impact of normalization differences. The evaluation was done with corrections of the yields of DIPHOX+ that on the average accounted for discrepancies more than three times as big as the ones seen in Table 9.1. Using the normalization corrected DIPHOX+ histograms to obtain the weights for the categories led to a difference in the expected significance of 0.5% with respect to using the uncorrected DIPHOX+ histograms. The observed significance was unchanged (only a change in the fourth digit was observed). The mass of the largest excess observed was also unchanged when switching between the two sets of weights. The impact of the normalization difference on the weights thus proves to have very little impact on the expected significance, and next to no impact on the observed significance, and this normalization difference in data and DIPHOX+ is thus neglected.

To check consistency of the weights in various samples, including data, the uncertainties were obtained at 135 GeV. The excess seen in data around 126 GeV

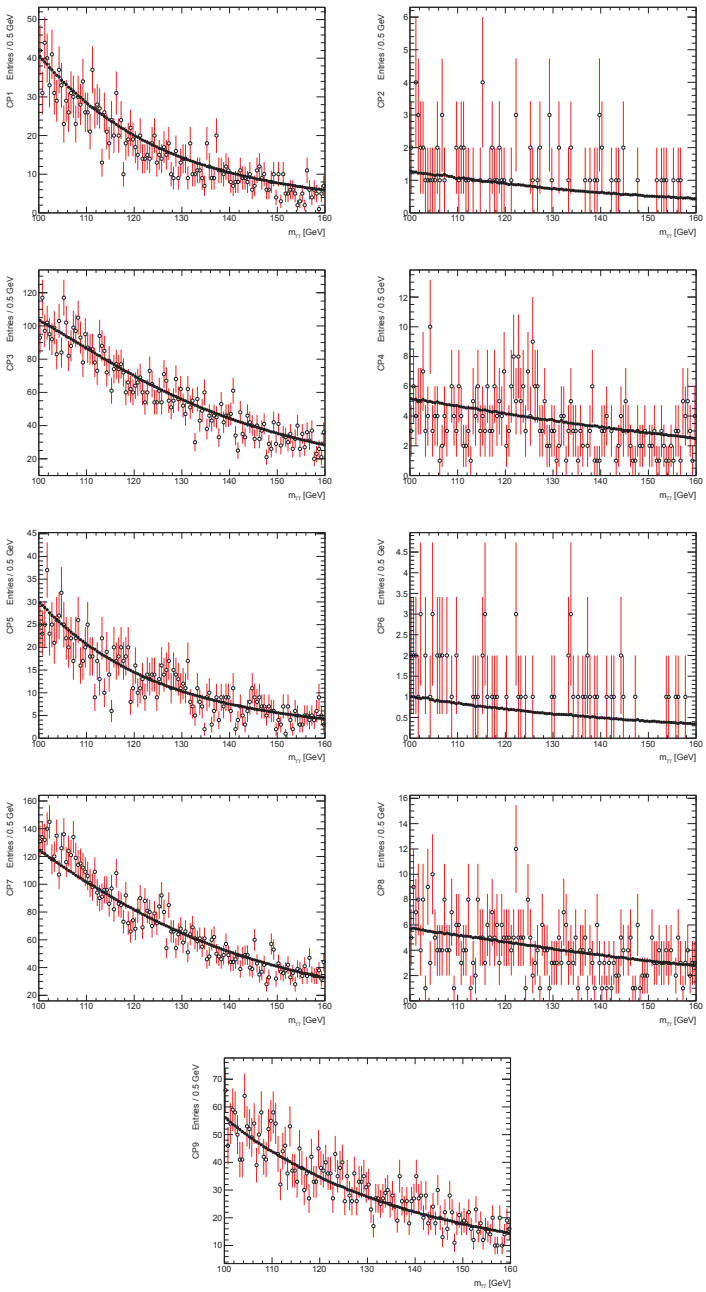

Figure 9.2: The invariant mass distributions in the DIPHOX+ sample (full circles, error bars are invisible at this scale) and data (open circles) for the nine categories.

should not contribute much to σ_0 at this mass. Toys based on DIPHOX+ are expected to reproduce the results of the raw DIPHOX+ distributions within uncertainties; we checked this. The resulting values of σ_0 for the categories, given for toys based on DIPHOX+ and the raw DIPHOX+ distributions, as well as for Sherpa+ and data can be seen in Table 9.2. The values of σ_0 found in the Sherpa+ MC samples are similar to the DIPHOX+ values (and closer to these than to the data values), so using DIPHOX+ to estimate the weights should not bias the results. The values for MC and data are similar for most categories, but we will come back to using weights based on the σ_0 obtained in data later on. The values obtained with DIPHOX+ toys and raw DIPHOX+ histograms are in rather good agreement. The discrepancy between these, in standard deviations with respect to the variation in the DIPHOX+ toys, can be seen in the third column. As a test of the overall discrepancy, the sum of the squares of the discrepancies in the categories can be evaluated. The value of this χ^2-test is given in the last column, and turns out to be close to one per degree of freedom, as there are nine measurements, which indicates good agreement. The χ^2-probability of getting a larger value than the one obtained for nine degrees of freedom is $P(\chi^2 > 8.74; n = 9) \simeq 46\%$. The toys seem to reproduce the raw MC estimates.

Category	$\text{Toys}^{\text{DIPHOX+}}$	DIPHOX+	Discrepancy [σ]	Sherpa+	Data
CP1	11.8 ± 1.06	12.7	-0.85	12.5	12.3
CP2	2.82 ± 0.291	2.81	0.026	2.78	2.32
CP3	32.1 ± 2.40	32.8	-0.31	32.5	31.5
CP4	6.82 ± 0.613	7.00	-0.30	6.88	5.87
CP5	10.3 ± 0.767	11.8	-2.0	11.6	10.6
CP6	2.79 ± 0.252	2.67	0.46	2.66	3.67
CP7	36.5 ± 2.77	40.3	-1.4	39.7	39.8
CP8	7.36 ± 0.519	8.00	-1.2	7.89	7.91
CP9	28.3 ± 3.47	29.9	-0.47	29.3	30.8
$\sum N_\sigma^2$			8.74		

Table 9.2: Values of σ_0 taken at 135 GeV, for toys based on the DIPHOX+ sample, the raw DIPHOX+ distributions and the discrepancies of these, given in standard deviations with respect to the variation in the toys. The values of σ_0 taken at 135 GeV for the Sherpa+ MC sample as well as for data are also shown.

The uncertainty on the fitted signal amplitude, σ_0, as functions of the invariant mass for each of the nine categories, for DIPHOX+ and data can be seen in Fig. 9.3. As the distributions in Fig. 9.3 show, the σ_0 of the simulation seem to suffer less

from statistical fluctuations than the data. In addition, σ_0 is not (easily) available if there is a signal present. One cannot be sure that there is no signal present in data, in fact, the evidence points in the opposite direction around 126 GeV. In that respect, data histograms should not be used to obtain σ_0. On the other hand, σ_0 does depend on the shape of the background, and one cannot be sure that the shape in MC is the true shape of the background. The dilemma is to choose the 'least wrong' approach. Thus, we chose to use the MC distributions. The values of σ_0 in MC and data are in quite good agreement for the high statistics categories, so the impact should be rather small. What matters is the *relative* weighting of the different categories, not the absolute values of the weights. In either case: an incorrect set of σ_0 values to use for the weights would merely make the analysis suboptimal.

Category	Weight	
	DIPHOX+	Data
CP1	1.62	1.66
CP2	6.23	8.3
CP3	0.685	0.66
CP4	2.03	1.22
CP5	1.23	1.05
CP6	4.76	6.77
CP7	0.458	0.413
CP8	1.61	1.44
CP9	0.327	0.285

Table 9.3: The weights of the categories, according to Eq. (9.8), using the full, raw signal rate at 125 GeV obtained by applying the thesis selection to MC signal simulations and the σ_0 as obtained from both DIPHOX+ histograms and data.

The values of the weights can be seen in Table 9.3. The DIPHOX+ weights were the default weights – unless anything else is specified, these were used. The resulting weighted invariant mass spectrum using DIPHOX+ weights can be seen in Fig. 9.4. For comparison, the official data selected with the PRL selection [121], weighted in the same manner, is overlaid, where the weighted sum of events have been normalized in order to compare shapes.

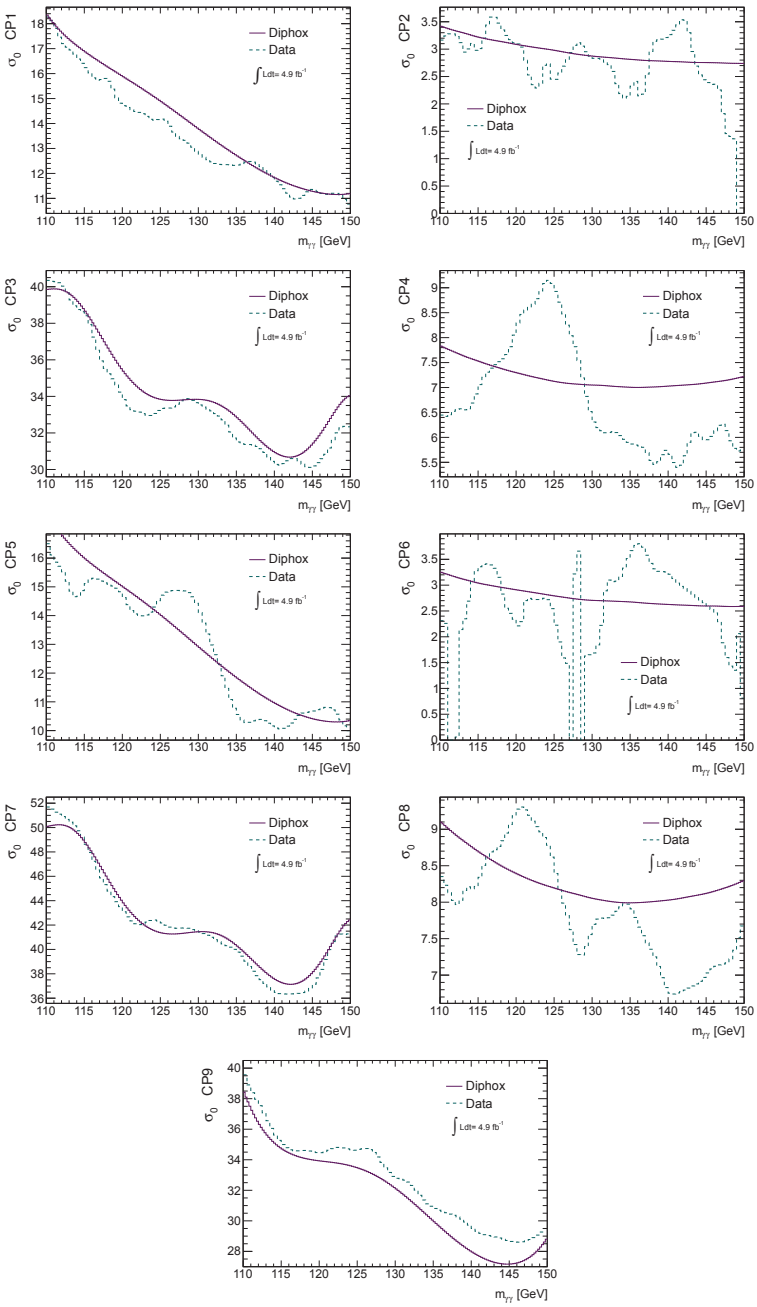

Figure 9.3: The uncertainty on the fitted signal amplitude, σ_0, as functions of invariant mass for data and the DIPHOX+ background template for each category.

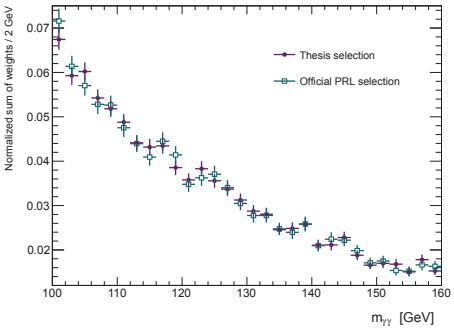

Figure 9.4: The weighted, invariant mass spectrum of the 2011 data, using thesis selection and the PRL selection and weights as in Table 9.3.

9.2 The Effect of a Signal on σ_0

The effect a signal has on σ_0 was evaluated. The DIPHOX+ histograms were used and a SM signal at 125 GeV was injected. The histogram errors were increased around the signal top, according to the additional number of events due to the injected signal. The effect of the signal on σ_0 of the categories was on average 3.3%, ranging from less than 1% for the smallest change in σ_0, to over 9% for the largest change. A breakdown for each of the categories can be seen in Table 9.4.

Whereas the σ_0 of the invariant mass distributions of the categories are only used for the weights, the σ_0 of the weighted invariant mass distribution is used to state the final result. The impact on σ_0 of an injected signal at 125 GeV, with an expected rate of 79.6 events, was also checked for the weighted model assigning the extra uncertainty of the bin due to the injected weighted signal, by adding the signal error to the background error in quadrature. The signal and background errors were found according to Eq. (9.10), respectively. The effect was a 3.6% increase in σ_0 with the injected signal; it changed from around 56.3 to 58.5 events. The observed significance with the presence of signal thus decreased by the same percentage. Since σ_0 is found in the sample at hand for each evaluated mass point and used to evaluate the significance of the excess (the fitted amplitude over σ_0), one can assume that a bias of this size exists when the evaluation is done in a sample with a 125 GeV Standard Model signal, causing an underestimation of the significance of the excess by around 3.6%.

9.3 Statistical Uncertainty on the Signal Yield

The signal yield is a function of the Higgs boson mass. In the Monte Carlo simulations, it can fluctuate from mass point to mass point, especially for low-

	DIPHOX+			Toys		
	σ_0	σ_0 w/signal	Change [%]	σ_0	σ_0 w/signal	Change [%]
CP1	14.9	15.3	2.7	13.6 ± 0.9	13.8 ± 1.0	1.7
CP2	2.98	3.28	9.2	2.80 ± 0.3	3.25 ± 0.3	16
CP3	33.8	34.3	1.3	32.8 ± 3.9	35.0 ± 4.3	6.8
CP4	7.12	7.34	3.0	6.87 ± 0.7	7.20 ± 0.6	4.7
CP6	2.79	3.02	7.6	2.84 ± 0.2	2.91 ± 0.3	2.5
CP7	41.4	41.7	0.9	40.2 ± 2.5	38.5 ± 2.9	−4.3
CP8	8.19	8.34	1.8	8.70 ± 1.0	8.54 ± 0.9	−1.8
CP9	33.5	33.7	0.7	33.2 ± 2.4	32.9 ± 2.6	−0.9

Table 9.4: The effect of an injected signal at 125 GeV on σ_0, as found from the DIPHOX+ samples and toys.

statistics categories. This can be seen in Fig. 9.5, displaying the expected (as gotten from the simulations) signal yield of the categories. In the official yields, to avoid statistical fluctuations in the signal rates, the values obtained are not the raw points gotten when running the selection over the simulation samples, but rather a polynomial fit to these points. Thus, in the official framework, the statistical uncertainty on the signal yield is not taken into account.

The discrepancy from a smooth evolution in the signal rate was found to be consistent with the statistics in the MC samples used to obtain them. To estimate the effect of the discrepancy, we propagated the uncertainties to the signal rate, by changing the value at one specific mass point in accordance with the relative uncertainty on the Monte Carlo sample. This changed the expected significance of this category at that mass point by approximately the same percentage. To give a concrete example: in the unconverted, central, high-p_{Tt} category (CP2), the signal yield obtained from Monte Carlo with the selection used in this thesis seemed to fluctuate down at around 120 GeV. The relative uncertainty on the sample is approximately 3.3%. Increasing the signal rate at 120 GeV by 3.3% leads to a change in the expected significance for this category alone at 120 GeV of 3.3%. The effect on the neighbouring mass point, 125 GeV, was negligible.

As already mentioned, these statistical uncertainties were neglected in the statistical analysis of HSG1. They should have next to no effect on the observed significance in data, which is completely dominated by the uncertainty in data, not the uncertainty stemming from the simulations; the statistics in MC is far exceeding the statistics in data. However, some consistency checks were performed.

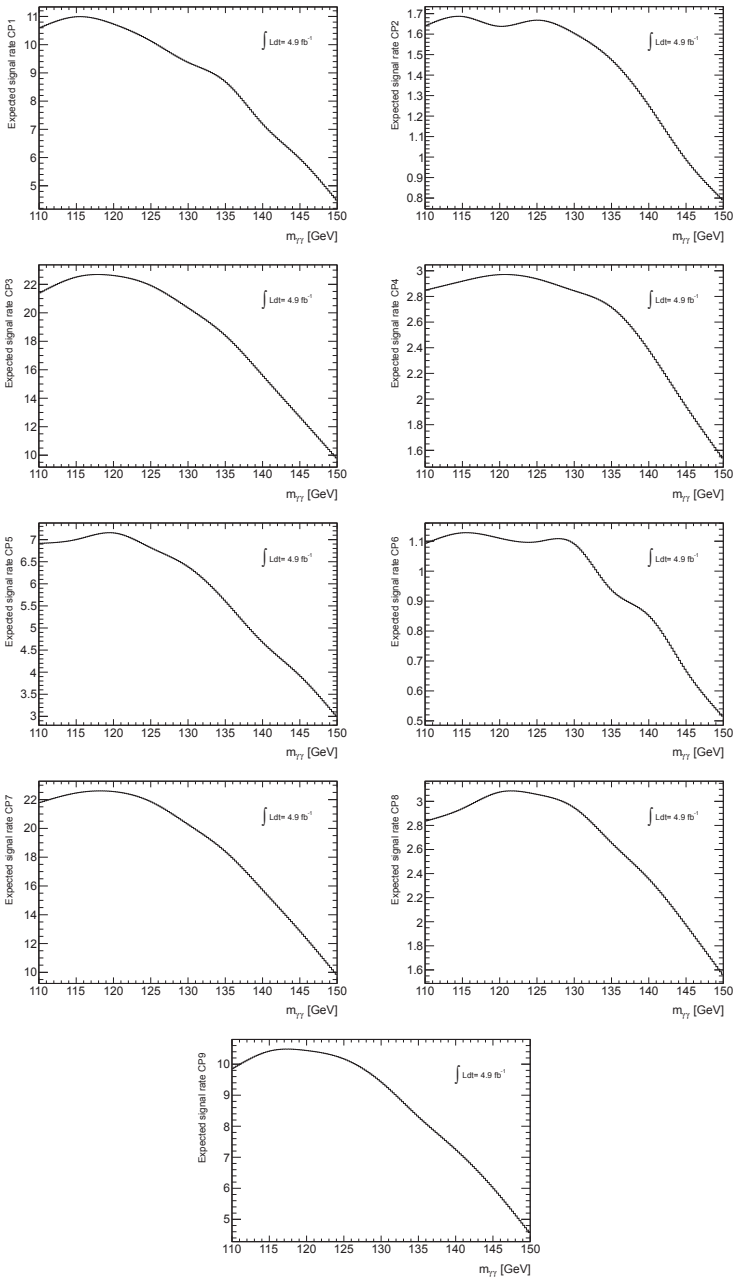

Figure 9.5: The expected signal yields, as obtained from an interpolation between the raw points gotten by running the thesis selection over the eleven mass points signal MC samples. Fluctuations in the yield are most obvious for the low-statistic categories.

We looked at the expected significance gotten from DIPHOX+ histograms (recall that the expected is gotten from an Asimov of the MC histogram, such that it mimics the level of statistics in data) in the weighted approach. The effect of changing the signal rate at 125 GeV, affecting the weights and the weighted signal model, on the resulting expected significance was of the miniscule order of 0.2% when changing the rate for the channel with the highest uncertainty, CP6, and 0.1% for the channel with the highest statistics, CP7. This impact on the expected sensitivity had next to no dependence on the mass. It seems that the resulting significance gotten from the weighted approach is not very sensitive to fine-tuning of the weights, and that the dominating factor is the statistics in data.

9.4 Closure Tests

Fitting the weighted, inclusive background spectrum with a Bernstein 4 polynomial gave a maximal fitted spurious signal amplitude of 4% of the background uncertainty for DIPHOX+, 11% for Sherpa+ and 4% for ResBos+ at 4.9 fb^{-1}. These are all within the requirement of 14%. Thus, this weighted approach passed the spurious signal test as described in Section 8.3.3.

Closure tests were performed to validate the code. Among these were making a sample of a weighted distribution of DIPHOX+ by combining the different categories according to their weights with the correct assigned uncertainties as in Eq. (9.10). The resulting distribution was fitted with the chosen background function, and to this smooth yield, a weighted signal was injected. This distribution was then fit with the chosen background function and a weighted signal model. Only when the code gave back the same signal as was injected, did we proceed.

Further validation of the code made it apparent that the inclusive spectrum, and the categories combined with weights all equal to one did not provide exactly the same numbers. Indeed, the sum of the categories and the inclusive spectrum were not indentical. This was due to the dijet category (CP10, which was introduced later), missing from the DIPHOX+ histograms, and the fact that these spectra were normalized to data in which the dijet category was implemented. The difference between the inclusive and the sum of the categories thus made up the missing CP10 category. This difference resulted in a difference of approximately 0.2% in the uncertainty on the background at 125 GeV, and thus equivalently in the significance, as the injected and fitted signal were the same. The resulting σ_0 and expected significance in DIPHOX+ were also tested with all the weights set to one. In comparison with the inclusive invariant mass spectrum and signal model, these agreed to better than 1%. Using the sum of the category histograms as the inclusive histogram, the bin content and errors were identical to the weighted

approach with the weights set to one. It was also checked that the signal model with weights set to one and the inclusive signal model were compatible. The code seemed to be doing what it was supposed to.

With these checks performed, we were ready to look at the significance using this weighted approach, which should be roughly comparable – although quite independent – to the official procedure of HSG1. Comparable, because the likelihood ratio method is effectively based on counting weighted events [113], independent because the setup, software and coding are different (apart from Minuit, the software used to do the fits).

9.5 Results

We will now have a look at the resulting expected and observed significances of the different analysis (different selections) of HSG1 and the one used in this thesis. For an explanation of the different selections, please see Section 7.7.

9.5.1 Public Results

The maximal excess in the official results were found at 126.5 GeV in the 2011 data. The expected significance of a SM signal at this mass in the 2011 data for the PRL-selection is 1.37σ [100], whereas the observed is 2.8. Taking the look-elsewhere effect in the range 110 – 150 GeV into account, this becomes 1.5σ [121]. The signal strength of the excess was around $\mu = 2.0 \pm 0.7$ [150]. The inclusive, expected significance for this mass with the selection presented for the ICHEP conference is 1.28σ for the 2011 data alone, whereas the observed is 2.7σ [127]. When exploiting the 10 categories used in that analysis, the expected significance increases to 1.60σ, and the observed significance is 3.5σ. This corresponds to a global significance of 2.2σ. The signal strength is about $\mu = 2.1 \pm 0.7$ [131].

9.5.2 Thesis Results

The biggest excess of events in the selection used for the thesis was also seen at 126.5 GeV. Using the weighted approach, the expected significance of a SM signal at this mass and a Bernstein polynomial for the background parametrization of order 4 was 1.39σ. The observed significance was 1.92σ, with a signal strength of $\mu = 1.3 \pm 0.7$. The background+signal fit to the weighted distribution can be seen in Fig. 9.6.

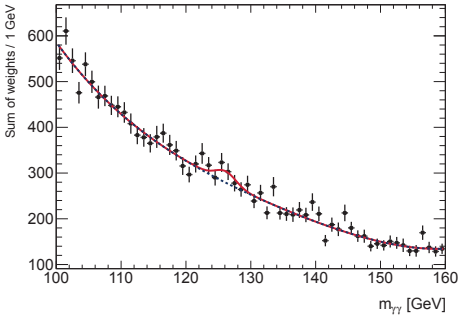

Figure 9.6: The sum of weights of the thesis selected 2011 data, with weights as in Table 9.3. The data is fitted with a background+signal model, given as a full line, where the background model is a Bernstein polynomial of the fourth order. The dashed curve indicates the fit with the signal subtracted.

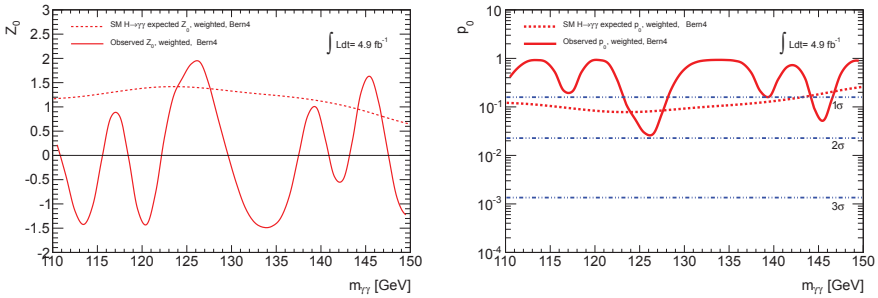

Figure 9.7: The expected (dashed) and observed (full) significance, Z_0 (left), and the expected (dashed) and observed (full) p_0 (right) when using the weighted approach and a Bernstein 4 polynomial for the background parametrization on the selection used in this thesis.

The expected and observed significance, Z_0, and the expected and observed p_0 when using the weighted approach and a Bernstein 4 polynomial for the background parametrization can be seen in Fig. 9.7. When taking the official PRL-selected data as in Fig. 9.4 through the weighting approach, the maximum excess is found at 125 GeV, with an observed signficance of $2.0\,\sigma$. The resulting observed significance, Z_0, and background compatibility, p_0, can be seen in Fig. 9.8. An overview over the results in the various analyses mentioned here can be seen in Table 9.5.

As a test, the effect of using the background rates obtained in data for the weights was also checked. Switching between the resulting weights, the impact on the expected significance in the weighted approach at 126.5 GeV was about 4%, from $1.39\,\sigma$ to $1.34\,\sigma$. The observed significance using data weights with respect to DIPHOX+ weights was unchanged, still at $1.92\,\sigma$ (only a change in the third digit was observed). The mass at which the biggest excess was observed was unchanged by changing the weights.

As mentioned earlier, this significance is probably underestimated by roughly 3.6%

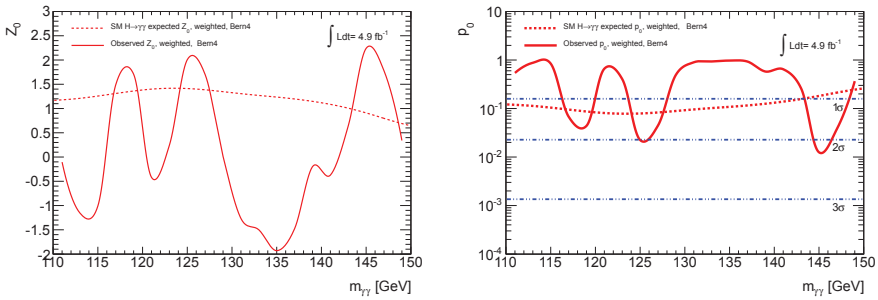

Figure 9.8: The expected (dashed) and observed (full) significance, Z_0 (left), and the expected (dashed) and observed (full) p_0 (right) when using the weighted approach and a Bernstein 4 polynomial for the background parametrization on the official data used for the PRL article.

if the excess in data had the expected size of the Standard Model signal, due to the impact of a signal on the σ_0. Thus a significance of $1.99\,\sigma$ would then in such a case probably be more correct. Furthermore, the maximal fitted signal amplitude is 105.2 events at $m_{\mathrm{H}} = 126.5$ GeV, in contrast to the SM expected signal of 78.3. The impact on σ_0 of an injected signal at 126.5 GeV with this amplitude was checked, and found to be an increase of 4.9%. Thus, more likely than 3.6%, the significance is underestimated by this percentage, and is of the order of $2.01\,\sigma$. These are, however, speculations under the assumption that the excess seen in data is due to a signal.

As a rough estimate of the look-elsewhere effect, the data can be used to obtain the trials factor. When counting the number of up-crossings of the observed Z_0 with the zero significance line in Fig. 9.7, one finds there are four (at approximately $m_{\gamma\gamma} \in \{116, 122, 137, 143\}$ GeV). Using this as an estimate of the average expected number, according to Eq. (8.6), this yields a trials factor of $f \simeq 4\,e^{-(1.92-0)/2} \simeq 1.53$. Thus, the significance when considering that the fluctuation could have occured anywhere in the considered mass range (the global significance) is $1.25\,\sigma$. For the significance taking into account that a signal would affect the σ_0, the local significance is reduced from $2.01\,\sigma$ to $1.31\,\sigma$ under the look-elsewhere effect. The global significances were $1.5\,\sigma$ for PRL (corresponding to a trials factor of about 1.87) and $2.2\,\sigma$ for ICHEP (corresponding to a trials factor of about 1.59).

Our observed result is almost $1\,\sigma$ less significant than the official result at the time of the PRL analysis. However, when taking the official PRL data through the weighted approach, the largest observed excess, albeit being at a slightly different mass, is similar to the one obtained using the thesis selected data. Thus, the selection of events seems not to be the reason for the difference in observed significance between the official procedure and the weighted approach. We get

	$m_{\mathrm{H}}{}^{max}$ [GeV]	Expected Z_0 [σ]	Observed Z_0 [σ]
PRL	126.5	1.37	2.8
ICHEP inclusive	126.5	1.28	2.7
ICHEP	126.5	1.60	3.5
PRL (weighted)	125.0	1.39	2.0
Thesis (weighted)	126.5	1.39	1.9

Table 9.5: The mass at the maximum excess, as well as the expected and observed significances for various analyses and selections of the 4.9 fb^{-1} of 2011 data. The official results of the PRL article in February 2012 [121], and the results presented at the ICHEP conference July 2012 [105], for the latter both the inclusive and the categorized samples, are stated. The results with the weighted approach presented in this thesis, both for the official PRL data and for the thesis selected data are also presented.

nearly the same sensitivity as the full machinery of HSG1 for the PRL selection, partly because the number of nuisance parameters of the background modeling is greatly reduced, from 27 with the 9-category selection, to five for this study. The sensitivity with respect to the ICHEP selection, adding a tenth category, is significantly lower, albeit the thesis selection being relatively closer to this selection than the PRL one. If further developed, and proven to be as sensitive as the complicated statistical procedure HSG1 is using now, this could be the method to be used in the future, to avoid the very intricate treatment of the categories and nuisance parameters related to them, while still having a good sensitivity.

9.6 Discussion of Systematic Uncertainties

The systematic uncertainties taken into consideration by the HSG1 group have been described in Section 8.1.3. These have not been directly incorporated into the analysis of the weighted approach described in this chapter. In this section, we will have a brief look at the expected effect of some of the systematic uncertainties, which are the uncertainties on the signal yield, the mass resolution, the migration between the categories due to Higgs boson $\mathrm{p_T}$ modeling and the spurious signal. Of course, to publish a result based on this approach, the analysis would need to be further developed, and the systematic uncertainties evaluated in a more detailed treatment, but the discussion to follow gives an indication of the importance of the systematic uncertainties.

The shape and normalization of the background are taken from the fit to data, so there are no systematic uncertainties related to this, apart from the spurious signal, which we will come back to shortly. Thus, for all systematic uncertainties,

δ, which scale the signal and background in the same way, only the impact on signal is left as a systematic uncertainty; $N_s + \delta$. Therefore, these systematic uncertainties influence the expected significance directly; $N_\sigma = \frac{\hat{N}_S}{\sigma_0}$ (remember that $\sigma_0^2 \simeq b$).

The uncertainties on signal yields will have a direct impact on the significance estimate; a 10% change in the signal expectation, N_S, will lead to a 10% change in the significance estimate, $N_\sigma = \frac{\hat{N}_S}{\sigma_0}$, as σ_0 will likely not change much. The signal injection test revealed that σ_0 as obtained from the weighted spectrum, which is used for the significance estimate, increased by approximately 3.6% when injecting a Standard Model Higg boson signal, leading the significance to be underestimated by this amount. Injecting a signal with 10% higher yield gave the very same σ_0 as injecting the nominal signal. Thus, the assumption that σ_0 does not change much under a resonably altered signal yield seems to hold.

Albeit yield and shape uncertainties on the background being eliminated because they are taken from the fit to data, the mass resolution will affect σ_0.[3] The narrower the peak, the smaller the amount of background under the peak. Despite the excellent mass resolution of the ATLAS ECAL, the statistical uncertainty on the background under the peak is still the dominant uncertainty. A narrow mass peak is therefore desirable. If the width of the signal changes by 14%, as is the estimated mass resolution uncertainty, the background changes by roughly the same amount. Thus, the denominator of the significance changes by approximately $\sqrt{1 + 0.14} - \sqrt{1} \simeq 6.8\%$, under the approximation that the background can be parametrized as a straight line under the signal peak and that the uncertainty of the signal amplitude is proportional to the square root of the background under the signal peak. Thus, with the same signal yield, but a change in mass resolution by 14%, the impact on the significance is around 7%.

The impact of migration of events between the categories can change the weighted signal model, as the different categories, with their varying resolutions, will be given other weights. To estimate the impact of this effect, we considered the largest migration effect, the Higgs p_T uncertainty, of $\pm 1.1\%$ in the low-p_{Tt} categories and $\mp 12.5\%$ in the high-p_{Tt} categories. We adjusted the signal model accordingly, by changing the signal yield used for the computation of the weighted signal model as in Eq. (9.9), where the weights, according to Eq. (9.8), used for this also were adjusted. The weights used to build up the weighted invariant mass spectrum, both for the background and data, were left untouched. This changed σ_0 and the fitted signal. The impact on the expected sensitivity at $m_H = 126.5$ GeV was a reduction of 0.3%, whereas there was a 0.2% increase in the observed significance

[3] With enough data available, the signal width could be added as an unconstrained nuisance parameter in the likelihood.

for the same mass.

The spurious signal will also impact σ_0. As indicated in Eq. (8.12), there is an ambiguity between the signal and the spurious signal. This ambiguity is partially removed thanks to the constraint term, $\rho(\theta_{SP})$, which introduces a penalty in the likelihood for the fits in which $\mu \neq 0$, such that the spurious signal cannot take up too large a part of an excess, only an amount corresponding to the uncertainty it is intended to account for.

For the unconstrained fit, in which the best fitted signal strength $\hat{\mu}$ is obtained, the spurious signal will not contribute at all; the maximal likelihood is obtained with the least amount of penalty, thus, all constrained nuisance parameters will be at their nominal values (zero), such that the constraint terms are all unity. So the spurious signal does not affect the fitted signal strength of the best fit. The question at hand is what happens to the width, σ_0, of the likelihood ratio parabola when introducing the spurious signal constraint term. For this evaluation, we make the simplification that the width of the parabola is independent of μ. Without the constraint term, the width of the parabola is σ_0. For this demonstration, we can approximate the likelihood with a χ^2, in which the only relevant parameters in the fit are μ and μ_{SP}; the signal strength and the strength of the spurious signal, respectively;

$$\chi^2 = \frac{(\mu + \mu_{SP} - \hat{\mu})^2}{\sigma_0^2} + \frac{\mu_{SP}^2}{\sigma_{SP}^2} \ . \tag{9.11}$$

The minimum is given by

$$\frac{\partial \chi^2}{\partial \mu} = \frac{2(\mu + \mu_{SP} - \hat{\mu})}{\sigma_0^2} = 0 \tag{9.12}$$

$$\frac{\partial \chi^2}{\partial \mu_{SP}} = \frac{2(\mu + \mu_{SP} - \hat{\mu})}{\sigma_0^2} + \frac{2\mu_{SP}}{\sigma_{SP}^2} = 0 \tag{9.13}$$

$$\Rightarrow \boxed{\mu = \hat{\mu}, \quad \mu_{SP} = 0} \ . \tag{9.14}$$

To find the width, we substitute μ_{SP}, as found from Eq. (9.13), into Eq. (9.12) and differentiate again with respect to the parameter of interest, μ:

$$\frac{\partial \chi^2}{\partial \mu} = \frac{2(\mu + \frac{(\hat{\mu}-\mu)\sigma_{SP}^2}{\sigma_0^2+\sigma_{SP}^2} - \hat{\mu})}{\sigma_0^2} \tag{9.15}$$

$$\frac{\partial^2\chi^2}{\partial^2\mu} = \frac{2}{\sigma_0^2 + \sigma_{SP}^2} = \frac{2}{\sigma^2} \ , \tag{9.16}$$

where σ is the effective resolution of μ. Thus, it is demonstrated that the width of the parabola increases when introducing this type of constrained nuisance parameter. The resolution of μ increases by σ_{SP} in quadrature when a spurious signal is implemented as a systematic uncertainty.

For the estimation of the increase in the resolution of μ due to the spurious signal, the uncertainty on the background-only fit to the weighted spectrum of simulation should be added in quadrature with the fitted spurious signal amplitude (which is used as the constraint size) in this fit. For the mass at which the maximal spurious amplitude is found ($m_{\mathrm{H}} = 147$ GeV), $\hat{s}_{SP} = 2.92$. The background uncertainty at the mass of the maximum excess, $m_{\mathrm{H}} = 126.5$ GeV i $\sigma_0 = 56.2$. Thus the impact is

$$\frac{\sqrt{56.2^2 + 2.92^2}}{56.2} \simeq 1.001, \tag{9.17}$$

about a per mil. This demonstrates also the robustness of the background model selection criteria.

The relative weights will scale as $\ln\left(1 + \frac{s}{b}\right) \simeq \frac{s}{b}$, since the signal-to-background rate is small. The background is taken from the uncertainty of the fit to simulation distributions of the categories, $b = \sigma_0^2$, so for the weights, uncertainties on the background must also be considered. However, as already mentioned, using weights which are not matching the expected sensitivity of the categories will merely render the analysis suboptimal. In addition, the systematic uncertainties that will scale both s and b will have no impact on the weights, and we have seen that the impact of the other systematic uncertainties are rather small.

Chapter 10

Conclusion

In this doctoral thesis, the search for a Standard Model Higgs boson decaying into two photons with the ATLAS detector connected to the LHC accelerator at CERN is described. The work was done as part of the Higgs SubGroup 1 (HSG1) of ATLAS, occupied with the $H \to \gamma\gamma$ search. The data collected in 2011 at a center-of-mass energy of $\sqrt{s} = 7$ TeV, corresponding to 4.9 fb^{-1}, is used to evaluate the existence of a SM Higgs boson. Several small studies were performed, as part of the puzzle, to be as sure as possible of the correctness of the complex published analyses. The HSG1 group has moved on and slightly improved the selection of the $\gamma\gamma$ candidate events since the studies described here: among other things, the p_T cuts, the categorization of Higgs boson candidate events, the method of finding the primary vertex and the isolation were changed.

The cuts on the transverse momenta of the two photons had not been evaluated since the 1990's; this was studied here. The sensitivity of the log-likelihood ratio test-statistic was estimated using an Asimov dataset, where the signal was taken from simulation, and the background was taken from the full 2011 data, both in a $\pm$ 2 GeV window around the hypothesized Higgs boson mass. The p_T cuts which rendered the highest log-likelihood ratio were taken as estimates of the optimal cuts. A linear fit suggests cuts on the transverse momenta which vary with the invariant mass of the diphoton pair; $p_T^{\gamma_{leading}} > \frac{m_{\gamma\gamma}}{2.5}$ GeV and $p_T^{\gamma_{subleading}} > \frac{m_{\gamma\gamma}}{3.4}$ GeV. A net gain in the inclusive sample of 3.2% in approximate sensitivity, as evaluated by $\frac{S}{\sqrt{B}}$, was obtained. However, some categories loose sensitivity and some gain; more studies are needed to be sure of the effect on the categories and the overall sensitivity. The use of p_{Tt} in the categorization has possibly already absorbed most of the gain that would come from using variable p_T cuts instead of fixed p_T cuts. Implementing variable cuts would require a new

evaluation of background parametrizations; if more distributions turn out to be adequately described by an exponential function, a gain in sensitivity could be achieved.

Describing the background of the $H \to \gamma\gamma$ signal is of utmost importance for the search. Since the signal is a small excess on top of a large, smoothly falling background, even small uncertainties on the background can have a large impact on the observed signal. The systematic uncertainty on the background was implemented into the likelihood function as a copy of the signal model, and therefore called *the spurious signal*. The constraint sizes on these spurious signal nuisance parameters, one for each category, were set to the amplitude of the spurious signal found when fitting the distributions of three internally produced, high statistics background samples with a background+spurious signal parametrization. This amplitude had to be smaller than *either* 10% of the expected signal *or* 20% of the background uncertainty at 10 fb^{-1} for the background parametrization to be accepted as unbiased. Although I have not analyzed the 2012 data myself, the work I did as part of HSG1 on background modeling (*e.g.* selection of functions) was used in the interpretation of this data [5, 105].

The final discriminant in the search for $H \to \gamma\gamma$ is the invariant mass of the diphoton pair. An alternative to the statistical procedure used in ATLAS is to fit the weighted sum of the invariant mass spectra of categories of events. In this approach, each event is assigned a weight based on the expected sensitivity of the category it belongs to, which is driven by the total signal and background yields and the invariant mass resolution of the signal. The maximum excess in the 2011 data is seen at $m_{\text{H}} = 126.5$ GeV. The expected significance at this mass using the weighted approach is $1.39\,\sigma$, whereas the observed local significance is $1.9\,\sigma$. Taking the look-elsewhere effect into account, the global deviation for the considered mass range of 110 – 150 GeV corresponds roughly to $1.3\,\sigma$.

The maximum excess was also seen at the same mass in the official analysis. The official expected significance of an excess due to a SM Higgs boson in 2011 data was $1.37\,\sigma$ with the so-called PRL selection (February 2011), and $1.60\,\sigma$ with the so-called ICHEP selection (July 2012). The respective local observed significances were $2.8\,\sigma$ and $3.5\,\sigma$, corresponding to $1.5\,\sigma$ and $2.2\,\sigma$ global significances.

The results from the CMS experiment on the search for $H \to \gamma\gamma$ in 2011 data, consisting of 4.8 fb^{-1}, as published in Ref. [114], also concerned the mass range 110 – 150 GeV. The largest excess over the Standard Model background expectation was at $m_{\text{H}} = 124$ GeV, of $3.1\,\sigma$ significance, corresponding to a global significance of $1.8\,\sigma$. The expected sensitivity was not published, but a rough estimate based on the uncertainty on the estimated signal strength at the maximum excess, 2.1 ± 0.6 times the Standard Model signal strength, indicates around $1.7\,\sigma$.

The event selection used in this thesis resides between the ATLAS PRL and ICHEP selections; although a direct comparison of the results is not possible, they are comparable. However, the indications for a SM Higgs boson signal in the data analyzed in this study are somewhat smaller than in the official results on the same amount of data, albeit the more similar expected significances.

My results are similar to the official results of ATLAS and CMS. They weakly hint at the production and decay of the SM Higgs boson with $m_{\mathrm{H}} = 126.5$ GeV into two photons in the 2011 data. However, on their own, they were non-conclusive; as discussed in the Epilogue, more data was needed to determine the nature of this excess.

Chapter 11

Epilogue

When finishing up the analysis of this thesis, a new particle ressembling the Standard Model Higgs boson was discovered. Bringing my analysis of the 2011 data to an end after the discovery, it was naturally difficult to stay unaffected, a bias is not humanly possible to fully avoid. However, with the results in this thesis alone, as with the official 2011 results, the outcome of the search for the SM Higgs boson was still unclear. At this stage, the results were still far from a discovery, but rather intriguing hints, to be kept an eye on. This is exactly what ATLAS did, and blinding the data of 2012 was taken very seriously by HSG1, as described in Section 8.3. To the level possible, the scientific method was preserved, both in ATLAS and in this thesis. We will now give a rough historical overview of the milestone notes of HSG1 (of which all the internal notes were co-authored) and development of the analysis of $H \to \gamma\gamma$. The discovery of a Higgs boson candidate through the combination of the various decay channels will be addressed, before prospects of the future are given at the very end.

11.1 $H \to \gamma\gamma$ Results

The first note with data was for the Aspen conference in February 2011, and contained the analysis of 37 pb^{-1} of 2010 data [151, 152]. It was aimed at measuring the composition of background in data, and contained a projection for the expected exclusion sensitivity with 1 fb^{-1}. At this point, 83 diphoton events were found in the mass range from 100 to 150 GeV, and the expected exclusion sensitivity with 1 fb^{-1} was estimated to be 3.2 – 4.2 times the Standard Model cross-section in the 110-140 GeV mass range. The decomposition yielded $83 \pm 14\%$, $13 \pm 7.6\%$, 1.4 ± 0.94 and $3.3 \pm 0.76\%$ diphoton, photon-jet, dijet and Drell-Yan contributions

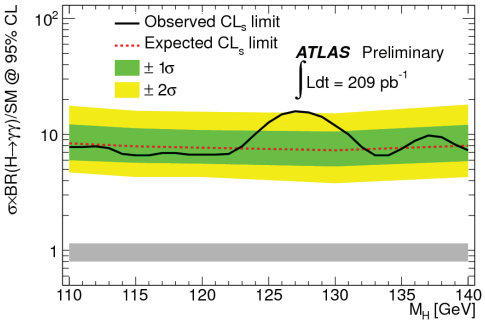

Figure 11.1: Exclusion limit at the 95% CL on the cross section of $H \to \gamma\gamma$ in relation to the SM prediction, presented for the PLHC conference in June 2011 [154]. The expected exclusion limit is indicated by the dashed line. Fluctuations of the background around this expectation at the $\pm 1\sigma$ and $\pm 2\sigma$ level are indicated by the colored bands. The observed result is given by the full line. If the observation is below one, a SM Higgs boson of this mass is excluded at the 95% CL. The theoretical uncertainty on the predicted Standard Model cross section was not included in the experimental limit, but is shown as a band around 1.

respectively.

In March 2011, the Moriond conference was held. For this conference, a note aimed at the search for a SM Higgs boson based on 38 pb^{-1} of 2010 data was written [115, 116], in which 99 events with a diphoton invariant mass between 100 and 150 GeV were found[1]. The angles of the photons were estimated from the PV with largest sum of p_T^2 of the tracks associated to it (in case there were more than one PV), and the measurement in the first sampling of the calorimeter. The expected upper limit on the cross-section for the search was around 20 times the Standard Model cross-section prediction, which was already comparable to the sensitivity of the $H \to \gamma\gamma$ search of Tevatron [153]. In the range of 110 – 140 GeV, the observed exclusion ranged from 8 times the Standard Model at 127 GeV, to 38 times at 116 GeV.

At the time of the PLHC conference in June 2011, a note was written based on 209 pb^{-1} of data, in which 926 diphoton candidate events were found [154]. The expected exclusion limit was just under 7 times the SM cross section. No statistically significant excess was observed in the range 110 – 140 GeV. However, there was a rather large deviation from the expected exclusion limit around 127 GeV, at the 2σ level, as can be seen in Fig. 11.1. The probability of such an excess to occur anywhere in the considered mass range was approximately 30%. In retrospect, it is entertaining and perplexing to see such a clear deviation from the background exactly at the region where a signal today is confirmed. At the time, it was merely taken as a fluctuation of the background.

[1] With respect to the previous publication, it was among other things benefitted from a better estimation of the luminosity, additional recovered data and improved photon identification with smaller systematic uncertainty.

In July 2011 the EPS conference inspired a paper, which was published in Physics Letters B [155–159]. In this paper, the limits for the production of a signal in 1.08 fb^{-1} were presented. At this point, categorization was introduced to the analysis. Five such were used, as defined in Section 7.8, but they did not yet exploit the p_{Tt} of the diphoton system. Photon pointing was introduced instead of utilizing the inner detector primary vertex reconstruction, which made the angles of the photons more precise, and thus improving the invariant mass resolution. The trigger was increased from demanding 15 GeV to 20 GeV in transverse momentum of the photon candidate. Within the mass range 100 – 160 GeV, 5063 events remained after the selection. Upper limits on the production cross section of 2.0 to 5.8 times the Standard Model cross section were set in the mass range 110 – 150 GeV, where the expected limits ranged from 3.3 to 5.8. The result was consistent with random fluctuations of the background around the median limit. Plots showing the exclusion limit and background compatibility can be seen in Fig. 11.2.

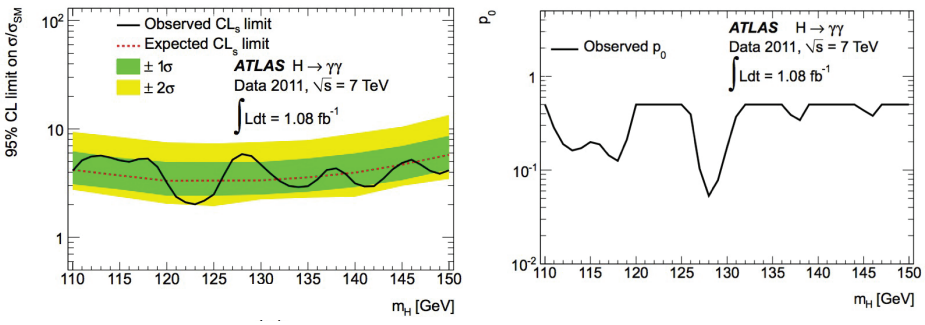

Figure 11.2: The exclusion limit on the cross section normalized to the Standard Model cross section is displayed to the left, and the probability of the data being compatible with the background-only hypothesis, p_0, is displayed to the right, both as a function of the hypothesized Higgs boson mass, as presented for the EPS conference in July 2011 [155]. For the background-only hypothesis, the median result is expected to be $p_0 \simeq 0.5$.

The CERN Council in December 2011 marked the next milestone. At this point, the amount of data gathered was about five times as much as at the previous conference (EPS 2011) for which an article was written. In addition to a conference note, an article was written and published in Physical Review Letters [95, 100, 120, 121]. At this point, the nine categories were applied, introducing the p_{Tt} of the diphoton system. For the background, all the categories were fitted with a single exponential. In the mass range 100 – 160 GeV, 22 489 diphoton candidate events were observed. A correction of the position in z of the photons in the end-caps was applied to take into account an oscillation pattern not seen in simulation.

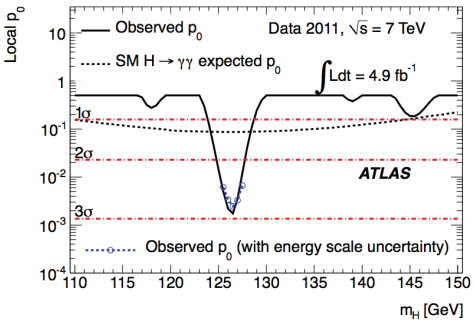

Figure 11.3: The probability, p_0, of the data to be in compliance with the background-only hypothesis as a function of the hypothesized Higgs boson mass for the 2011 data, published in PRL February 2012 [121]. The expected (observed) p_0 for a SM H $\rightarrow \gamma\gamma$ signal is indicated by the dashed (full) line. Fluctuations from the background-only hypothesis of 1, 2 and 3 standard deviations are indicated by the horizontal, dashed lines. The open circles are results when the energy scale uncertainty for the peak position is taken into consideration.

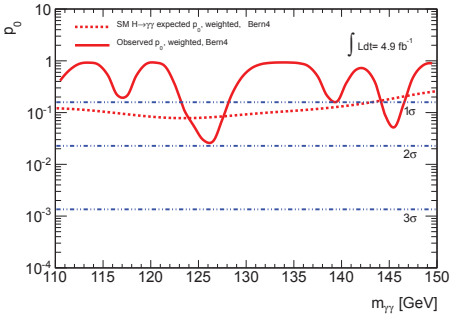

Figure 11.4: The expected (dashed) and observed (full) p_0 in 2011 data with the weighted approach as described in Chapter 9 and a Bernstein polynomial of 4^{th} order background parametrization for the selection used in this thesis.

This thus influenced the pseudorapidity, improving the resolution of the invariant mass. The measure for compatibility with the background hypothesis, p_0, can be seen in Fig. 11.3. The largest excess with respect to the background-only hypothesis was observed at 126.5 GeV in the mass range 110 – 150 GeV. The local significance of the excess was at 2.8 standard deviations, which was reduced to 1.5 standard deviations when taking the look-elsewhere effect into account. The expected limit varied between 1.6 and 2.9 times the Standard Model cross section in the considered mass range, whereas the observed exclusions ranged from 0.9 and 4.0 times the Standard Model cross section. In the mass ranges 113 – 115 GeV and 137.5 – 136 GeV, the Standard Model Higgs boson was excluded at 95% confidence level.

In Fig. 11.4 (from Chapter 9), the expected and observed p_0 for 2011 data as a function of the diphoton invariant mass found in the weighted approach with the thesis selection can be seen. There are several structures in the observed significance. Looking at this figure, one can wonder what the new data might bring, perhaps for instance the second most significant dip around 145 GeV will be a place to keep an eye on for a new resonance, or perhaps it is just a statistical fluctuation.

For the ICHEP conference in July 2012, 5.9 fb^{-1} of 2012 data recorded with a center-of-mass collision energy of $\sqrt{s} = 8$ TeV was added to the 2011 data recorded with $\sqrt{s} = 7$ TeV [105]. These were the results that were used in the July 2012 "discovery paper" [5], which we shortly will come back to. In the mass range 100 – 160 GeV, 59 059 diphoton events were observed. A tenth category was added, specialized on the VBF production mechanism, in which cuts on two forward jets were part of the selection criteria. Much effort was put into the background parametrization of the invariant mass spectra in the categories, as described in Section 8.3. For the VBF category, the exponential function was used, and selected functions for the remaining nine categories can be seen in Table 8.8. In addition, the photon identification was moved from a cut based discrimination to a neural network based one, the cut on the subleading photon was increased from 25 GeV to 30 GeV, the p_{Tt} threshold between the categories was increased from 40 GeV to 60 GeV, the selection of the primary vertex changed to include track information due to the jet selection and the isolation changed to using topological clusters. The search for $H \to \gamma\gamma$ was performed in the mass range 110 – 150 GeV. The expected exclusion limits at 95% CL ranged from 0.8 and 1.6 times the Standard Model cross section, corresponding to an expected exclusion in the range 110 – 139.5 GeV. The Standard Model Higgs boson was excluded in 112 – 122.5 GeV and 132 – 143 GeV, as can be seen in Fig. 11.5. The presence of a signal is particularly hard to rule out around the middle of the mass spectrum. The background compatibility of the data is also shown in Fig. 11.5, an excess of events was seen at $m_H = 126.5$ GeV with a local significance of 4.5σ, corresponding to a global significance of 3.6σ, with a signal strength of $\mu = 1.9 \pm 0.5$.

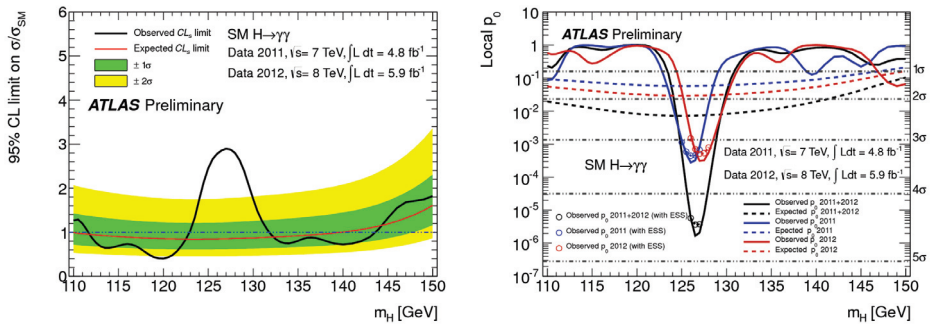

Figure 11.5: The results presented for the ICHEP conference in July 2012 [105]. Left: exclusion limit on the signal cross section with respect to the Standard Model prediction. The expected (observed) exclusion in the absence of a signal is given as a red (black) full line. Right: probability, p_0, of the data to be in compliance with the background-only hypothesis. The expected (observed) p_0 is given as a dashed (full) blue line for 2011, red for 2012 and black for the full dataset. The open circles are results taking the energy scale uncertainty for the peak position into consideration.

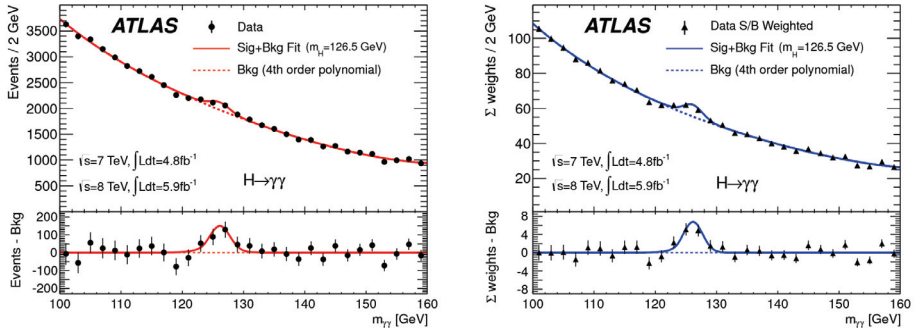

(a) Unweighted (b) Weighted

Figure 11.6: Invariant mass spectrum of the H $\to \gamma\gamma$ search for the July 2012 "discovery paper" [160]. The spectrum is fitted with a 4^{th} order Bernstein polynomial (dashed), and the sum of a 4^{th} order Bernstein polynomial and a $m_{\text{H}} = 126.5$ GeV signal model (full). The lower pad displays the data and fit results where the expected background from the background-only fit has been subtracted. The small but clear excess of events around 126.5 GeV can be seen. The weights applied in the weighted spectrum are defined to be $\ln(1 + s_i/b_i)$, where s_i is 90% of the expected signal for $m_{\text{H}} = 126.5$ GeV.

The invariant mass spectrum of the H $\to \gamma\gamma$ search for the combined 2011 and 2012 data up to July can be seen in Fig. 11.6, both for the inclusive unweighted spectrum, and for the spectrum when weighting the categories according to their expected sensitivity. The weights applied in the weighted spectrum are defined to be $\ln(1 + s_i/b_i)$, where s_i is 90% of the expected signal for $m_{\text{H}} = 126.5$ GeV. The spectra are fitted with a 4^{th} order Bernstein polynomial, shown as a dashed curve, as well as the sum of a 4^{th} order Bernstein polynomial and a $m_{\text{H}} = 126.5$ GeV signal model as a full line. The lower pads display the data and fit results where the expected background from the background-only fit has been subtracted. The small but clear excess of events around 126.5 GeV is seen.

For the CERN Council in December 2012, an update of the H $\to \gamma\gamma$ analysis was presented [161], for which the amount of 2012 data was more than doubled with respect to the July 2012 "discovery paper", from 5.9 fb^{-1} to 13 fb^{-1}. In the mass region 100 – 160 GeV, 77 430 diphoton candidate events were selected. The events of 2011 data were classified into the 10 categories as in the ICHEP 2012 conference note, whereas the 2012 data were divided into 12 categories. Two categories aimed at the associated production of the Higgs boson with a vector boson were added, one singling out the vector boson decaying to leptons, $ZH \to ll\gamma\gamma$ or $WH \to l\nu\gamma\gamma$, and one singling out the vector boson decaying into jets, $ZH \to jj\gamma\gamma$ or $WH \to jj\gamma\gamma$. For the lepton category, cuts demanding at least one electron or muon were included in the selection criteria, and for the dijet

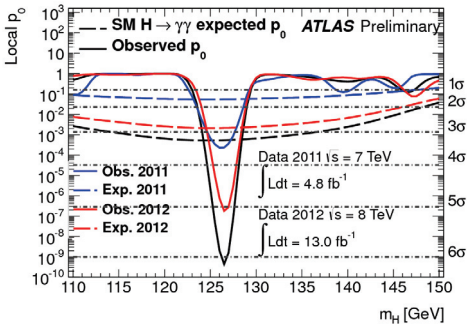

Figure 11.7: The expected (dashed) and observed (full) p_0 of the official analysis of $H \to \gamma\gamma$ as of December 2012 [161]. The results of the 2011 and 2012 data are shown separately, in blue and red respectively, and the combined result is shown in black. The excess is consistent in the two years of data-taking, and reaches over $6\,\sigma$ for the full dataset. The excess is more pronounced than expected from the SM Higgs boson, with a signal strength of $1.80 \pm 0.30(\text{stat})\,^{+0.21}_{-0.15}(\text{syst})\,^{+0.20}_{-0.14}(\text{theory})$.

category two jets within a certain separation in the detector and a certain invariant mass were sought for. Some additional changes in the analysis with respect to the ICHEP 2012 conference analysis were that track isolation was added to the calorimeter isolation, and that the primary vertex was estimated using a neural network. The expected and observed p_0 can be seen in Fig. 11.7, both for 2011 and 2012 separately, and for the two years combined. The excess is consistent in the two years of data-taking, and reaches $6.1\,\sigma$ at a mass of $126.6 \pm 0.3(\text{stat}) \pm 0.7(\text{syst})$ GeV for the full dataset – a single channel discovery. This is a somewhat stronger signal than expected from the SM Higgs boson, with a signal strength of $1.80 \pm 0.30(\text{stat})\,^{+0.21}_{-0.15}(\text{syst})\,^{+0.20}_{-0.14}(\text{theory})$.

The latest $H \to \gamma\gamma$ results from the CMS experiment are from the July 2012 "discovery article" [6], based on the results in the conference note for the July 2012 ICHEP article [162]. For a Higgs boson mass of $m_H = 125$ GeV, an excess of events above the expected Standard Model background is observed with a local significance of $4.1\,\sigma$, as can be seen in Fig. 11.8. Taking the look-elsewhere effect into account for the mass region 110 – 150 GeV, the significance is estimated to be $3.2\,\sigma$. The signal strength of this excess is 1.56 ± 0.43 times the signal expected from the SM Higgs boson. Thus the results of the two general purpose LHC experiments strongly confirm each other.

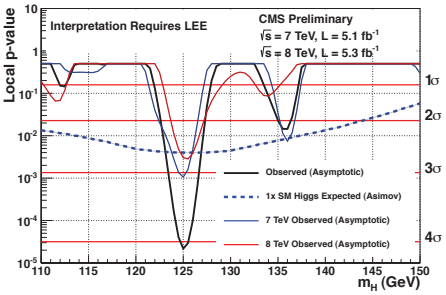

Figure 11.8: The expected (dashed) and observed (full) p_0 of the CMS $H \to \gamma\gamma$ analysis as of July 2012 [162]. The results of the 2011 and 2012 data are shown separately, in blue and red respectively, and the combined result is shown in black. The excess is consistent in the two years of data-taking, and reaches $4.1\,\sigma$ for the full dataset. The excess is more pronounced than expected from the SM Higgs boson, with a signal strength of 1.56 ± 0.43 at $m_{\mathrm{H}} = 125$ GeV.

11.2 Discovery of a Higgs Boson Candidate

As mentioned in the introduction, to render the search for the Higgs boson as sensitive as possible, the various decay channels of the Higgs boson should be combined; this was done as described in Ref. [132, 133]. The result of the combination of the Higgs boson searches in the July 2012 "discovery paper" [5] can be seen in Fig. 11.9, where three plots are displayed, all as a function of the hypothesized Higgs boson mass in the range 110 – 600 GeV. The plot on top shows the 95% CL exclusion limit on the signal strength of the process, normalized to the SM signal strength. The exclusion expectation under the background-only hypothesis is given as a dashed line; where this line drops under 1, the experiment is sensitive enough to exclude the SM Higgs boson with at least 50% probability. This is the case for nearly the full mass range, except at the high end, close to 600 GeV. The expected $\pm 1\,\sigma$ and $\pm 2\,\sigma$ fluctuations of the background are indicated by the green and yellow bands, respectively. The Standard Model Higgs boson is excluded at 95% CL in the mass range 111 – 559 GeV, except for the narrow region 122 – 131 GeV. Thus, in this narrow region where the SM Higgs boson cannot be excluded, exclusion of the background hypothesis must be considered. The compatibility with the background-only hypothesis is given by p_0 in the middle figure. The expectation from a SM signal is given by the dashed line, whereas the observation is given by the full line. Across the mass range, the compatibility with background hypothesis is good, except for a region around 126 GeV, where the compatibility with background is poor. The probability that the background has fluctuated to produce such a signal-like excess corresponds to a $6\,\sigma$ deviation. The requirement for a discovery of new physics is traditionally in particle physics set to $5\,\sigma$, approximately a three-in-ten-million chance of the observation not being due to a signal, but merely an unlikely fluctuation of the background. In the last of the three plots, the signal strength is displayed, including an approximate $\pm 1\,\sigma$ uncertainty on its estimate, indicated by the cyan band. The

signal strength is compatible with the background ($\mu = 0$) across the mass range, except around 126 GeV, where it peaks, reaching 1.4 ± 0.3 at the fitted mass of $126.0 \pm 0.4(\text{stat}) \pm 0.4(\text{sys})$ GeV.

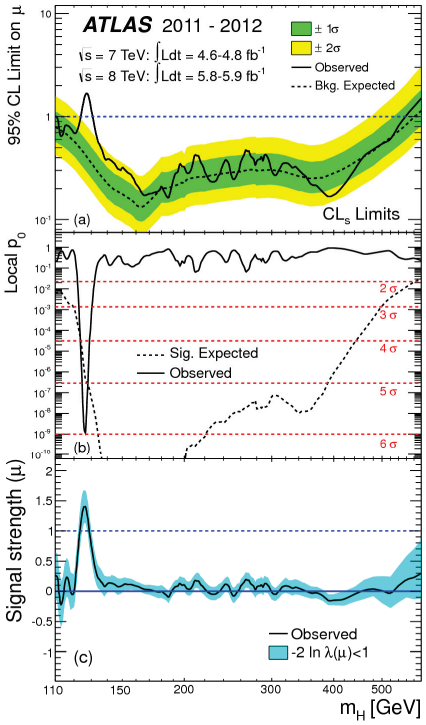

Figure 11.9: Results of the combined Higgs search for the July 2012 "discovery paper" [5]. The plots are all functions of the hypothesized Higgs boson mass, ranging from 110 – 600 GeV. The 95% CL exclusion limit on the signal strength normalized to the SM signal strength, μ, can be seen on top. The exclusion limit expectation under the background hypothesis is shown as a dashed line, the expected $\pm 1\sigma$ and $\pm 2\sigma$ fluctuations of the background are indicated by the green and yellow bands, respectively. The observed result is given by the full line. The signal hypothesis can clearly not be excluded in the low-mass region. The probability, p_0, of the data being in compliance with the background-only hypothesis is given in the middle plot. The expectation of a SM Higgs boson signal is given by the dashed line, the observation by the full line. The probability of the data being in compliance with background for $m_{\text{H}} = 126$ GeV is $1.7 \cdot 10^{-9}$. In the bottom, the signal strength, μ, with an approximate $\pm 1\sigma$ uncertainty indicated by the cyan band can be seen, reaching 1.4 ± 0.3 at the maximum excess and being in compliance with background across the rest of the mass range.

In Fig. 11.10, the evolution of p_0 in the combined Higgs analysis can be seen, for some milestone presentations of the results. The excess has been consistent in all the datasets, and with the exception of the reduction of the excess from the CERN Council in December 2011 to the Physical Review Letters D article in Spring 2012, it has been steadily increasing. As already mentioned, in July 2012 the p_0 crossed the "magical" 5σ limit, needed to claim a discovery.

The CMS experiment at CERN has also reported on findings in the search for the SM Higgs boson. The combined results of CMS [6] can be seen in Fig. 11.11. The probability for the data to be in compliance with the background, p_0, is shown separately for all the studied Higgs boson decay channels, $H \to \gamma\gamma, ZZ, WW, bb, \tau\tau$, as well as for the combination of these. Around $m_{\text{H}} = 125$ GeV, the compatibility with background is poor; an excess of events with respect to the background hypothesis is seen, reaching a significance of 5.0σ.

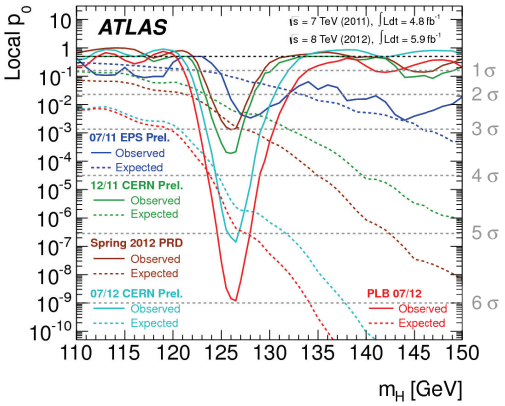

Figure 11.10: The evolution of p_0 in the combined Higgs analysis for some milestone presentations [160]. With the increase of integrated luminosity and continuous optimization of the analyses, the excess around 126 GeV got more significant.

The results give a fitted mass of $125.3 \pm 0.4(\text{stat}) \pm 0.5(\text{syst})$ GeV, with a signal strength of 0.87 ± 0.23. The results of CMS and ATLAS are consistent, and the papers claiming the observation of a new particle with properties consistent with the Standard Model Higgs boson by CMS and ATLAS were published together in the PLB journal in July 2012. This scientific achievement was considered to be the breakthrough of the year by Science magazine [163–165]

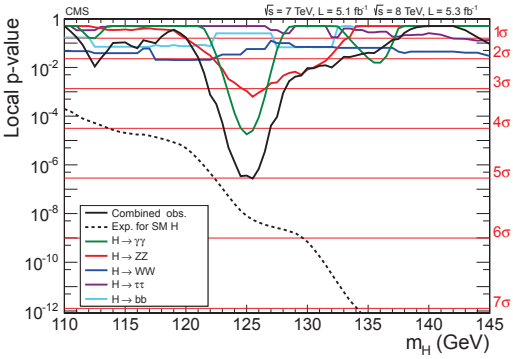

Figure 11.11: Results of the combined Higgs search of CMS for the July 2012 "discovery paper" [6], based on 5.1 fb^{-1} of 2011 data and 5.3 fb^{-1} of 2012 data. The background compatibility probability, p_0, is shown as a function of the hypothesized Higgs boson mass in the mass range $m_{\text{H}} = 110-145$ GeV, separately for the studied decay channels, $H \to \gamma\gamma, ZZ, WW, bb, \tau\tau$ and for the combination of these. The combined observation is shown as a black full line, while the expectation from a SM signal is shown as a dashed line. The observation reaches the "magical" 5σ criterion for claiming a discovery of a new particle.

11.3 Outlook

An era has now ended; the hunt for a 'Higgs boson'-like particle is successfully completed. Now begins the era of measuring the new particle that was observed, pinpointing its properties, to see whether they are in compliance with the ones of the Standard Model Higgs boson. Furthermore, one must be on the outlook for siblings of the new particle. When searching for such additional resonances, the observed signal must from now on be taken into account in the background to the search, in order not to bias the background estimation in the rest of the mass spectrum. There is no doubt that there *is* a new particle present – the question to be answered, is whether it truly is the Standard Model Higgs boson.

Luckily, at the mass where the candidate Higgs boson is found, there is a variety of different decay channels available, as can be appreciated in Fig. 6.4. The channels most important for discovery are the sensitive, high mass resolution $\mathrm{H} \to \gamma\gamma$ channel, the sensitive, high mass resolution $H \to ZZ \to 4l$ channel, and the sensitive, but poor mass resolution $H \to WW \to l\nu l\nu$. In addition, the lower sensitivity channels $H \to bb$ and $H \to \tau\tau$ are also feasible to study at this Higgs boson mass with larger datasets and are important to confirm the full set of predictions made for Higgs boson decays. The range of available decay channels makes it possible to retrieve a great deal of information about how this particle behaves, making the job of pin-pointing whether this truly is in accordance with the Standard Model behaviour easier. Properties that must be measured to determine the nature of the particle include its mass, spin (including parity), behavior under charge-parity transformations, decay width, cross-section, branching fractions into the various decay channels, and its coupling to fermions and bosons. Regarding the spin, the observation of the resonance in the decay into two photons disfavors the spin-1 hypothesis, as a spin-1 particle cannot decay into two massless spin-1 particles (like photons), according to the Landau-Yang theorem [92, 93].

The newest results on the signal strength of the various channels can be seen in Fig. 11.12 for the ATLAS experiment, as presented for the CERN Council in December 2012 [166], and in Fig. 11.13 for the CMS experiment, as presented for the HCP conference in November 2012 [167]. In Fig. 11.12, the background-only result of $\mu = 0$ is indicated by the full, vertical line, whereas the signal+background result of $\mu = 1$ is given by the vertical, dashed line. The $H \to bb$ channel seems to be in better accordance with the background-only hypothesis, albeit not very sensitive, and the $\mathrm{H} \to \gamma\gamma$ channel seems to have a stronger signal than expected from the Standard Model, while the other channels are in good agreement with the SM prediction. The combined signal strength, computed at $m_{\mathrm{H}} = 125$ GeV, is $\mu = 1.35 \pm 0.19(\mathrm{stat}) \pm 0.15(\mathrm{syst})$. The best fitted value found by CMS, as indicated by the vertical band in Fig. 11.13, was $\mu = \sigma/\sigma_{SM} = 0.88 \pm 0.21$ at

$m_{\mathrm{H}} = 125.8$ GeV. The $\mathrm{H} \to \gamma\gamma$ yield is slightly higher than expected, the WW a bit on the low side, while the other channels are very consistent with $\mu = 1$. The results seem to be consistent with the expectation from a SM Higgs boson. To see how the signal strengths in the various channels develop with more data will be very interesting to see, a treat in the future.

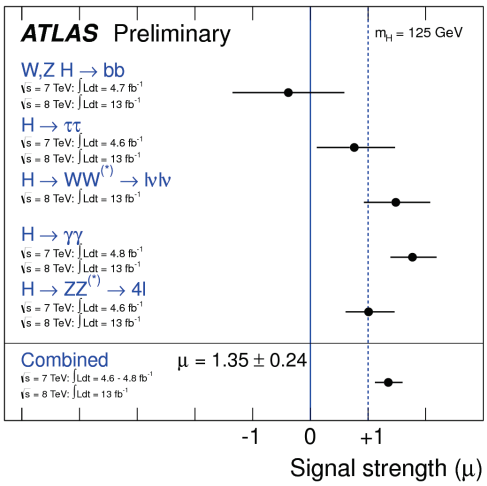

Figure 11.12: Signal strength of the different Higgs boson decay channels normalized to the expectation from the SM Higgs boson as of December 2012 [166]. The background-only result of $\mu = 0$ is indicated by the full, vertical line, whereas the signal+background result of $\mu = 1$ is given by the vertical, dashed line. The combined signal strength, computed at $m_{\mathrm{H}} = 125$ GeV, is $1.35 \pm 0.19(\mathrm{stat}) \pm 0.15(\mathrm{syst})$.

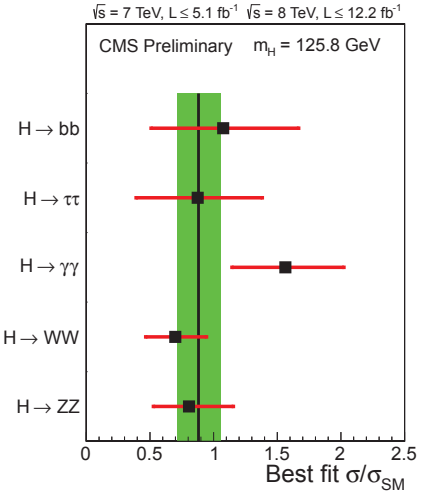

Figure 11.13: Observed signal strength normalized to the expectation from the SM Higgs boson of CMS, as presented for the HCP conference in November 2012 [167]. The notation σ represents the cross-section times the relevant branching fraction. The vertical band indicates the best fitted value of $\sigma/\sigma_{SM} = 0.88 \pm 0.21$ for $m_{\mathrm{H}} = 125.8$ GeV, consistent with the expectation from a SM Higgs boson. The $\mathrm{H} \to \gamma\gamma$ yield is slightly higher than expected, the WW slightly lower than expected, while the other channels are very consistent with $\mu = 1$.

Looking back, knowing what we know today, the realization that the data was really looking like a pronounced deviation from the background came rather quickly, unexpectedly. Before the end of the year 2011, it was hardly noticed at all, and at least never taken seriously. In preparation for the new data to come in 2012, the excess was taken earnestly into consideration for the first time. With the excellent performance of the LHC and the ATLAS detector, data was recorded with a high rate, which gave a large increase in statistics from one conference to the next, and thus the sudden realization.

These have been exceptionally intoxicating times, during which the painstaking efforts of thousands of dedicated, hard-working people stretching over decades have been rewarded with the discovery of a new particle. And more is yet to come; we are still awaiting an exciting period, as the LHC continues to take data,[2] with double the beam energy and increased integrated luminosity, letting us glimpse previously unseen regions of the wondrous universe we are part of.

[2]The data-taking at LHC will seize in the period 2013-2015, as a major shutdown to upgrade the LHC and perform maintainance and small upgrades of the experiments will take place.

Appendix A

Abbreviations and Expressions

ALFA	Absolute Luminosity For ATLAS (detector)
AR	Ambiguity Resolver (b-layer related identification criterium)
ALICE	A Large Ion Collider Experiment
AOD	Analysis Object Data (data format)
Asimov	The Asimov dataset represents the median of all statistically possible outcomes of an experiment
ATLAS	A Toroidal Lhc ApparatuS (detector at LHC)
BC	Bunch Crossing
BEH	Brout-Englert-Higgs (electroweak symmetry breaking)
BR	Branching Ratio (probability fraction)
CASTOR	CERN Advanced STORage manager
CB	Crystal Ball distribution (part of the signal model)
CDF	Collider Detector at Fermilab
CDS	CERN Document Server
CERN	Conseil Européen pour la Recherche Nucléaire (European Organization for Nuclear Research)

CI	Contact Interaction
CL	Confidence Level
CMS	Compact Muon Spectrometer, detector at LHC
CSC	Cathode Strip Chamber (muon system)
CP	Charge-Parity
DPD	Derived Physics Data (data format)
CR	Control Region
D0	DØ/DZero, detector at Tevatron
DIPHOX+	Monte Carlo generator ($\gamma\gamma$ background modeling)
DY	Drell-Yan
ECAL	Electromagnetic CALorimeter
EF	Event-Filter (last level trigger, part of HLT)
EM	ElectroMagnetic
EPS	European Physical Society
ESD	Event Summary Data (data format)
EW	ElectroWeak
fb^{-1}	Inverse femtobarn, the measure for integrated luminosity, representing an amount of data. A process with a cross-section of 1 fb is expected to occur once, on the average, in a dataset of $1\,\mathrm{fb}^{-1}$
FEB	Front End Boards
FWHM	Full Width Half Max (width of a peaked distribution at half the function maximal value)
G	Gaussian distribution (part of the signal model)
GR	(the theory of) General Relativity
GRL	Good Runs List
GMSB	Gauge Mediated Supersymmetry Breaking
GUT	Grand Unified Theory
HCAL	Hadronic CALorimeter
HCP	Hadron Collider Physics symposium (conference)
HEP	High Energy Physics
HLT	High Level Trigger (L2 and EF)
HSG1	Higgs SubGroup 1 ($\mathrm{H} \to \gamma\gamma$ working group within ATLAS)

HV	High Voltage
ICHEP	International Conference on High Energy Physics
ID	Inner Detector
JVF	Jet Vertex Fraction
L1	Level-1 (first level trigger)
L2	Level-2 (second level trigger, part of HLT)
LAr	Liquid Argon
LEIR	Low Energy Ion Ring
LEP	Large Electron-Positron collider (LHC predecessor)
LHC	Large Hadron Collider
LINAC	LINear ACellerator
LO	Leading Order (theory calculations)
LQ	Leptoquarks
LSP	Lightest Supersymmetric Particle
LUCID	LUminosity measurement using Cerenkov Integrating Detector
MC	Monte Carlo (simulations)
MDT	Monitored Drift Tubes (muon system)
MS	Muon Spectrometer
mSUGRA	minimal SUper GRAvity
MSSM	Minimal Supersymmetric extention to the SM
NLO	Next to Leading Order (theory calculations)
NN	Neural Network (multivariate analysis method)
nuisance parameters	Fitted parameters of a statistical model which are necessary, but not of direct interest
OTX	Optical Transmitters (optical fibre cables)
PDG	Particle Data Group
PDF	Parton Distribution Function
pdf	Probability Distribution Function
PLB	Physics Letters B (journal)
PLHC	Physics at LHC (conference)
PRL	Physical Review Letters (journal)
PS	Proton Synchrotron

PT	Pass-Through (trigger)
PV	Primary Vertex
QCD	Quantum ChromoDynamics
QED	Quantum ElectroDynamics
QFT	Quantum Field Theory
RDO	Raw Data Output (data format)
ResBos	Monte Carlo generator ($\gamma\gamma$ background modeling)
RMS	Root Mean Square (measure of spread in a distribution)
RoI	Region of Interest
ROS	ReadOut System
RPC	Resistive-Plate Chamber (muon system)
RPV	R-Parity Violation (SUSY)
SCT	SemiConductor Tracker
Sherpa	Monte Carlo generator (includes $\gamma\gamma$ background modeling)
SLAC	Stanford Linear ACcelerator
SLD	SLAC Large Detector
SM	Standard Model
SMDP	Standard Model Direct Photon (working group within ATLAS)
SPS	Super Proton Synchrotron
SR	Signal Region
SSB	Spontaneous Symmetry Breaking
SSM	Sequential Standard Model
SUSY	SUperSYmmerty
Tevatron	Accelerator at Fermilab, colliding $p\bar{p}$
TGC	Thin Gap Chamber (muon system)
TRT	Transition Radiation Tracker (inner detector)
Toy	Nickname for a Monte Carlo experiment, generated from a template
UE	Underlying Event
VBF	Vector Boson Fusion (Higgs production mechanism)
ZDC	Zero-Degree Calorimeter

Appendix B

Qualification Task in the E/Gamma Trigger Community

To qualify for authorship for the ATLAS experiment,[1] a task in the e/gamma trigger community was designed, under the leadership of Alessandro Tricoli (CERN). This work started the summer of 2011 and was finished summer 2012, qualification being fulfilled the 9$^{\text{th}}$ of June 2012. Two different tools were developed: one for looking at online and offline histograms for e/gamma trigger [169], and one for a run-by-run test of the efficiency of e/gamma triggers, using the bootstrap and $Z \to e^+e^-$ tag&probe methods [170]. These are tools to discover significant variations in performance between runs and reprocessings, as for instance changes in rejection, efficiency or composition. They are used daily by the on-call trigger e/gamma expert to promptly discover problems in the online running or reprocessing.

The code developed for looking at online and offline histograms, `plotEgammaData.cxx`, produces a pdf document containing around fifty pages of plots of general trigger variables, along with variables for the desired trigger hypotheses, e.g. 2D histograms, counters and errors. One example of what is plotted is the so-called *cut counter*, as in the bottom plot of Figure B.1. This shows how many events passed the different cuts required to pass a trigger, and is useful in order to be able

[1] To qualify as an ATLAS author, one has to spend a *minimum* of 80 *full* working days on a chosen project over the course of (at least) a year. Authorship is valid as long as one is part of the collaboration. Authors who leave the collaboration are retained for a further year as an author [168].

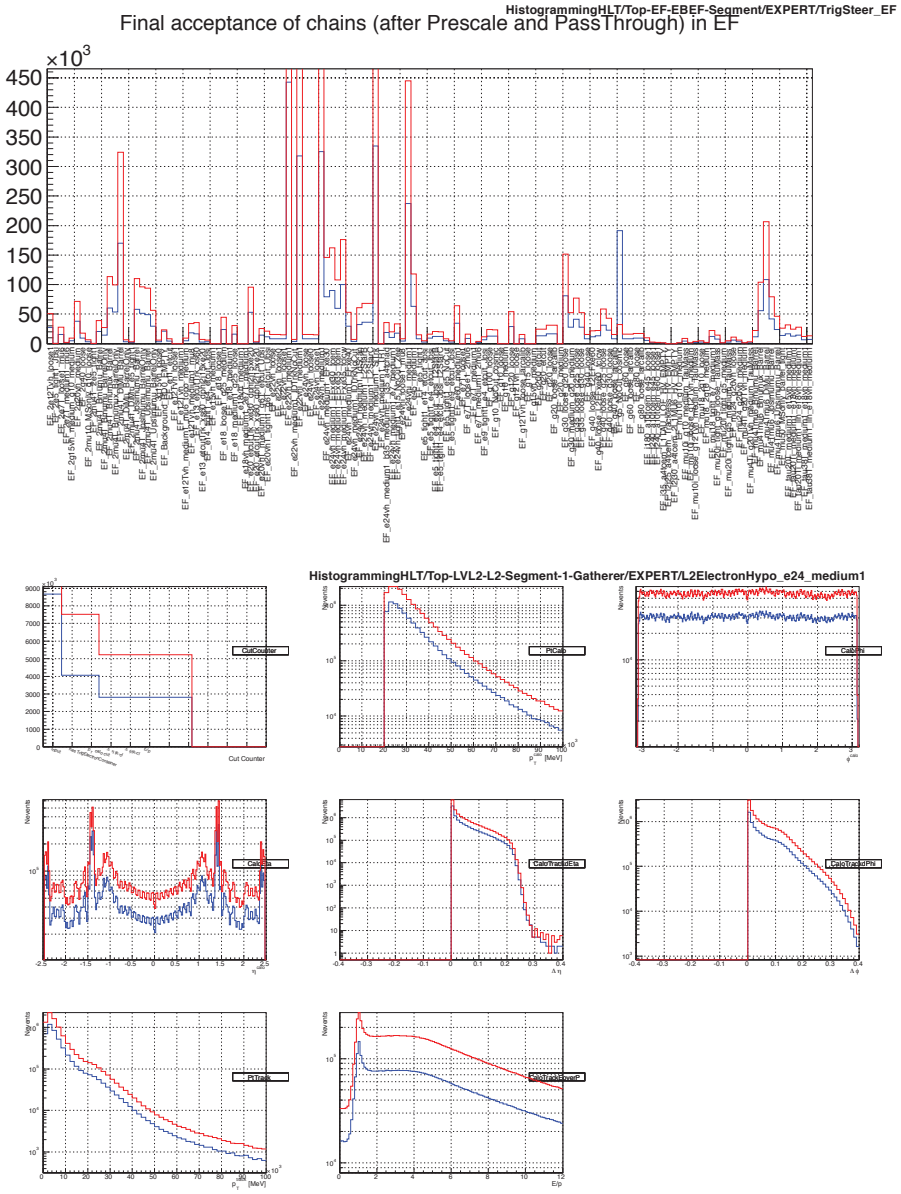

Figure B.1: Plots from the online/offline histogram plotting tool, developed for the e/gamma trigger community. On top, the final acceptance number of all e/gamma trigger chains at EF. On bottom, the cut counter for the L2_e24_medium1 trigger chain is plotted on the top left, along with (among others) some of the variables listed in the cut counter plot. The two different graphs in each plot represent different runs or reprocessings.

to spot at which stage the problem emerged, should a chain have an unexpectedly low rate. The possibility to plot a reference run for comparison was implemented. The options for this was to have the run in question normalized to the reference run or unnormalized. Normalizing to the reference run would be the natural choice when looking at offline histograms – for instance to validate a new reprocessing before implementing it at Point 1. In this case, the run would be the same, but the reprocessing different. Keeping the run in question unnormalized would be the natural choice when looking at two different online runs, with different integrated luminosities. See Figure B.2 for an example of normalized and unnormalized versions of some of the plots that this tool produces.

The code for measuring the efficiency, `TrigEgammaD3PD.cxx`, is more complex, and will therefore be addressed more thoroughly. This tool produces a root file, from which information later can be retrieved, such as the cutflow and plots of the efficiency. Several macros were written to retrieve said information, for instance to visually compare efficiencies of different triggers, runs or reprocessings. Among the things plotted are efficiency versus η, ϕ and E_T, as well as a two-dimensional plot of efficiency for the different trigger levels (L1, L2 and EF) in the (η, ϕ)-plane. An example of plots can be seen in Figure B.3, and an example of the cutflow follows in Figure B.4.

In order to make sure that the code worked the way it was supposed to, several tests based on the reprocessing of the EnhancedBias stream[2] were constructed. The reason for choosing the reprocessed EnhancedBias was that, in this stream, one would have access to triggers not being run online, via the Monte Carlo menu, which contained a setup of triggers similar to that used for collecting data, but with the possibility of having more trigger chains and different options, like prescalings and thresholds. This being available, orthogonal tests to what is run at Point 1 could be made, which could be profitable. However, these tests turned out to not give the expected results. The reason was that, although reprocessing with the MC menu was done with all chains unprescaled, the data already recorded in the EnhancedBias stream suffered from heavy prescaling (see previous footnote for an explanation of prescaling). This came as a surprise to us. A validation of the code through this stream was thus abandoned. Turning to "proper" data (which in this context means the e/gamma stream), for which we had better knowledge of the prescaling that was used, tests were successfully constructed to validate the code. Constructing such tests involved making a reasonable choice of chains to select the

[2]In the EnhancedBias stream, no HLT decision is made – what is passed are only highly *prescaled* L1 items. Prescaling means to allow only some number of the objects accepted by the trigger to pass. For instance; a prescaling of 100 of a L1 item would lead to only every 100^{th} random trigger object accepted by this L1 item being passed on to Level-2. The HLT decisions are created later on, when reprocessing the EnhancedBias stream.

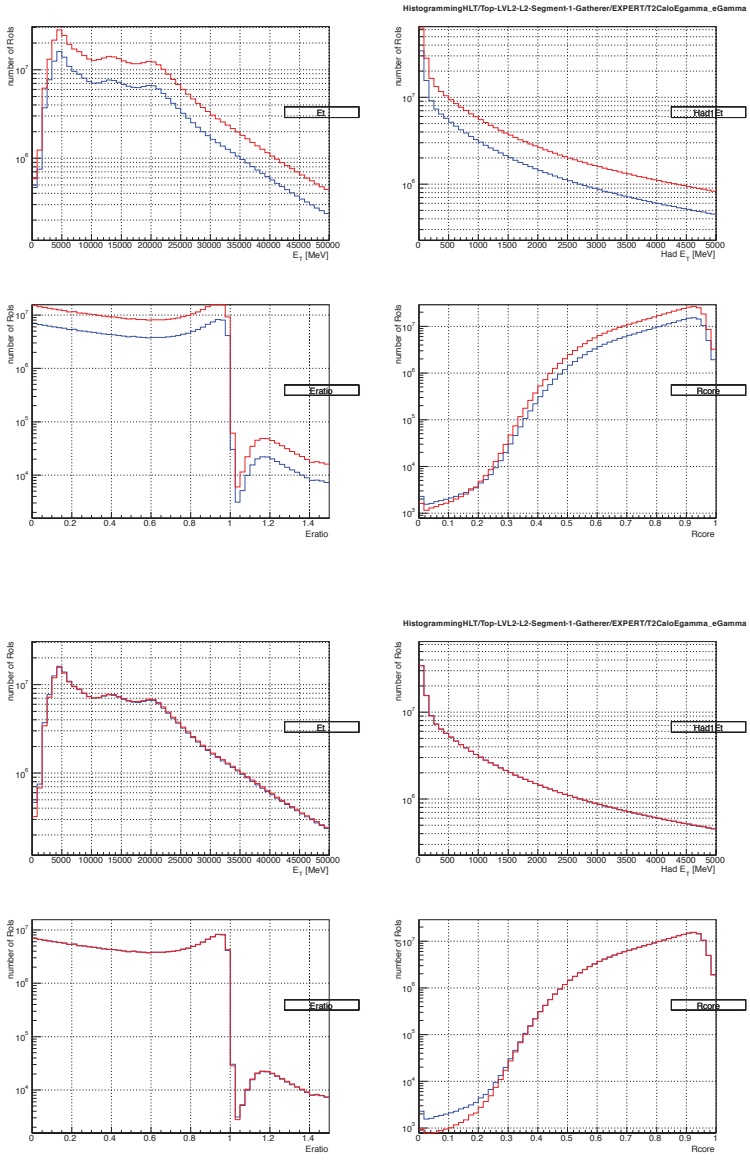

Figure B.2: Plots from the online/offline histogram plotting tool, developed for the e/gamma trigger community group. On the top, some L2 calorimeter variables, used among others in the identification of objects, for two different runs – on the bottom are the same plots, only normalized to the number of entries in the reference run.

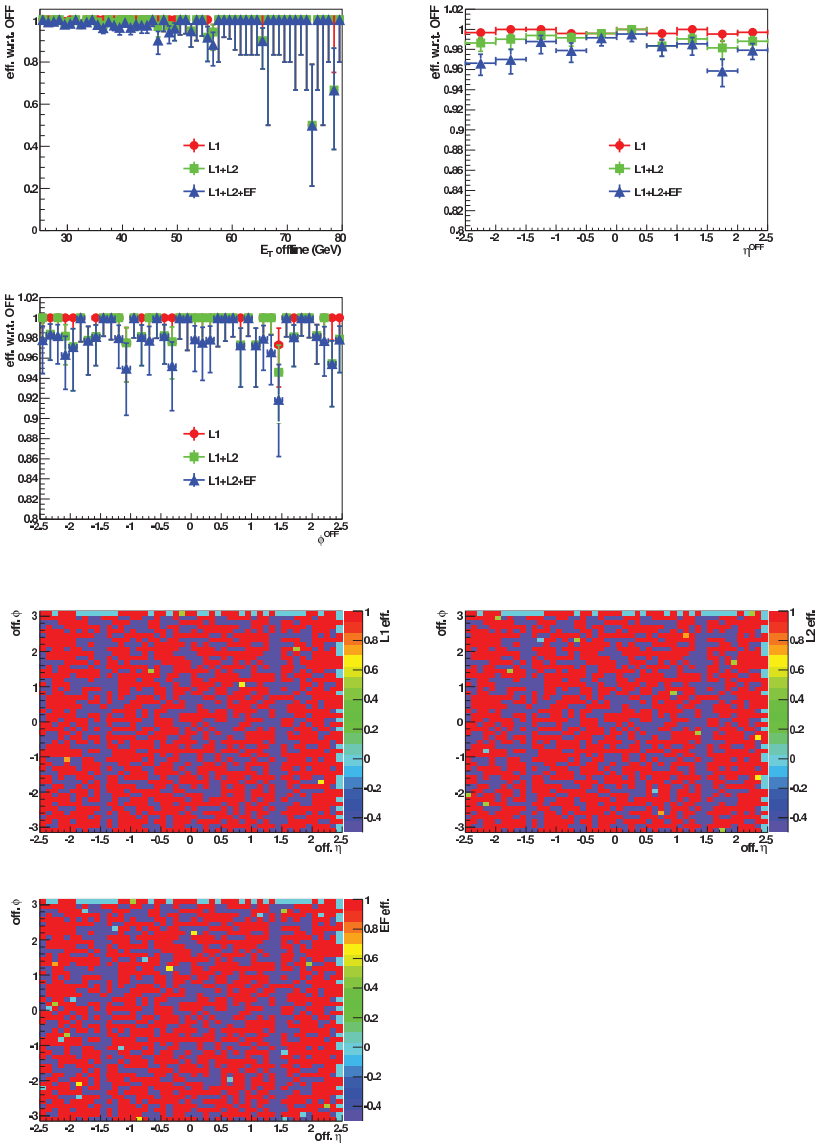

Figure B.3: Efficiency for e22vh_medium1 versus η, ϕ and E_T, as well as efficiency in the (η, ϕ)-plane for L1, L2 and EF, as produced by the macros of the efficiency code developed for the e/gamma trigger community.

```
--------------------------------------------------------------------------------
RunSummary
GRL : NONE
Entries : 2153819
Presel : ELE
trig : e22vh_medium1
--- for bootstrap:
isem     : mediumPP
MCmenu   : 0
EtCut    : 25 GeV
BaseChain: EM12
L1chain  : EM16VH
L2chain  : trig_L2_el_L2_e22vh_medium1
EFchain  : trig_EF_el_EF_e22vh_medium1
--------------------------------------------------------------------------------

Initial Events: 2153819
After LBselection: 2153819

============== Results for Bootstrap ========================================
Events passing baseline chain (EM12) : 1909809


Initial offline electrons : 11190133
--> passing author cut    : 5571306
--> passing eta cut       : 5239346
--> passing isem cut      : 955105
--> matching to baseline  : 867533

Selected electrons (with Et>25 GeV) : 604713

L1 passing : 601146     w.r.t. selected electrons     99.41 ( +0.0097 -0.0099 ) %
L2 passing : 595071     w.r.t. L1 passed              98.99 ( +0.013 -0.013 ) %
EF passing : 586270     w.r.t. L2 passed              98.52 ( +0.015 -0.016 ) %

Cumulative Efficiencies:
L1: 99.41 ( +0.0097 -0.0099 ) %
L2: 98.41 ( +0.016 -0.016 ) %
EF: 96.95 ( +0.022 -0.022 ) %

EF+L2 w.r.t. L1: 97.53 ( +0.02 -0.02 ) %



============== Result for Z tag&probe ========================================
Number of tag&probe pairs
    --> before trigger on probe : 20609
    --> passing trigger on probe : 19329

Efficiency : 93.79 ( +0.17 -0.17 ) %
--------------------------------------------------------------------------------
```

Figure B.4: An example of the cutflow, for the `e22vh_medium1` trigger chain, as printed to the screen by the main code, or by running a macro on the root-file produced by the main code.

ensembles which the efficiencies were measured with respect to. Such a chain is called the *baseline chain*. These tests gave the results that were expected.

In order to quickly assess whether the efficiency in data is according to expectation, the express stream is used, in which only a few chains are recorded and the events are promptly reconstructed and processed into D3PDs, which can be used for the monitoring code. However, special care needs to be taken to choose ways of measuring efficiency in this limited sample which will yield meaningful results. For instance, if there is only *one* chain that is triggered by a L1 item, the efficiency will always be 100% for this chain using that L1 item as the baseline. In the scenario of the trigger object failing at the EF, the event would never have been recorded – so all objects of this trigger chain in the event recorded will have passed both the EF chain and L1 item in question. Note that this would not have been the case if that L1 item was in Pass-Through (PT), and only PT objects were being looked at. Pass-Through means that at a pre-defined frequency, the full trigger chain is passed after having passed a certain level (most commonly L1), without the subsequent levels being evaluated. For instance, this could mean that for every 100^{th} event passing the L1 item L1_EM12, the event is stored with the EF_g20_loose trigger chain being passed, marked with a PT flag. This way, a data sample which is fully unbiased from the HLT decision is obtained. Thus, whenever possible, it is preferred to use chains in PT to assess the efficiency of a trigger chain.

The code was completely rewritten (from `TrigEgammaNtuple` to `TrigEgammaD3PD`), when the group decided to switch from using specially made trigger ntuples, to more standard e/gamma-trigger D3PDs. Adapting the code to run over a different data format involved, needless to say, extensive work. In addition, many features were implemented:

- passing the event using an EF baseline, as well as passing the event using chains in PT;
- running directly over files on CASTOR and EOS[3] without having to download them;
- the $Z \to e^+e^-$ tag&probe method (L1, L2 and EF efficiency) and (filling, writing and plotting of) histograms and counters;
- offline isolation for e24vhi_medium1 (when a drop in efficiency with respect to e24vh_medium1 was observed);
- changing the efficiency error from binomial to Wilson (see following section);
- whether to choose Monte Carlo or data menu (implying different trigger setup, and whether to accept the event based on chains in PT or not);

[3]CASTOR and EOS are two different locations and systems for storage of various types of data.

- the choice to provide a text file with a list of the files to run over (handy if there were many of them).

There was also a lot of work done on the usability of the tools (several of these implementations were mirrored in the command-line options for how to run the code) and tweaking for better-looking plots. Towards the end, when the tools were mature for being integrated in the work of the e/gamma trigger expert on-call shifters, the attention was turned to developing wrapper scripts. In the end, this was done in cooperation with the monitoring responsible of the tau trigger group, as the tau and e/gamma trigger expert on-call shifts were merged.

Among the command-line options for the `TrigEgammaD3PD` tool were:

- which preselection to choose (running over electron or photons),
- how many events to run over,
- which trigger to look at,
- what level of information to print to screen (shifter or expert),
- which identification level to demand (loose, medium, tight),
- which file to write to (if something other than the default)
- and whether to run over local files or to read from CASTOR (online files) or EOS (offline files).

Some examples of how to run the code follow:

```
./run_TrigEgammaD3PD.exe --castor 200863 x191_m1109 --trig e24vh_medium1
--isem mediumPP --presel ELE --info expert

./run_TrigEgammaD3PD.exe --eos r3720_r3721_p931 merge 189421 00856127
--mcmenu true --trig g80_loose --isem loose --presel GAM

./run_TrigEgammaD3PD.exe --filelist --Ev 1000 --trig g20_loose
--isem tight --presel GAM --out myoutputfile.root

./run_TrigEgammaD3PD.exe --file file1.root file2.root file3.root
--trig e22vh_medium1 --isem mediumPP --presel ELE
```

To examine the job log (with expert level information):

```
root -l macro/GetInfo.C
... and supply the root file name
```

To plot efficiency histograms with more information (the Boolean indicates expert level information):

```
root -l 'macro/display_eff.C(1)'
... and supply the root file name
```

To compare efficiency histograms:

```
root -l macro/compare_eff.C
... and supply the root file names that will be compared
```

If a third root file is wanted in the comparison (the Boolean indicates whether two histograms are used; if it is false, three are used):

```
root -l 'macro/compare_eff.C(0)'
```

An example of the trigger setup is shown below:

```
if ( m_trig=="e22vh_medium1") {
  if(!m_MCmenu){
    m_usePT=true;
    m_ChainWithPT="EF_g20_loose"; //L1_EM12 in PT
    m_BaselineChain="EM12";
  }
  else {
    m_BaselineChain="trig_EF_el_EF_e20_tight_e15_NoCut_Zee";
    //m_BaselineChain = "EM12";
    //m_BaselineChain = "EM16VH";
    //m_BaselineChain="trig_EF_ph_EF_g20_loose";
    //m_BaselineChain="trig_EF_ph_EF_g20_etcut_xe30_noMu";
    //m_BaselineChain="trig_EF_el_EF_e13_etcut_xs60_noMu";
    //m_BaselineChain="trig_EF_el_EF_e13_etcut_xs60_noMu_dphi2j10xe20";
  }
  m_L1chain="EM16VH";
  m_L2chain="trig_L2_el_L2_e22vh_medium1";
  m_EFchain="trig_EF_el_EF_e22vh_medium1";
  m_EtCut=25.0;
}
```

Here (for the bootstrap method) the baseline chain (which can either be a L1 item or an EF chain) is used to pass the event – unless m_usePT=true, in which case m_ChainWithPT is used. The variable m_ChainWithPT is an EF chain having a L1 chain in PT to it. Choosing to pass the event via PT is only possible in data, and when using a chain in PT, it is preferable to use the L1 chain that was in PT as the baseline chain. In addition, the baseline chain is used to select the objects comprising the ensemble which the efficiency is measured with respect to. An object (electron or photon) is considered only if it passed this baseline trigger. Thus, changing the baseline trigger might yield a different efficiency (although, with sensible choices of the baseline trigger, the resulting efficiency should not differ much). Some reasonable options for the choice of baseline chain for e22vh_medium1 are listed above. The m_L1chain, m_L2chain and m_EFchain are what the trigger-to-be-checked is built up of. The efficiency is only calculated for objects passing the m_EtCut. At this E_T, the intention is to be at the plateau of the trigger turn-on curve (see next paragraph for more detailed explanation). Objects passing the trigger, but not the E_T cut, are still used for the trigger turn-on curve.

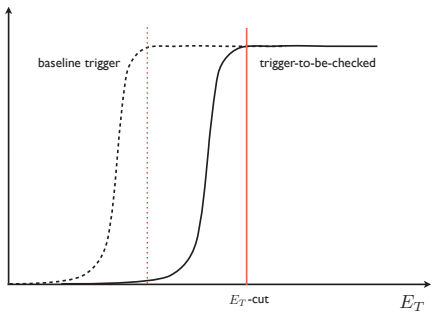

Figure B.5: Illustration of how the baseline trigger in the bootstrap method should be at its plateau at the start of the turn-on curve of the trigger-to-be-checked for the resulting efficiency to be unbiased. As a rule-of-thumb, the turn-on of electrons and photons is approximately 10 GeV wide; choosing a baseline trigger which is approximately 5 GeV lower in threshold should be adequate to get an unbiased efficiency measurement.

To correctly assess the efficiency, the aim is to be on the plateau of the trigger turn-on curve for the E_T cut applied. Furthermore, to correctly assess the efficiency, the baseline trigger needs to envelope the trigger-to-be-checked – that is, the baseline trigger needs to be at the plateau of its turn-on curve for the full turn-on of the trigger-to-be-checked, if one wishes to assess the turn-on of the trigger-to-be-checked. This is illustrated in Figure B.5. The closer the two curves, the more biased the resulting efficiency estimate will be – fully overlapping curves will claim an efficiency of 100%. As a rule-of-thumb, the turn-on is approximately 10 GeV wide; choosing a baseline trigger which is approximately 5 GeV lower in threshold should be adequate to get an unbiased efficiency measurement.

For all levels except L1, the trigger object must be matched to the offline object – meaning that the objects must be as close or closer than 0.15 in the (η, ϕ)-plane ($\Delta R = \sqrt{\Delta\eta^2 + \Delta\phi^2} \leq 0.15$). This requirement is not necessary at L1, because the closest L1 cluster is bound to be the one passing the trigger; L1 is based on a very coarse read-out of the detector information, and leaves no room for duplication. A test was implemented, checking for duplication in matching. It was verified that a specific trigger object was not repeatedly matched to different offline objects. However, this check turned out to have no impact on the chosen candidates. Most likely, this is because there is quite some duplication of trigger objects. For electrons, choosing slightly different hits for reconstruction of the track, a new trigger object is created. Thus, one has several different trigger objects which represent the same real-life object. If one of them is rejected, there is (in all probability) a very similar one (representing the same, true object) that will pass a matching to the offline object.

For the $Z \to e^+e^-$ tag&probe method – only applicable when considering electron

triggers – at least one object had to pass the EF chain of the trigger-to-be-checked in order for the event to be evaluated. The further selection included the following requirements on the tag electron:

- author[4] 1 or 3,
- at least one pixel hit, and at least 7 pixel+SCT hits,
- medium identification level,
- $|\eta| < 2.47$, excluding the crack region ($1.37 < |\eta| < 1.52$),
- $E_T > 20$ GeV and
- matched ($\Delta R < 0.15$) to trigger electron passing the trigger.

For the probe electron the same author, hits, identification and fiducial cuts as the tag were required, as well as the charge being opposite from that of the tag. In addition, not more than one jet with $E_T > 20$ GeV which was closer than $\Delta R = 0.4$ was allowed. Further, the probes used for efficiency had to have $E_T > 25$ GeV, and triggered probes were matched ($\Delta R < 0.15$). For the tag&probe pairs, the invariant mass was required to lie between 80 GeV and 100 GeV. All of the tag&probe pairs in the event passing these requirements were considered.

Errors on Trigger Efficiencies

As part of the authorship task in the e/gamma community, some methods on how to compute trigger efficiencies were briefly looked at.

Using binomial uncertainties for efficiency, $\epsilon \pm \delta\epsilon$, where

$$\delta\epsilon = \sqrt{\frac{\epsilon \cdot (1-\epsilon)}{N}}\,, \tag{B.1}$$

and N is the total number of events, is not a satisfactory estimate when the efficiency approaches 100%. For the specific case of 100% efficiency, the binomial uncertainty is 0%. This does not represent reality in a satisfying manner; asymmetric errors need to be taken into account. With asymmetric errors, it is accommodated for that the efficiency can never be higher than 100%, but still have (a possibly substantial) downwards uncertainty.

Different methods for measuring the uncertainty on the trigger efficiency can be used. Four methods were applied to four different test cases, constructed from

[4]The "author" of an electron indicates with which algorithm it was reconstructed. Several different algorithms to reconstruct electrons are run independently in the reconstruction. Author 1 corresponds to electrons being found only by the standard cluster based algorithm, and author 3 corresponds electrons being reconstructed both with the cluster based and with the track based algorithms.

combinations of high/low statistics and high/low efficiencies. The four methods were binomial, Wilson, Feldman-Cousins and Bayesian with Jeffrey's prior.

Jeffrey's prior is the beta function (also called the Euler integral of the first kind),

$$B(\alpha,\beta) = \int_0^1 t^{\alpha-1}(1-t)^{\beta-1}dt\ , \tag{B.2}$$

with $\alpha = 0.5, \beta = 0.5$. For the purpose of this study, the test cases included "high statistics" – implying 5000 events, with 4990 passed for high efficiency and 500 passed for low efficiency, and "low statistics" – implying 50 events, with 49 passed for high efficiency and 5 passed for low efficiency. A confidence level of 68% was used. The result can be seen in Table B.1.

In the following assessments, the unrealistic binomial intervals are excluded. For the category of low statistics, low efficiency, all the methods seem to agree. In the other categories, Wilson and Bayesian with Jeffrey's priors seem to agree better than either of them with Feldman-Cousins (except perhaps for the low statistics, high efficiency category). For the purpose of the trigger efficiency monitoring tool, the Wilson interval was chosen.

Method	High statistics case		Low statistics case	
	High efficiency	Low efficiency	High efficiency	Low efficiency
binomial	99.8 ± 0.0632 %	10 ± 0.424 %	98 ± 1.98 %	10 ± 4.24 %
Wilson	$99.8^{+0.0537}_{-0.0734}$ %	$10^{+0.43}_{-0.414}$ %	$98^{+1.23}_{-3.09}$ %	$10^{+5.03}_{-3.47}$ %
Feldman-Cousins	$99.8^{+0.2}_{-0.0761}$ %	$10^{+0.437}_{-10}$ %	$98^{+1.26}_{-3.53}$ %	$10^{+5.68}_{-4.47}$ %
Bayesian with Jeffrey's prior	$99.8^{+0.0534}_{-0.0732}$ %	$10^{+0.43}_{-0.414}$ %	$98^{+1.16}_{-3.06}$ %	$10^{+5.01}_{-3.44}$ %

Table B.1: Efficiencies with asymmetric errors (for all rows except the binomial one), applying different methods on combinations of high/low statistics and high/low efficiency samples. High statistics implies 5000 events, with 4990 passed for high efficiency and 500 passed for low efficiency. Low statistics implies 50 events, with 49 passed for high efficiency and 5 passed for low efficiency. A confidence level of 68 % was used.

Appendix C

The Log-normal Constraint Term

The log-normal constraint term in the likelihoods used by ATLAS (and HSG1) in the statistical procedure, seems not to be properly documented within the community, therefore, this section aims at making it clearer. It was chosen to use the log-normal probability distribution function for some penalty terms in the likelihood, instead of a Gaussian constraint, in order to circumvent the problematic, unphysical scenario of negative events by a better motivated solution than a simple truncation of the Gaussian pdf. The problem is solved with this choice, as the log-normal distribution can never go negative, whereas the Gaussian distribution can. Whenever the parameter in question should not be allowed to have negative values, the log-normal distribution is a natural choice. The formalism through which this was implemented will be documented here, taking the example of the luminosity.

The name 'log-normal' stems from that the variable $\ln(x)$ is normally distributed:

$$\frac{\mathrm{d}n}{\mathrm{d}\ln(x)} = \frac{1}{\sqrt{2\pi\kappa^2}}\, e^{-\frac{(\ln x-\mu)^2}{2\kappa^2}} \ . \tag{C.1}$$

This leads us to the form in which the log-normal distribution is frequently seen:

$$\frac{\mathrm{d}n}{\mathrm{d}x} = \frac{1}{\sqrt{2\pi\kappa^2}}\frac{1}{x} e^{-\frac{(\ln x-\mu)^2}{2\kappa^2}} \ , \tag{C.2}$$

which, with the substitution $\mu = \ln(x_0)$, can be rewritten as

$$\frac{\mathrm{d}n}{\mathrm{d}x} = \frac{1}{\sqrt{2\pi}\kappa}\frac{1}{x}e^{-\left(\ln\frac{x}{x_0}\right)^2/2\kappa^2}\,. \tag{C.3}$$

The expectation value of the log-normal distribution, $E[x]$, is

$$E[x] = x_0\, e^{\kappa^2/2} \tag{C.4}$$

and the variance is

$$Var[x] = (e^{\kappa^2} - 1)\, x_0^2\, e^{\kappa^2}\,. \tag{C.5}$$

We can find an expression for the spread of the log-normal distribution by taking the relative variance:

$$\frac{Var[x]}{E^2[x]} = \frac{\langle (x - \langle x\rangle)^2\rangle}{\langle x\rangle^2} \tag{C.6}$$

$$= \frac{(e^{\kappa^2} - 1)\, x_0^2\, e^{\kappa^2}}{x_0^2\, e^{\kappa^2}} \tag{C.7}$$

$$= e^{\kappa^2} - 1\,. \tag{C.8}$$

Solving for κ gives

$$\kappa = \sqrt{\ln\left(1 + \frac{Var[x]}{E^2[x]}\right)}\,. \tag{C.9}$$

Demanding that the relative variance of the log-normal distribution be the same as the relative variance of the Gaussian distribution, σ^2_{Gauss}, we get

$$\kappa = \sqrt{\ln(1 + \sigma^2_{Gauss})}\,. \tag{C.10}$$

For the specific case of the luminosity, where $x = \theta_L$, this is

$$\kappa = \sqrt{\ln(1 + \sigma_L^2)}\ , \tag{C.11}$$

where the parameter σ_L corresponds to the Gaussian uncertainty on the luminosity, as decided by the team measuring the luminosity for ATLAS, *e.g.* 3.9 % for the

2011 data.

The luminosity, however far off from the value it is measured to be, can never be negative. If a variable can be considered as being the product of several random, independent measurements which all are positive, it can be distributed according to the log-normal distribution. Thus, a natural choice is to have the real nuisance parameter, the luminosity, L, be log-normally-distributed (the log of L be normally distributed); $\theta_L\,\kappa = \ln(L)$. The normally-distributed nuisance parameter θ_L used in the likelihood should be close to zero; this indicates no significant deviation from the measurement made by the ATLAS luminosity team. Consequently, the fitted L should preferably remain close its nominal measured value, L_0. Now, we want to demonstrate that when θ_L is normally-distributed, $L = L_0\,e^{\theta_L\cdot\kappa}$ is log-normally-distributed. For this purpose, let us first list some useful relations:

$$L = L_0\,e^{\theta_L\cdot\kappa} \qquad \Rightarrow \qquad \theta_L = \frac{\ln(\frac{L}{L_0})}{\kappa} \tag{C.12}$$

$$\frac{\partial L}{\partial \theta_L} = L_0\,\kappa\,e^{\theta_L\cdot\kappa} \qquad \Rightarrow \qquad \frac{1}{\partial\theta_L} = \frac{1}{\partial L} L_0\,\kappa\,e^{\theta_L\cdot\kappa} \tag{C.13}$$

It is thus of interest to make sure the density function represented by this formulation, $\frac{\partial\, n}{\partial L}$, is the same as the log-normal pdf. Requiring that θ_L is normally-distributed with spread $\kappa = 1$ and mean zero yields

$$\frac{\partial\, n}{\partial \theta_L} = \frac{1}{\sqrt{2\pi}} e^{-\frac{\theta_L^2}{2}}\,. \tag{C.14}$$

Using Eqs. (C.12) and (C.13) to substitute for $\frac{1}{\partial\theta_L}$ and θ_L renders

$$\frac{\partial\, n}{\partial L} = \frac{1}{\sqrt{2\pi}\kappa}\frac{1}{L} e^{-\frac{\left(\ln\frac{L}{L_0}\right)^2}{2\kappa^2}}\,, \tag{C.15}$$

which indeed is of the same form as Eq. (C.3). Wherever L appears in the likelihood, for instance in the signal yield, it is replaced with the left formula of Eq. (C.12), where κ is as given in Eq. (C.10), and the effective log-normal constraint on L is implemented by a Gaussian with width one and mean zero as in Eq. (C.14).

The distribution as a function of L for the log-normal and the Gaussian implementation can be seen in Fig. C.1, for two different uncertainties, σ_L. The distributions are more alike, the smaller the uncertainty – for $\sigma_L = 3.9\%$, they are difficult to tell apart. We can demonstrate that there is a close relationship between the log-normal distribution and the Gaussian distribution when the spread

is small. In this case, $\sigma_L \ll 1$, and $\kappa = \sqrt{\ln(1+\sigma_L^2)} \approx \sigma_L$. Thus, this corresponds to simply replacing κ with σ_L in the log-normal formula,

$$\frac{\partial n}{\partial L} = \frac{1}{\sqrt{2\pi}\sigma_L}\frac{1}{L}e^{-\frac{\left(\ln\frac{L}{L_0}\right)^2}{2\sigma_L^2}} \quad . \tag{C.16}$$

When the spread is small, L does not deviate much from the measured value L_0, such that $\ln\frac{L+\delta L}{L_0} \simeq \frac{\delta L}{L_0}$, where δL is a small number. The width of the Gaussian distribution, $\sigma = \sigma_L L_0$, can be approximated by $\sigma \simeq \sigma_L L$. Thus, the log-normal distribution in Eq. (C.16) is similar to a Gaussian distribution;

$$\frac{\partial n}{\partial L} \simeq \frac{1}{\sqrt{2\pi}(\sigma_L L)}e^{-\frac{\left(\frac{\delta L}{L_0}\right)^2}{2\sigma_L^2}} \tag{C.17}$$

$$\simeq \frac{1}{\sqrt{2\pi}\sigma}e^{-\frac{(\delta L)^2}{2\sigma^2}} \quad . \tag{C.18}$$

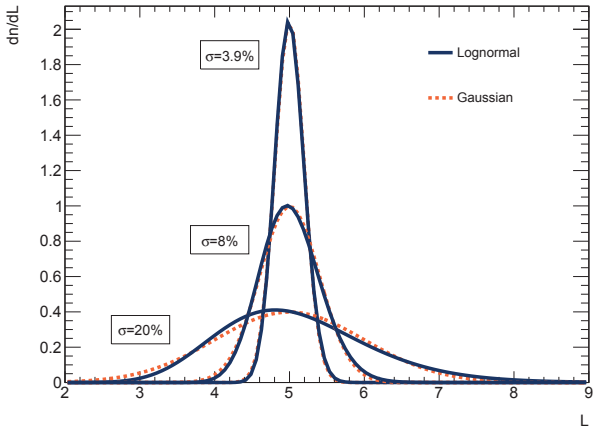

(a) $\sigma_L \in \{3.9\%, 8\%, 20\%\}$

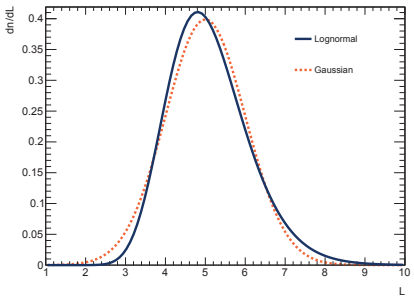

(b) $\sigma_L = 20\%$

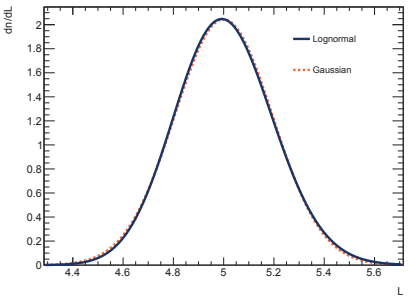

(c) $\sigma_L = 3.9\%$

Figure C.1: Log-normal distribution (full) in comparison with Gaussian distribution (dashed) as a function of L, with three different values of σ_L. The smaller the uncertainty, the more alike the Gaussian and the log-normal distributions are, which can be appreciated from the top figure. In the two bottom figures, the distributions for $\sigma_L = 20\%$ and $\sigma_L = 3.9\%$ are shown separately, to clearer display the difference of the log-normal and Gaussian distribution for small and larger uncertainties.

Appendix D

Photon Identification; Cuts on the Discriminating Variables

In this appendix, the actual cut values for the photon ID discriminating variables are presented[1]. They differ for converted and unconverted photons, separated for the tight cuts only, especially in R_ϕ, as the charged electron pair of the conversion radiate in the ϕ direction because they are bent by the solenoid magnetic field. At the end of 2011, photon identification based on a more complex Neural Network was introduced. The simple cut values presented here are thus not used in this thesis, but can be taken as guidelines to get a feeling for how the cuts on the different variables might look. The loose and tight cuts for the last menu of 2011 before the NN photon ID was introduced are presented underneath. These are followed by the cuts for 2012, before a solid Neural Network could be established.

[1] The cut values are stored in Reconstruction/egamma/egammaPIDTools/python/egammaPhotonCutIDToolBase.py for Athena reconstruction, and in PhotonIDTool.cxx of the CombPerf/EGamma/PhotonID/PhotonIDTool software package for D3PD production.

Variable	$\lvert\eta\rvert$interval (from previous column to the present, *e.g.* 0 – 0.6 for the first)								
	0.6	0.8	1.15	1.37	1.52	1.81	2.01	2.37	2.47
R_{had}	0.010	0.010	0.010	0.008	0.010	0.025	0.015	0.014	0.019
R_{η}	0.927	0.912	0.925	0.916	0.750	0.906	0.920	0.908	0.915
w_{η_2}	0.012	0.012	0.013	0.013	0.025	0.015	0.013	0.013	0.012

Table D.1: The 2011 loose cuts on the photon identification discriminating variables.

Variable	$\lvert\eta\rvert$interval (from previous column to the present *e.g.* 0 – 0.6 for the first)								
	0.6	0.8	1.15	1.37	1.52	1.81	2.01	2.37	2.47
R_{had}	0.02425	0.02275	0.02575	0.01975	0.01975	0.02725	0.02725	0.02725	0.01975
R_{η}	0.8825	0.8825	0.8575	0.8875	0.750	0.8725	0.9025	0.8875	0.7575
w_{η_2}	0.013	0.014	0.015	0.015	0.025	0.016	0.015	0.015	0.014

Table D.2: The 2012 loose cuts on the photon identification discriminating variables.

	Variable	$\|\eta\|$interval (from previous column to the present – (0.-0.6) for the first)								
		0.6	0.8	1.15	1.37	1.52	1.81	2.01	2.37	2.47
unconverted	R_{had}	0.0089	0.007	0.006	0.008	-999	0.019	0.015	0.0137	-999
	R_{η}	0.950784	0.9398	0.9418	0.9458	-999	0.932066	0.928	0.924	-999
	R_{ϕ}	0.954	0.95	0.59	0.82	-999	0.93	0.947	0.935	-999
	$w_{\eta 2}$	0.0107194	0.011459	0.010759	0.011359	-999	0.0114125	0.0110	0.0125	-999
	$w_{s\,\mathrm{tot}}$	2.95	4.4	3.26	3.4	-999	3.8	2.4	1.64	-999
	$w_{s\,3}$	0.66	0.69	0.697	0.81	-999	0.73	0.651	0.610	-999
	F_{side}	0.284	0.36	0.36	0.514	-999	0.67	0.211	0.181	-999
	ΔE	92	92	99	111	-999	92	110	148	-999
	E_{ratio}	0.63	0.84	0.823	0.887	-999	0.88	0.71	0.78	-999
converted	R_{had}	0.00748	0.007	0.00489	0.008	-999	0.0149	0.015	0.011	-999
	R_{η}	0.940784	0.9268	0.9298	0.9308	-999	0.918066	0.924	0.913	-999
	R_{ϕ}	0.4	0.426	0.493	0.437	-999	0.535	0.479	0.692	-999
	$w_{\eta 2}$	0.0116194	0.011359	0.012859	0.012659	-999	0.0138125	0.012	0.0129	-999
	$w_{s\,\mathrm{tot}}$	2.8	2.95	2.89	3.14	-999	3.7	2.0	1.48	-999
	$w_{s\,3}$	0.697	0.709	0.749	0.78	-999	0.773	0.672	0.644	-999
	F_{side}	0.32	0.428	0.483	0.51	-999	0.508	0.252	0.215	-999
	ΔE	200	200	122	86	-999	123	80	132	-999
	E_{ratio}	0.908	0.911	0.808	0.803	-999	0.67	0.915	0.962	-999

Table D.3: The 2011 tight cuts on the photon identification discriminating variables. The value -999 means the region is not in the acceptance of the tight cuts.

	Variable	$\|\eta\|$interval (from previous column to the present – (0.-0.6) for the first)								
		0.6	0.8	1.15	1.37	1.52	1.81	2.01	2.37	2.47
unconverted	R_{had}	0.020	0.020	0.01975	0.01825	-999	0.02425	0.02575	0.02325	-999
	$R_{\text{had}}1$	0.01825	0.01975	0.01525	0.01675	-999	0.02125	0.02275	0.01975	-999
	R_{η}	0.92	0.92	0.93	0.925	-999	0.925	0.925	0.910	-999
	R_{ϕ}	0.93	0.93	0.93	0.92	-999	0.93	0.93	0.93	-999
	$w_{\eta 2}$	0.011	0.0115	0.0115	0.0115	-999	0.012	0.012	0.0128	-999
	$w_{s\,\text{tot}}$	3.0	3.0	3.3	3.5	-999	3.3	2.3	2.0	-999
	$w_{s\,3}$	0.67	0.69	0.69	0.715	-999	0.72	0.66	0.645	-999
	F_{side}	0.28	0.33	0.38	0.425	-999	0.42	0.255	0.24	-999
	ΔE	180	170	165	160	-999	425	500	560	-999
	E_{ratio}	0.80	0.80	0.76	0.82	-999	0.78	0.80	0.80	-999
converted	R_{had}	0.020	0.018	0.01975	0.018	-999	0.02425	0.024	0.024	-999
	$R_{\text{had}}1$	0.01825	0.01975	0.01525	0.01675	-999	0.02125	0.02275	0.01975	-999
	R_{η}	0.92	0.9125	0.915	0.91	-999	0.908	0.917	0.903	-999
	R_{ϕ}	0.57	0.60	0.60	0.64	-999	0.68	0.72	0.72	-999
	$w_{\eta 2}$	0.011	0.0117	0.012	0.0120	-999	0.0130	0.012	0.0127	-999
	$w_{s\,\text{tot}}$	2.8	2.9	3.1	3.3	-999	3.5	2.2	1.8	-999
	$w_{s\,3}$	0.73	0.715	0.74	0.75	-999	0.75	0.69	0.66	-999
	F_{side}	0.33	0.38	0.46	0.52	-999	0.52	0.31	0.25	-999
	ΔE	160	160	120	125	-999	350	520	525	-999
	E_{ratio}	0.85	0.85	0.80	0.78	-999	0.82	0.86	0.88	-999

Table D.4: The 2012 tight cuts on the photon identification discriminating variables. The value -999 means the region is not in the acceptance of the tight cuts.

Appendix E

Data and Monte Carlo Files

In this appendix, the data and signal Monte Carlo files that were used for this thesis are listed. The rightmost part of the filename (after PHOTON) document the versions of the reconstruction (and simulation in the case of MC) software used in the central production system to produce the files.

Data Files

```
data11_7TeV.00177986.physics_Egamma.merge.NTUP_PHOTON.r2603_p659_p682_p868
data11_7TeV.00178020.physics_Egamma.merge.NTUP_PHOTON.r2603_p659_p682_p868
data11_7TeV.00178021.physics_Egamma.merge.NTUP_PHOTON.r2603_p659_p682_p868
data11_7TeV.00178026.physics_Egamma.merge.NTUP_PHOTON.r2603_p659_p682_p868
data11_7TeV.00178044.physics_Egamma.merge.NTUP_PHOTON.r2603_p659_p682_p868
data11_7TeV.00178047.physics_Egamma.merge.NTUP_PHOTON.r2603_p659_p682_p868
data11_7TeV.00178109.physics_Egamma.merge.NTUP_PHOTON.r2603_p659_p682_p868
data11_7TeV.00179710.physics_Egamma.merge.NTUP_PHOTON.r2603_p659_p682_p868
data11_7TeV.00179725.physics_Egamma.merge.NTUP_PHOTON.r2603_p659_p682_p868
data11_7TeV.00179739.physics_Egamma.merge.NTUP_PHOTON.r2603_p659_p682_p868
data11_7TeV.00179771.physics_Egamma.merge.NTUP_PHOTON.r2603_p659_p682_p868
data11_7TeV.00179804.physics_Egamma.merge.NTUP_PHOTON.r2603_p659_p682_p868
data11_7TeV.00179938.physics_Egamma.merge.NTUP_PHOTON.r2603_p659_p682_p868
data11_7TeV.00179939.physics_Egamma.merge.NTUP_PHOTON.r2603_p659_p682_p868
data11_7TeV.00179940.physics_Egamma.merge.NTUP_PHOTON.r2603_p659_p682_p868
data11_7TeV.00180122.physics_Egamma.merge.NTUP_PHOTON.r2603_p659_p682_p868
data11_7TeV.00180124.physics_Egamma.merge.NTUP_PHOTON.r2603_p659_p682_p868
data11_7TeV.00180139.physics_Egamma.merge.NTUP_PHOTON.r2603_p659_p682_p868
data11_7TeV.00180144.physics_Egamma.merge.NTUP_PHOTON.r2603_p659_p682_p868
data11_7TeV.00180153.physics_Egamma.merge.NTUP_PHOTON.r2603_p659_p682_p868
data11_7TeV.00180149.physics_Egamma.merge.NTUP_PHOTON.r2603_p659_p682_p868
data11_7TeV.00180212.physics_Egamma.merge.NTUP_PHOTON.r2603_p659_p682_p868
data11_7TeV.00180225.physics_Egamma.merge.NTUP_PHOTON.r2603_p659_p682_p868
```

data11_7TeV.00180241.physics_Egamma.merge.NTUP_PHOTON.r2603_p659_p682_p868
data11_7TeV.00180164.physics_Egamma.merge.NTUP_PHOTON.r2603_p659_p682_p868
data11_7TeV.00180242.physics_Egamma.merge.NTUP_PHOTON.r2603_p659_p682_p868
data11_7TeV.00180309.physics_Egamma.merge.NTUP_PHOTON.r2603_p659_p682_p868
data11_7TeV.00180400.physics_Egamma.merge.NTUP_PHOTON.r2603_p659_p682_p868
data11_7TeV.00180448.physics_Egamma.merge.NTUP_PHOTON.r2603_p659_p682_p868
data11_7TeV.00180481.physics_Egamma.merge.NTUP_PHOTON.r2603_p659_p682_p868
data11_7TeV.00180614.physics_Egamma.merge.NTUP_PHOTON.r2603_p659_p682_p868
data11_7TeV.00180636.physics_Egamma.merge.NTUP_PHOTON.r2603_p659_p682_p868
data11_7TeV.00180776.physics_Egamma.merge.NTUP_PHOTON.r2603_p659_p682_p868
data11_7TeV.00182013.physics_Egamma.merge.NTUP_PHOTON.r2603_p659_p682_p868
data11_7TeV.00182161.physics_Egamma.merge.NTUP_PHOTON.r2603_p659_p682_p868
data11_7TeV.00180664.physics_Egamma.merge.NTUP_PHOTON.r2603_p659_p682_p868
data11_7TeV.00182284.physics_Egamma.merge.NTUP_PHOTON.r2603_p659_p682_p868
data11_7TeV.00182346.physics_Egamma.merge.NTUP_PHOTON.r2603_p659_p682_p868
data11_7TeV.00182449.physics_Egamma.merge.NTUP_PHOTON.r2603_p659_p682_p868
data11_7TeV.00182450.physics_Egamma.merge.NTUP_PHOTON.r2603_p659_p682_p868
data11_7TeV.00182454.physics_Egamma.merge.NTUP_PHOTON.r2603_p659_p682_p868
data11_7TeV.00182424.physics_Egamma.merge.NTUP_PHOTON.r2603_p659_p682_p868
data11_7TeV.00182455.physics_Egamma.merge.NTUP_PHOTON.r2603_p659_p682_p868
data11_7TeV.00182456.physics_Egamma.merge.NTUP_PHOTON.r2603_p659_p682_p868
data11_7TeV.00182486.physics_Egamma.merge.NTUP_PHOTON.r2603_p659_p682_p868
data11_7TeV.00182516.physics_Egamma.merge.NTUP_PHOTON.r2603_p659_p682_p868
data11_7TeV.00182518.physics_Egamma.merge.NTUP_PHOTON.r2603_p659_p682_p868
data11_7TeV.00182519.physics_Egamma.merge.NTUP_PHOTON.r2603_p659_p682_p868
data11_7TeV.00182726.physics_Egamma.merge.NTUP_PHOTON.r2603_p659_p682_p868
data11_7TeV.00182747.physics_Egamma.merge.NTUP_PHOTON.r2603_p659_p682_p868
data11_7TeV.00182787.physics_Egamma.merge.NTUP_PHOTON.r2603_p659_p682_p868
data11_7TeV.00182766.physics_Egamma.merge.NTUP_PHOTON.r2603_p659_p682_p868
data11_7TeV.00182796.physics_Egamma.merge.NTUP_PHOTON.r2603_p659_p682_p868
data11_7TeV.00182879.physics_Egamma.merge.NTUP_PHOTON.r2603_p659_p682_p868
data11_7TeV.00182886.physics_Egamma.merge.NTUP_PHOTON.r2603_p659_p682_p868
data11_7TeV.00182997.physics_Egamma.merge.NTUP_PHOTON.r2603_p659_p682_p868
data11_7TeV.00183003.physics_Egamma.merge.NTUP_PHOTON.r2603_p659_p682_p868
data11_7TeV.00183021.physics_Egamma.merge.NTUP_PHOTON.r2603_p659_p682_p868
data11_7TeV.00183038.physics_Egamma.merge.NTUP_PHOTON.r2603_p659_p682_p868
data11_7TeV.00183054.physics_Egamma.merge.NTUP_PHOTON.r2603_p659_p682_p868
data11_7TeV.00183045.physics_Egamma.merge.NTUP_PHOTON.r2603_p659_p682_p868
data11_7TeV.00183078.physics_Egamma.merge.NTUP_PHOTON.r2603_p659_p682_p868
data11_7TeV.00183079.physics_Egamma.merge.NTUP_PHOTON.r2603_p659_p682_p868
data11_7TeV.00183127.physics_Egamma.merge.NTUP_PHOTON.r2603_p659_p682_p868
data11_7TeV.00183129.physics_Egamma.merge.NTUP_PHOTON.r2603_p659_p682_p868
data11_7TeV.00183130.physics_Egamma.merge.NTUP_PHOTON.r2603_p659_p682_p868
data11_7TeV.00183216.physics_Egamma.merge.NTUP_PHOTON.r2603_p659_p682_p868
data11_7TeV.00183081.physics_Egamma.merge.NTUP_PHOTON.r2603_p659_p682_p868
data11_7TeV.00183286.physics_Egamma.merge.NTUP_PHOTON.r2603_p659_p682_p868
data11_7TeV.00183347.physics_Egamma.merge.NTUP_PHOTON.r2603_p659_p682_p868
data11_7TeV.00183272.physics_Egamma.merge.NTUP_PHOTON.r2603_p659_p682_p868
data11_7TeV.00183391.physics_Egamma.merge.NTUP_PHOTON.r2603_p659_p682_p868
data11_7TeV.00183407.physics_Egamma.merge.NTUP_PHOTON.r2603_p659_p682_p868
data11_7TeV.00183412.physics_Egamma.merge.NTUP_PHOTON.r2603_p659_p682_p868
data11_7TeV.00183426.physics_Egamma.merge.NTUP_PHOTON.r2603_p659_p682_p868
data11_7TeV.00183462.physics_Egamma.merge.NTUP_PHOTON.r2603_p659_p682_p868
data11_7TeV.00183580.physics_Egamma.merge.NTUP_PHOTON.r2603_p659_p682_p868
data11_7TeV.00183581.physics_Egamma.merge.NTUP_PHOTON.r2603_p659_p682_p868
data11_7TeV.00183602.physics_Egamma.merge.NTUP_PHOTON.r2603_p659_p682_p868
data11_7TeV.00183780.physics_Egamma.merge.NTUP_PHOTON.r2603_p659_p682_p868
data11_7TeV.00183544.physics_Egamma.merge.NTUP_PHOTON.r2603_p659_p682_p868
data11_7TeV.00183963.physics_Egamma.merge.NTUP_PHOTON.r2603_p659_p682_p868
data11_7TeV.00184022.physics_Egamma.merge.NTUP_PHOTON.r2603_p659_p682_p868

data11_7TeV.00184066.physics_Egamma.merge.NTUP_PHOTON.r2603_p659_p682_p868
data11_7TeV.00184072.physics_Egamma.merge.NTUP_PHOTON.r2603_p659_p682_p868
data11_7TeV.00184088.physics_Egamma.merge.NTUP_PHOTON.r2603_p659_p682_p868
data11_7TeV.00184074.physics_Egamma.merge.NTUP_PHOTON.r2603_p659_p682_p868
data11_7TeV.00184130.physics_Egamma.merge.NTUP_PHOTON.r2603_p659_p682_p868
data11_7TeV.00184169.physics_Egamma.merge.NTUP_PHOTON.r2603_p659_p682_p868
data11_7TeV.00185353.physics_Egamma.merge.NTUP_PHOTON.r2713_p705_p682_p868
data11_7TeV.00185518.physics_Egamma.merge.NTUP_PHOTON.r2713_p705_p682_p868
data11_7TeV.00185536.physics_Egamma.merge.NTUP_PHOTON.r2713_p705_p682_p868
data11_7TeV.00185649.physics_Egamma.merge.NTUP_PHOTON.r2713_p705_p682_p868
data11_7TeV.00185747.physics_Egamma.merge.NTUP_PHOTON.r2713_p705_p682_p868
data11_7TeV.00185644.physics_Egamma.merge.NTUP_PHOTON.r2713_p705_p682_p868
data11_7TeV.00185761.physics_Egamma.merge.NTUP_PHOTON.r2713_p705_p682_p868
data11_7TeV.00185731.physics_Egamma.merge.NTUP_PHOTON.r2713_p705_p682_p868
data11_7TeV.00185823.physics_Egamma.merge.NTUP_PHOTON.r2713_p705_p682_p868
data11_7TeV.00185856.physics_Egamma.merge.NTUP_PHOTON.r2713_p705_p682_p868
data11_7TeV.00185976.physics_Egamma.merge.NTUP_PHOTON.r2713_p705_p682_p868
data11_7TeV.00185998.physics_Egamma.merge.NTUP_PHOTON.r2713_p705_p682_p868
data11_7TeV.00186049.physics_Egamma.merge.NTUP_PHOTON.r2713_p705_p682_p868
data11_7TeV.00186156.physics_Egamma.merge.NTUP_PHOTON.r2713_p705_p682_p868
data11_7TeV.00186169.physics_Egamma.merge.NTUP_PHOTON.r2713_p705_p682_p868
data11_7TeV.00186178.physics_Egamma.merge.NTUP_PHOTON.r2713_p705_p682_p868
data11_7TeV.00186180.physics_Egamma.merge.NTUP_PHOTON.r2713_p705_p682_p868
data11_7TeV.00186182.physics_Egamma.merge.NTUP_PHOTON.r2713_p705_p682_p868
data11_7TeV.00186216.physics_Egamma.merge.NTUP_PHOTON.r2713_p705_p682_p868
data11_7TeV.00186275.physics_Egamma.merge.NTUP_PHOTON.r2713_p705_p682_p868
data11_7TeV.00186361.physics_Egamma.merge.NTUP_PHOTON.r2713_p705_p682_p868
data11_7TeV.00186217.physics_Egamma.merge.NTUP_PHOTON.r2713_p705_p682_p868
data11_7TeV.00186396.physics_Egamma.merge.NTUP_PHOTON.r2713_p705_p682_p868
data11_7TeV.00186399.physics_Egamma.merge.NTUP_PHOTON.r2713_p705_p682_p868
data11_7TeV.00186493.physics_Egamma.merge.NTUP_PHOTON.r2713_p705_p682_p868
data11_7TeV.00186456.physics_Egamma.merge.NTUP_PHOTON.r2713_p705_p682_p868
data11_7TeV.00186516.physics_Egamma.merge.NTUP_PHOTON.r2713_p705_p682_p868
data11_7TeV.00186532.physics_Egamma.merge.NTUP_PHOTON.r2713_p705_p682_p868
data11_7TeV.00186533.physics_Egamma.merge.NTUP_PHOTON.r2713_p705_p682_p868
data11_7TeV.00186673.physics_Egamma.merge.NTUP_PHOTON.r2713_p705_p682_p868
data11_7TeV.00186669.physics_Egamma.merge.NTUP_PHOTON.r2713_p705_p682_p868
data11_7TeV.00186721.physics_Egamma.merge.NTUP_PHOTON.r2713_p705_p682_p868
data11_7TeV.00186729.physics_Egamma.merge.NTUP_PHOTON.r2713_p705_p682_p868
data11_7TeV.00186753.physics_Egamma.merge.NTUP_PHOTON.r2713_p705_p682_p868
data11_7TeV.00186755.physics_Egamma.merge.NTUP_PHOTON.r2713_p705_p682_p868
data11_7TeV.00186873.physics_Egamma.merge.NTUP_PHOTON.r2713_p705_p682_p868
data11_7TeV.00186878.physics_Egamma.merge.NTUP_PHOTON.r2713_p705_p682_p868
data11_7TeV.00186923.physics_Egamma.merge.NTUP_PHOTON.r2713_p705_p682_p868
data11_7TeV.00186933.physics_Egamma.merge.NTUP_PHOTON.r2713_p705_p682_p868
data11_7TeV.00186934.physics_Egamma.merge.NTUP_PHOTON.r2713_p705_p682_p868
data11_7TeV.00186965.physics_Egamma.merge.NTUP_PHOTON.r2713_p705_p682_p868
data11_7TeV.00187014.physics_Egamma.merge.NTUP_PHOTON.r2713_p705_p682_p868
data11_7TeV.00187196.physics_Egamma.merge.NTUP_PHOTON.r2713_p705_p682_p868
data11_7TeV.00187219.physics_Egamma.merge.NTUP_PHOTON.r2713_p705_p682_p868
data11_7TeV.00187453.physics_Egamma.merge.NTUP_PHOTON.r2713_p705_p682_p868
data11_7TeV.00187501.physics_Egamma.merge.NTUP_PHOTON.r2713_p705_p682_p868
data11_7TeV.00187543.physics_Egamma.merge.NTUP_PHOTON.r2713_p705_p682_p868
data11_7TeV.00187552.physics_Egamma.merge.NTUP_PHOTON.r2713_p705_p682_p868
data11_7TeV.00187763.physics_Egamma.merge.NTUP_PHOTON.r2713_p705_p682_p868
data11_7TeV.00187812.physics_Egamma.merge.NTUP_PHOTON.r2713_p705_p682_p868
data11_7TeV.00187811.physics_Egamma.merge.NTUP_PHOTON.r2713_p705_p682_p868
data11_7TeV.00187815.physics_Egamma.merge.NTUP_PHOTON.r2713_p705_p682_p868
data11_7TeV.00180710.physics_Egamma.merge.NTUP_PHOTON.r2603_p659_p682_p868
data11_7TeV.00182372.physics_Egamma.merge.NTUP_PHOTON.r2603_p659_p682_p868

data11_7TeV.00186179.physics_Egamma.merge.NTUP_PHOTON.r2713_p705_p682_p868
data11_7TeV.00187457.physics_Egamma.merge.NTUP_PHOTON.r2713_p705_p682_p868
data11_7TeV.00188949.physics_Egamma.merge.NTUP_PHOTON.f415_m1025_p682_p868
data11_7TeV.00188951.physics_Egamma.merge.NTUP_PHOTON.f403_m975_p682_p868
data11_7TeV.00189011.physics_Egamma.merge.NTUP_PHOTON.f403_m975_p682_p868
data11_7TeV.00189027.physics_Egamma.merge.NTUP_PHOTON.f403_m975_p682_p868
data11_7TeV.00189028.physics_Egamma.merge.NTUP_PHOTON.f403_m975_p682_p868
data11_7TeV.00189049.physics_Egamma.merge.NTUP_PHOTON.f403_m975_p682_p868
data11_7TeV.00189079.physics_Egamma.merge.NTUP_PHOTON.f415_m1025_p682_p868
data11_7TeV.00189090.physics_Egamma.merge.NTUP_PHOTON.f403_m975_p682_p868
data11_7TeV.00189184.physics_Egamma.merge.NTUP_PHOTON.f403_m980_p682_p868
data11_7TeV.00189205.physics_Egamma.merge.NTUP_PHOTON.f403_m980_p682_p868
data11_7TeV.00189207.physics_Egamma.merge.NTUP_PHOTON.f404_m980_p682_p868
data11_7TeV.00189242.physics_Egamma.merge.NTUP_PHOTON.f404_m980_p682_p868
data11_7TeV.00189280.physics_Egamma.merge.NTUP_PHOTON.f404_m980_p682_p868
data11_7TeV.00189288.physics_Egamma.merge.NTUP_PHOTON.f404_m980_p682_p868
data11_7TeV.00189366.physics_Egamma.merge.NTUP_PHOTON.f404_m980_p682_p868
data11_7TeV.00189372.physics_Egamma.merge.NTUP_PHOTON.f404_m980_p682_p868
data11_7TeV.00189421.physics_Egamma.merge.NTUP_PHOTON.f404_m980_p682_p868
data11_7TeV.00189425.physics_Egamma.merge.NTUP_PHOTON.f404_m980_p682_p868
data11_7TeV.00189481.physics_Egamma.merge.NTUP_PHOTON.f404_m985_p682_p868
data11_7TeV.00189483.physics_Egamma.merge.NTUP_PHOTON.f405_m985_p682_p868
data11_7TeV.00189530.physics_Egamma.merge.NTUP_PHOTON.f405_m985_p682_p868
data11_7TeV.00189536.physics_Egamma.merge.NTUP_PHOTON.f405_m985_p682_p868
data11_7TeV.00189561.physics_Egamma.merge.NTUP_PHOTON.f405_m985_p682_p868
data11_7TeV.00189598.physics_Egamma.merge.NTUP_PHOTON.f405_m985_p682_p868
data11_7TeV.00189602.physics_Egamma.merge.NTUP_PHOTON.f405_m985_p682_p868
data11_7TeV.00189610.physics_Egamma.merge.NTUP_PHOTON.f405_m985_p682_p868
data11_7TeV.00189639.physics_Egamma.merge.NTUP_PHOTON.f405_m985_p682_p868
data11_7TeV.00189655.physics_Egamma.merge.NTUP_PHOTON.f405_m985_p682_p868
data11_7TeV.00189660.physics_Egamma.merge.NTUP_PHOTON.f405_m985_p682_p868
data11_7TeV.00189693.physics_Egamma.merge.NTUP_PHOTON.f405_m985_p682_p868
data11_7TeV.00189719.physics_Egamma.merge.NTUP_PHOTON.f405_m985_p682_p868
data11_7TeV.00189751.physics_Egamma.merge.NTUP_PHOTON.f405_m985_p682_p868
data11_7TeV.00189774.physics_Egamma.merge.NTUP_PHOTON.f405_m985_p682_p868
data11_7TeV.00189781.physics_Egamma.merge.NTUP_PHOTON.f405_m985_p682_p868
data11_7TeV.00189813.physics_Egamma.merge.NTUP_PHOTON.f405_m985_p682_p868
data11_7TeV.00189822.physics_Egamma.merge.NTUP_PHOTON.f415_m1025_p682_p868
data11_7TeV.00189836.physics_Egamma.merge.NTUP_PHOTON.f406_m991_p682_p868
data11_7TeV.00189845.physics_Egamma.merge.NTUP_PHOTON.f406_m991_p682_p868
data11_7TeV.00189875.physics_Egamma.merge.NTUP_PHOTON.f406_m991_p682_p868
data11_7TeV.00189963.physics_Egamma.merge.NTUP_PHOTON.f406_m991_p682_p868
data11_7TeV.00189965.physics_Egamma.merge.NTUP_PHOTON.f406_m997_p682_p868
data11_7TeV.00190046.physics_Egamma.merge.NTUP_PHOTON.f407_m997_p682_p868
data11_7TeV.00190116.physics_Egamma.merge.NTUP_PHOTON.f407_m997_p682_p868
data11_7TeV.00190119.physics_Egamma.merge.NTUP_PHOTON.f407_m997_p682_p868
data11_7TeV.00190120.physics_Egamma.merge.NTUP_PHOTON.f407_m997_p682_p868
data11_7TeV.00190236.physics_Egamma.merge.NTUP_PHOTON.f408_m1002_p682_p868
data11_7TeV.00190256.physics_Egamma.merge.NTUP_PHOTON.f408_m1007_p682_p868
data11_7TeV.00190297.physics_Egamma.merge.NTUP_PHOTON.f408_m1007_p682_p868
data11_7TeV.00190300.physics_Egamma.merge.NTUP_PHOTON.f409_m1007_p682_p868
data11_7TeV.00190343.physics_Egamma.merge.NTUP_PHOTON.f409_m1007_p682_p868
data11_7TeV.00190608.physics_Egamma.merge.NTUP_PHOTON.f411_m1007_p682_p868
data11_7TeV.00190611.physics_Egamma.merge.NTUP_PHOTON.f411_m1007_p682_p868
data11_7TeV.00190618.physics_Egamma.merge.NTUP_PHOTON.f411_m1007_p682_p868
data11_7TeV.00190643.physics_Egamma.merge.NTUP_PHOTON.f411_m1007_p682_p868
data11_7TeV.00190644.physics_Egamma.merge.NTUP_PHOTON.f411_m1007_p682_p868
data11_7TeV.00190661.physics_Egamma.merge.NTUP_PHOTON.f411_m1007_p682_p868
data11_7TeV.00190689.physics_Egamma.merge.NTUP_PHOTON.f411_m1007_p682_p868
data11_7TeV.00190872.physics_Egamma.merge.NTUP_PHOTON.f411_m1014_p682_p868

data11_7TeV.00190878.physics_Egamma.merge.NTUP_PHOTON.f415_m1025_p682_p868
data11_7TeV.00190933.physics_Egamma.merge.NTUP_PHOTON.f412_m1007_p682_p868
data11_7TeV.00190934.physics_Egamma.merge.NTUP_PHOTON.f412_m1007_p682_p868
data11_7TeV.00190975.physics_Egamma.merge.NTUP_PHOTON.f411_m1007_p682_p868
data11_7TeV.00191138.physics_Egamma.merge.NTUP_PHOTON.f411_m1007_p682_p868
data11_7TeV.00191139.physics_Egamma.merge.NTUP_PHOTON.f415_m1025_p682_p868
data11_7TeV.00191149.physics_Egamma.merge.NTUP_PHOTON.f411_m1019_p682_p868
data11_7TeV.00191150.physics_Egamma.merge.NTUP_PHOTON.f411_m1019_p682_p868
data11_7TeV.00191190.physics_Egamma.merge.NTUP_PHOTON.f413_m1019_p682_p868
data11_7TeV.00191217.physics_Egamma.merge.NTUP_PHOTON.f413_m1019_p682_p868
data11_7TeV.00191218.physics_Egamma.merge.NTUP_PHOTON.f413_m1019_p682_p868
data11_7TeV.00191235.physics_Egamma.merge.NTUP_PHOTON.f413_m1019_p682_p868
data11_7TeV.00191239.physics_Egamma.merge.NTUP_PHOTON.f413_m1019_p682_p868
data11_7TeV.00191425.physics_Egamma.merge.NTUP_PHOTON.f413_m1019_p682_p868
data11_7TeV.00191426.physics_Egamma.merge.NTUP_PHOTON.f413_m1019_p682_p868
data11_7TeV.00188921.physics_Egamma.merge.NTUP_PHOTON.f415_m1025_p682_p868
data11_7TeV.00191428.physics_Egamma.merge.NTUP_PHOTON.f413_m1025_p682_p868
data11_7TeV.00191513.physics_Egamma.merge.NTUP_PHOTON.f413_m1025_p682_p868
data11_7TeV.00191517.physics_Egamma.merge.NTUP_PHOTON.f413_m1025_p682_p868
data11_7TeV.00191635.physics_Egamma.merge.NTUP_PHOTON.f414_m1025_p682_p868
data11_7TeV.00191676.physics_Egamma.merge.NTUP_PHOTON.f414_m1025_p682_p868
data11_7TeV.00191715.physics_Egamma.merge.NTUP_PHOTON.f414_m1025_p682_p868
data11_7TeV.00191920.physics_Egamma.merge.NTUP_PHOTON.f414_m1025_p682_p868
data11_7TeV.00191933.physics_Egamma.merge.NTUP_PHOTON.f415_m1025_p682_p868

Monte Carlo Files

mc11_7TeV.116064.PythiattH100gamgam.merge.NTUP_PHOTON.e893_s1310_s1300_r3043_r2993_p868
mc11_7TeV.125170.PowHegPythia_VBFH100_gamgam.merge.NTUP_PHOTON.e893_s1310_s1300_r3043_r2993_p868
mc11_7TeV.125489.PythiaZH100_gamgam.merge.NTUP_PHOTON.e825_s1310_s1300_r3043_r2993_p868
mc11_7TeV.125329.PythiaWH100_gamgam.merge.NTUP_PHOTON.e825_s1310_s1300_r3043_r2993_p868
mc11_7TeV.116064.PythiattH100gamgam.merge.NTUP_PHOTON.e893_s1310_s1300_r3043_r2993_p868

mc11_7TeV.116868.PowHegPythia_ggH110_gamgam.merge.NTUP_PHOTON.e873_s1310_s1300_r3043_r2993_p868
mc11_7TeV.125172.PowHegPythia_VBFH110_gamgam.merge.NTUP_PHOTON.e893_s1310_s1300_r3043_r2993_p868
mc11_7TeV.125491.PythiaZH110_gamgam.merge.NTUP_PHOTON.e825_s1310_s1300_r3043_r2993_p868
mc11_7TeV.125331.PythiaWH110_gamgam.merge.NTUP_PHOTON.e825_s1310_s1300_r3043_r2993_p868
mc11_7TeV.116060.PythiattH110gamgam.merge.NTUP_PHOTON.e893_s1310_s1300_r3043_r2993_p868

mc11_7TeV.116869.PowHegPythia_ggH115_gamgam.merge.NTUP_PHOTON.e873_s1310_s1300_r3043_r2993_p868
mc11_7TeV.125173.PowHegPythia_VBFH115_gamgam.merge.NTUP_PHOTON.e893_s1310_s1300_r3043_r2993_p868
mc11_7TeV.125492.PythiaZH115_gamgam.merge.NTUP_PHOTON.e825_s1310_s1300_r3043_r2993_p868
mc11_7TeV.125332.PythiaWH115_gamgam.merge.NTUP_PHOTON.e825_s1310_s1300_r3043_r2993_p868
mc11_7TeV.116061.PythiattH115gamgam.merge.NTUP_PHOTON.e893_s1310_s1300_r3043_r2993_p868

mc11_7TeV.116610.PowHegPythia_ggH120_gamgam.merge.NTUP_PHOTON.e873_s1310_s1300_r3043_r2993_p868
mc11_7TeV.116620.PowHegPythia_VBFH120_gamgam.merge.NTUP_PHOTON.e893_s1310_s1300_r3043_r2993_p868
mc11_7TeV.125493.PythiaZH120_gamgam.merge.NTUP_PHOTON.e825_s1310_s1300_r3043_r2993_p868
mc11_7TeV.125333.PythiaWH120_gamgam.merge.NTUP_PHOTON.e825_s1310_s1300_r3043_r2993_p868
mc11_7TeV.106369.PythiattH120gamgam.merge.NTUP_PHOTON.e825_s1310_s1300_r3043_r2993_p868

mc11_7TeV.116870.PowHegPythia_ggH125_gamgam.merge.NTUP_PHOTON.e873_s1310_s1300_r3043_r2993_p868
mc11_7TeV.116870.PowHegPythia_ggH125_gamgam.merge.NTUP_PHOTON.e873_s1310_s1300_r3043_r2993_p868
mc11_7TeV.125494.PythiaZH125_gamgam.merge.NTUP_PHOTON.e825_s1310_s1300_r3043_r2993_p868
mc11_7TeV.125334.PythiaWH125_gamgam.merge.NTUP_PHOTON.e825_s1310_s1300_r3043_r2993_p868
mc11_7TeV.116066.PythiattH125gamgam.merge.NTUP_PHOTON.e825_s1310_s1300_r3043_r2993_p868

mc11_7TeV.116871.PowHegPythia_ggH130_gamgam.merge.NTUP_PHOTON.e873_s1310_s1300_r3043_r2993_p868
mc11_7TeV.125175.PowHegPythia_VBFH130_gamgam.merge.NTUP_PHOTON.e893_s1310_s1300_r3043_r2993_p868
mc11_7TeV.125495.PythiaZH130_gamgam.merge.NTUP_PHOTON.e825_s1310_s1300_r3043_r2993_p868
mc11_7TeV.125335.PythiaWH130_gamgam.merge.NTUP_PHOTON.e825_s1310_s1300_r3043_r2993_p868
mc11_7TeV.116062.PythiattH130gamgam.merge.NTUP_PHOTON.e893_s1310_s1300_r3043_r2993_p868

mc11_7TeV.116872.PowHegPythia_ggH135_gamgam.merge.NTUP_PHOTON.e873_s1310_s1300_r3043_r2993_p868
mc11_7TeV.125176.PowHegPythia_VBFH135_gamgam.merge.NTUP_PHOTON.e893_s1310_s1300_r3043_r2993_p868
mc11_7TeV.125496.PythiaZH135_gamgam.merge.NTUP_PHOTON.e825_s1310_s1300_r3043_r2993_p868
mc11_7TeV.125336.PythiaWH135_gamgam.merge.NTUP_PHOTON.e825_s1310_s1300_r3043_r2993_p868
mc11_7TeV.116067.PythiattH135gamgam.merge.NTUP_PHOTON.e825_s1310_s1300_r3043_r2993_p868

mc11_7TeV.116873.PowHegPythia_ggH140_gamgam.merge.NTUP_PHOTON.e873_s1310_s1300_r3043_r2993_p868
mc11_7TeV.125177.PowHegPythia_VBFH140_gamgam.merge.NTUP_PHOTON.e893_s1310_s1300_r3043_r2993_p868
mc11_7TeV.125497.PythiaZH140_gamgam.merge.NTUP_PHOTON.e825_s1310_s1300_r3043_r2993_p868
mc11_7TeV.125337.PythiaWH140_gamgam.merge.NTUP_PHOTON.e825_s1310_s1300_r3043_r2993_p868
mc11_7TeV.116063.PythiattH140gamgam.merge.NTUP_PHOTON.e893_s1310_s1300_r3043_r2993_p868

mc11_7TeV.116874.PowHegPythia_ggH145_gamgam.merge.NTUP_PHOTON.e873_s1310_s1300_r3043_r2993_p868
mc11_7TeV.125178.PowHegPythia_VBFH145_gamgam.merge.NTUP_PHOTON.e893_s1310_s1300_r3043_r2993_p868
mc11_7TeV.125498.PythiaZH145_gamgam.merge.NTUP_PHOTON.e825_s1310_s1300_r3043_r2993_p868
mc11_7TeV.125338.PythiaWH145_gamgam.merge.NTUP_PHOTON.e825_s1310_s1300_r3043_r2993_p868
mc11_7TeV.116068.PythiattH145gamgam.merge.NTUP_PHOTON.e825_s1310_s1300_r3043_r2993_p868

mc11_7TeV.116875.PowHegPythia_ggH150_gamgam.merge.NTUP_PHOTON.e873_s1310_s1300_r3043_r2993_p868
mc11_7TeV.125179.PowHegPythia_VBFH150_gamgam.merge.NTUP_PHOTON.e893_s1310_s1300_r3043_r2993_p868
mc11_7TeV.125499.PythiaZH150_gamgam.merge.NTUP_PHOTON.e825_s1310_s1300_r3043_r2993_p868
mc11_7TeV.125339.PythiaWH150_gamgam.merge.NTUP_PHOTON.e825_s1310_s1300_r3043_r2993_p868
mc11_7TeV.116069.PythiattH150gamgam.merge.NTUP_PHOTON.e825_s1310_s1300_r3043_r2993_p868

List of Figures

List of Tables

Bibliography

[1] The ALEPH, CDF, DØ, DELPHI, L3, OPAL, SLD Collaborations, the LEP Electroweak Working Group, the Tevatron Electroweak Working Group, and the SLD electroweak and heavy flavour groups, *Precision Electroweak Measurements and Constraints on the Standard Model*, CERN-PH-EP-2010-095 (2010) 18, arXiv:1012.2367 [hep-ex].

[2] LEP Working Group for Higgs boson searches, ALEPH Collaboration, DELPHI Collaboration, L3 Collaboration, OPAL Collaboration Collaboration, R. Barate et al., *Search for the standard model Higgs boson at LEP*, Phys.Lett. **B565** (2003) 61–75, arXiv:hep-ex/0306033 [hep-ex].

[3] The ATLAS Collaboration, *Combined search for the Standard Model Higgs boson using up to 4.9 fb^{-1} of pp collision data at $\sqrt{s} = 7$ TeV with the ATLAS detector at the LHC*, Phys. Lett. **B 710** (2012) 49, arXiv:1202.1408.

[4] CMS Collaboration, *Combined results of searches for the Standard Model Higgs boson in pp collisions at $\sqrt{s} = 7$ TeV*, Phys. Lett. **B 710** (2012) 26, arXiv:1202.1488 [hep-ex].

[5] ATLAS Collaboration, G. Aad et al., *Observation of a new particle in the search for the Standard Model Higgs boson with the ATLAS detector at the LHC*, Phys.Lett. **B716** (2012) 1–29, arXiv:1207.7214 [hep-ex].

[6] CMS Collaboration, S. Chatrchyan et al., *Observation of a new boson at a mass of 125 GeV with the CMS experiment at the LHC*, Phys.Lett. **B716** (2012) 30–61, arXiv:1207.7235 [hep-ex].

[7] CDF Collaboration, D0 Collaboration, T. Aaltonen et al., *Evidence for a particle produced in association with weak bosons and decaying to a bottom-antibottom quark pair in Higgs boson searches at the Tevatron*, Phys. Rev. Lett. **071804** (2012) 12, arXiv:1207.6436 [hep-ex].

[8] J. J. Thomson, *Cathode rays*, Philosophical Magazine no. 44, (1897) 293.

[9] Wikipedia. Figures of hadron multiplets. http://commons.wikimedia.org/wiki/Category:Hadron_multiplets.

[10] Super-Kamiokande Collaboration, C. Regis et al., *Search for Proton Decay via $p \to \mu^+ K^0$ in Super-Kamiokande I, II, and III*, Phys.Rev. **D86** (2012) 012006, arXiv:1205.6538 [hep-ex].

[11] J. Beringer et al., *Review of Particle Physics*, Phys. Rev. D86, 010001 (2012). http://pdg.lbl.gov/.

[12] C. L. Cowan, Jr., F. Reines, F. B. Harrison, H. W. Kruse, and A. D. McGuire, *Detection of the Free Neutrino: A Confirmation*, Science **124** (1956) 103–104.

[13] S. L. Glashow, *Partial-symmetries of weak interactions*, Nucl. Phys. **22** no. 4, (1961) 579.

[14] S. Weinberg, *A Model of Leptons*, Phys. Rev. Lett. **19** (1967) 1264.

[15] A. Salam, ed. N. Svartholm, *Weak and electromagnetic interactions in elementary particle physics: relativistic groups and analyticity.* Almqvist & Wiksell, Stockholm proceedings of the eighth Nobel symposium, 1968. p. 367.

[16] D. Denegri, *The discovery of the W and Z*, Physics Reports **403 - 404** no. 0, (2004) 107 – 145. http://www.sciencedirect.com/science/article/pii/S0370157304003825. and references therein.

[17] G. 't Hooft and M. Veltman, *Regularization and Renormalization of Gauge Fields*, Nucl. Phys. **B44** (1972) 189.

[18] C. Anderson, *The positive electron*, Phys.Rev. **43** (1933) 491–494.

[19] P. Langacker, J. Erler, and E. Peinado, *Neutrino physics*, J.Phys.Conf.Ser. **18** (2005) 154–187, arXiv:hep-ph/0506257 [hep-ph].

[20] T. Schwetz, M. Tortola, and J. W. Valle, *Three-flavour neutrino oscillation update*, New J.Phys. **10** (2008) 113011, arXiv:0808.2016 [hep-ph].

[21] J. Donoghue, E. Golowich, and B. Holstein, *Dynamics of the Standard Model.* Cambridge Monographs on Particle Physics, Nuclear Physics and Cosmology. Cambridge University Press, 1992.

[22] W. Cottingham and D. Greenwood, *An Introduction to the Standard Model of Particle Physics.* Cambridge University Press, 2007.

[23] A. Das and T. Ferbel, *Introduction to Nuclear and Particle Physics.* World Scientific, 2003.

[24] F. Mandl and G. Shaw, *Quantum Field Theory.* A Wiley-Interscience publication. John Wiley & Sons, 1993.

[25] F. Halzen and A. D. Martin, *QUARKS AND LEPTONS: An Introductory Course in Modern Particle Physics.* John Wiley & Sons, 1984.

[26] P. Langacker, *Structure of the Standard Model*, Precision Tests of the Standard Electroweak Model, ed. P. Langacker (World, Singapore, 1995) (2003) 22. http://arXiv.org/abs/hep-ph/0304186v1.

[27] F. Englert and R. Brout, *Broken symmetry and the mass of gauge vector mesons*, Phys. Rev. Lett. **13** (1964) 321.

[28] P. W. Higgs, *Broken symmetries, massless particles and gauge fields*, Phys. Lett. **12** (1964) 132.

[29] P. W. Higgs, *Broken symmetries and the masses of gauge bosons*, Phys. Rev. Lett. **13** (1964) 508.

[30] G. S. Guralnik, C. R. Hagen, and T. W. B. Kibble, *Global conservation laws and massless particles*, Phys. Rev. Lett. **13** (1964) 585.

[31] P. W. Higgs, *Spontaneous symmetry breakdown without massless bosons*, Phys. Rev. **145** (1966) 1156.

[32] T. W. B. Kibble, *Symmetry breaking in non-Abelian gauge theories*, Phys. Rev. **155** (1967) 1554.

[33] L. Alvarez-Gaume and J. Ellis, *Eyes on a prize particle*, Nature Physics **7** (2011) 2–3.

[34] M. J. Dolan, C. Englert, and M. Spannowsky, *Higgs self-coupling measurements at the LHC*, arXiv:1206.5001 [hep-ph].

[35] J. Tian, K. Fujii, and Y. Gao, *Study of Higgs Self-coupling at ILC*, arXiv:1008.0921 [hep-ex].

[36] The ATLAS Collaboration. ATLAS Public Results. https://twiki.cern.ch/twiki/bin/view/AtlasPublic.

[37] Michael Peskin. Higgs Hunting Conference in Orsay, Paris, 2012. http://video.lal.in2p3.fr/higgshunting2012/PESKIN.mp4. 25:58.

[38] M. K. Gaillard, P. D. Grannis, and F. J. Sciulli, *The Standard model of particle physics*, Rev.Mod.Phys. **71** (1999) S96–S111, arXiv:hep-ph/9812285 [hep-ph].

[39] The Clay Mathematics Institute. The Millennium Prize Problems. http://www.claymath.org/millennium/.

[40] U. Amaldi, W. de Boer, and H. Furstenau, *Comparison of grand unified theories with electroweak and strong coupling constants measured at LEP*, Phys.Lett. **B260** (1991) 447–455.

[41] A. A. El-Okaby, *The exceptional E-infinity theory holographic boundary, F-theory and the number of particles in the standard model*, Chaos, Solitons & Fractals **38** no. 5, (2008) 1286 – 1291.

[42] H. Baer and X. Tata, *Weak Scale Supersymmetry: From Superfields to Scattering Events*. Cambridge University Press, 2006.

[43] S. Weinberg, *Implications of Dynamical Symmetry Breaking*, Phys.Rev. **D13** (1976) 974–996.

[44] L. Susskind, *Dynamics of Spontaneous Symmetry Breaking in the Weinberg-Salam Theory*, Phys.Rev. **D20** (1979) 2619–2625.

[45] R. Jackiw and K. Johnson, *Dynamical Model of Spontaneously Broken Gauge Symmetries*, Phys.Rev. **D8** (1973) 2386–2398.

[46] C. T. Hill and E. H. Simmons, *Strong dynamics and electroweak symmetry breaking*, Phys.Rept. **381** (2003) 235–402, arXiv:hep-ph/0203079 [hep-ph].

[47] K. Lane, *Two Lectures on Technicolor*, arXiv:hep-ph/0202255 [hep-ph]. These two lectures on technicolor and extended technicolor (ETC) were presented at l'Ecole de GIF at LAPP, Annecy-le-Vieux, France, in September 2001.

[48] T. Appelquist, H.-C. Cheng, and B. A. Dobrescu, *Bounds on universal extra dimensions*, Phys.Rev. **D64** (2001) 035002, arXiv:hep-ph/0012100 [hep-ph].

[49] L. Randall and R. Sundrum, *An Alternative to compactification*, Phys.Rev.Lett. **83** (1999) 4690–4693, arXiv:hep-th/9906064 [hep-th].

[50] N. Arkani-Hamed, S. Dimopoulos, and G. Dvali, *The Hierarchy problem and new dimensions at a millimeter*, Phys.Lett. **B429** (1998) 263–272, arXiv:hep-ph/9803315 [hep-ph].

[51] The LEP Electroweak Working Group. http://lepewwg.web.cern.ch/LEPEWWG/.

[52] C. Lefvre, *The CERN accelerator complex*, Dec, 2008. http://cds.cern.ch/record/1260465.

[53] L. Evans, *The Large Hadron Collider*, Phil.Trans.Roy.Soc.Lond. **A370** (2012) 831–858.

[54] L. Evans and P. Bryant, *LHC Machine*, Journal of Instrumentation **3** no. 08, (2008) S08001. http://stacks.iop.org/1748-0221/3/i=08/a=S08001.

[55] C. Lefevre, *LHC: the guide*, Feb, 2009. https://cdsweb.cern.ch/record/1165534.

[56] L. Rossi, *Superconductivity: its role, its success and its setbacks in the Large Hadron Collider of CERN*, Superconductor Science and Technology **23** no. 3, (2010) 034001. http://stacks.iop.org/0953-2048/23/i=3/a=034001.

[57] *Aerial view of CERN and the surrounding region*, May, 1991. http://cds.cern.ch/record/39026.

[58] CERN PhotoLab, "Cross section of an lhc dipole in the tunnel." http://cds.cern.ch/record/1365795.

[59] The ATLAS Collaboration, *ATLAS: letter of intent for a general-purpose pp experiment at the large hadron collider at CERN*, CERN-LHCC-92-004 (1992) 108. http://cdsweb.cern.ch/record/291061.

[60] The ATLAS Collaboration, *ATLAS Technical Proposal for a General-Purpose pp Experiment at the Large Hadron Collider at CERN*, CERN-LHCC-94-43 (1994). http://atlas.web.cern.ch/Atlas/TP/tp.html.

[61] The ATLAS Collaboration, *ATLAS detector and physics performance: Technical Design Report, 1.* Technical Design Report ATLAS. CERN, Geneva, 1999. https://cdsweb.cern.ch/record/391176.

[62] The ATLAS Collaboration, *ATLAS detector and physics performance: Technical Design Report, 2.* Technical Design Report ATLAS. CERN, Geneva, 1999. https://cdsweb.cern.ch/record/391177.

[63] The ATLAS Collaboration, *The ATLAS Experiment at the CERN Large Hadron Collider*, Journal of Instrumentation **3** no. 08, (2008) S08003. http://stacks.iop.org/1748-0221/3/i=08/a=S08003.

[64] Airlines Inform, "Boeing 747-400.". http://www.airlines-inform.com/commercial-aircraft/Boeing-747-400.html.

[65] The ATLAS Collaboration, *Expected Performance of the ATLAS Experiment - Detector, Trigger and Physics*, tech. rep., CERN, Geneva, Aug, 2009. arXiv:0901.0512v4.

[66] P. Jenni, M. Nessi, M. Nordberg, and K. Smith, *ATLAS high-level trigger, data-acquisition and controls: Technical Design Report.* Technical Design Report ATLAS. CERN, Geneva, 2003. http://cdsweb.cern.ch/record/616089/.

[67] The ATLAS experiment, "Public Event Displays.". https://twiki.cern.ch/twiki/bin/view/AtlasPublic/EventDisplayPublicResults.

[68] The ATLAS experiment, "Electron/Gamma Public Results, Collision data plots." https://twiki.cern.ch/twiki/bin/view/AtlasPublic/ElectronGammaPublicCollisionResults.

[69] The ATLAS experiment, "Public data quality information." https://twiki.cern.ch/twiki/bin/view/AtlasPublic/RunStatsPublicResults2010.

[70] LHC Performance and Statistics, "Supertable, 2011, 3.50 TeV, proton-proton, stable beams." http://lhc-statistics.web.cern.ch/LHC-Statistics/.

[71] The ATLAS experiment, "Public luminosity results.". https://twiki.cern.ch/twiki/bin/view/AtlasPublic/LuminosityPublicResults.

[72] GEANT4 Collaboration, S. Agostinelli et al., *GEANT4: A Simulation toolkit*, Nucl.Instrum.Meth. **A506** (2003) 250–303.

[73] J. Allison et al., *Geant4 developments and applications*, Nuclear Science, IEEE Transactions on **53** no. 1, (2006) 270 –278.

[74] The ATLAS experiment, "The ATLAS Computing Workbook." `https://twiki.cern.ch/twiki/bin/viewauth/Atlas/WorkBook`. ATLAS internal.

[75] The ATLAS Collaboration, *Electron and photon reconstruction and identification in ATLAS: expected performance at high energy and results at 900 GeV*, Tech. Rep. ATLAS-CONF-2010-005, CERN, Geneva, June, 2010. `http://cdsweb.cern.ch/record/1273197/`.

[76] The ATLAS Collaboration, *Expected photon performance in the ATLAS experiment*, Tech. Rep. ATL-PHYS-PUB-2011-007, CERN, Geneva, Apr, 2011. `http://cdsweb.cern.ch/record/1345329/`.

[77] The ATLAS Collaboration, *Measurements of the photon identification efficiency with the ATLAS detector using 4.9 fb1 of pp collision data collected in 2011*, Tech. Rep. ATLAS-CONF-2012-123, CERN, Geneva, Aug, 2012. `https://cdsweb.cern.ch/record/1473426`.

[78] ATLAS HSG1 Working Group, *Improved analysis of the Search for the Higgs Boson Decaying to Two Photons with 4.9 fb^{-1} of 7 TeV data.*, Tech. Rep. ATL-COM-PHYS-2012-502, CERN, Geneva, May, 2012. `https://cdsweb.cern.ch/record/1447437`. ATLAS internal, co-authored supporting note.

[79] H. Abreu, B. Brelier, V. Dao, M. Delmastro, M. Fanti, J. Hartert, G. Marchiori, T. Koffas, J. Marchand, F. Martin, V. Perez Reale, K. Tackmann, N. Trinh, H. Wang, M. Wielers, S. Wu, and L. Yuan, *Expected photon performance in the ATLAS experiment*, Tech. Rep. ATL-COM-PHYS-2010-240, CERN, Geneva, May, 2010. `http://cdsweb.cern.ch/record/1264379/`. ATLAS internal.

[80] T. Sjöstrand, P. Eden, C. Friberg, L. Lonnblad, G. Miu, et al., *High-energy physics event generation with PYTHIA 6.1*, Comput.Phys.Commun. **135** (2001) 238–259, `arXiv:hep-ph/0010017 [hep-ph]`.

[81] T. Sjöstrand, S. Mrenna, and P. Skands, *A Brief Introduction to PYTHIA 8.1*, Comput.Phys.Commun. **178** (2008) 852–867, `arXiv:0710.3820`.

[82] P. Nason, *A new method for combining NLO QCD with shower Monte Carlo algorithms*, Journal of High Energy Physics **2004** no. 11, (2004) 040, `arXiv:hep-ph/0409146`.

[83] The ATLAS Experiment, "Data/MC correction factors (a.k.a. "fudge factors") for photons.". https://twiki.cern.ch/twiki/bin/viewauth/AtlasProtected/PhotonFudgeFactors ATLAS internal.

[84] Q.-H. Cao, C.-R. Chen, C. Schmidt, Z. Li, and C. P. Yuan, *Improved Predictions for Higgs Q_{T} at the Tevatron and the LHC*, arXiv:0909.2305v2.

[85] The ATLAS Experiment, "Svn repository for the ggFReweighting software package." https://svnweb.cern.ch/trac/atlasoff/browser/PhysicsAnalysis/HiggsPhys/ggFReweighting. ATLAS internal.

[86] The ATLAS Experiment, "The E/Gamma Working Group, energy scale resolution recommendations." https://twiki.cern.ch/twiki/bin/viewauth/AtlasProtected/EnergyScaleResolutionRecommendations. ATLAS internal.

[87] The ATLAS Experiment, "The E/Gamma Working Group, the EnergyRescaler tool." https://twiki.cern.ch/twiki/bin/viewauth/AtlasProtected/EnergyRescaler. ATLAS internal.

[88] The ATLAS Experiment, "The E/Gamma Working Group, the ConvertedPhotonCalibrationTool." https://twiki.cern.ch/twiki/bin/viewauth/AtlasProtected/ConvertedPhotonCalibrationTool. ATLAS internal.

[89] J. Marchand and E. Scifo, *Oscillation of calorimeter pointing z position as a function of pseudo-rapidity in the end-cap*, Tech. Rep. ATL-COM-CAL-2012-003, CERN, Geneva, Apr, 2012. https://cdsweb.cern.ch/record/1438738. ATLAS internal.

[90] LHC Higgs Cross Section Working Group, S. Dittmaier, C. Mariotti, G. Passarino, and R. Tanaka (Eds.), *Handbook of LHC Higgs Cross Sections: 1. Inclusive Observables*, CERN-2011-002 (CERN, Geneva, 2011) 151, arXiv:1101.0593 [hep-ph].

[91] LHC Higgs Cross Section Working Group, S. Dittmaier, C. Mariotti, G. Passarino, and R. Tanaka (Eds.), *Handbook of LHC Higgs Cross Sections: 2. Differential Distributions*, CERN-2012-002 (CERN, Geneva, 2012) 275, arXiv:1201.3084 [hep-ph].

[92] L. D. Landau, *The moment of a 2-photon system*, Dokl. Akad. Nawk. **USSR 60** (1948) 207.

[93] C. N. Yang, *Selection Rules for the Dematerialization of a Particle Into Two Photons*, Phys. Rev. **77** (1950) 242.

[94] J. F. Gunion, S. Dawson, H. E. Haber, and G. L. Kane, *The Higgs Hunter's Guide*. Brookhaven Nat. Lab., Upton, NY, 1989.

[95] ATLAS HSG1 Working Group, *Search for the Standard Model Higgs boson in the diphoton decay channel with 4.9 fb^{-1} of ATLAS data at $\sqrt{s} = 7$ TeV*, Tech. Rep. ATLAS-CONF-2011-161, CERN, Geneva, Dec, 2011. https://cdsweb.cern.ch/record/1406356.

[96] C. Balazs, P. M. Nadolsky, C. Schmidt, and C. Yuan, *Diphoton background to Higgs boson production at the LHC with soft gluon effects*, Phys.Lett. **B489** (2000) 157–162, arXiv:hep-ph/9905551 [hep-ph]. http://arxiv.org/abs/hep-ph/9905551.

[97] T. Binoth, J. Guillet, E. Pilon, and M. Werlen, *A Full next-to-leading order study of direct photon pair production in hadronic collisions*, Eur.Phys.J. **C16** (2000) 311–330, arXiv:hep-ph/9911340 [hep-ph]. http://arxiv.org/abs/hep-ph/9911340.

[98] Z. Bern, L. Dixon, and C. Schmidt, *Isolating a light Higgs boson from the diphoton background at the CERN LHC*, Phys. Rev. D **66** (2002) 074018. http://arxiv.org/abs/hep-ph/0206194.

[99] Z. Bern, L. Dixon, and C. Schmidt, *The di-photon background to a light Higgs boson at the LHC*, Nuclear Physics B - Proceedings Supplements **116** no. 0, (2003) 178 – 182. http://arXiv.org/abs/hep-ph/0211216v1. Proceedings of the 6th International Symposium on Radiative Corrections and the 6th Zeuthen Workshop on Elementary Particle Theory.

[100] ATLAS HSG1 Working Group, *Search for the Higgs Boson Decaying to Two Photons with 4.9 fb^{-1}*, Tech. Rep. ATL-COM-PHYS-2011-1748, CERN, Geneva, Dec, 2011. https://cdsweb.cern.ch/record/1409761. ATLAS internal, co-authored supporting note.

[101] H. Abreu, M. Aurousseau, B. Brelier, Q. Buat, F. Bucci, L. Carminati, O. Davignon, R. Daya, S. De Cecco, M. Delmastro, J. De Vivie, M. Dova, M. Escalier, M. Fanti, M. Fayard, M. Hance, R. Ishmukhametov, M. Jimenez Belenguer, M. Kado, M. Kataoka, T. Koffas, I. Koletsou, M. Kuna, R. Lafaye, S. Laplace, G. Marchiori, K. Peters, F. Polci, L. Roos, J. Schaarschmidt, M. Stockton, H. Torres, M. Tripiana, R. Turra, G. Unal, H. Williams, and L. Yuan, *Measurement of isolated di-photon cross section in pp collision at s = 7 TeV with the ATLAS detector*, Tech. Rep. ATL-PHYS-INT-2011-071, CERN, Geneva, Sep, 2011. https://cdsweb.cern.ch/record/1381549. ATLAS internal.

[102] ATLAS Collaboration, The ATLAS Collaboration, *Measurement of the isolated di-photon cross-section in pp collisions at sqrt(s) = 7 TeV with the ATLAS detector*, Phys.Rev. **D85** (2012) 012003, arXiv:1107.0581 [hep-ex].

[103] The ATLAS Collaboration, *Measurement of the inclusive isolated prompt photon cross section in pp collisions at $\sqrt{s} = 7$ TeV with the ATLAS detector*, Phys. Rev. D **83** (2011) 052005.

[104] Auxiliary material to Ref. [155]
https://atlas.web.cern.ch/Atlas/GROUPS/PHYSICS/PAPERS/HIGG-2011-04/.

[105] ATLAS HSG1 Working Group, *Observation of an excess of events in the search for the Standard Model Higgs boson in the gamma-gamma channel with the ATLAS detector*, Tech. Rep. ATLAS-CONF-2012-091, CERN, Geneva, Jul, 2012. https://cdsweb.cern.ch/record/1460410.

[106] M. Cacciari and G. P. Salam, *Pileup subtraction using jet areas*, Phys.Lett. **B659** (2008) 119–126, arXiv:0707.1378 [hep-ph].

[107] M. Cacciari, G. Salam, and S. Sapeta, *On the characterisation of the underlying event*, Journal of High Energy Physics **2010** (2010) 1–42, arXiv:0912.4926.

[108] W. Lampl, S. Laplace, D. Lelas, P. Loch, H. Ma, S. Menke, S. Rajagopalan, D. Rousseau, S. Snyder, and G. Unal, *Calorimeter Clustering Algorithms: Description and Performance*, Tech. Rep. ATL-LARG-PUB-2008-002. ATL-COM-LARG-2008-003, CERN, Geneva, Apr, 2008. https://cdsweb.cern.ch/record/1099735/files/larg-pub-2008-002.pdf.

[109] S. Laplace and J. de Vivie, *Calorimeter isolation and pile-up*, Tech. Rep. ATL-COM-PHYS-2012-467, CERN, Geneva, May, 2012. https://cdsweb.cern.ch/record/1444890.

[110] The ATLAS experiment, "Calorimeter isolation corrections." https://twiki.cern.ch/twiki/bin/viewauth/AtlasProtected/CaloIsolationCorrections. ATLAS internal.

[111] The ATLAS Collaboration, *Performance of the ATLAS Trigger System in 2010*, The European Physical Journal C - Particles and Fields **72** (2012) 1–61, arXiv:1110.1530. http://dx.doi.org/10.1140/epjc/s10052-011-1849-1. 10.1140/epjc/s10052-011-1849-1.

[112] ECFA Higgs working group, C.Seez, T. Virdee, L. DiLella, R.Kleiss, Z.Kunszt, and W.J.Stirling, *Photon decay modes of the intermediate mass Higgs*,. http://cdsweb.cern.ch/record/220524/files/p474.pdf.

[113] DELPHI Collaboration, A. L. Read, *Optimal Statistical Analysis of Search Results based on the Likelihood Ratio and its Application to the Search for the MSM Higgs Boson at 161 and 172 GeV*, DELPHI 97-158 PHYS 737 (1997) 37. delphiwww.cern.ch/pubxx/delnote/public/97_158_phys_737.ps.gz.

[114] The CMS Collaboration, *Search for the standard model Higgs boson decaying into two photons in pp collisions at sqrt(s)=7 TeV*, Phys.Lett. **B710** (2012) 403–425, arXiv:1202.1487 [hep-ex].

[115] The ATLAS Collaboration, *Search for the Higgs boson in the diphoton final state with 38 pb^{-1} of data recorded by the ATLAS detector in proton-proton collisions at $\sqrt{s}$ = 7 TeV*, Tech. Rep. ATLAS-CONF-2011-025, CERN, Geneva, Mar, 2011. `https://cdsweb.cern.ch/record/1336758`. Note that the sentence regarding the primary vertex, in Section 2 (Data Sample); "(...) the vertex associated with tracks having the highest sum of p_T is used", is wrong. The correct statement would be sum of p_T^2.

[116] ATLAS HSG1 Working Group, *Search for the Higgs boson in the diphoton final state with 38 pb^{-1} of data recorded by the ATLAS detector at $\sqrt{s}$ = 7 TeV*, Tech. Rep. ATL-PHYS-INT-2011-024, CERN, Geneva, Mar, 2011. `https://cdsweb.cern.ch/record/1336475`. ATLAS internal, co-authored supporting note.

[117] ATLAS Collaboration, The ATLAS Collaboration, *Search for the Standard Model Higgs boson in the two photon decay channel with the ATLAS detector at the LHC*, Phys.Lett. **B705** (2011) 452–470, `arXiv:1108.5895 [hep-ex]`.

[118] ATLAS HSG1 Working Group, *Signal studies for Higgs to gamma gamma*, Tech. Rep. ATL-COM-PHYS-2011-781, CERN, Geneva, Jun, 2011. `https://cdsweb.cern.ch/record/1361986`. ATLAS internal, co-authored supporting note.

[119] M. Escalier, L. Fayard, and J.-F. Marchand, *Reconstruction of the z vertex and direction of the photon*, Tech. Rep. ATL-PHYS-INT-2010-013, CERN, Geneva, Jan, 2010. `https://cdsweb.cern.ch/record/1235791`.

[120] ATLAS HSG1 Working Group, *Search for the Higgs Boson Decaying to Two Photons with 4.9 fb^{-1}*, Tech. Rep. ATL-COM-PHYS-2011-1600, CERN, Geneva, Nov, 2011. `https://cdsweb.cern.ch/record/1399646`. ATLAS internal, co-authored supporting note.

[121] The ATLAS Collaboration, *Search for the Standard Model Higgs boson in the diphoton decay channel with 4.9 fb^{-1} of pp collisions at sqrt(s)=7 TeV with ATLAS*, Phys.Rev.Lett. **108** (2012) 111803, `arXiv:1202.1414 [hep-ex]`.

[122] "HSG1 winter 2012, selection, categorization, etc.." `https://twiki.cern.ch/twiki/bin/viewauth/AtlasProtected/HSG1WinterConf2012`. , ATLAS internal.

[123] `https://twiki.cern.ch/twiki/bin/viewauth/AtlasProtected/LArCleaningAndObjectQuality`. ATLAS internal.

[124] Q. Buat, J. Leveque, N. Lorenzo Martinez, F. Polci, and B. Trocme, *Definition of the photon cleaning procedure for 2011 data*, Tech. Rep. ATL-COM-PHYS-2012-134, CERN, Geneva, Feb, 2012. `https://cdsweb.cern.ch/record/1422649/`. ATLAS internal.

[125] ATLAS HSG1 Working Group, *Improved analysis of the Search for the Higgs Boson Decaying to Two Photons with 4.9 fb-1 of 7 TeV data.*, Tech. Rep. ATL-COM-PHYS-2012-502, CERN, Geneva, May, 2012. `https://cdsweb.cern.ch/record/1447437`. ATLAS internal, co-authored supporting note.

[126] "HSG1 april notes 2012, selection, acceptance challenge etc.." https://twiki.cern.ch/twiki/bin/viewauth/AtlasProtected/HSG1AprilNote2012. ATLAS internal.

[127] ATLAS HSG1 Working Group, *Search for the Higgs boson in the diphoton decay channel with data collected at 7 TeV and 8 TeV*, Tech. Rep. ATL-COM-PHYS-2012-503, CERN, Geneva, May, 2012. https://cdsweb.cern.ch/record/1447438. ATLAS internal, co-authored supporting note.

[128] M. Vesterinen and T. Wyatt, *A novel technique for studying the Z boson transverse momentum distribution at hadron colliders*, Nuclear Instruments and Methods in Physics Research Section A: Accelerators, Spectrometers, Detectors and Associated Equipment **602** no. 2, (2009) 432 – 437, arXiv:0807.4956.

[129] T. Gleisberg, S. Hoeche, F. Krauss, M. Schonherr, S. Schumann, et al., *Event generation with SHERPA 1.1*, JHEP **0902** (2009) 007, arXiv:0811.4622 [hep-ph].

[130] M. L. Mangano, M. Moretti, F. Piccinini, R. Pittau, and A. D. Polosa, *ALPGEN, a generator for hard multiparton processes in hadronic collisions*, JHEP **0307** (2003) 001, arXiv:hep-ph/0206293 [hep-ph].

[131] https://atlas.web.cern.ch/Atlas/GROUPS/PHYSICS/CONFNOTES/ATLAS-CONF-2012-091/. Auxiliary material to Ref. [105].

[132] ATLAS Collaboration, G. Aad et al., *Combined search for the Standard Model Higgs boson in pp collisions at $\sqrt{s} = 7$ TeV with the ATLAS detector*, Phys.Rev. **D86** (2012) 032003, arXiv:1207.0319 [hep-ex].

[133] The ATLAS Collaboration, the CMS Collaboration and the LHC Higgs Combination Group, *Procedure for the LHC Higgs boson search combination in summer 2011,*. https://cds.cern.ch/record/1375842.

[134] ATLAS statistics forum, *Frequentist Limit Recommendation*, Tech. Rep. Draft 1.6, CERN, Geneva, June 21, 2011. https://twiki.cern.ch/twiki/pub/AtlasProtected/StatisticsTools/Frequentist_Limit_Recommendation.pdf. ATLAS internal.

[135] E. G. Glen Cowan, Kyle Cranmer and O. Vitells, *Asymptotic formulae for likelihood-based tests of new physics*, Eur.Phys.J. C71:1554 (2011) 32, arXiv:1007.1727v2.

[136] A. L. Read, *Presentation of search results: The CL(s) technique*, J.Phys.G **G28** (2002) 2693–2704.

[137] E. Gross and O. Vitells, *Trial factors or the look elsewhere effect in high energy physics*, Eur.Phys.J. **C70** (2010) 525–530, arXiv:1005.1891 [physics.data-an].

[138] ATLAS HSG1 Working Group, *Signal studies in H to gamma gamma search with 4.9 fb^{-1} of 7 TeV data.*, Tech. Rep. ATL-COM-PHYS-2012-501, CERN, Geneva, May, 2012. https://cdsweb.cern.ch/record/1447436/. ATLAS internal, co-authored supporting note.

[139] ATLAS HSG1 Working Group, *Statistics studies for H to gamma gamma search in the full 2011 dataset*, Tech. Rep. ATL-COM-PHYS-2012-732, CERN, Geneva, Jun, 2012. https://cdsweb.cern.ch/record/1453249. ATLAS internal, co-authored supporting note.

[140] ATLAS Collaboration Collaboration, G. Aad et al., *Electron performance measurements with the ATLAS detector using the 2010 LHC proton-proton collision data*, Eur.Phys.J. **C72** (2012) 1909, arXiv:1110.3174 [hep-ex].

[141] ATLAS HSG1 Working Group, *Background Studies for the Search of Higgs Boson Decaying to Two Photons with 4.9 fb^{-1} of 7 TeV data with the ATLAS Experiment*, Tech. Rep. ATL-COM-PHYS-2012-515, CERN, Geneva, May, 2012. https://cdsweb.cern.ch/record/1447803. ATLAS internal, co-authored supporting note.

[142] T. Skwarnicki, *A study of the radiative cascade transitions between the Upsilon-prime and Upsilon resonances*, DESY-F31-86-02 (1986). http://inspirehep.net/record/230779/files/f31-86-02.pdf. Appendix E, Ph.D. Thesis.

[143] J. E. Gaiser, *Charmonium Spectroscopy from Radiative Decays of the J/Psi and Psi-Prime*, SLAC-R-255 (1982) 178. http://www.slac.stanford.edu/cgi-wrap/getdoc/slac-r-255.pdf. Appendix F, Ph.D. Thesis.

[144] M.J.Oreglia, *A Study of the Reactions psi prime → gamma gamma psi*, SLAC-236 (1980). http://www.slac.stanford.edu/cgi-wrap/getdoc/slac-r-236.pdf. Appendix D, Ph.D. Thesis.

[145] "DIPHOX - a program to calculate the hadroproduction of two photons at NLO." http://lapth.in2p3.fr/PHOX_FAMILY/diphox.html. Homepage.

[146] "Resbos - calculation of resummed initial-state contributions in unpolarized drell-yan-like processes at hadron-hadron colliders." http://hep.pa.msu.edu/resum/. Homepage.

[147] "Sherpa - monte carlo event generator for the simulation of high-energy reactions of particles in lepton-lepton, lepton-photon, photon-photon, lepton-hadron and hadron-hadron collisions." http://www.sherpa-mc.de/. Homepage.

[148] G. Phillips, *Interpolation and Approximation by Polynomials*. Springer, 2003. Chapter 7, Bernstein Polynomials.

[149] J. Neyman and E. S. Pearson, *On the Problem of the Most Efficient Tests of Statistical Hypotheses*, Philosophical Transactions of the Royal Society of London. Series A, Containing Papers of a Mathematical or Physical Character **231** (1933) pp. 289–337. http://www.jstor.org/stable/91247.

[150] Auxiliary material to Ref. [121] https://atlas.web.cern.ch/Atlas/GROUPS/PHYSICS/PAPERS/HIGG-2012-02/.

[151] The ATLAS Collaboration, *Measurement of the backgrounds to the $H \to \gamma\gamma$ search and reappraisal of its sensitivity with 37 pb^{-1} of data recorded by the ATLAS detector*, Tech. Rep. ATLAS-CONF-2011-004, CERN, Geneva, Feb, 2011. https://cdsweb.cern.ch/record/1327196.

[152] ATLAS HSG1 Working Group, *Study of the Di-Photon Backgrounds to the $H \to \gamma\gamma$ Search with the ATLAS detector at sqrts= 7 TeV*, Tech. Rep. ATL-PHYS-INT-2011-011, CERN, Geneva, Feb, 2011. https://cdsweb.cern.ch/record/1331810. ATLAS internal, co-authored supporting note.

[153] K. Peters, *Search for the Higgs boson in the $\gamma\gamma$ final state at the Tevatron*, PoS ICHEP2010 (2010) 071, arXiv:1009.0859 [hep-ex].

[154] ATLAS Collaboration, G. Aad et al., *Search for the Higgs Boson in the Diphoton Channel with the ATLAS Detector using 209 pb^{-1} of 7 TeV Data taken in 2011*,. https://cds.cern.ch/record/1356193.

[155] ATLAS Collaboration, G. Aad et al., *Search for the Standard Model Higgs boson in the two photon decay channel with the ATLAS detector at the LHC*, Phys.Lett. **B705** (2011) 452–470, arXiv:1108.5895 [hep-ex].

[156] ATLAS HSG1 Working Group, *Search for the Higgs Boson in the Diphoton Decay Channel with 1.08 fb^{-1}*, Tech. Rep. ATL-COM-PHYS-2011-786, CERN, Geneva, Jun, 2011. https://cds.cern.ch/record/1362003. ATLAS internal, co-authored supporting note.

[157] ATLAS HSG1 Working Group, *Background Studies for Higgs to gamma-gamma*, Tech. Rep. ATL-COM-PHYS-2011-782, CERN, Geneva, Jun, 2011. https://cds.cern.ch/record/1361987. ATLAS internal, co-authored supporting note.

[158] ATLAS HSG1 Working Group, *Signal studies for Higgs to gamma gamma*, Tech. Rep. ATL-COM-PHYS-2011-781, CERN, Geneva, Jun, 2011. https://cds.cern.ch/record/1361986. ATLAS internal, co-authored supporting note.

[159] ATLAS HSG1 Working Group, *Statistical studies for Higgs to gamma gamma*, Tech. Rep. ATL-COM-PHYS-2011-783, CERN, Geneva, Jun, 2011. https://cds.cern.ch/record/1361988. ATLAS internal, co-authored supporting note.

[160] Auxiliary material to Ref. [5] https://atlas.web.cern.ch/Atlas/GROUPS/PHYSICS/PAPERS/HIGG-2012-27/.

[161] The ATLAS Collaboration, *Observation and study of the Higgs boson candidate in the two photon decay channel with the ATLAS detector at the LHC*, Tech. Rep. ATLAS-CONF-2012-168, CERN, Geneva, Dec, 2012. http://cdsweb.cern.ch/record/1499625.

[162] The CMS Collaboration, *Evidence for a new state decaying into two photons in the search for the standard model Higgs boson in pp collisions*,. https://cds.cern.ch/record/1460419.

[163] Science Magazine, *Breakthrough of the Year, 2012*, Dec, 2012. http://www.sciencemag.org/site/special/btoy2012/.

[164] ATLAS Collaboration, G. Aad et al., *A Particle Consistent with the Higgs Boson Observed with the ATLAS Detector at the Large Hadron Collider*, Science **338** (2012) 1576–1582.

[165] CMS Collaboration, S. Chatrchyan et al., *A New Boson with a Mass of 125 GeV Observed with the CMS Experiment at the Large Hadron Collider*, Science **338** (2012) 1569–1575.

[166] The ATLAS Collaboration, *An update of combined measurements of the new Higgs-like boson with high mass resolution channels*,. `http://cdsweb.cern.ch/record/1499629`.

[167] The CMS Collaboration, *Combination of standard model Higgs boson searches and measurements of the properties of the new boson with a mass near 125 GeV*,. `http://cds.cern.ch/record/1494149`.

[168] The ATLAS Experiment, "ATLAS Authorship policy." `https://twiki.cern.ch/twiki/bin/viewauth/AtlasProtected/AuthorShipCommittee`. ATLAS internal, containing Authorship Policy Document.

[169] "The svn repository for the online/offline egamma trigger histogram monitoring tool." `https://svnweb.cern.ch/trac/atlasoff/browser/Trigger/TrigAnalysis/TrigEgammaAnalysis/TrigEgammaMacros/`. ATLAS internal.

[170] "The svn repository for the run-by-run tool for efficiency of egamma triggers." `https://svnweb.cern.ch/trac/atlasoff/browser/Trigger/TrigAnalysis/TrigEgammaAnalysis/TrigEgammaD3PD/`. ATLAS internal.